Measurement of the Light Flux of Stars and the Night-Sky with Silicon Photomultipliers

Von der Fakultät für Mathematik, Informatik und Naturwissenschaften der RWTH Aachen University zur Erlangung des akademischen Grades eines Doktors der Naturwissenschaften genehmigte Dissertation vorgelegt von

Diplom-Physiker
Eugène Antoine Maurice Stephan
aus Tegelen, Niederlande

Berichter: Universitätsprofessor Dr. rer. nat. Thomas Hebbeker
Universitätsprofessor Dr. rer. nat. Martin Erdmann

Tag der mündlichen Prüfung: 15. Dezember 2014

Per aspera ad astra.

- Seneca

Contents

1. Introduction

Even more than 100 years after the discovery of cosmic rays by V. Hess in 1912 [1], their study is still a vivid field of research and their existence retains a couple of mysteries. *Cosmic rays* are charged particles originating from space which permanently hit the atmosphere of Earth. By interaction of these high-energetic particles with atmospheric nuclei, cascades of secondary particles are created which can be observed at ground. Such a cascade is referred to as an *extensive air shower* and was first observed by P. Auger in 1938 [2].

Until now a huge variety of ground-based, airborne, and spaceborne experiments have measured the energy spectrum of cosmic rays which covers more than 30 orders of magnitude in flux and more than 10 orders of magnitude in energy. Particles with energies higher than $10^{20}\,\mathrm{eV}$ have been observed — energies far beyond of those which man-made particle accelerators are able to reach.

However, the flux of cosmic rays of the highest energies is very low. At an energy of $10^{15}\,\mathrm{eV}$ one particle per m^2 per year can be measured, at $10^{18.5}\,\mathrm{eV}$ it is only one particle per km^2 per year. Thus, giant ground-based detectors are needed to observe a significant number of ultra-high-energy cosmic rays which are defined as these cosmic rays whose energies exceed $10^{18}\,\mathrm{eV}$.

While for energies up to about $10^{14}\,\mathrm{eV}$ cosmic rays originate from our own galaxy and are believed to be accelerated in supernova remnants, little is known about the origin of cosmic rays of the highest energies. Fundamental questions regarding their sources and acceleration mechanism, the cause for the flux suppression at the upper end of the energy spectrum, as well as the chemical composition of cosmic rays are still subjects of current research.

An appropriate cosmic ray observatory thus measures the energy and arrival direction of the particle which enters the atmosphere as well as its type. Established detection methods are the measurement of secondary particles at ground level, as well as the observation of fluorescence light caused by air showers. The first method has the advantage of an duty cycle of 100%, whereas just the lateral shower distribution can be detected. On the contrary, fluorescence light detection is able to observe the longitudinal shower development. The price to pay is a significantly reduced duty cycle of about 15% since this technique can only be employed during dark, moonless nights. The largest hybrid detector taking advantage of both detection techniques is the Pierre Auger Observatory. It instruments $3000\,\mathrm{km}^2$ of the Pampa

Amarilla close to Malargüe in the province of Mendoza, Argentina. The observatory acquires high-quality data since 2004 and is raring to pursue its mission for another decade. In addition to the well established detectors both upgrades and alternative measurement techniques are investigated.

The joint research project AugerNext is dedicated to innovative research studies for the next generation ground-based ultra-high-energy cosmic ray experiment. These studies performed at the Pierre Auger Observatory are a principal element of the ASPERA/ApPEC strategic roadmap [3].
Within the scope of AugerNext the test of a large scale application of new generation photosensors is studied. Besides high quantum efficiency photomultiplier tubes, novel kinds of photodiodes referred to as silicon photomultipliers (SiPMs) are studied.

Regarding the observation of cosmic rays by means of fluorescence light detection, SiPMs seem to be very promising photosensors. Recent types possess photon detection efficiencies of about 60% featuring single photon detection and resolution. Together with their rather small sizes SiPMs will likely lead to innovative designs of fluorescence telescopes with higher efficiencies, better angular resolutions, and higher duty cycles. Their property to be semiconductor devices holds the potential for cost efficient mass production, and many prospective technological improvements.

To study the feasibility of a fluorescence telescope instrumented with SiPMs, the small prototype FAMOUS (First Auger Multi-pixel photon counter camera for the Observation of Ultra-high-energy air showers) has been designed and recently constructed. Like all fluorescence telescopes FAMOUS is intended to measure fluorescence signals with a continuous luminous night-sky background. To evaluate a certain design of a fluorescence telescope, the knowledge of the diffuse night-sky brightness is crucial, since it defines the sensitivity for measurements of air showers. The light originating from stars is also of great interest since those stars, which are well-studied by observational astronomy, can be regarded as calibrated reference light sources.

In general these measurements can be performed with conventional photosensors like photomultiplier tubes or CCD-sensors, but the use of SiPMs offers the benefit to gain a deeper understanding of these novel photosensors and results in data directly applicable to an evaluation of FAMOUS. Still this choice means that a reliable reconstruction of continuous light fluxes detected with SiPMs is required.

This thesis makes progress in reconstructing these continuous light fluxes measured with SiPMs. An experimental setup of a one-pixel-SiPM-telescope has been realized in parallel to the design phase of FAMOUS to measure the light flux of stars and the diffuse night-sky background. The acquired data are analyzed with a photon counting method, especially developed for the reconstruction of continuous light fluxes. Since the employed SiPM is not cross-calibrated with a reference sensor, extensive, related characterization studies are performed to yield in a reliable result.

The following chapter 2 will give a short introduction to cosmic rays and extensive air showers, whereas chapter 3 will present their detection using the Pierre Auger Observatory as a prime example. Here, special attention will be given to the fluorescence detection technique. Chapter 4 introduces SiPMs. Their light detection principle, major advantages compared to other photosensors, but also drawbacks, as well as recent technological innovations are discussed. FAMOUS, the first fluorescence telescope instrumented with SiPMs, will be introduced in chapter 5. In chapter 6 the setup to measure the night-sky brightness is discussed and the principal idea how to reconstruct the measured light flux is introduced. Conjoined characterization studies of SiPMs and the reconstruction analysis itself are presented in chapter 7. The comparison of the results to astronomical reference models is discussed in chapter 8. Chapter 9 will summarize this work and give an outlook towards further studies.

2. Ultra-High-Energy Cosmic Rays and Extensive Air Showers

Observing the sky and drawing conclusions from the motion of celestial objects is as old as mankind itself. The deep desire to understand what surrounds us, has led to many great breakthroughs and innovations in history, for example the concept of heliocentrism which rejected the Earth from being the center of the universe.
For ages astronomers were limited to the observation of visible light. In the beginning of the 19^{th} century the window to the cosmos extended when infrared radiation was discovered. At this time the exploration of the absorption lines in the spectrum of the Sun and their explanation within the following decades, created the basis for modern astronomy. And with it astrophysics, a new area of astronomy, was born.

In the first half of the 20^{th} century, the window to the cosmos further expanded when x-rays were discovered and the first radio signals from the center of our galaxy were observed.
Already at this time a completely new window had opened, although it should take more than half a century until it became established in astronomy: in 1912 during his famous balloon flights V. Hess found that the conductivity of air steadily increased the higher his balloon ascended, once he had reached a certain altitude [1]. This had to be caused by ionizing radiation originating from space — cosmic rays were discovered.

The history of elementary particle physics is strongly connected to the study of cosmic rays. For instance positrons, as well as muons and pions have been first observed in experiments measuring cosmic rays. Most definitions describe cosmic rays as charged particles originating from space. Thus, the mentioned positrons, muons, and pions should be referred to as secondary particles to make a difference to the primary particle which has propagated through space. These secondary particles are part of extensive air showers which can — depending on the energy of the primary particle — spread among a wide area at ground level of the order of square kilometers. The first to observe these air showers was P. Auger in 1938 [2].

The idea that the spectrum of cosmic rays might extend to energies far beyond those which can be reached with man-made particle accelerators, leveraged the study of cosmic rays to a separate research field. Today, astroparticle physics is the link between elementary particle physics, astrophysics, and cosmology and provides a new astronomical window to the cosmos besides the observation of electromagnetic radiation.

Astroparticle physics not exclusively concentrates on the observation of cosmic rays but also of photons and neutrinos. These uncharged particles are not deflected by magnetic fields during their propagation to Earth, and thus point back to their sources. These might be the same sources as for the charged particles, since many models of acceleration of cosmic rays produce high-energy photons and neutrinos. Further cornerstones of astroparticle physics are searches for dark matter and gravitational waves.

Many progress was made in the study of cosmic rays since their discovery about one hundred years ago. But especially for ultra-high-energy cosmic rays (UHECRs) with energies exceeding $10^{18}\,\mathrm{eV}$ many questions remain. The central ones concern the atomic masses of the primary particles, their propagation through space, and the objects which can accelerate particles to such high energies, likely the most prominent mystery in cosmic rays physics.

2.1 Energy spectrum

The energy spectrum of cosmic rays has been measured by a huge variety of experiments. Data of some of these experiments are shown in figure 2.1. Direct measurements for energies $E \lesssim 10^{15}\,\mathrm{eV}$ are performed with balloon- or satellite-based detectors. By observing extensive air showers at ground, indirect measurements are performed for $E \gtrsim 10^{14}\,\mathrm{eV}$.
Below $10^{10}\,\mathrm{eV}$ the flux of cosmic rays $J(E)$ is modulated by solar magnetic fields. For higher energies it is non-thermal and follows a *broken power law* for about ten orders of magnitude:

$$J(E) = \frac{\mathrm{d}^2\phi(E)}{\mathrm{d}E\,\mathrm{d}\Omega} \sim \left(\frac{E}{\mathrm{eV}}\right)^{-\gamma} . \tag{2.1}$$

Here γ is the spectral index. The power law is *broken* since γ varies with the energy range. Around $E = 10^{15.5}\,\mathrm{eV}$ it changes from 2.7 at lower energies to 3.1. This region is referred to as the *knee*. At about $10^{18.5}\,\mathrm{eV}$ the spectrum gets harder with γ changing back to 2.7. Here the spectrum has its *ankle*. At about $5 \cdot 10^{19}\,\mathrm{eV}$ the flux of cosmic rays steeply decreases. In order to visually emphasize these features, the flux shown in the right plot of figure 2.1 is multiplied by $E^{2.7}$.

The reason for the change of the spectral index at the knee is still not fully understood. Possible explanations are typically grouped in four classes [4]: (i) the maximum energy to which certain sources can accelerate cosmic rays is reached, (ii) cosmic rays escape from our galaxy during their diffusive propagation process, (iii) the cosmic rays interact with background particles during propagation, and (iv) new physics include interactions within the atmosphere which carry away energy into hidden channels.
If the third class would be the cause of the knee, nuclei with higher atomic numbers would break up leading to lighter nuclei. Thus, a rather light composition around the knee consisting mainly of protons and α-particles would be expected. But the opposite is the case. Recent data indicate a rather high and increasing mass through

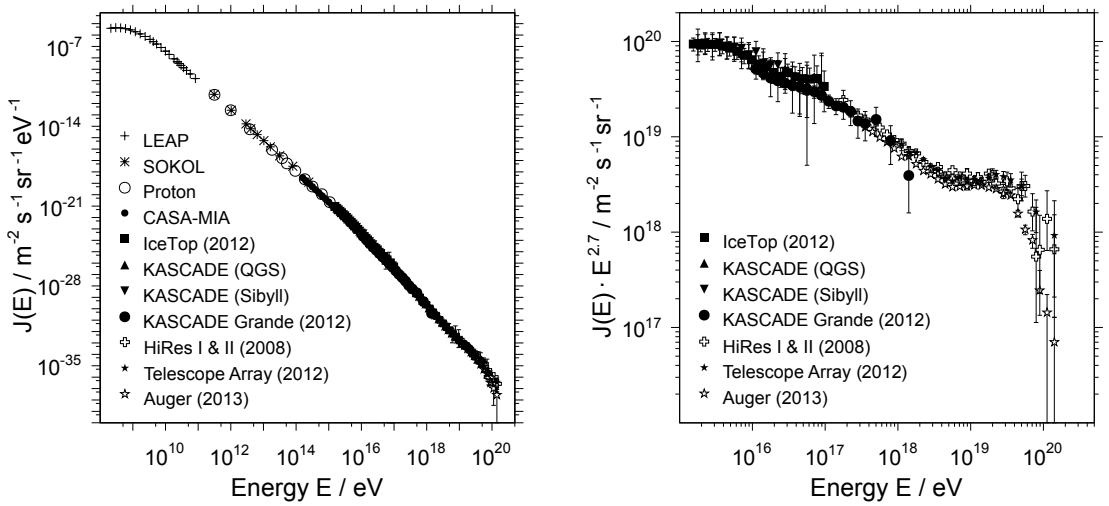

Figure 2.1: **Left:** Differential flux J of cosmic rays as a function of the energy E measured with the airborne experiment LEAP [7], the spaceborne experiments SOKOL [8] and Proton [9], and with the ground-based experiments CASA-MIA [10], IceTop [11], KASCADE [12] and KASCADE Grande [13], HiRes I & II [14], the Telescope Array [15], and the Pierre Auger Observatory [16]. **Right:** The same data as in the left plot, but the flux is scaled by $E^{2.7}$. Only the higher energies are displayed. Original plots, data assembled from the quoted references.

the knee (see section 2.3). The fourth class can also be disregarded by taking recent results into account: data from the air shower experiment KASCADE-Grande have been used to check predictions of hadronic interaction models. These predictions agree with the measurements on a 10% level [5], and there is little room to hide for new physics occuring during air shower development at the energies of the knee. Furthermore, data from the Large Hadron Collider at 7 TeV are in good agreement with the predictions from the hadronic interaction models [6]. The change of the spectral index at the knee is more likely to be caused by some astrophysical reason and might be a combination of (i) and (ii). For a detailed discussion of various scenarios and comparisons of models with data please refer to [4].

As already mentioned in (ii) cosmic rays can escape from our galaxy. The cause which keeps them bound to it in the first place is the galactic magnetic field. The Larmor radius R_L of a particle with charge number Z and energy E in a magnetic field of strength B is given by[1]

$$\left(\frac{R_L}{\mathrm{kpc}}\right) \approx 1.1\,\frac{1}{Z}\,\left(\frac{E}{10^{18}\,\mathrm{eV}}\right)\left(\frac{B}{\mu\mathrm{G}}\right)^{-1}. \tag{2.2}$$

The magnetic field strength of our galaxy is in the order of μG [17]. A proton with an energy of 10^{18} eV has a Larmor radius sufficiently large to escape from it, since the size of the galaxy is in the order of kpc. From this simple consideration emerges

[1] parsec: $1\,\mathrm{pc} = 3.086 \cdot 10^{16}\,\mathrm{m}$, Gauss: $1\,\mathrm{G} = 10^{-4}\,\mathrm{T}$

the conclusion, that at the ankle a transition from galactic to extra-galactic sources might take place. With rising energy more and more particles are able to leave our galaxy. Contrariwise, particles from other galaxies are able to reach us.

At several 10^{19} eV the flux of cosmic rays rapidly decreases. Already in 1966 K. Greisen, G. T. Zatsepin, and V. A. Kuzmin predicted this fall-off due to interactions of protons with the cosmic microwave background (CMB) [18, 19]. The suppression of the proton flux is thus called *GZK-effect*. The dominant process is the creation of a Δ^+ resonance with subsequent decay into nucleons and pions.

$$\begin{array}{rcll} p + \gamma_{\mathrm{CMB}} & \longrightarrow & \Delta^+ & \longrightarrow \quad n + \pi^+ \\ & & \Delta^+ & \longrightarrow \quad p + \pi^0 \end{array}$$

If the energy of a proton propagating through space is high enough to produce a pion, it will lose part of its energy. This energy loss iterates during propagation until the energy of the proton is insufficient to create another pion. The GZK-effect introduces a horizon for protons of the highest energies. For instance all protons with energies greater than 10^{20} eV should originate from sources closer than 100 Mpc (see e.g. figure 3 in reference [20]).
The interaction of havier nuclei of the cosmic rays with the CMB leads to their excitation and subsequent photodisintegration [21, 22].
In contrats to interactions of cosmic rays with the CMB, their flux suppression at the upper end of the spectrum might also be due to a cutoff in the reachable energy of cosmic accelerators. Anyhow, the truth might be a combination of these two effects.

2.2 Origin of ultra-high-energy cosmic rays

The steady shape of the cosmic ray spectrum over about ten orders of magnitude in energy might suggest the assumption that the acceleration mechanism is the same for all energies. However, even with this assumption sources do not necessarily have to be of the same type for all energy intervals.

In 1949 E. Fermi proposed the acceleration of cosmic rays in large-scale magnetic fields [24]. From his work, the currently accepted diffusive shock acceleration (or first-order Fermi acceleration) model emerged. Here, cosmic rays gain their energy in shock fronts which appear for instance in supernova remnants.
When a charged particle moves upstream through the shock front (i.e. from the un-shocked region to the shocked region) it can be reflected by the magnetic field. When the particle then crosses the shock front downstream is can also be reflected by the field. This cycle continues until the particle is not scattered back into the un-shocked region. On average it will gain energy with each cycle of crossing the shock front. There is a certain probability that the particle is not back-scattered and thus escapes the accelerating region. Hence, the particles which stay longer within the shock zone are those which possess higher energies. The gain of energy is proportional to the velocity of the shock front. This is the reason for the expression

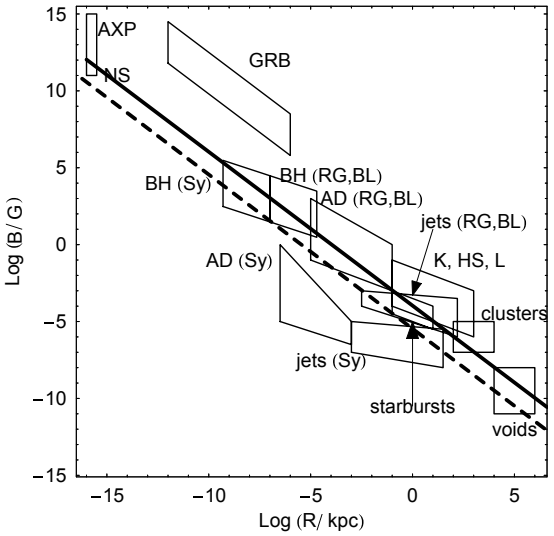

Figure 2.2: The Hillas plot — parameter space of radius R and magnetic field strength B. The thick solid line represents the lower boundary of the area allowed by the Hillas criterion given by equation (2.3) with $\beta = 1$ for a 10^{20} eV proton. The dashed line corresponds to a 10^{20} eV iron nucleus. The boxes display potential sources of cosmic rays: anomalous x-ray pulsars and magnetars (AXP), neutron stars (NS), gamma-ray bursts (GRB), super-massive black holes (BH) of active galactic nuclei from low-power Seyfert galaxies (Sy) to powerful radio galaxies (RG) and blazars (BL), the central parsec (AD) of active galaxies, relativistic jets (jets), knots (K), hot spots (HS) and lobes (L) of powerful active galaxies, non-relativistic jets of low-power galaxies (Sy), starburst galaxies, galaxy clusters, and inter-cluster voids. Adapted, original taken from reference [23].

first order Fermi acceleration.
The loss probability yields a power law spectrum which is slightly harder than the one observed at Earth, but the discrepancy can be explained by diffusion of cosmic rays out of the galaxy or other propagation models (see e.g. reference [25]).

Recent related results from the very-high-energy γ-ray telescopes H.E.S.S. [26, 27] are obtained from a detailed analysis of supernova remnant RX J1713.7-3946.
The measured spectral index is very close to the one predicted by diffusive shock acceleration. In addition, the photon flux fits well to a model in which hadrons interact with interstellar matter to neutral pions, which subsequently decay to photons. This flux clearly dominates electromagnetic emission caused by inverse Compton scattering and non-thermal bremsstrahlung in the region of the supernova remnant [17]. The observed photons have energies up to about 10^{14} eV, thus, there is a hint for supernova remnants being accelerators of cosmic rays up to at least these energies.

The greater the size R_s of a cosmic accelerator and its magnetic field strength B are, the longer a cosmic ray can experience diffusive shock acceleration. Therefore, it is clear that the accelerator can only produce particles with energies up to a

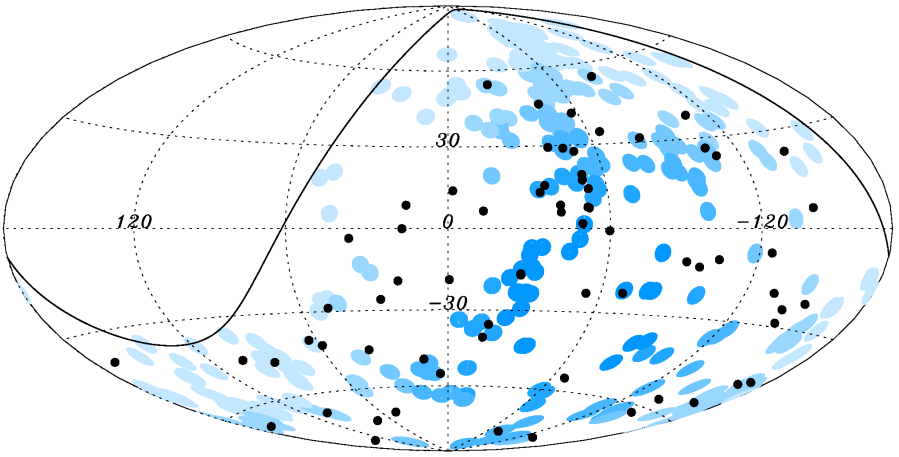

Figure 2.3: The 69 arrival directions of cosmic rays with energy $E > 55\,\mathrm{EeV}$ detected by the Pierre Auger Observatory up to December 31, 2009 are plotted as black dots in an Aitoff-Hammer projection of the sky in galactic coordinates. The solid line represents the border of the field of view of the observatory for zenith angles of arrival directions smaller than 60°. Blue circles of radius 3.1° are centered at the positions of the 318 AGN in the Veron–Cetty & Veron catalog that lie within 75 Mpc and that are within the field of view of the Observatory. Darker blue indicates larger relative exposure. Taken from reference [28].

maximum energy E_{max}. This energy can be calculated from equation (2.2) taking β, the velocity of the accelerating region divided by the speed of light into account:

$$\left(\frac{E_{\mathrm{max}}}{10^{18}\,\mathrm{eV}}\right) \approx 0.9\,\beta\,Z\,\left(\frac{B}{\mu\mathrm{G}}\right)\left(\frac{R_{\mathrm{s}}}{\mathrm{kpc}}\right) \tag{2.3}$$

A. M. Hillas has been the first to plot different astronomical objects in the parameter space of R_{s} and B to evaluate whether they can produce cosmic rays of a certain energy [29]. Such a Hillas plot is shown in figure 2.1. The solid line represents equation (2.3) with $\beta = 1$ for a $10^{20}\,\mathrm{eV}$ proton, the dashed line for an iron nucleus of the same energy. A cosmic accelerator which produces protons with this energy has to lie above the solid line.
Hence, cosmic rays of the highest energies are not likely to be produced within supernova remnants, since they have sizes in the order of 1 pc and field strengths in the order of $10^{-4}\,\mathrm{G}$ (see e.g. figure 7 in reference [30]).

Regarding the Hillas plot, active galactic nuclei (AGN) seem to be promising candidates for sources of ultra-high-energy cosmic rays.
In reference [31] the Pierre Auger Collaboration reported a directional correlation between cosmic rays of the highest energies and AGN indexed in the Veron–Cetty & Veron catalog. The first 14 events were used to adjust the search parameters to minimize the probability that a correlation could derive from an isotropic background fluctuation. The following values were found: the energy threshold $E_{\mathrm{th}} = 55\,\mathrm{EeV}$, the angular separation of a cosmic ray event and an AGN $\Psi \leq 3.1\,^{\circ}$, and the redshift $z \leq 0.018$. The latter parameter was introduced due to the horizon of UHECRs

caused by the interaction with the cosmic microwave background (cf. section 2.1). It corresponds to a maximum distance of 75 Mpc. The need for an energy threshold derives from the fact that only the arrival directions of cosmic rays of the highest energies point back towards their sources. These cosmic rays are less affected by deflections caused by intergalactic magnetic fields compared to those of lower energies. The exploratory scan succeeded 13 events which rejected the hypothesis of an isotropic distribution at the 99% confidence level. The collaboration reported that $69^{+11}_{-13}\%$ of the events correlated with AGN.
An updated sky map of the events measured with the Pierre Auger Observatory is shown in figure 2.3. The sky is depicted in an Aitoff–Hammer projection in galactic coordinates. Shown are data until 2009[2] resulting in 69 events with energies above E_{th}. They are displayed by the black dots. The blue circles have an angular size of Ψ and are centered around the 318 AGN of the Veron–Cetty & Veron catalog which have a redshift smaller than 0.018 and which lie within the field of view of the Pierre Auger Observatory. The field of view is defined by a 60° maximum zenith angle of the arrival direction of cosmic rays and is shown in the plot as the solid black line. The color intensity of the blue circles denotes the relative exposure. Darker blue denotes a larger exposure.
The most updated estimate for the fraction of correlated events has reduced to $33^{+5}_{-5}\%$ [32]. The probability that this correlation derives from an isotropic distribution of arrival directions is $P = 0.006$.
Similar searches for an AGN correlation have been performed by the ultra-high-energy cosmic ray experiments High Resolution Fly's Eye (HiRes) and Telescope Array (TA). While the HiRes data do not differ from the assumption of an isotropic sky, the TA data include 11 correlating events out of 25, while the expected number from isotropy is 5.9. The probability that this correlation is produced by chance from isotropy is $P = 0.02$ [33]. For a more detailed description and comparison, as well as further discussions of these results please refer to reference [33].

2.3 Chemical composition

In contrast to direct measurements of cosmic rays the determination of the type of the primary particle proves to be more difficult for indirect measurements. Here, the particle type has to be reconstructed from observables gained from the observation of secondary particles. Often applied in this context is the quantity of the mean logarithmic mass

$$\langle \ln A \rangle = \sum_i r_i \ln A_i \tag{2.4}$$

with r_i being the relative fraction of nuclei with mass A_i. It can be derived from the measured numbers of electrons N_{e} and muons N_{μ} at ground level, $\langle \ln A \rangle \propto \log_{10} N_{\mathrm{e}}/N_{\mu}$ [17]. Furthermore, it is proportional to the observed depth of the shower maximum X_{max} (which is the atmospheric depth at which the air showers has its maximum number of particles, cf. section 2.4) according to the relation[3]

[2] Similar plots have not been published since then. The text includes more recent results.
[3] The derivation of equation (2.5) will be discussed in the following section.

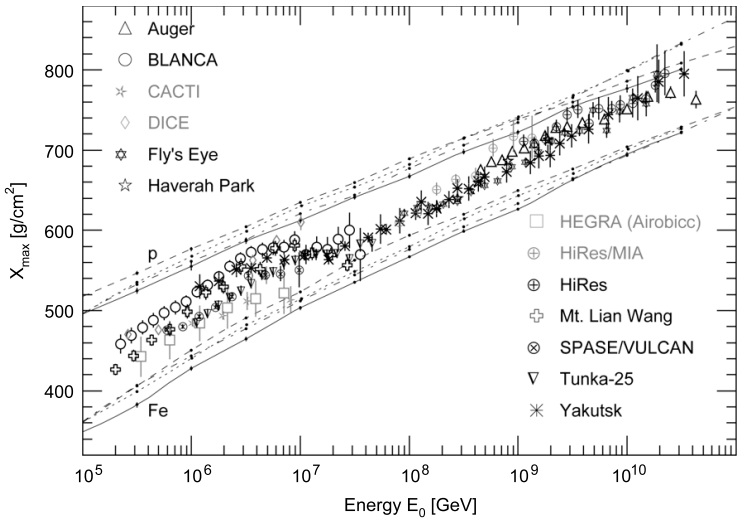

Figure 2.4: Average depth of the shower maximum $X_{\max}$ as a function of the reconstructed energy of the primary particle as obtained by various experiments. The lines indicate simulations for primaries being protons (p) and iron nuclei (Fe) using the CORSIKA code (cf. section 2.4) with the hadronic interaction model QGSJet 01 (solid lines), QGSJet II-3 (dashed lines), SIBYLL 2.1 (dotted lines), and EPOS 1.6 (dash dotted lines). Taken from reference [17].

$$X^A_{\max} = X^{\mathrm{p}}_{\max} - \lambda_{\mathrm{em}} \ln A \,. \tag{2.5}$$

Here, $\lambda_{\mathrm{em}} = 36.6\,\mathrm{g\,cm^{-2}}$ is the radiation length in air [34]. This means that an iron induced air shower ($A = 56$) should have its shower maximum at about $150\,\mathrm{g\,cm^{-2}}$ higher altitude than the depth of the shower maximum for a proton induced air shower $X^{\mathrm{p}}_{\max}$.

It is common to use the quantity *atmospheric depth* X to describe the longitudinal profile of air showers. X corresponds to the amount of matter an air shower has traversed, and is defined by

$$X = \int \rho(s)\, ds \tag{2.6}$$

where $\rho(s)$ is the local density of the air, and s is the path along the shower axis, starting at the top of the atmosphere.

Figure 2.4 shows the average $X_{\max}$ as a function of the reconstructed energy of the primary particle for various experiments. The lines represent simulations for proton (p) and iron (Fe) primaries and different hadronic interaction models. Since these models differ significantly from each other for a certain primary particle, it is non-trivial to draw conclusions on the mass composition of cosmic rays by comparison of measured data with the predictions of these models.
Starting at lower energies, the data seem to rise steeper than the predictions for iron up to an energy of about $10^{15.5}\,\mathrm{eV}$. Hence, the composition appears to become lighter. With increasing energy up to about $10^{16.5}\,\mathrm{eV}$ the data flatten, indicating

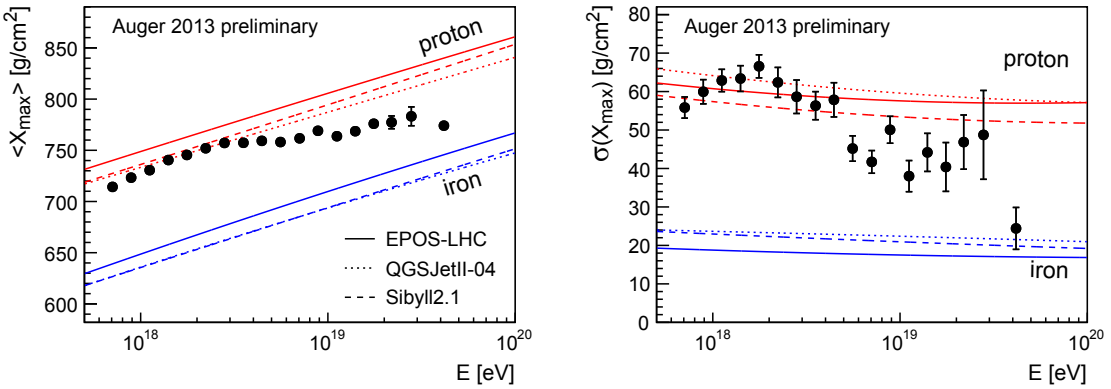

Figure 2.5: Average depth of the shower maximum $X_{\max}$ (left) and standard deviation of $X_{\max}$ (right) as a function of the primary energy measured with the Pierre Auger Observatory. The lines are predictions from different interaction models for protons (red) and iron nuclei (blue). Taken from reference [36].

the composition getting heavier. Above $10^{16.5}$ eV the data rise again, hinting at a lighter composition at the highest energies.

In figure 2.5 the mean $X_{\max}$ and the standard deviation of $X_{\max}$ measured with the Pierre Auger Observatory are given as a function of the reconstructed energy of the primary particle. Also plotted are the corresponding predictions of hadronic interaction models. These recent (but preliminary) data indicate a heavier composition at the highest energies.
In fact, this is what one would expect from sources which provide a maximum energy which scales with the charge number of the primary cosmic ray particle.
But the data are not unambiguous. There is a discrepancy between measurements from the Pierre Auger Observatory and from the High Resolution Fly's Eye (HiRes) which cannot be explained by systematic uncertainties. Regarding these two experiments, data are taken on different hemispheres, which might be the cause for the discrepancy. Since HiRes has stopped its data acquisition, the answer might be found with more statistics from the Telescope Array, which operates – as HiRes – in the northern hemisphere. Recent Telescope Array data are in agreement with both Auger and HiRes data taking systematic uncertainties into account. For a more detailed discussion of this discrepancy please refer to reference [35].

2.4 Extensive air showers

The following discussion of the development of air showers will consider a proton to be the primary particle which evokes the shower. Since for UHECRs the binding energy of heavier nuclei is much smaller than the energy of the primary particle E_0, a nucleus can be regarded as a superposition of A protons with energies E_0/A.
The atmosphere has an atmospheric depth of about $1000\,\mathrm{g\,cm^{-2}}$. This corresponds to 11 hadronic interaction lengths $X_0^{\mathrm{hadr}} = 90.1\,\mathrm{g\,cm^{-2}}$ and 27 radiation lengths $\lambda_{\mathrm{em}} = 36.6\,\mathrm{g\,cm^{-2}}$ [34]. The height of the first interaction of the proton takes place at an

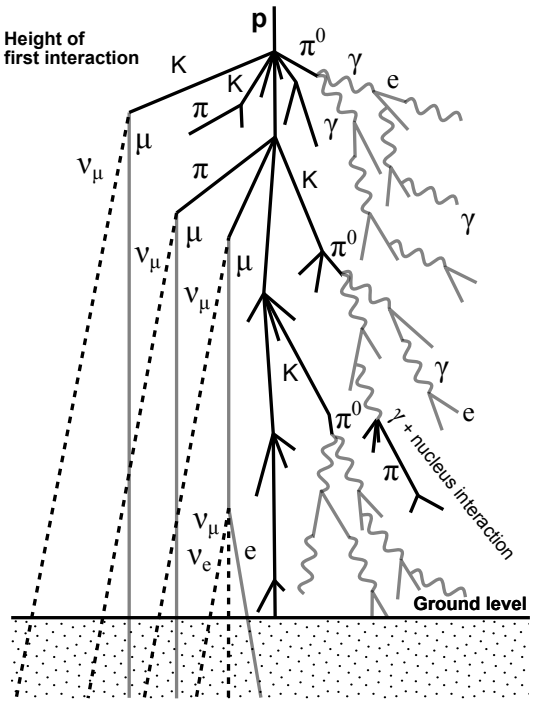

Figure 2.6: Schematic view of an air shower development. Modified, original taken from reference [37].

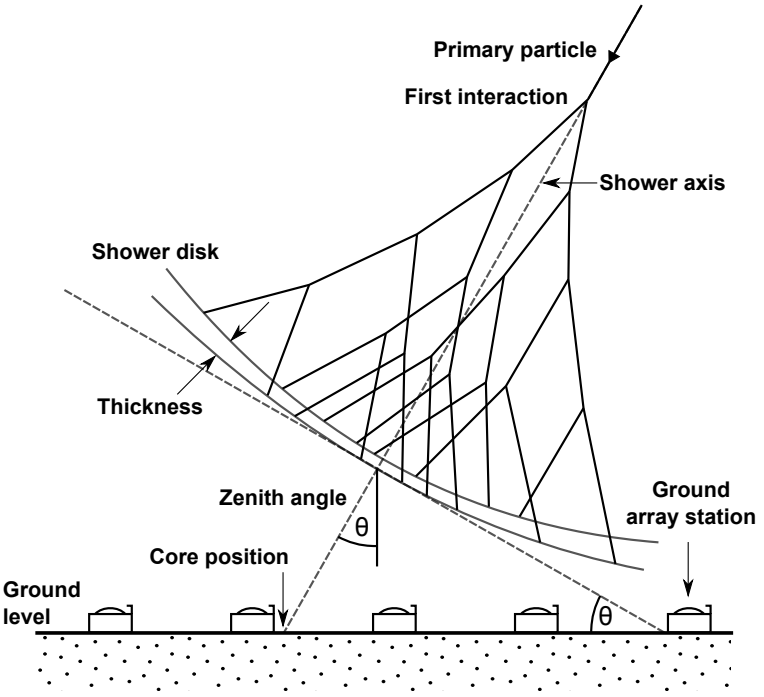

Figure 2.7: Schematic view of an air shower approaching a ground array. Modified, original taken from reference [37].

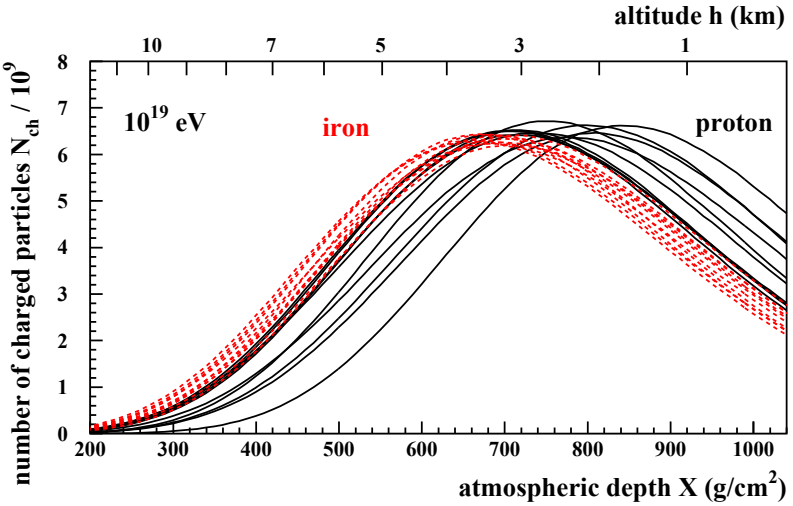

Figure 2.8: Number of charged particles in vertical air showers as a function of the atmospheric depth simulated with CORSIKA (see below). Solid black lines are for proton and dashed red lines for iron primaries. The energy of the primary particles is 10^{19} eV. Taken from reference [38].

altitude between 15 km and 20 km a.s.l.[4] In a reaction with a nucleus of a molecule of the air, it loses about 50% of its energy and creates about 90% pions ($\pi^{\pm}$, π^0) and 10% kaons ($K^{\pm}$, K^0) [39]. The pion multiplicity per interaction scales slightly with the energy: for cosmic rays within the energy range of 10^{18} eV to 10^{20} eV it ranges from the order of 10 (after several interaction lengths) to the order of 100 (at the first interaction) [40].
About 1/3 of the pions are neutral. With a mean life time of $\tau_{\pi^0} \approx 10^{-6}$ s (see reference [34], as for other decay modes and branching ratios) they typically decay to 2γ (99%) or $e^+e^-\gamma$ (1%) before they have the chance to interact. This is the starting point of an *electromagnetic cascade*. When kaons or charged pions interact with a nucleus, they themselves create further kaons and pions feeding the *hadronic cascade*. With a branching ratio of 99.99% almost all π^+ decay to $\mu^+\nu_\mu$, contributing to the *muonic cascade*. The uncharged kaons will decay to $\pi^+\pi^-$ (69%) or $\pi^0\pi^0$ (31%), whereas the K^+ will end in $\mu^+\nu_\mu$ (63%) and $\pi^+\pi^0$ (21%). For the K^+ there are many more decay modes which predominantly will produce pions. The decay modes for π^- and K^- can be taken from charge conjugation of their anti-particles. Figure 2.6 gives a schematic overview of a particle cascade generated by cosmic rays.

Within the electromagnetic cascade the photons can interact with the nuclei of the atmosphere as well, again creating pions and kaons, and thus re-transferring energy to the hadronic cascade. But this is only a very small effect. More likely the photons will create electrons and positrons by pair production. These particles will create photons by annihilation and bremsstrahlung.
Due to their relatively high mass, muons are only little affected by bremsstrahlung.

[4] An empirical derived parametrization of the atmospheric depth as a function of the altitude is given in appendix A.1.

Their energy loss due to ionization is about $2\,\mathrm{MeV\,g^{-1}\,cm^2}$, and with typical energies of several GeV most of them will reach the ground. Some muons decay to electrons, positrons, and neutrinos. The neutrinos do not interact. Overall, their number equals almost the number of muons and they contain only a small amount of the total shower energy.

The electromagnetic cascade starts to die out when the electrons reach their critical energy in air $E^{\mathrm{e}}_{\mathrm{crit}} = 87\,\mathrm{MeV}$. Here, they start to lose more energy by interacting with the atomic shell of their collision partners than in radiative processes, and thus get absorbed. The ionization process continues down to energies below 1 MeV [41]. The hadronic cascade comes to an end when the decay length becomes smaller than the interaction length. This happens at critical energies $E^{\mathrm{hadr}}_{\mathrm{crit}}$ in the range of 10 GeV to several 100 GeV, depending on the zenith angle of the shower axis [40].
The point at which the air shower contains the maximum number of particles is typically stated in terms of atmospheric depth and called X_{max} (cf. section 2.3).
The number of electrons and positrons N_{e} within an air shower as a function of the atmospheric depth can be approximated by the Gaisser–Hillas equation [42]

$$N_{\mathrm{e}}(X) = N_{\mathrm{max}} \left(\frac{X - X_0}{X_{\mathrm{max}} - X_0} \right)^{(X_{\mathrm{max}} - X_0)/\lambda_{\mathrm{GH}}} \exp\left(\frac{X_{\mathrm{max}} - X}{\lambda_{\mathrm{GH}}} \right) \tag{2.7}$$

N_{max} is the number of electrons and positrons at X_{max}, while X_0 and λ_{GH} are parameters of the shape of the shower. For pure electromagnetic showers X_0 is considered to be the atmospheric depth at which the first interaction takes place, whereas λ_{GH} is the radiation length.
In figure 2.8 simulated X_{max} distributions for proton and iron primaries are shown.[5] As can be seen from the figure, the mean X_{max} for proton lies about $150\,\mathrm{g\,cm^{-2}}$ higher than for iron. The fluctuation of X_{max} is larger for proton primaries than for iron, since the latter can be regarded as a superposition of 56 nucleons.

Regarding the particles of an air shower 90% are within the electromagnetic cascade. 5% of the other particles are muons and further 5% are neutrinos. A very small amount are hadrons. While the latter reside within a radius of $\sim 10\,\mathrm{m}$ around the shower axis, electrons, positrons, and muons can reach distances of several kilometers away from the shower axis (cf. references [38] and [43]). The region in which the secondary particles are located is referred to as the *shower disk* (cf. figure 2.7). It moves with almost the speed of light towards Earth, and has a longitudinal stretch of several meters close to the core, and several tens of meters in the outer regions. Due to the huge number of interactions inside an air shower development, the shape of the shower disk does not depend on the energy. But it depends on the zenith angle of the shower axis θ: Charged particles are deflected by the magnetic field of the Earth. With increasing θ the air shower has more atmosphere to traverse, and charge separation becomes larger, leading to a deformation of the shape of the shower disk. However, in reference [41] it was shown that this effect is negligible for $\theta < 60\,^\circ$.

[5] A measured Gaisser–Hillas profile is shown in figure 3.9.

Heitler model

Some basic properties of air showers can already be derived from a very simple model. It has been initially proposed for electromagnetic showers [44], but it can also be applied to hadronic showers [45].

Electromagnetic showers

To keep this discussion simple we will consider only one kind of particle instead of three (γ, e^-, e^+). The primary particle is considered to have an initial energy E_0. After a fixed interaction length λ_{em} it produces two particles of energy $E_0/2$. This is the beginning of a successive process like it is sketched in figure 2.9 (left), with j indicating the number of generation. After j generations the shower has covered a distance of $X = j \cdot \lambda_{em}$, and consists of

$$N(X) = 2^j = 2^{X/\lambda_{em}}$$

particles. Hence, the energy of a particle can be stated as a function of the atmospheric depth X,

$$E(X) = \frac{E_0}{N} = \frac{E_0}{2^{X/\lambda_{em}}} .$$

The maximum number of particles N_{max} can be calculated taking the critical energy E^e_{crit} into account. With

$$E_0 = N_{max} \cdot E^e_{crit} \qquad \text{and} \qquad E^e_{crit} = \frac{E_0}{2^{X^e_{max}/\lambda_{em}}}$$

we find

$$N_{max} = \frac{E_0}{E^e_{crit}} \qquad \text{and} \qquad X^e_{max} \sim \lambda_{em} \cdot \ln \frac{E_0}{E^e_{crit}} . \tag{2.8}$$

With this simple approach we cannot describe an electromagnetic shower in all detail, however two basic features are already well described: the number of particles at the shower maximum is proportional to the energy of the primary particle E_0, and the atmospheric depth of the shower maximum X_{max} depends logarithmically on the primary energy E_0.

Hadronic showers

In this model we start with a primary hadron of energy E_0 which interacts after a mean interaction length X_0^{hadr}. It produces n_{gen} new particles with energies E_0/n_{gen}. Two thirds of these particles are charged, n_{ch} (charged pions), and one third is neutral, n_{neut} (neutral pions). The neutral particles decay immediately into electromagnetic particles ($\pi^0 \to \gamma\gamma$), while the charged particles might re-interact producing new particles of the next generation. This interaction takes place after the mother particles have covered a distance corresponding to the mean interaction length, and if their energy is higher than some typical decay energy E_{dec}. This process is illustrated in figure 2.9 (right).

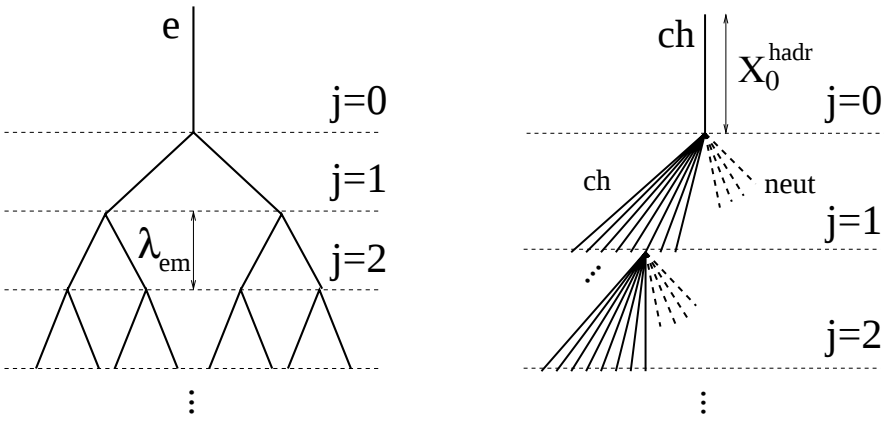

Figure 2.9: Schematic view of electromagnetic (left) and hadronic (right) cascades. For the sake of simplicity only one kind of particle (e) is shown in the electromagnetic cascade which produces two particles of the same type after each interaction length λ_{em}. For the hadronic cascade dashed lines represent neutral particles (π^0) and solid lines charged particles ($\pi^{\pm}$). Only one charged hadron interaction is shown for each generation j. Modified, original taken from reference [6].

The energies E_{hadr} and E_{e} contained within the hadronic and the electromagnetic cascade, respectively, within generation j are given by

$$E_{\mathrm{hadr}} = \left(\frac{2}{3}\right)^{j} \cdot E_0 \qquad \text{and} \qquad E_{\mathrm{e}} = [\,1 - \left(\frac{2}{3}\right)^{j}\,] \cdot E_0\,.$$

Simulations show that the number of generations typically is about 5 to 6 [46]. After 5 generations about 87% of the energy of a hadron initiated air shower is contained within the electromagnetic cascade.[6] Therefore, the depth of the shower maximum X_{max} is given to a good approximation by the one of the electromagnetic component $X^{\mathrm{e}}_{\mathrm{max}}$. The energy of the electromagnetic particles created within the first generation is $\sim E_0/n_{\mathrm{gen}}$. Thus,

$$\begin{aligned} X_{\mathrm{max}}\,(E_0) \;&\sim\; X_0^{\mathrm{hadr}} + X^{\mathrm{e}}_{\mathrm{max}}\,(E_0/n_{\mathrm{gen}}) \\ &\sim\; X_0^{\mathrm{hadr}} + \lambda_{\mathrm{em}} \cdot \ln\left(\frac{E_0}{n_{\mathrm{gen}}\,E^{\mathrm{e}}_{\mathrm{crit}}}\right). \end{aligned} \tag{2.9}$$

Taking also higher generations into account will not change the structure of equation (2.9), but only the coefficients [6, 47].

Following the intention to keep this discussion simple we now assume that each charged hadron will decay into a muon, when it reaches the characteristic decay

[6] For instance a $10^{19}\,\mathrm{eV}$ vertical proton air shower at sea level consists of $3 \cdot 10^{10}$ particles in total. 99% of these are photons, electrons, and positrons with a ratio of $N_\gamma/N_{\mathrm{e}^\pm} = 6/1$. The electromagnetic particles carry about 85% of the shower energy. The rest of the particles are mouns with energies around 1 GeV, pions with energies of a few GeV, neutrinos, and small numbers of baryons. The muons carry about 10% of the shower energy and the pions about 4% [39].

energy E_{dec}. This energy can be considered as the energy at which interaction length and decay length are equal. Charged hadrons will reach this energy by construction after j' interactions:

$$E_{\mathrm{dec}} = \frac{E_0}{n_{\mathrm{gen}}^{j'}}$$

The number of muons N_μ equals the number of charged hadrons which decay, $N_\mu = n_{\mathrm{ch}}^{j'}$. With the definitions

$$\alpha \equiv \frac{\ln n_{\mathrm{ch}}}{\ln n_{\mathrm{gen}}} = 1 + \frac{\ln R}{\ln n_{\mathrm{gen}}}\,, \qquad R \equiv \frac{n_{\mathrm{ch}}}{n_{\mathrm{gen}}}$$

the number of muons can be expressed as a function of the primary energy E_0:

$$N_\mu = n_{\mathrm{ch}}^{j'} = \left(n_{\mathrm{gen}}^{j'}\right)^\alpha = \left(\frac{E_0}{E_{\mathrm{dec}}}\right)^\alpha . \tag{2.10}$$

From this we see, that the number of muons does not only depend on the primary energy, but also on the total particle multiplicity and the ratio of charged over all hadronic particles. It furthermore depends on the mass of the primary particle. Let the primary hadron in the discussion above be a proton. If we now consider a havier nucleus with mass number A to be the primary hadron, it can be approximated by a superposition of A protons with the energies E_0/A since the binding energy of the nucleus is small compared to E_0. Thus, for this nucleus we find the number of muons in the air shower to be

$$N_\mu^A = A \cdot \left(\frac{E_0/A}{E_{\mathrm{dec}}}\right)^\alpha = A^{1-\alpha} \cdot \left(\frac{E_0}{E_{\mathrm{dec}}}\right)^\alpha . \tag{2.11}$$

Regarding the depth of the shower maximum we find

$$X_{\mathrm{max}}^A = X_{\mathrm{max}}^{\mathrm{p}} - \lambda_{\mathrm{em}} \cdot \ln A \tag{2.12}$$

with $X_{\mathrm{max}}^{\mathrm{p}}$ being the depth of the shower maximum of a proton shower.

Air shower simulations

For several reasons it seems clear that the yet discussed model is far from describing air showers correctly in detail. However, Monte Carlo methods are the common way to proceed. A visualization of an air shower simulated with CORSIKA [49] is given in figure 2.10. CORSIKA is one of the classical simulation programs, but there are many more available. For an overview of these different code packages please refer for instance to reference [50] and those therein.[7] In CORSIKA all particles above a user-specific energy threshold are simulated and tracked, until they produce new particles or decay. For high-energy showers this can become very time consuming. Therefore, a method referred to as *thinning* can be applied. With thinning only a representative set of particles is included within the simulations. To account

[7] The same applies for hybrid simulations and external programs mentioned further below in this section.

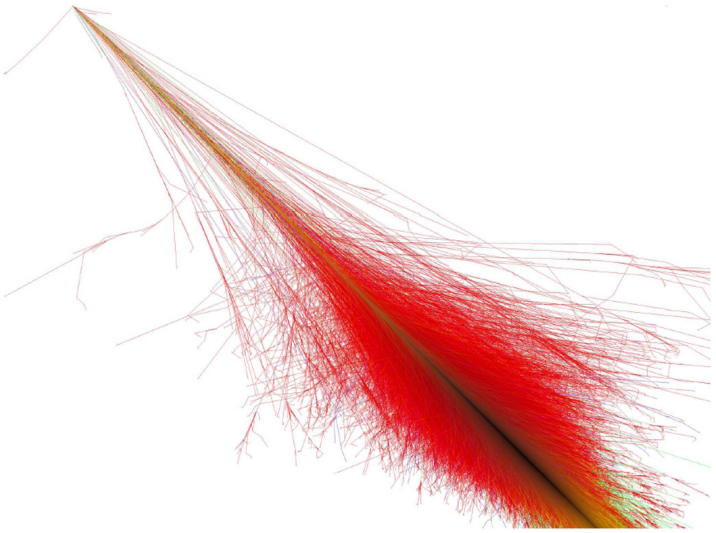

Figure 2.10: Visualization of an air shower simulated with CORSIKA. The electromagnetic cascade is illustrated in red, muons in green, and hadrons in blue. The longitudinal stretch of this shower is about 72 km. This and more visualizations can be found in reference [48].

for the discarded particles, those within the representative set obtain appropriately increased statistical weights. This can lead to artificial fluctuations of the simulation results if small fluctuations of single particles are amplified drastically due to huge weights. Another challenge arising from thinning is the need for a method to deal with weighted particles in detector simulations.

In addition to these explicit Monte Carlo simulation tools, there is a variety of hybrid simulation programs. One of these is CONEX [51]. CONEX combines Monte Carlo simulations of high-energy interactions with fast numerical solutions of cascade equations. This allows to run simulations without thinning or with significantly reduced weights within reasonable CPU time. However, using these hybrid simulation tools includes the risk to discard some local correlations which might not be covered by the cascade equations. Furthermore, CONEX simulates and calculates the air shower development only within one dimension, whereas for instance CORSIKA results in a complete three-dimensional air particle cascade. Nevertheless, the one-dimensional results of CONEX are sufficient for various considerations, where the lateral distribution of shower particles is inessential.

Different external code packages are available for the simulation of the electromagnetic cascade and the hadronic interactions. Since air showers incorporate energies higher than those which can be reached by man-made particle accelerators, the models for hadronic interaction are typically divided into low-energy and high-energy models. Some standard high-energy models are for example EPOS [52], QGSJet [53], and SIBYLL [54]. They derive from extrapolations of low-energy data by applying certain assumptions. The most important parameters regarding hadron production are the cross section, the multiplicity of secondary particles, and the production ratio

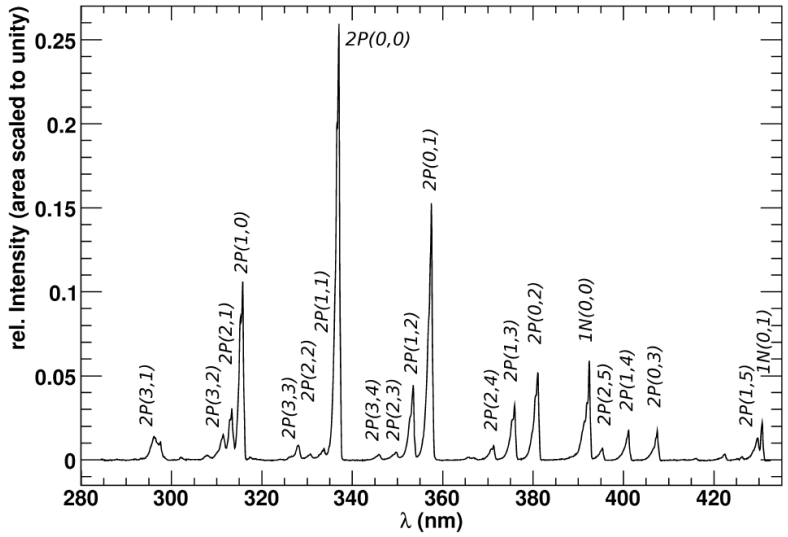

Figure 2.11: Fluorescence spectrum of dry air, excited by 3 MeV electrons, at 800 hPa, 293 K as measured by AIRFLY. The labels indicate the 21 major transitions of the air molecules. Taken from reference [55].

of neutral to charged particles. With different assumptions how to extrapolate these parameters, the hadronic interaction models lead to different results; for instance, the variation of the number of muons (electrons/positrons) at a certain atmospheric depth X differs typically by about 5% to 10% (1% to 5%), with a smaller variation for higher values of X [50]. Typically the user applies several of the high-energy models to compare the measured data to (see e.g. figure 2.5).

At high energies cosmic rays can only be detected with ground-based experiments, since their flux is extremely low and huge detection areas are needed. Since ground based detectors — which will be discussed in detail within the next chapter — only measure secondary particles or radiation produced by these particles, the determination of the properties of the primary particle is a great challenge. The reconstruction of its energy, as well as its particle type rely to a great extend on air shower simulations. These reconstructions will also be discussed in chapter 3.

Fluorescence and Cherenkov light from air showers

The secondary particles of an air shower excite the molecules of the atmosphere by inelastic collisions. As discussed earlier most of the particles of the shower are photons, electrons, and positrons. Most of the energy deposited in the atmosphere arises from electrons and positrons with energies below 1 GeV. At the shower maximum only 2–3% of the deposited energy emerges from hadrons and muons [38, 56].
When the molecules de-excite they emit light isotropically within the UV region. This light is predominantly produced by N_2 molecules, with amounts of oxygen and argon small enough to discard them [57]. Nitrogen produces significant amounts of light between 390 nm and 430 nm. An air fluorescence spectrum is shown in figure 2.11. The fact that fluorescence light is emitted isotropically implies that an air

shower can be observed from the side, leading to the possibility of observing huge volumina of the atmosphere with appropriate detectors.

Assuming that all particles of an air shower are absorbed in the atmosphere, the integral of the energy deposit per atmospheric depth interval $\mathrm{d}E^{\mathrm{dep}}/\mathrm{d}X$ along the track of the air shower would equal E_0, the energy of the primary particle: $\int \mathrm{d}E^{\mathrm{dep}}/\mathrm{d}X\,\mathrm{d}X = E_0$. Hence, observing the amount of fluorescence light generated by an air shower will reveal the primary energy.
However, not all particles will be absorbed in the atmosphere. Corrections due to this can be calculated from air shower simulations, as far as the geometry of the shower and the atmospheric conditions are known. Furthermore, it is essential to know how many fluorescence photons are emitted by a certain energy deposit. We can write the number of emitted photons N_γ generated in a layer of atmosphere with thickness $\mathrm{d}X$ per wavelength interval $\mathrm{d}\lambda$ as

$$\frac{\mathrm{d}^2 N_\gamma}{\mathrm{d}X\,\mathrm{d}\lambda} = Y(\lambda, P, T, u) \cdot \frac{\mathrm{d}E^{\mathrm{dep}}}{\mathrm{d}X}\,. \tag{2.13}$$

The quantity Y which describes the proportionality between the number of emitted photons and deposited energy is called *fluorescence yield*. The amount of light emitted at a certain wavelength λ depends on the pressure of the air P, its temperature T, and humidity u. So far measurements indicate that a dependence of Y on the energy is inexistent or at least negligible [57].
There are several dedicated experiments which measure the fluorescence yield. The method is typically the same: Within a temperature and pressure controlled chamber, nitrogen (or another gas mixture) is excited by a well monitored electron beam. The fluorescence light is then measured with suitable optical detectors. The most prominent peak within the fluorescence spectrum lies at 337 nm. Thus, the fluorescence yield is often stated for a narrow band around this particular wavelength. Recent results from the AIRFLY experiment measured this fluorescence yield Y_{337} in dry air at 1013 hPa and 293 K to be $Y_{337} = 5.61\,\mathrm{photons/MeV} \pm 4\%$ [58].

Besides fluorescence light extensive air showers also produce Cherenkov light. Generally speaking, when a charge particle traverses a dielectric medium it temporarily polarizes the atoms (or molecules) of this medium. Due to this polarization the atoms emit radiation which typically interferes destructively. But if the charged particle moves faster than the speed of light within the medium, the interference becomes constructive for a certain angle θ_{Ch} with respect to the direction of movement of the particle. Let $\beta = v/c$ be the velocity of the particle divided by the vacuum speed of light c, and $c_{\mathrm{m}} = c_{\mathrm{m}}(\lambda)$ the speed of light within the medium which depends on the wavelength λ. From a geometric consideration of the constructive interference, a relation can be found for θ_{Ch} by regarding the distances the particle and the light have traveled within the time t:

$$\cos\theta_{\mathrm{Ch}} = \frac{c_{\mathrm{m}}(\lambda)\,t}{\beta\,c\,t} = \frac{1}{\beta\,n(\lambda)} \tag{2.14}$$

with $n(\lambda) = c/c_{\mathrm{m}}$ being the refractive index of the medium. From this we find the minimal velocity to produce Cherenkov radiation to be $\beta_{\mathrm{min}}(\lambda) = 1/n(\lambda)$. In air,

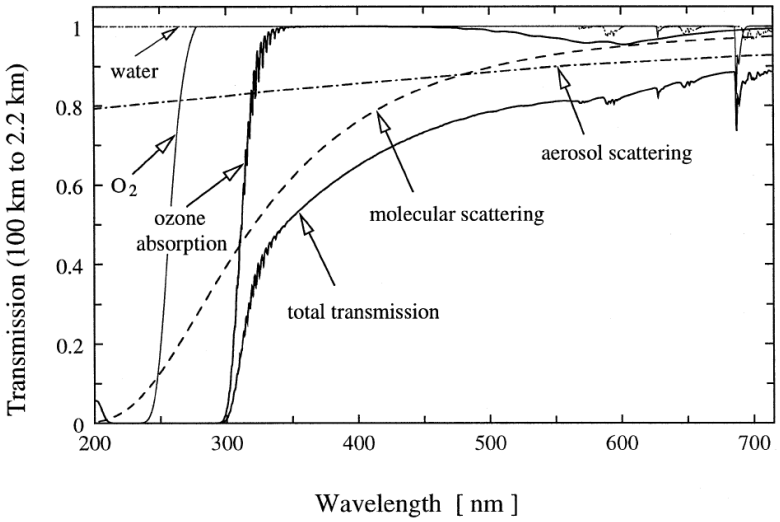

Figure 2.12: Direct transmission of light from space (here 100 km altitude) along a vertical path to an altitude of 2.2 km, as calculated with MODTRAN – a program to model atmospheric propagation of electromagnetic radiation within the range of 200 nm to 1000 nm. The impact of the most important absorbers and scatterers is shown. Taken from [59].

close to the ground, relativistic charged particles with $\beta \approx 1$ will produce light in forward direction within a cone with the aperture $2 \cdot \theta_{\mathrm{Ch}} = 2.8\,^{\circ}$. Here, the Cherenkov threshold energy for electrons is $\sim 21\,\mathrm{MeV}$.
The number of Cherenkov photons N_{Ch} per unit path length $\mathrm{d}x$ emitted in the wavelength band $\mathrm{d}\lambda$ is given by [59]

$$\frac{\mathrm{d}^2 N_{\mathrm{Ch}}}{\mathrm{d}x\,\mathrm{d}\lambda} = 2\,\pi\,\alpha\,\frac{Z^2}{\lambda^2}\left(1 - \frac{1}{\left(\beta\,n(\lambda)\right)^2}\right) \tag{2.15}$$

where Z is the charge number of the particle, and $\alpha \approx 1/137$ is the fine-structure constant. The wavelength spectrum follows a $1/\lambda^2$ distribution. For refractive indices $n < 1$ (which is the case for very short wavelengths) the condition for Cherenkov radiation cannot be fulfilled since β must not be greater than 1. Hence, there are no x-rays originating from the Cherenkov effect, and the emitted light has its maximum in the UV region.

In the atmosphere the spectra of Cherenkov and fluorescence light will be modulated due to absorption of UV light below 340 nm by ozone — not only in the ozone layer, but also close to the ground [59]. Further important wavelength-dependent attenuations are due to molecular and aerosol scattering. These and further effects reducing the transmission of light through the atmosphere are shown in figure 2.12. It is worth noticing, that the spectra of Cherenkov light and fluorescence light have their maxima very close to each other.

Direct Cherenkov light is only observed if a detector is located within the small cone defined by θ_{Ch}. However, a detector looking from the side at an air shower, intended

to measure only fluorescence light, will receive indirect Cherenkov light over large distances as well, due to the scattering of the Cherenkov photons in the atmosphere. The amount depends on the air shower geometry and distance, the primary energy, as well as the atmospheric conditions.

Let us consider a $10^{19}\,\mathrm{eV}$ vertical air shower initiated by a proton. $X_{\max}$ will be at about $800\,\mathrm{g\,cm^{-2}}$, corresponding to an altitude of about 2.0 km a.s.l. While propagating one radiation length ($\lambda_\mathrm{e} = 36\,\mathrm{g\,cm^{-2}}$, relating to a distance of about 365 m) the shower will produce about $3.3 \cdot 10^{13}$ Cherenkov photons in the wavelength interval of 290 nm to 430 nm, which are beamed into the forward direction. At the same time is will generate about $1.5 \cdot 10^{13}$ isotropically radiated fluorescence photons in the same wavelength region.[8]

In the next chapter we will discuss how extensive air showers can be detected, and how the properties of a primary particle can be reconstructed. For this discussion we will consider the detectors of the Pierre Auger Observatory as prime examples of air shower detectors.

[8] See appendix A.1 for calculations and underlying assumptions.

3. The Pierre Auger Observatory

As the flux of ultra-high-energy cosmic rays (UHECRs) is very low, large detection areas are needed which can only be provided at ground. Unlike with typical spaceborne or airborne experiments, here indirect measurements are performed by observation of air showers initiated by cosmic rays. Suitable detectors allow to reconstruct the properties of the air shower and gain insight on the type of primary particle, its energy, and its arrival direction.
During the last decades two major detection techniques were established: the measurement of secondary shower particles at ground level with arrays of detector stations, and the measurement of fluorescence light generated along the track of the air shower with appropriate telescopes. As discussed in the previous chapter, fluorescence telescopes are able to measure the longitudinal shower development. This yields information on the mass number A of the primary particle, and represents a calorimetric measurement of the energy of an air shower. The major drawback of this technique is the low duty cycle. It is typically 10 – 15%, since clear, moonless nights are needed to achieve an adequate signal-to-noise ratio. On the other hand, ground arrays provide duty cycles close to 100%. But these detectors sample only the secondary shower particles at ground level. The arrival direction can be well reconstructed from the timing information, but the energy reconstruction incorporates large systematic uncertainties as far as A is unknown. The simultaneous exploit of both detection principles allows to cross calibrate the detectors. One detector cancels the handicap of the other, and the results becomes more than the sum of its parts — a detector with good energy and angular resolution with a very high duty cycle. The first experiment to employ both a ground array and fluorescence telescopes, and thus introducing the era of UHECR hybrid detection was the Pierre Auger Observatory.

The Pierre Auger Observatory is located on a plateau with a mean altitude of 1420 m a.s.l. close to the town of Malargüe in the province of Mendoza, Argentina. It instruments about 3000 km^2 of the Pampa Amarilla and is the world's largest cosmic ray detector. It started stable data acquisition while it was still in the deployment phase in January, 2004. The detector was completely deployed in 2007. Its original design aimed at the detection of cosmic rays with energies larger than 10^{18} eV.

The following sections will give an introduction to the detection of cosmic rays with ground arrays and fluorescence telescopes. This introduction will use the surface detector and the fluorescence detector of the Pierre Auger Observatory as prime examples. Also the reconstruction of the key parameters of the air shower and the

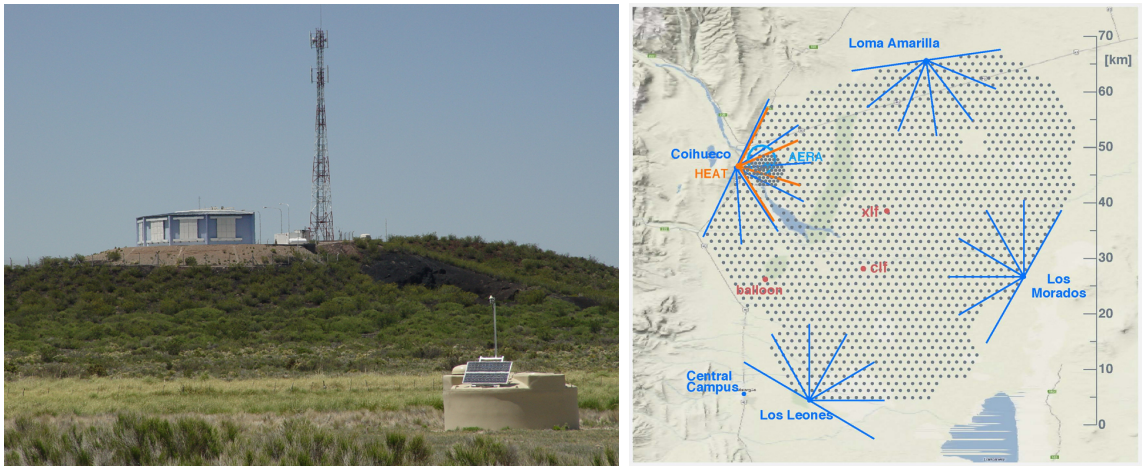

Figure 3.1: **Left:** Photo of a surface detector station in front of a fluorescence detector building housing six telescopes. Taken from reference [60]. **Right:** Map of the Pierre Auger Observatory. North direction is facing upwards. Each gray dot indicates the position of a surface detector station. The blue and orange lines depict the fields of view of the five fluorescence telescope sites. Also shown are the positions of the Auger Engineering Radio Array (AERA), the central and extreme laser facilities (CLF and XLF), the balloon launch station, and the central campus of the observatory located in the town of Malargüe. Picture credit: the Pierre Auger Collaboration

primary particle will be discussed. To provide the detection of air showers with energies down to at least 10^{17} eV the observatory was upgraded with low-energy extensions recently. These extensions, as well as alternative measurement techniques which are investigated at the Pierre Auger Observatory will also be introduced. The alternative approaches make use of totally different signals as discussed so far: the emission of electromagnetic radiation from air showers in the radio and microwave range.

3.1 Surface detector

The surface detector stations are arranged on a triangular grid across the approximately 3000 km^2 wide area of the Pierre Auger Observatory. The detection efficiency at the trigger level reaches 100% for air showers with energies larger than $3 \cdot 10^{18}$ eV. Regarding the distance of a single station to its next neighbors a compromise between the energy detection threshold and the cost efficiency had to be made. The requirement of at least five stations triggering at an energy of an air shower of 10^{19} eV leads to a maximum distance of 1500 m. With this particular choice of spacing a vertical 10^{20} eV shower is expected to trigger 10 stations, whereas the same shower but with a zenith angle $\theta \approx 60\,^\circ$ is likely to trigger more than 20 stations [61]. Thus, the surface detector array consists of about 1600 identical stations.

A photo and a schematic view of a single station are shown in figure 3.2. Each one has a diameter of 3.6 m and a height of 1.2 m and contains about 12000 l of

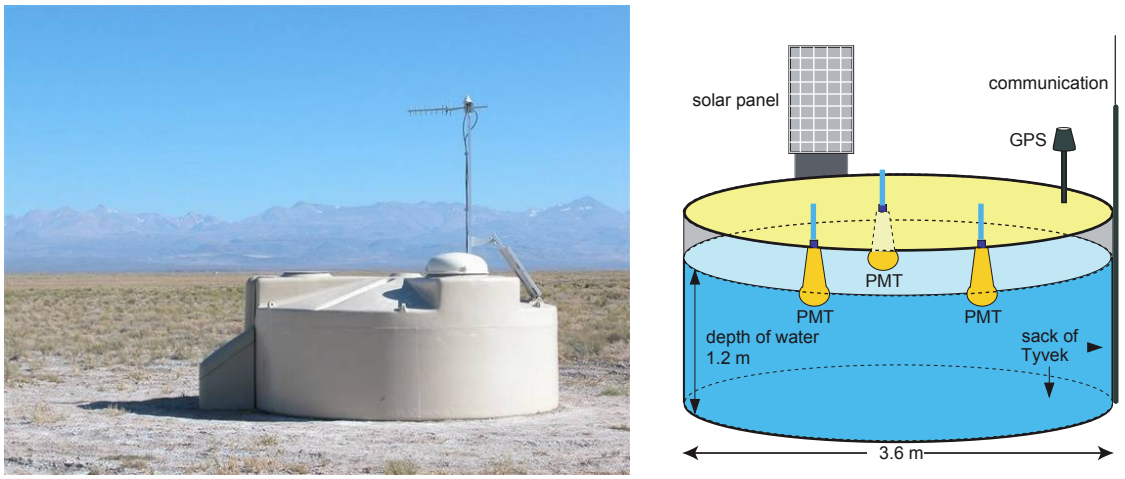

Figure 3.2: **Left:** Photo of one of the 1600 surface detector stations. Taken from reference [60]. **Right:** Schematic view of a surface detector station. Taken from reference [62].

ultra-pure water inside a highly reflective liner. If charged shower particles pass through the station faster than the speed of light in water, they produce Cherenkov light (cf. section 2.4) which is measured with photomultiplier tubes (PMTs). The housing of the detectors is made from polyethylene and the whole system is designed to cope with the harsh environmental conditions of the Argentine pampa for at least 20 years. These conditions include temperature differences between -15° C and 50° C, intense UV radiation, storms, dust, and snow. For more information on the overall design considerations, mechanics, water, and testing procedures please refer to reference [61].

The Cherenkov light is measured with three PMTs of 9 inch diameter (Photonis XP1802). They are mounted facing downwards and are symmetrically distributed with a distance of 1.2 m from the center. They are located on top of a clear polyethylene windows inside the liner and are optically coupled to these. Each PMT provides two signal channels to the front-end electronics — one from its anode, and one from its last dynode. The signal of the dynode is amplified internally at the base of the PMT to a nominal value of 32 times the anode signal. The use of these two different channels ensures the high dynamic range needed for the surface detector stations to cover both the particle flux close to the shower core ($\sim 1000\,\text{particles}\,\mu\text{s}^{-1}$) and far away from it ($\sim 1\,\text{particle}\,\mu\text{s}^{-1}$) [63]. The front-end electronics digitize the signals with a 10 bit flash analog-to-digital-converter (FADC) which operates at 40 MHz [64](see this reference also for further specifications of electronics in this section). The digitized signals are then passed to a programmable logic device (PLD) board, which takes care of first level trigger decisions. If a trigger is generated, the FADC data will be copied to a buffer of 19.2 µs length.
The electronics within a surface detector station are controlled by a CPU board (hosting a Power PC 403GCX at 40 MHz, OS9 operating system) which decides which triggers from the PLD board are caused by air showers. Timing information

is provided to the CPU board by a commercial GPS board (Motorola OnCore UT) and time tags of air shower events have a precision of about 8 ns. On the decision of a trigger interpreted to be caused by an air shower, the trigger information, as well as the timing information are transmitted to the central data acquisition system (CDAS) at the central campus of the observatory. If CDAS receives this information from several surface detector stations within a certain time window, it will search for patterns in the spacial distribution of triggered stations which relate to air shower events. If such a pattern is found, CDAS will request data from the corresponding stations. Not only the FADC data which are stored in the buffer of the front-end electronics are sent to CDAS, but also slow control data like information on calibration and monitoring (temperatures, bias voltages, etc.).
The triggers are implemented in sequent levels. Some of these levels feature more than just one trigger algorithm. A detailed description of these algorithms is given in reference [65].
The stations are designed to have a power consumption lower than 10 W. Two solar panels are mounted on top of each detector and are connected to two 12 V batteries. For more information on the electronics and the wireless LAN communication system please refer to reference [64].

Calibration

The calibration of the surface detector stations is performed autonomously in various routines and steps by each station every 60 s. Given here is a brief overview following the detailed discussion published in reference [63].

The aim of the calibration is to provide signals for the whole detector array in a common reference unit which is independent of fluctuations of individual detector characteristics. These characteristics are for instance the gain of the PMTs, the efficiency of the optical coupling of the PMTs to the water, etc. Furthermore, the calibration is intended to result in a stable and equal trigger rate for all surface detector stations.
The stations acquire signals from atmospheric muons produced by cosmic rays of lower energies. These events take place with a rate of approximately 2500 Hz. From geometrical considerations follows that the distribution of track lengths of muons within the detector peaks at a length which is identical to the one of a vertical muon. Therefore, the measured charge and current pulse height distributions also peak at values related to vertical muons. The common reference unit into which signals are converted is thus the vertical-equivalent muon (VEM). Within intervals of 60 s each surface detector station measures pulse height distributions of the three individual PMTs (i.e. distributions of amplitudes of the FADC signals), charge distributions of the three individual photosensors as well as the sum of all three (i.e. distributions of integrated FADC signals), and distributions of the baseline currents of each FADC channel. The corresponding histograms contain approximately 150000 entries. If CDAS generates a trigger and requests data from detector stations, these calibration histograms are also transmitted to CDAS and the calibration is performed offline.

The precision in the determination of the charge which corresponds to a vertical muon is 3%. The signal S used for the reconstruction of air shower events (see below) is taken from the measured charge Q and normalized to the charge given by a vertical-equivalent muon Q_{VEM}: $S = Q/Q_{\mathrm{VEM}}\,\mathrm{VEM}$.

Unlike the reconstruction of air shower events, the triggers of local stations make use of the measured pulse heights instead of the charge. The detector stations perform a continuous end-to-end online calibration adjusting the gain of the PMTs and the pulse height thresholds to obtain a stable trigger rate common to the whole detector array.
When the electronics of a station initially is turned on, the high-voltage of the PMTs is varied until each PMT is adjusted to a trigger rate of 100 Hz for a reference point in the pulse height spectrum 150 channels above the baseline. Beforehand, this choice was taken by applying measurements of the atmospheric muon flux with a reference station. The high-voltage of the PMTs of this particular station has been adjusted by use of the histogram-based offline calibration discussed above. These reference measurements showed that a trigger rate of 100 Hz corresponds to a pulse height of roughly $3\,I_{\mathrm{VEM}}$, where I_{VEM} indicates the position of the VEM peak in the pulse height spectrum.
After this initial adjustment the high-voltage of the PMTs is kept constant. Later on drifts of the end-to-end gain are compensated by adjusting the trigger levels which results in a stable trigger rate. This procedure cancels out biases which are caused by different gain characteristics, as well as different efficiencies, e.g. due to the optic coupling of the photosensors to the water. I_{VEM} is determined with a precision of 6%. Finally, all stations will trigger uniformly on atmospheric muons above a certain energy.
A further calibration procedure is the measurement of the ratio of the dynode to the anode signal. The nominal value of this ratio is 32 (see above). Its real value, determined with a precision of 2%, as well as the other calibration data are sent to CDAS together with the air shower data.

3.2 Fluorescence detector

At the borders of the surface detector array four buildings are located which house six identical fluorescence telescopes each (cf. map in figure 3.1). These telescopes overlook the atmosphere above the surface detector with a duty cycle of 15% [68].[1] Close to the fluorescence detector (FD) site *Coihueco* at the north-west of the array three further telescopes are situated which are the High-Elevation Auger Telescopes (HEAT). HEAT are the low-energy extension of the FD and will be introduced in section 3.4. The section at hand is a summary of the detailed description of the fluorescence detector system published in reference [66].

Each telescope has a field of view of $30\,^\circ \times 30\,^\circ$. The telescopes are aligned to result in a total field of view per FD site of $180\,^\circ$ in azimuth and are observing elevations

[1] The duty cycle has increased over the years, and thus lower values have been quoted in the literature.

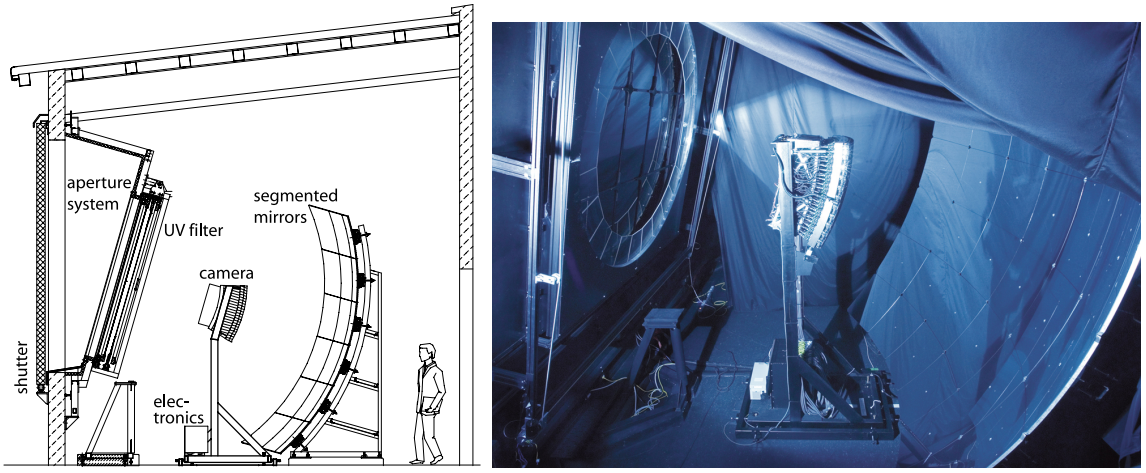

Figure 3.3: **Left:** Schematic drawing of a fluorescence telescope. Taken from reference [66]. **Right:** Photo of a fluorescence telescope. Taken from reference [67].

from approximately 0 ° to 30 °.
A schematic view and a photo of a telescope are shown in figure 3.3. The instruments are Schmidt telescopes and use photomultiplier tubes (PMTs) as light sensitive devices: The UV light caused by the particles of an air shower enters the telescope through the circular aperture and is reflected by a spherical mirror onto a spherical camera. To correct for the spherical aberration caused by the mirror a Schmidt telescope features a corrector plate at its entrance aperture which refracts the light appropriately.

The center of an aperture of a fluorescence telescope is located in the center of the sphere given by the curvature of the mirror. The aperture has a diameter of 2.2 m and houses a 3.25 mm thick UV band-pass filter of the colored glass Schott M–UG 6. The size of the aperture is optimized to collect 90% of the incoming light from a distant point source within a circle of 15 mm diameter at the focal plane. The telescope does not feature a full Schmidt corrector plate, but merely a Schmidt corrector ring with inner and outer radii of 0.85 m and 1.1 m. For practical reasons this ring is segmented into 24 parts. A full corrector plate is not necessary, since this simplified configuration meets already the design goals regarding the imaging quality of the telescope. If the telesope is not operating, e.g. during day or bright moonlit nights, the aperture is closed by a shutter.

As a result of the large size of the mirrors (area $\sim 13\,\mathrm{m}^2$) they are segmented to achieve more viable construction, transportation, and deployment routines. Two segmentation configurations are used.[2] Common to all mirrors is the spherical inner radius of 3.4 m.
The twelve telescopes at the FD sites Los Leones and Los Morados use mirrors consisting of 36 rectangular segments with three different sizes made from aluminium.

[2]For reasons of a fast and cost-effective production the mirrors have been produced in two different laboratories, one specialized on the production of aluminium mirrors and the other one on the production of glass mirrors.

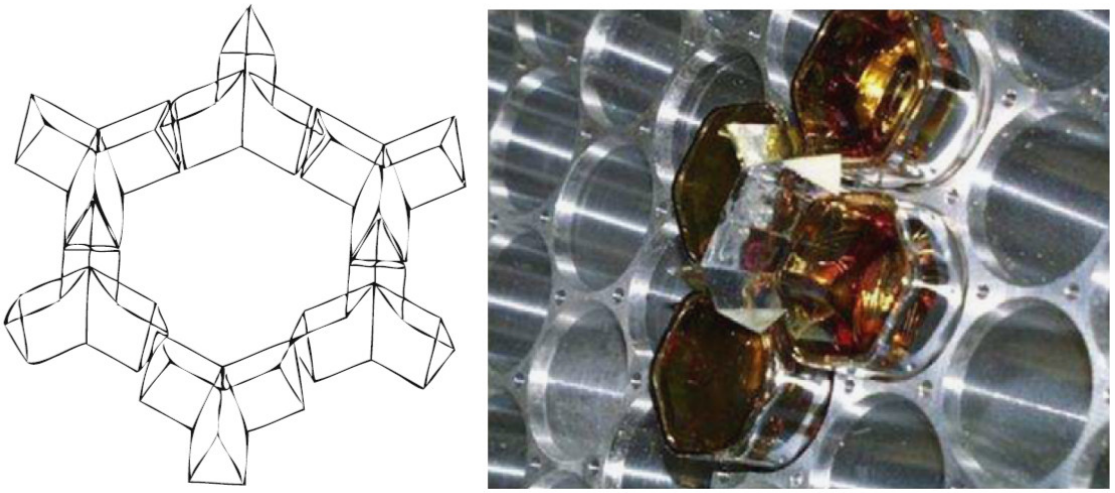

Figure 3.4: **Left:** Drawing of six light concentrators referred to as Mercedes Stars. They are arranged to form a camera pixel. Each Mercedes Star has three arms which are orientated 120° apart. The bottom Mercedes Star is slightly displaced for clarity. **Right:** Photo of the camera body with four PMTs and two Mercedes Stars being mounted. Both taken from reference [66].

The reflective surface is covered with 2 mm of $AlMgSiO_5$. To provide additional protection the surface is anodized and covered with a 90 nm thick layer of aluminium-oxide.
The twelve mirrors at Coihueco and Loma Amarilla are made of 60 hexagonal segments of four different shapes and sizes. They are made of the borosilicate glass SIMAX. The reflecting surface is a 90 nm layer of aluminium. For mechanical resistance the aluminium is coated with a 110 nm thick layer of $Si0_2$. The measured mean reflectivity of this mirror type exceeds 90% at a wavelength of 370 nm.

The mirror of a telescope reflects the light onto the spherical camera. It is located in the focal surface of the telescope, which is concentric to the mirror and has a radius of 1743 mm. 440 hexagonal pixels in 22 rows and 20 columns, arranged on a triangular grid, consist of PMTs (Photonis XP3062) with hexagonal windows of 40 mm size side-to-side. This design leads to a field of view per pixel of 1.5°. The camera has full acceptance for 30° in azimuth and 28.1° in elevation. The design of the mechanical structure of the camera, as well as the design of the PMTs themselves lead to dead spaces between the individual pixels. Monte Carlo ray tracing simulations show that 30% of the light would be lost due to this geometric fill factor without taking appropriate action. To increase the efficiency, light concentrators are mounted between the pixels which reflect the light into the PMTs. They are shaped similar to Mercedes Stars, with three arms orientated 120° apart, and arm lengths equal to about half the size of the side of a pixel. A drawing of the light concentrators and a photo mounted on the camera are shown in figure 3.4. Including these light concentrators the simulations yield that only 6% of the photons do not reach the sensitive area of the camera.

The quantum efficiency of the PMTs has its maximum near 400 nm where it reaches about 30%. To keep expenses for high-voltage power supply units at a moderate level, always 44 PMTs with similar gain characteristics are grouped together and share a common high-voltage source. The spread of the gain within one group of PMTs is ± 10%.

Each column of PMTs is connected to an analog board. This board provides a matching of the overall gain with a final precision of 0.6% by employing individual amplifiers for each PMT channel. Furthermore the analog board contains anti-aliasing filters to prepare the signals for the 10 MHz digitization rate. Digitization is performed later on with 12 bits. However, air showers lead to signals of about 3 to 10^5 photons/100 ns. Since the electronics have to cover this huge dynamic range, the analog board supports a technique to cover a dynamic range of 15 bits by the use of *virtual channels*: Every channel splits into a high-gain channel (gain ≈ 20), and a low-gain channel (gain ≈ 1). The low-gain channels of 11 non-adjacent pixels (let them be called a to k) are then summed up to a virtual channel. If the signal of a pixel in the high-gain channel is saturated, let pixel a be this pixel, the shower geometry together with the choice of pixels for the virtual channel lead typically to non-saturated pixels b to k in the high-gain channel for the same time bin of 100 ns. This allows to reconstruct the signal of pixel a within the virtual channel, by subtracting signals from b to k, with their levels obtained by regarding their high-gain channels.

Each analog board is followed by a first level trigger (FLT) board. This board continuously digitizes the signal with 12 bits at 10 MHz and stores the data in a circular buffer with a depth of 100 µs for later readout. The functions of the FLT board are implemented in a field programmable gate array (FPGA) firmware. The trigger uses adjustable thresholds on pixel level, and adapts these thresholds to keep the trigger rate of the pixels constant at 100 Hz.
The digitized signals of 20 FLT boards are then processed to a second level trigger (SLT) board. The main task of this module is to look for first level triggers which correspond to patterns being likely caused by air showers. These patterns consist of five adjacent pixels representing a track of an air shower. Since the track does not have to be centered in all pixels, it might be the case that a pixel does not receive enough light to generate a first level trigger. Thus, the SLT board looks for patterns with four triggered pixels out of five. If such a pattern is found the trigger information is stored. The trigger rate for this trigger level is 0.1–10 Hz per telescope.
The SLT board also accesses a GPS unit (Motorola UnCore UT, the same as applied to the surface detector stations) and provides a time stamp to the triggered events.

The FLT and SLT boards of a telescope can be accessed by its MirrorPC. It performs a third level trigger implemented in software. This trigger is intended to reject hardware-based triggers generated by far-distant lightnings, muons which passed through the camera, or randomly triggered pixels. The remaining trigger rate is 0.01 Hz per telescope. Events which have passed the third level trigger are processed

to the EyePC which manages all six MirrorPCs of a telescope building. It runs an event builder which merges information from all telescopes, and sends it to the central data acquisition system (CDAS) at the central campus of the observatory. The transmitted data also include various monitoring data, containing the mean and variance of ADC traces recorded each 6.5 ms to analyze the background light levels. If a third level trigger is processed, CDAS will generate an external trigger for the surface detector (SD). This is called a hybrid trigger. It is needed for air showers with energies below $3 \cdot 10^{18}$ eV, where the SD is not fully efficient. A preliminary reconstruction of the arrival direction and ground impact time of the air shower is performed online, and SD stations with signals recorded close to the impact time are read out. In section 3.3 where we will discuss the reconstruction of air shower events, we will see that also hybrid events with a low signal in the SD will significantly increase the precision of reconstructed shower properties. The trigger rate of a hybrid trigger is 0.02 Hz per telescope building. It is smaller than the sum of the third level trigger rates of all six telescopes at an FD site since several quality cuts are required to perform the preliminary reconstruction of the air shower.

Calibration

To obtain the photon flux at the aperture of an fluorescence telescope from the acquired ADC counts, it is essential to calibrate the telescope by the use of well known light sources. For the FD three different methods are applied: absolute calibration is performed up to twice a year with a large light source of known intensity, called *drum*. To keep track of short and long term variations of the characteristics of the telescope, in addition, a relative calibration is performed before and after each nightly measurement. Furthermore, distant pulsed lasers can generate air shower-like signal traces in the telescopes. The light sources partly employ different discrete wavelengths to measure the spectral response of the detector as well.

The drum is cylindrically shaped with a diameter of 2.5 m and a depth of 2.5 m. It is portable and can be mounted in front of the aperture outside of a telescope to provide an absolute end-to-end calibration. The drum is designed to provide a well known light flux simultaneously to all pixels of the camera of the telescope. Its light source is a pulsed (375 ± 12) nm LED. The light is diffusely reflected inside the drum, and diffusely transmitted into the fluorescence telescope. The uniformity and radiation pattern is measured in the laboratory. The drum is a good Lambertian radiator.[3] Its light output is uniform with a precision of 2% (except from a dark central spot). Ray tracing simulations show a 1% variation of the photon flux among all camera pixels. The light intensity of the drum is also measured in the laboratory with NIST-calibrated photodiodes. It is known to a precision of 6%. Additional uncertainties like temperature dependencies, spectral characteristics, and the variation of the camera response with time lead to an overall uncertainty of the

[3]The observed intensity $I(\theta)$ of a Lambertian radiator is proportional to the considered area A and the cosine of the observation angle θ with respect to the normal: $I(\theta) \sim A \cos(\theta)$. A Lambertian surface is regarded as an ideal diffuse reflector.

light intensity of the drum of 9%.
The drum also contains a xenon flash lamp behind a filter wheel to perform relative calibration measurements regarding the spectral response of a fluorescence telescope. The filter wheel contains five narrow band pass filters (15 nm FWHM) with central wavelengths at 320, 337, 355, 380, and 405 nm.

The Pierre Auger Observatory operates two stationary laser facilities in the surface detector array: the eXtreme laser facility (XLF), and the central laser facility (CLF) [69] (cf. map in figure 3.1). The facilities provide remotely operated, pulsed laser shots at 355 nm with monitored intensity. The generated light can also be used for an end-to-end calibration of the fluorescence telescopes. The laser beam can be steered in any direction above the horizon and its intensity can be varied. A fraction of the light is scattered to the fluorescence telescopes. This fraction can be calculated if the atmospheric conditions are known. A small fraction of the laser light can be sent through an optical fiber to the nearest surface detector station, and thus be used for timing calibration between FD and SD. Further benefits of the laser facilities are atmospheric monitoring, geometric reconstruction of laser-generated signals measured with the FD, and pixel pointing and trigger efficiency studies of the FD.
In addition, the FD can be calibrated with a mobile, vertical nitrogen laser system (373 nm). This laser is operated in a distance of 4 km from the considered telescope. Here, the scattered light flux is within the required range and the uncertainties caused by aerosol scattering are minimal. The phase function of aerosol scattering shows a significant maximum into the forward direction, whereas molecular scattering shows a more constant phase function. While molecular scattering can be calculated in a relatively easy way without taking many parameters into account, the treatment of aerosol scattering is much more complicated and requires the knowledge of the current atmospheric conditions to a great extend (see e.g. reference [59]).

The fluorescence telescopes feature another system for relative calibration which enables an end-to-end calibration, as well as calibrations of certain components of the telescope by comparison of the different subsystems. Each subsystem has its own light source A, B, and C.
A is a pulsed LED at 470 nm. Its light is processed to a 7:1 beam splitter which guides the light to diffusers in the center of the six mirrors within one telescope building. Another light guide leads to a calibrated, monitoring photodiode. B and C are xenon flash lamps. Their light is collimated and sent to filter wheels, as well as monitoring photodiodes. B uses a Johnson-U filter, common to optical astronomy, whose transmission band is close to the spectral acceptance of the fluorescence telescopes. Light source C applies interference filters centered at 330, 350, 370, 390, and 410 nm. The filtered light of B and C is then focused on 7:1 splitters and sent to the six telescopes at one site, as well as to a reference sensor like for light source A. The light originating from B is furthermore divided by 2:1 splitters, and illuminates diffusers left and right of each camera, casting it onto the mirror. The light originating from C is also divided by 2:1 splitters, and guided to diffusers outside the aperture. Inside the shutter, reflecting sheets are mounted which return the light into the telescopes if the shutters are closed.

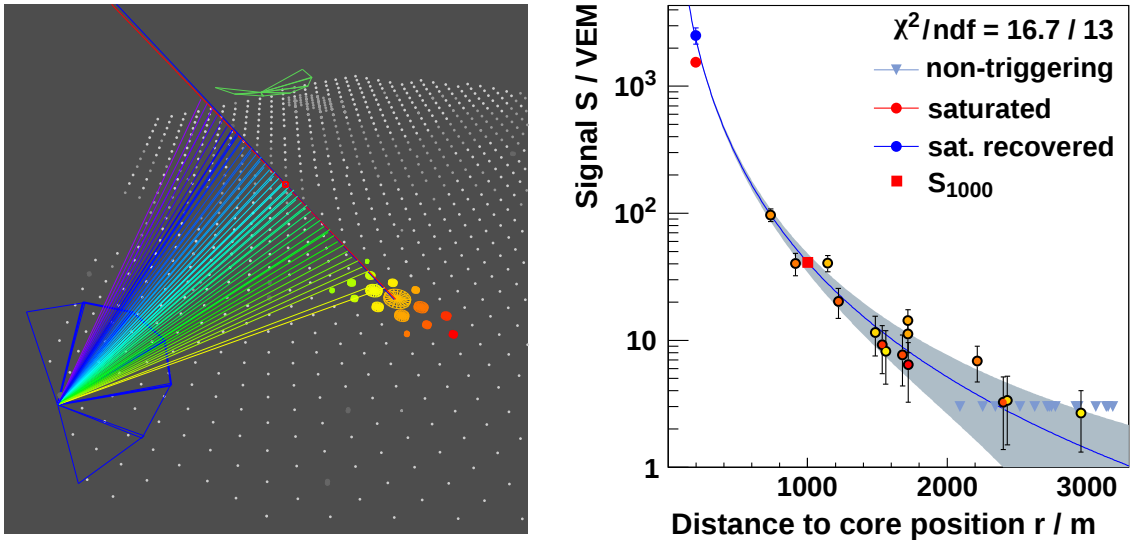

Figure 3.5: **Left:** Three-dimensional event view of event SD_2276329. The air shower has been detected by sixteen SD stations and three telescopes at one of the FD sites. The reconstructed shower axes are denoted by the blue (FD) and red (SD) lines entering the picture at the upper border. The reconstructed energy is about $1.5 \cdot 10^{19}$ eV. See text for further details. **Right:** Signal of SD stations given in vertical-equivalent muon (VEM) as a function of the distance of the stations to the shower core. The blue line is the fitted lateral density function according to equation (3.1). This is the same event as shown to the left. See text for further details.

3.3 Event reconstruction

In this section we briefly discuss the geometrical reconstruction of an air shower measured with the hybrid detector of the Pierre Auger Observatory, as well as the reconstruction of the energy of the primary particle E_0. The discussion is based on references [66, 70]. In figure 3.5 (left) a three-dimensional event view of an air shower detected with both the fluorescence detector (FD) and the surface detector (SD) is shown (event ID: SD_2276329). The gray dots represent the SD stations. The light gray dots represent those stations which had not yet been deployed when the event was recorded on May 21, 2006. The stations which contain a signal above the threshold are displayed as colored cylinders. The size of the cylinder denotes the height of the signal, whereas the color contains timing information from violet (early) to red (late). The blue and green triangles are the fields of view of the fluorescence telescopes (Los Leones in blue, Coihueco in green). The colored lines pointing from the shower axis to a telescope display the directions from which its camera has received light from the air shower. Again the timing information is color coded. The reconstructed shower axes are given by the red line (reconstructed by FD) and the related blue line (reconstructed by SD). The resulting zenith angle is $\theta = (56.0 \pm 0.2)\,^\circ$. On the red line the reconstructed shower maximum $X_{\max} = (779 \pm 8)\,\mathrm{g\,cm^{-2}}$ is displayed as a red circle. The reconstructed energy of this event is $E_0 = (1.53 \pm 0.06) \cdot 10^{19}\,\mathrm{eV}$.

The **surface detector (SD)** measures the density of the charged particles of an air shower at ground level. In a first reconstruction step the arrival direction is determined from the timing information of the triggered SD stations. At this instant the shower front is regarded as a plane. Once this preliminary arrival direction is determined, the core position and the lateral distribution function (LDF) of the signal S in the stations are estimated by a fit. The fit function is a modified version of an LDF proposed by J. Nishimura, K. Greisen, and K. Kamata [71, 72]:

$$S = S_{1000} \cdot \left(\frac{r}{1000\,\mathrm{m}}\right)^{\beta} \cdot \left(\frac{r + 700\,\mathrm{m}}{1700\,\mathrm{m}}\right)^{\beta} . \tag{3.1}$$

Here, r is the distance of the station to the core position, S_{1000} is a parameters which relates to a signal level in a distance of 1000 m from the core position, and β is the slope parameter of the LDF. As long as the core position is still undetermined β is fixed to a value only depending on the yet preliminary reconstructed zenith angle of the arrival direction θ. With an initial guess of the core position, the estimated core position can be found for instance by using a likelihood method. S_{1000} is the estimator for the energy of the air shower. It has been shown that this particular choice of an energy estimator is least affected by shower-to-shower fluctuations [73]. With the estimates of core position and S_{1000} the arrival direction is determined again. This time the shower front is regarded as a curved surface — the core position is fixed and again the timing information of the SD stations is taken into account. With the updated arrival direction the core position and S_{1000} are determined once more. Now β is given by a parametrization and depends on θ and S_{1000}. From this point on the procedure to reconstruct the arrival direction with a curved shower front and the subsequent LDF fit to determine the core position and S_{1000} are iterated several times. The angular resolution of the SD is better than 1° for energies E_0 larger than about 10^{19} eV [61].
An LDF fit to data and its uncertainty is shown in figure 3.5 (right). The data are from the same event we discussed in the introduction of this section (i.e. event SD_2276329). Data points with a black border denote the signal S in vertical-equivalent muon (VEM, see section 3.1) for the SD stations, where the color inside the border gives the timing information (yellow – early, red – late). Stations without a trigger are displayed by light blue triangles, providing an upper limit to the signal for these stations which is 3 VEM. One station has a saturated signal. It is shown by the red data point without a black border. Saturated stations contribute with a lower limit to the signal. Some saturated signals can be recovered, e.g. by fitting a response function to the non-saturated part of the signal. The blue data point represents the recovered signal. The fitted LDF is shown as the blue curve. The shaded area is its uncertainty. S_{1000} is marked as the red square.
To reconstruct the energy of the primary particle E_0 from the acquired data a formula to convert the energy estimator S_{1000} to E_0 has been found. This formula was obtained from hybrid events, where the energy estimator was calibrated with the energy measured by the FD. The statistical uncertainty in the determination of S_{1000} is about 10% for events with an energy of $5 \cdot 10^{18}$ eV [61].

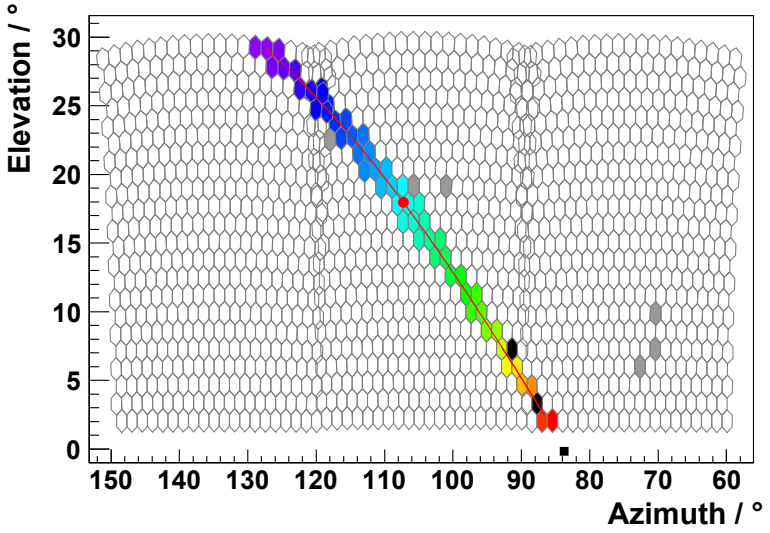

Figure 3.6: The air shower event shown in figure 3.5 as seen in the event viewer of the fluorescence detector. The hexagons correspond to the fields of view (FOV) of the 1320 pixels of the three telescopes which detected the air shower. The FOV is given in terms of azimuth and elevation. Filled pixels contain signals above the threshold. The color code denotes the timing information (violet – early, red – late, black – timing does not match shower development, gray – not considered to be caused by the air shower). The reconstructed shower-detector-plane is given by the red line. The shower maximum $X_{\max}$ is depicted by the red circle. The black square denotes the position of the direction of the SD station with the highest signal.

The **fluorescence detector (FD)** measures UV light emitted along the track of the air shower. An event display of the triggered pixels for our example event, discussed in the introduction of this section, can be seen in figure 3.6. The first step in the reconstruction of the shower geometry is the determination of the shower-detector-plane (SDP). The SDP is the plane containing the telescope as well as the shower axis. In other words, it is the plane spanned by the ray traces of the detected photons. It is illustrated in figure 3.7. The accuracy of determining the SDP can be studied with air shower-like signals of known geometry. These signals can be generated with pulsed lasers pointing in the sky (cf. section 3.2). The uncertainty is in the order of 0.1° depending on the length of the recorded track.
Once the SDP is assigned the timing information of the camera pixels is used to determine the parameters R_{p} and χ_0 which fully describe the shower geometry. R_{p} is the perpendicular distance of the telescope to the shower axis, and χ_0 is the angle within the SDP between the ground and the shower axis (cf. figure 3.7). The photons will arrive at pixel i of the telescope at the time

$$t_i = t_0 + \frac{R_{\mathrm{p}}}{c} \cdot \tan\left(\frac{1}{2} \cdot (\chi_0 - \chi_i)\right) \quad . \tag{3.2}$$

Here, t_0 is the time when the shower front is at the closest distance to the telescope (i.e. the distance R_{p}), χ_i is the angle within the SDP between the ground and the

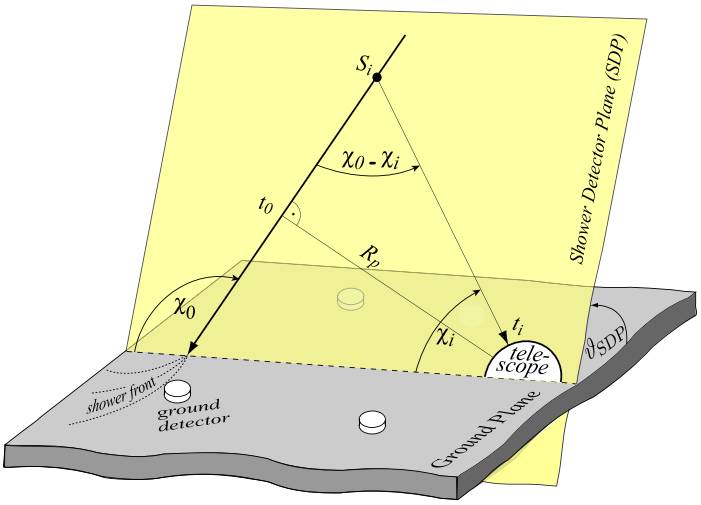

Figure 3.7: **Left:** Schematic drawing of the shower-detector-plane (SDP). The SDP contains the shower axis and the telescope which observes the air shower. It is tilted with respect to the ground by the angle ϑ_{SDP}. The angle between the ground and the shower axis is χ_0. At the time t_0 the shower has the closest distance to the telescope R_{p}. The signal S_i is observed in camera pixel i at the time t_i. The angle between the ground and the direction of the field of view of pixel i is χ_i. Taken from reference [74].

light ray pointing at the pixel i, and c is the speed of light. In general the shower geometry can be well determined by a single fluorescence telescope only. But if the timing information of the SD is also taken into account the uncertainties of the shower parameters can be significantly reduced, especially for showers with short tracks detected by the camera. For these showers the incorporation of information from the SD results in less possibilities of variation of R_{p}, χ_0, and t_0 to result in a good fit. Typically the fit results can already be improved by taking just one SD station into account. An example of the improvement of the fit results is given in figure 3.8. Since the SD has a duty cycle of almost 100%, most of the events detected with the FD are hybrid events. As some of the events which the FD records are below the trigger acceptance of the SD, the FD generates triggers for the SD. The core position can be determined with a resolution of about 50 m. The angular resolution of hybrid events is typically 0.6°.
After the reconstruction of the arrival direction and the core position, the energy of the primary particle E_0 is reconstructed. The atmosphere acts as a calorimeter for extensive air showers, and in this picture it is read out by the FD. To calculate the energy deposited in this calorimeter, it has to be converted from the measured light at the aperture of the telescope. In figure 3.9 both the detected light and the reconstructed energy deposit are displayed. For the conversion the different light contributions, i.e. direct fluorescence and Cherenkov light, as well as their scattered amounts, have to be disentangled from the signal. Furthermore, the attenuation of the light in the atmosphere has to be considered. These considerations need the

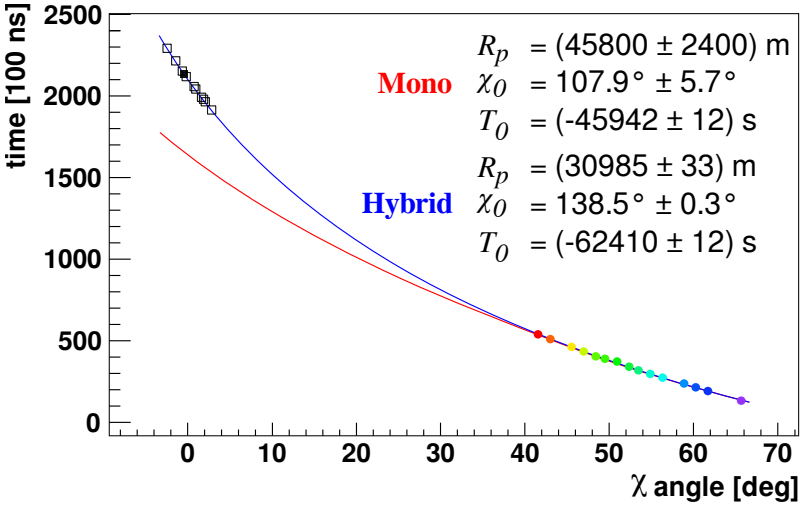

Figure 3.8: Arrival times of light signals t_i as a function of the observation angle χ_i. The colored circles are the data from the FD. The color code contains the timing information from violet (early) to red (late). The squares are the data of the SD, with the filled square representing the station with the highest signal. The red line is a fit according to equation (3.2) not taking the data of SD into account (Mono). The blue line is a fit to the data of both detectors (Hybrid). Reprinted from reference [66].

knowledge of the current characteristics of the atmosphere to outcome in results with sensible uncertainties. In addition, the fluorescence yield (cf. section 2.4) depends on the condition of the atmosphere. Therefore, different measurements are performed to monitor the atmospheric conditions [75], e.g. at each FD site a LIDAR (LIght Detection And Ranging) system is operated to measure the amount of back-scattered laser light as a function of the altitude. These measurements can also be performed with the laser systems for calibrating the FD, mentioned in section 3.2, and lead to the determination of the aerosol content of the air. In addition, weather balloons have been frequently used for atmospheric monitoring.
Once the energy deposit as a function of the atmospheric depth is calculated, a Gaisser–Hillas profile corresponding to equation (2.7) is fitted to the data. Its integral gives the energy within the electromagnetic cascade of the air shower. With corrections for invisible energy carried predominantly by muons, the energy of the primary particle E_0 can be determined. These corrections are performed by means of air shower simulation studies (cf. section 2.4). The energy resolution of the FD, defined as the event-to-event statistical uncertainty, is 10%. The current systematic uncertainties on the energy scale are given in table 3.1. The different contributions sum up to a total uncertainty of 14% and are approximately independent of energy. The fit of the Gaisser–Hillas profiles to the data yields the shower maximum $X_{\max}$. For high-quality events its uncertainty is smaller than $40\,\mathrm{g\,cm^{-2}}$. The shower maximum $X_{\max}$ serves as a measure of the mass of the primary particle as discussed in section 2.3.

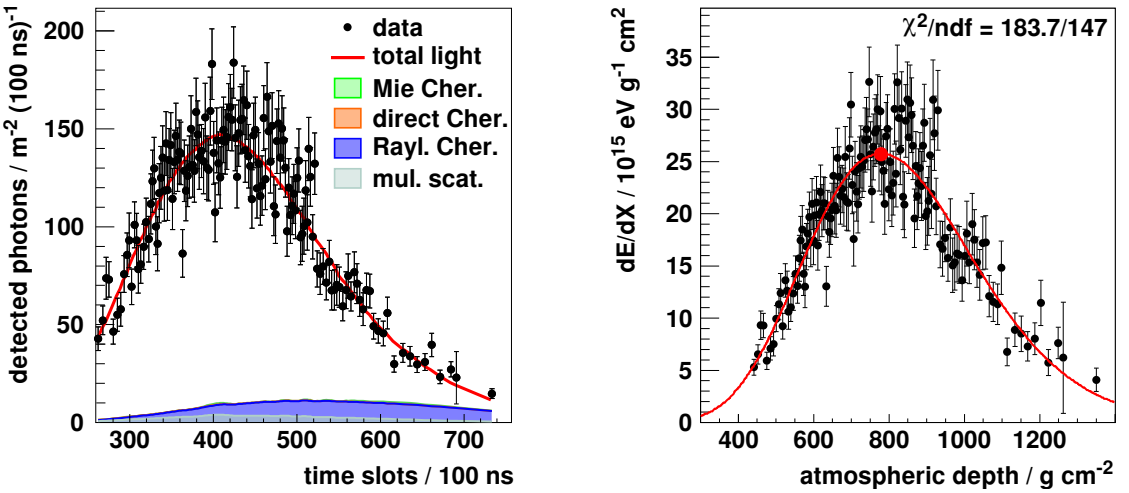

Figure 3.9: **Left:** Number of detected photons at the aperture of the corresponding fluorescence telescopes as a function of time. This is the same air shower event as shown in figure 3.5. The red line is a fit to the data according to a Gaisser–Hillas profile (cf. right plot and equation (2.7)). The shaded areas refer to contributions different from direct fluorescence light (multiple scattered fluorescence light, direct and scattered Cherenkov light — the later is due to scattering on molecules (Rayleigh) and aerosols (Mie)). **Right:** Reconstructed energy deposit $\mathrm{d}E/\mathrm{d}X$ as a function of the atmospheric depth X for the same data as shown in the left plot. The red line is a fit to the data according to a Gaisser–Hillas profile. The red data point indicates the position of the reconstructed shower maximum $X_{\max}$.

3.4 Low-energy extensions and R&D detectors

Initially the Pierre Auger Observatory was designed for the detection of cosmic rays with energies above 10^{18} eV. However, since the energy range between 10^{17} and 10^{18} eV might be the transition region, where the sources of cosmic rays change with increasing energy from galactic to extra-galactic, the desire to access this energy range with the observatory seems natural. Furthermore, a broader energy acceptance leads to the possibility of data comparison with a larger number of air shower experiments. To lower the energy threshold of the observatory to at least 10^{17} eV, extensions to the hybrid detector system have been built. For the surface detector this is AMIGA (Auger Muons and Infill for the Ground Array), and for the fluorescence detector this is HEAT (High Elevation Auger Telescopes).
With its hybrid detector acquiring high-quality data the Pierre Auger Observatory is the ideal place for the test of alternative methods for the detection of cosmic rays. Five autonomous R&D projects, which will be introduced here briefly, aim at the detection of radio and microwave signals generated by air showers.

AMIGA — Auger Muons and Infill for the Ground Array

The AMIGA extension consists of two parts. The first is an infill array [77] of surface detector stations to the regular array. While the regular one has a distance of

Table 3.1: Systematic uncertainties of the energy scale of the Pierre Auger Observatory. If the dependence of an uncertainty on the energy is non-negligible the corresponding values at the borders of the energy range $3 \cdot 10^{18}$ eV and 10^{20} eV are stated. Taken from reference [76].

Absolute fluorescence yield	3.4%
Fluorescence spectrum and quenching parameter	1.1%
Sub total (Fluorescence yield)	**3.6%**
Aerosol optical depth	3% ÷ 6%
Aerosol phase function	1%
Wavelength dependence of aerosol scattering	0.5%
Atmospheric density profile	1%
Sub total (Atmosphere)	**3.4% ÷ 6.2%**
Absolute FD calibration	9%
Nightly relative calibration	2%
Optical efficiency	3.5%
Sub total (FD calibration)	**9.9%**
Folding with point spread function	5%
Multiple scattering model	1%
Simulation bias	2%
Constraints in the Gaisser–Hillas fit	3.5% ÷ 1%
Sub total (FD profile reconstruction)	**6.5% ÷ 5.6%**
Invisible energy	**3% ÷ 1.5%**
Statistical error on the SD calibration fit	**0.7% ÷ 1.8%**
Stability on the energy scale	**5%**
Total	**14%**

a station to its next neighbors of 1500 m, the infill array reduces this distance to 750 m. It consists of 71 surface detector stations covering about 27 km^2 (cf. map[4] in figure 3.10). 35 of these stations started data acquisition in 2008. The infill was completed in 2012. It reaches full trigger efficiency above $3 \cdot 10^{17}$ eV for air showers with zenith angles smaller than 55°, thus increasing the energy range of the SD system by one order of magnitude.

The second part of AMIGA are muon detectors [78] buried about 2.25 m beneath the ground, where the electromagnetic component of air showers has been absorbed. The detectors are situated close to the stations of the infill array and cover an area of 30 m^2 each, divided into two modules of 10 m^2 and two modules of 5 m^2 size. The modules are segmented scintillation bars which are connected by wavelength-shifting

[4] In addition to the 71 mentioned stations on the area of the infill array, the map also shows stations on a 433 m grid. This is an additional low energy extension especially intended for the Auger Engineering Radio Array (see below). Furthermore, a *triplet* is shown whichs consists of three SD stations in a distance of 200 m from each other.

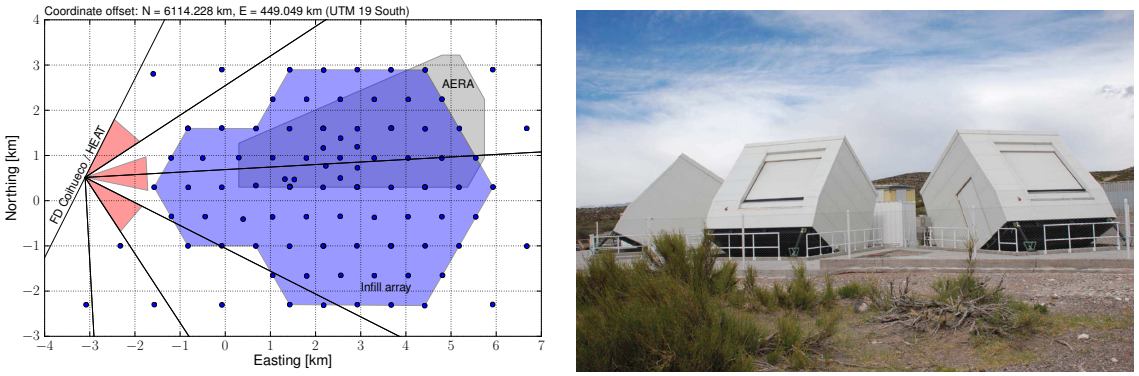

Figure 3.10: **Left:** Map of the north-western part of the observatory. Blue circles denote the position of SD stations. The blue shaded area is the infill array where the distance between neighboring stations is reduced. The gray-shaded area depicts the location of AERA. The lines to the left denote the fields of view of the fluorescence telescopes of Coihueco (black) and HEAT (red). Taken from reference [80]. **Right:** Photo of HEAT with the telescope buildings in upward mode and closed shutters. In the background the FD site Coihueco is partly visible. Taken from reference [81].

fibers to multi-anode PMTs. Until now seven surface detector stations have been provided with muon counters (one central detector station and its six next neighbors). As discussed in section 2.4 the number of muons in an air shower is sensitive to the energy of a primary particle, but also to the particle multiplicity in hadronic interactions, and the ratio of charged over all hadronic particles. Furthermore, the study of arrival times of muons from an air shower results in the atmospheric production depth of these particles. With this measure the longitudinal profile of the air shower can be studied with a ground detector array. Hence, the mass composition of cosmic rays can be investigated by means of the muon production depth [79].
AMIGA is located in the north-western part of the surface detector array. It is overlooked by three of the telescopes of the FD site Coihueco and by two of the telescopes of HEAT.

HEAT — High Elevation Auger Telescopes

Regarding a fluorescence telescope, air showers with low energy are typically detected closer to the telescope than those of high energy, since they produce less light. Therefore the viewing angle between the horizon and the point of the shower maximum X_{max} is typically larger for low energy air showers. For a reliable determination of the shower maximum in the reconstruction of an air shower event, X_{max} should lie within the field of view of the telescope.
HEAT [81] consists of fluorescence telescopes similar to the ones of the 24 standard FD telescopes. However, together with the buildings they are housed in, the telescopes can be tilted upwards by 29°. A photo of the tilted telescope buildings is shown in figure 3.10. The flexibility to operate HEAT in upward, as well as in downward mode allows a cross calibration with telescopes from the Coihueco site, which is less than 200 m away, and shares the field of view partly with HEAT (cf.

map in figure 3.10). In contrast to the standard FD, HEAT takes advantage of upgraded electronics with larger and faster FPGAs, and an increased digitization rate of 20 MHz, accommodating the higher angular velocity air showers possess, if they are closer to the telescope. Regarding data acquisition and operation, HEAT can be regarded as a fifth *eye* of the fluorescence detector. It extends the energy range of the FD downwards to energies below 10^{17} eV.

AERA - Auger Engineering Radio Array

The particles of an extensive air shower produce electromagnetic radiation not only in the UV range, but also with longer wavelengths. Radio signals are predominantly produced by geomagnetic effects [82], where charged particles are deflected in the magnetic field of the Earth, leading to time-varying transverse currents and a geosynchrotron effect. A smaller contribution arises from the time-varying charge excess within the shower front (Askaryan effect). It is mainly caused by electrons which have been created by ionization from air molecules and are dragged along with the shower front. For a detailed discussion of these effects please refer to reference [83] and those therein. The emission shows coherence for frequencies below ~ 100 MHz [83]. Its pulse amplitude is related to the energy of the primary particle, and its detection is sensitive to the longitudinal shower development. An array of suitable receivers should therefore allow to reconstruct the key properties of an extensive air shower: the primary energy, the shower axis, and the mass of the primary particle. With a duty cycle of almost 100% this array might be an excellent detector for ultra-high-energy cosmic rays.

Such an array is realized with AERA [84]. AERA started data acquisition in 2011 with 24 radio detector stations arranged in a triangular grid on an area of about 0.5 km^2. Around this dense core with a spacing of 150 m between neighboring stations, 100 further detector stations have been deployed recently. These additional stations with spacings of 250 and 375 m increase the instrumented area to 6 km^2. Deployment of 36 additional stations is planned to achieve an area of at least 10 km^2. The current borders of the AERA array are illustrated in the map in figure 3.10.
The centerpiece of each station are two antennas, receiving radio signals from air showers in the range from 30 to 80 MHz. These antennas are dipole antennas and perpendicular to each other to measure the north-south and east-west polarizations independently. The recently deployed stations implement active bowtie antennas [85] — a photo is shown in figure 3.11, whereas the other 24 stations employ log-periodic dipole antennas [85, 86]. Since AERA is an engineering array, different setups, also regarding electronics and trigger mode, are investigated. Already with its 24-antenna-configuration AERA has measured 365 high-quality events [84]. Two third of these events were acquired in a self-trigger mode and coincident with the SD. The remaining events were externally triggered by the SD.
AERA is addressed at answering the key questions of the radio detection of cosmic rays: Which are the underlying effects for the radio emission? Can radio detectors compete with existing methods regarding precision? Can all parameters of interest of an air shower be accessed with the radio detection technique — or in other words,

Figure 3.11: **Left:** Photo of a radio detector station of AERA. Visible in the center of the picture are two active bowtie antennas perpendicular to each other. An antenna for communication is mounted on top. The box at the bottom is covered with solar panels and houses the electronics and batteries. Taken from reference [84]. **Right:** Photo of AMBER, one of the microwave detector prototypes of the Pierre Auger Observatory. In the focus of a 2.4 m off-axis parabolic dish a camera with 16 pixels is located. The pixels are commercial C-band and Ku-band microwave receivers. Taken from reference [87].

can a radio detector act as a stand-alone solution for cosmic ray detection? And, is it effective to build a radio detector on a very large scale?

Microwave detectors

Further signals from air showers are expected within the microwave range. In reference [88] P. Gorham *et al.* reported microwave radiation from a weakly ionized plasma. This plasma was generated by an electron beam which showered in a target. Subsequently, the plasma entered an anechoic chamber which was instrumented with commercial microwave receivers. The radiation was attributed to molecular bremsstrahlung radiation (MBR). MBR is created in weakly ionized air when free electrons and positrons are accelerated by collisions with the fields of the surrounding molecules. It is unpolarized and isotropic. The observation of air showers by means of microwave detection would therefore be similar to the fluorescence detection technique, but promising a duty cycle of nearly 100%. In addition, detectors can take advantage of commercial receivers.

The Pierre Auger Observatory includes several microwave detector prototypes. AMBER (Air shower Microwave Bremsstrahlung Experimental Radiator) and MIDAS (MIcrowave Detection of Air Showers) are imaging telescopes with feed horn antennas in the focus of parabolic dishes. The have fields of view of $14° \times 14°$ and $20° \times 10°$, respectively. While AMBER is triggered by the SD, MIDAS is operated in a self-trigger mode. They are operating at the Pierre Auger Observatory since 2011 and 2013, respectively.
A different approach is investigated with EASIER (Extensive Air Shower Identification with Electron Radiometer). This microwave detector consists of wide-angle feed

horn antennas mounted on top of 61 SD stations in the southern part of the ground detector array. The first seven antennas were deployed in 2011, the remaining in 2012. Their effective area is much smaller compared to AMBER and MIDAS, but EASIER stations are typically closer to the air shower, and the microwave signal is compressed in time due to geometrical reasons. Altogether EASIER provides a sensitivity close to the ones of the imaging detectors. The signals of an EASIER station are processed to a channel of the electronics of the SD station it is mounted on. This simplifies the experimental setup to a great extend, since EASIER uses the same data acquisition, trigger, and communication system as the SD stations. If an SD trigger is generated and the data of the corresponding SD station are acquired, the EASIER data will be acquired automatically as well. The EASIER site is overlooked by MIDAS. EASIER has detected three events with significant signals in the microwave range. Whether these signals are produced by MBR is still a topic of discussion. A serious argument against MBR signals is the fact that no significant number of microwave event candidates from the other two detectors has been reported. Recent discussions also consider the radio emission from air showers to be the cause for the signals detected by EASIER. Under certain geometrical conditions regarding the point of observation, the radio signals can feature non-negligible signal levels in the microwave bands as well. For more information on the microwave detectors please refer to references [87, 89].

Besides the discussed low-energy enhancements of the Pierre Auger Observatory and the R&D detectors for alternative air shower detection, many further upgrade plans and complementary experiments are investigated. A description of all of these endeavors exceeds the scope of this work. In the following we will only consider one of these upgrade projects: FAMOUS (First Auger Multi-pixel-photon-counter camera for the Observation of Ultra-high-energy air Showers). FAMOUS is intended as the prototype of a potential successor to the fluorescence telescopes of the observatory. It implies novel types of photodiodes with single photon counting ability referred to as silicon photomultipliers. These photosensors will be discussed in detail in the next chapter. The overall design of FAMOUS and its components will be presented in the subsequent chapter 5.
A proof-of-principle for FAMOUS are measurements of the night-sky photon flux with a silicon photomultiplier camera. The experimental setup with which such measurements have been performed will be presented in chapter 6. It will be followed by a detailed analysis, how to reconstruct continuous light fluxes measured with silicon photomultipliers.
The measured light flux of the night-sky is crucial for the evaluation of the dynamic range of a fluorescence telescope like FAMOUS. It defines the sensitivity for the detection of air showers at the considered observational site. The light originating from stars which are well-studied by observational astronomy is of special interest since these stars can be regarded as calibrated light sources. A comparison of star light photon fluxes, which have been measured with a silicon photomultiplier camera, with fluxes derived from independent photometric measurement will be discussed in chapter 8.

4. Silicon Photomultipliers

Silicon photomultipliers (SiPMs) are semiconductor photosensors with single photon counting ability and high photon detection efficiency. They consist of arrays of avalanche photodiodes operated in Geiger-mode, which ensure a high internal gain and a linear response to the incident photon flux within their dynamic range.

Pioneering work regarding SiPMs goes back to the 1960s, whereas the device in its form as we know it today was successfully produced around the millennium change (see e.g. reference [90]). Many different names are common to these photosensors, although SiPM seems to become the most prevalent one. Other frequently used names are MPPC (Multi-Pixel Photon Counter), PPD (Pixelated Photon Detector), and sometimes in the literature G-APD (Geiger-mode Avalanche Photo Diode) and SPAD (Single Photon Avalanche Diode) are used as synonyms for SiPM.[1]

SiPMs possess a large variety of desirable features: they provide a high photon detection efficiency, single photon detection and resolution, an excellent timing ability, they are compact, rugged, and insensitive to magnetic fields, have a low power consumption, tolerate accidental illumination, and, since they are semiconductor devices, have the potential for cost-efficient mass production. Hence, there is already a number of applications where SiPMs replaced photomultiplier tubes. These include detectors in high-energy and astroparticle physics, as well as in medical imaging. Further efforts also study their use for three-dimensional time-of-flight imaging (for instance for security agencies or archeology) and for optical communication.

We will continue this chapter with a short introduction to photodiodes to explain the working principle of SiPMs. This discussion is predominantly based upon reference [91]. SiPMs themselves and their properties will be reviewed subsequently. Special attention will be paid to the measurements of characteristics which are of interest particular for the reconstruction of detected photon fluxes. We will also introduce the simulation toolkit G4SiPM developed by T. Niggemann *et al.* It exploits a phenomenological model of SiPMs based on laboratory measurements to simulate the response of SiPMs. At the end of this chapter we will have a brief look at recent developments in SiPM technology.

[1] Here we will separate SiPM strictly from G-APD/SPAD since an SiPM is composed of many cells with each them of them being an individual G-APD/SPAD. See the following sections for detailed information.

4.1 Introduction to photodiodes

pn–junction

When a photon is absorbed within a semiconductor it can create an electron-hole-pair (eh-pair). This creation requires an energy of the photon E being greater (or equal) than the band gap E_g of the semiconductor. Silicon for example has a band gap of about 1.11 eV at a temperature of 300 K. Thus, photons with wavelengths greater than $\lambda = c/f = hc/E_g \approx 1117\,\text{nm}$ cannot produce an eh-pair in silicon at room temperature. Here, c is the speed of light, f is the frequency of the photon, and h is Planck's constant. The requirement $E \geq E_g$ leads to typical sharp cutoffs in the spectral sensitivities of semiconductors.
Once created, the electron and hole will likely recombine unless they will be separated from each other. In general, a pn–junction can separate them, and thus can act as a photodiode since the separation leads to a current.
A pn–junction is created when a positively (p) doped semiconductor is brought into contact with a negatively (n) doped semiconductor. Positive charge carriers (holes) will diffuse into the n region, whereas negative charge carriers (electrons) will diffuse into the p region. Following the diffusion the electrons will recombine with the holes in the p region. Likewise for the diffused holes which recombine with electrons in the n region. This recombination leaves a depletion zone close to the junction with positive and negative ions, and no mobile charge carriers. Therefore, the depletion zone is also referred to as space charge region. Here the ions create an electric field which counteracts the diffusion process. The pn–junction reaches a state of equilibrium as soon as the electric field is strong enough to prevent further diffusion of charge carriers. A schematic view of a pn–junction, as well as qualitative displays of its charge density, electric field, and potential curve are shown in figure 4.1 (panels a–d). The potential difference between the n region and the p region is given by the diffusion voltage

$$U_{\text{diff}} = \frac{k_B T}{e} \ln\left(\frac{n_a n_d}{n_i^2}\right) \tag{4.1}$$

where k_B is the Boltzmann constant, T is the temperature, n_a and n_d are the concentrations of acceptors and donators respectively, and n_i is the charge concentration of the intrinsic (i.e. non-doped) semiconductor. The width of the charge separation zone w can be expressed as

$$w = \sqrt{\frac{2\epsilon_0\epsilon_r}{e}\frac{(n_a + n_d)}{n_a n_d} \cdot (U_{\text{diff}} - V_{\text{bias}})} \tag{4.2}$$

where ϵ_0 is the vacuum permittivity, ϵ_r the relative permittivity of the semiconductor, and V_{bias} is the externally applied bias voltage. Furthermore, charge conservation requires

$$d_n n_D = d_p n_A \tag{4.3}$$

with d_n and d_p being the spatial extends of the charge separation region into the n and the p region, respectively. This means that the charge separation region will be

symmetrical for equal impurity concentrations n_D and n_A. Otherwise, it will extend farther into the less doped region.

If the pn–junction is reversely biased (i.e. '+'-terminal of the voltage source connected to the n region and '–'-terminal connected to the p region, negative sign to V_bias), the electric field across the charge separation zone will increase and the zone itself will broaden. Apparently w will reach its maximum if the pn–junction is fully depleted. Only a very low reverse leakage current will flow, unless the applied voltage reaches a level where a breakdown occurs. If the pn–junction is forwardly biased (i.e. '+'-terminal connected to the p region and '–'-terminal connected to the n region) the electric field will decrease, and if the applied voltage is high enough, a significant current will flow. The pn–junction thus forms the principle of a diode.

If a photon creates an eh-pair in the charge separation region, the electric field can separate them. Being separated they drift into opposite directions towards the anode and the cathode of the diode. If the diode is short-circuited, a photo current I_ph will flow which has the direction of a reverse current. The photocurrent is small and typically has to be amplified for detection. It can be measured for example by the voltage it creates at a resistor or by operational amplifiers which transfer the current to a well-measurable voltage.[2]
Let us assume the illumination of a pn–junction with a monochromatic light source of radiant flux ϕ. In an ideal photodiode (quantum efficiency[3] QE = 1) the photon flux $\dot{N} = \phi/(hf)$ from the light source will create the photo current $I_\mathrm{ph} = e\dot{N} = (e\phi)/(hf)$, where e is the elementary charge. For real devices, where $\mathrm{QE} = \mathrm{QE}(\lambda) < 1$, we find

$$I_\mathrm{ph} = \frac{e\phi}{hf} \cdot \mathrm{QE}(\lambda)\,. \tag{4.4}$$

The photo current depends linearly on the absorbed radiant flux. For most diodes this is the case over several orders of magnitude in the radiant flux until saturation effects commence. For a homogeneous illumination of the pn–junction the photo current increases linearly with the sensitive area of the diode. It depends only little on the temperature T and the reverse bias voltage V_bias (cf. figure 4.1 (panel g)).

To enable the absorption of light in a photodiode in the first place, the device needs an entrance which photons can pass. Anti-reflecting coatings are typically applied to this entrance to increase the sensitivity of the sensor. Inside the semiconductor the intensity of the light is decreasing according to the Beer–Lambert law to

$$I = I_0 \cdot e^{-\alpha(\lambda)\,x} \tag{4.5}$$

where I_0 is the intensity of the light upon its entrance into the semiconductor, α is the absorption coefficient, and x is the traversed distance. The absorption

[2] Such devices are called transimpedance amplifiers. The name arises from the fact that the unit of the gain is the same as the one of an impedance.

[3] The quantum efficiency is defined as the probability that a photon creates an eh-pair, and that electron and hole will be separated from each other.

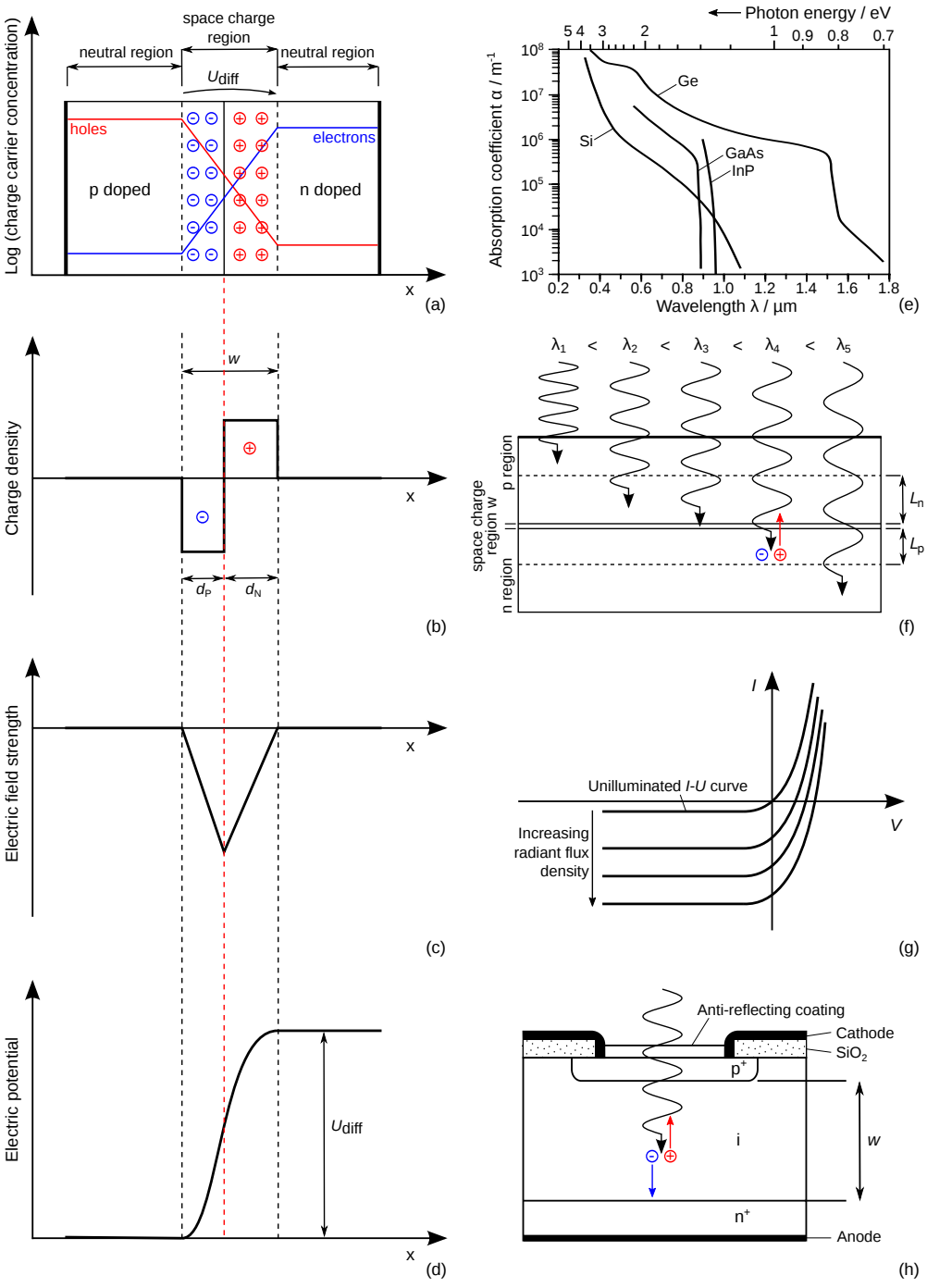

Figure 4.1: **Panels (a)–(d):** Qualitative illustration of a pn–junction, its charge carrier concentration, charge density, electric field strength, and electric potential. See text for details. **Panel (e):** Absorption coefficient as a function of the wavelength for silicon (Si), germanium (Ge), gallium arsenide (GaAs), and indium phosphide (InP). Plotted are data as presented in reference [92]. **Panel (f):** Absorption of radiation with different wavelengths inside a photodiode. See text for details. **Panel (g):** Current(I)–voltage(V) characteristics of a photodiode. The reverse photo current does almost not depend on the voltage for a wide range. In forward direction the current increases vastly with the voltage. **Panel (h):** Schematic illustration of a pin–photodiode. Sandwich structure: between heavily doped p^+ and n^+ layers a layer of undoped material (i for intrinsic) is applied. The silicon oxide (SiO_2) acts as an insulator. See text for details.

coefficient as a function of the wavelength λ for several semiconductors is shown in figure 4.1 (panel e). This dependence on the wavelength leads to the fact that photons with a specific wavelength are more likely to be absorbed at the location of the charge separation zone (cf. figure 4.1 (panel f)). If the wavelength is very short, the photons are absorbed close to the entrance. If the wavelength gets too large, the semiconductor becomes transparent for the light.[4] This is the reason for the dependency of the quantum efficiency QE on the wavelength λ as stated already implicitly in equation (4.4).
However, not only photons which are absorbed within the charge separation zone are contributing to the photo current.[5] Charge carriers which are created outside the charge separation zone can diffuse into it and be affected by its electric field. The average distances charge carriers can diffuse through the semiconductor are the diffusion lengths L_n and L_p for electrons and holes, respectively. They are illustrated in figure 4.1 (panel f). L_n is greater than L_p due to the higher mobility of the electrons compared to the holes. For silicon at a temperature of $T = 300\,\mathrm{K}$ the diffusion lengths are $L_\mathrm{n} = 59\,\mu\mathrm{m}$ and $L_\mathrm{n} = 35\,\mu\mathrm{m}$, which is up to two orders of magnitude larger than the width of the charge separation zone in the absence of a bias voltage V_bias.

Changes of the temperature T affect predominantly the dark current, which is the reverse current along the diode in the absence of light. With an increase in T the number of thermally generated free charge carriers which reach the charge separation zone increases. The noise which is caused by charged carriers crossing a potential barrier is called shot noise. Per temperature change $\Delta T = 10\,\mathrm{K}$ the dark current increases by a factor of 2 up to 4.
Another effect which is caused by changes of the temperature is the small reduction of the band gap with an increase of the temperature. As an example let us consider a typical, domestic tungsten-filament lighting, or to be more precise a Planck radiator at a temperature of 2856 K which is defined as the Standard Illuminant A [93]. It has its radiation maximum at a wavelength of about 1015 nm. The photo current due to its radiant flux measured with a silicon photodiode increases by about 0.1 to 0.2% per K increase in temperature.

Different mechanisms inside the photodiode lead to a delayed response of the sensor to a prompt change in the radiant flux of a light source.
The capacitance of the charge separation zone C is de-charged and re-charged along the load resistance R_L. This leads to a time constant $\tau_{RC} = R_\mathrm{L}C$. Commonly used is a load of $R_\mathrm{L} = 50\,\Omega$. With a typical capacitance of several 100 pF the time constant is in the order of several 10 ns. A reverse bias voltage will reduce the capacitance and result in a smaller time constant.
When charge carriers are created outside of the charge separation region they have to diffuse to it to contribute to the photo current. The diffusion process is typically

[4] Technically speaking this is not correct since photons can also be absorbed in solids due to different processes than the creation of an eh-pair.

[5] In fact the charge separation zone is so small (typically 0.1 – 1 µm) that absorption of photons within it has a very low probability.

slow. Its time constant τ_{diff} depends quadratically on the diffusion length L: $\tau_{\text{diff}} = L^2/(2D)$, with the diffusion constant D. For silicon τ_{diff} is in the order of 1 µs.
The time, which a charge carrier with the velocity v_{drift} needs to cross the charge separation region with the width w, is $\tau_{\text{drift}} = w/v_{\text{drift}}$. With a high electric field strength v_{drift} is approximately the saturation drift velocity v_{sat}. For silicon $v_{\text{sat}} \approx 10^5\,\text{m}\,\text{s}^{-1}$. To cross the distance w it will take the charge carrier about $\tau_{\text{drift}} = 10\,\text{ps}$.
The three contributions sum up to the total time constant $\tau = \tau_{RC} + \tau_{\text{diff}} + \tau_{\text{drift}}$. It is dominated by the diffusion process. With $\tau \approx 1\,\mu\text{s}$ the -3 dB cutoff frequency is $f_c \approx 1\,\text{MHz}$. Commercially available silicon photodiodes show typical cutoff frequencies ranging from 200 kHz to 50 MHz. To increase the speed of a photodiode a pin–structure can be used.

pin–photodiode

A pin–photodiode is a sandwich structure with an intrinsic (i) semiconductor between a heavily doped p^+ region and a heavily doped n^+ region. It leads to a much larger width of the charge separation region w than a common pn–junction. A schematic of a pin–diode is shown in figure 4.1 (panel h).
If w is sufficiently large, almost all eh-pairs will be created inside the charge separation region. And with sufficiently thin p^+ and n^+ regions the contribution to the total time constant τ due to the diffusion process becomes negligible. Moreover, with a broad i region the capacitance of the charge separation region decreases (typically to values of several 0.1 to 1 pF) and so does the RC time constant. τ is now dominated by the drift time constant. As an example, for a silicon pin–diode with $w = 10\,\mu\text{m}$ the drift time constant is $\tau_{\text{drift}} = w/v_{\text{sat}} = 100\,\text{ps}$. The small time constants lead to -3 dB cutoff frequencies in the GHz region, which makes the diodes also interesting for optical fiber communications. Transmitters in optical fiber communications are mostly operated at wavelengths in the near infrared (typically 1.1 to 1.6 µm). With a broader i region the photodiode also becomes more sensitive to longer wavelengths. But on the other hand, τ_{drift} increases with w and the light sensor reacts slower. However, silicon is not applicable for wavelengths greater than about 1.1 µm, since the energy of these photons is smaller than the band gap, and thus no eh-pairs will be created. For these wavelengths germanium is the typically applied semiconductor.

Avalanche photodiode

So far in our discussion, each eh-pair, which did not recombine, provided exactly one charge carrier to the measurable photo current. With an avalanche photodiode (APD) an intrinsic amplification of the photo current can be achieved.

A common structure of an APD is depicted in figure 4.2. It is referred to as an n-on-p structure since it is built on a p^+ substrate. On top of the substrate a π layer is deposited, where π stands for an almost intrinsic p material. It is followed by a p layer and a heavily doped n^+ layer. Furthermore, the figure shows an even heavier doped n^{++} layer and a lesser doped n^- guard ring. The former ensures good

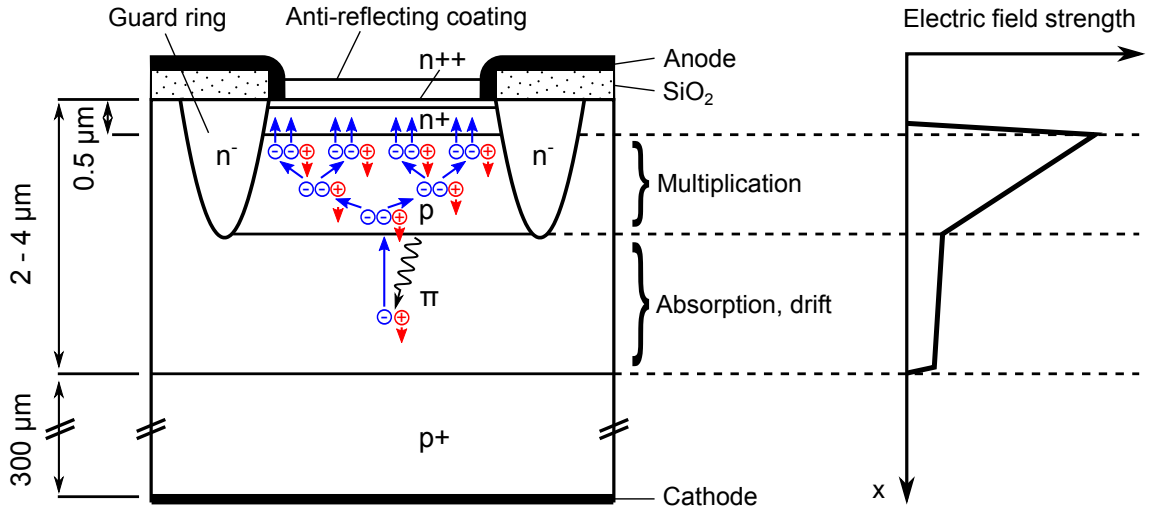

Figure 4.2: Qualitative display of an avalanche photodiode and its electric field strength. Shown is an n-on-p structure. A photon creates an eh-pair with the electron drifting into the multiplication region where it triggers an avalanche. The heavily doped n^{++} layer ensures a good conductivity between the device and its anode. The guard ring is intended to minimize surface leakage currents. The silicon oxide (SiO_2) acts as an insulator. Not to scale, especially the p layer is considerably thinner than the π layer. (π means positively doped but with a very low level of doping.) Layer thicknesses should only be regarded as reference values.

conductivity between the diode and its anode, whereas the latter minimizes surface leakage currents from the periphery of the active area of the photosensor. Both are not essential for the fundamental concept of an APD but enhance its performance. When a photon creates an eh-pair in the π layer the electron drifts towards the n^+ region. When it reaches the p region it gets intensely accelerated by the high electric field. If its kinetic energy exceeds the band gap, it can create another eh-pair by collision with an electron, which is referred to as impact ionization. Both electrons will again be accelerated and can create further eh-pairs. As long as the multiplication region is wide enough this avalanche-like effect will continue, leading to an internally amplified photo current.

Shown in figure 4.2 is the case of a semiconductor where the probability $\alpha_n dx$ of an electron creating an eh-pair along the distance dx is greater than the probability $\alpha_p dx$ of a hole creating an eh-pair on the same distance. Here, α_n and α_p are the ionizations coefficients of electrons and holes, respectively, which depend exponentially on the electric field strength. In silicon for example $\alpha_n \gg \alpha_p$, and typically only the electrons will cause impact ionization. Thus, the current pulse caused by an absorbed photon stops with the last hole reaching the cathode. This will not be the case if both kinds of charge carriers are able to effectively create eh-pairs by impact ionization. The diode will break down as long as the multiplication region is sufficiently wide enough: the avalanche process is self-sustaining and will not come to an end as long as it will not be quenched. Such a breakdown will occur within a

silicon diode if the device is operated beyond a characteristic voltage referred to as breakdown voltage. This behavior is desired for a special kind of APDs, specifically Geiger-mode APDs (G-APDs). We will discuss them subsequently.

The n-on-p structure is more sensitive to long wavelengths. For a qualitative discussion let us regard a photon with a short wavelength entering the photodiode. It is likely to be absorbed within a fraction of a micrometer. Thus, in contarst to the illustration in figure 4.2, the eh-pair is created between the entrance window and the pn–junction. Instead of an electron, now a hole has to drift into the multiplication region to start the avalanche process. Since the ionization coefficient of holes is smaller than the one of electrons for silicon, the probability of an avalanche to be triggered is reduced compared to the event, where a photon is absorbed at the opposite side of the multiplication region. Hence, the n-on-p structure is more sensitive for red light than for blue light.
If a diode is requested to have its peak sensitivity at shorter wavelengths, a p-on-n structure can be realized. Basically the doping of the layers of the photodiode are inverted compared to the n-on-p structure. This means that also the directions into which the charge carriers will drift are inverted. Hence, an eh-pair which is created between the entrance window of an APD and its pn–junction will have the electron to drift towards the multiplication region to trigger an avalanche.

The primary photo current of an APD, $I_{\mathrm{ph}} = e\phi/(hf) \cdot \mathrm{QE}$, is amplified by the gain M of the diode to

$$I = M \cdot I_{\mathrm{ph}} \,. \tag{4.6}$$

With a constant gain the output photo current is still proportional to the absorbed radiant flux $\phi \cdot \mathrm{QE}$. The gain depends on the applied bias voltage V_{bias}. For a small bias voltage the electric field is completely contained inside the region of the diode which is intended to be the multiplication region. Hence, with an increase of V_{bias} the gain steeply rises. At a certain bias voltage the electric field starts to reach into the π region. Therefore, the further rise of the gain with a further increase of V_{bias} is not as steep as before. Above this kink in the M–V_{bias} characteristic the gain for a constant temperature T is approximately given by

$$M = \left[1 - \left(\frac{V_{\mathrm{bias}} - I \cdot R_{\mathrm{s}}}{V_{\mathrm{bd}}}\right)^{m}\right]^{-1} \tag{4.7}$$

where $I \cdot R_{\mathrm{s}}$ is the voltage drop along the serial resistance of the APD, V_{bd} is the breakdown voltage, and $m < 1$ is an exponent depending on the material and the radiant flux density. An increase in the temperature will lead to a decrease in the gain, since vibrations of the crystal lattice of the semiconductor are more intense with higher temperatures. This way the accelerated charge carriers are likely to lose more energy by collisions with the lattice. Consequently, impact ionization becomes less frequent and the gain decreases.

With its high internal gain, which is typically in the order of a few hundred for silicon, an APD has a high photon sensitivity: the minimal detectable signal of

a silicon APD can already be generated by 10 – 20 electrons triggering avalanche processes. For comparison, a silicon PIN photodiode provides a minimal detectable signal for 200 – 300 separated eh-pairs [90]. Nevertheless, the sensitivity can decrease with increasing gain. The signal-to-noise ratio degrades with increasing gain since the noise power rises. Photodiodes without internal amplification of the primary photo current generate thermal noise and shot noise.[6] Like these two kinds of noise incidents, the avalanche process of an APD has a statistical nature. Hence, the gain is not a constant value but varies from avalanche to avalanche. (Implicitly we were considering the mean gain in the previous paragraphs.) The internal amplification of an APD contributes to the shot noise by a factor called excess noise factor (ENF). It depends on the mean gain M and the ratio k of the ionization coefficients of electrons and holes. If $\alpha_\mathrm{n} > \alpha_\mathrm{p}$ as for silicon, then $k = \alpha_\mathrm{n}/\alpha_\mathrm{p}$. If $\alpha_\mathrm{n} < \alpha_\mathrm{p}$ as for instance for germanium or indium phosphide, then $k = \alpha_\mathrm{p}/\alpha_\mathrm{n}$.

$$\mathrm{ENF}(M) = kM + (1-k)\left(2 - \frac{1}{M}\right) \tag{4.8}$$

The ENF becomes maximal for $k = 1$ and is equal to the gain in this case. For $k = 0$ the ENF has a maximum value of 2.
This additional noise due to the internal amplification is a prominent reason why APDs are often made from silicon. In silicon $k < 0.02$, whereas for example for germanium and indium phosphide $k \approx 0.5$ [94].

Geiger-mode avalanche photodiode

When an APD is operated with a bias voltage V_bias greater than its breakdown voltage V_bd both electrons and holes will create new eh-pairs by impact ionization. This mode of operation is often called Geiger-mode, following the Geiger–Müller tube, and the photosensor is thus called Geiger-mode avalanche photodiode (G-APD). The operation beyond the breakdown voltage leads to an even increased gain compared to APDs. For silicon it is typically in the range of 10^5 to 10^6 which allows the detection of single photons.[7] This feature has led to the alternative name of single photon avalanche photodiodes (SPADs) for G-APDs. Regarding the manufacturing process of APDs the technical challenge has been the precise creation of the small volume where the multiplication of charge carriers takes place. If the volume is too large, the number of thermally generated eh-pairs which cause a breakdown will increase to a quantity where the device is in a permanent breakdown, and thus will only produce noise. Technological progress has led to APDs which offer a controlled mode of operation with reasonable noise.

Once an avalanche is triggered within an G-APD, the process will continue until it is quenched. A common possibility of quenching is the use of a serial quenching

[6] thermal noise: eh-pairs created by thermal excitation trigger an avalanche; shot noise: fluctuation of the output signal due to the stochastic process of charge carriers crossing a potential barrier

[7] In theory also devices with lower gain allow the detection of single photons. In practice this ability is limited due to the combined noise of photosensor and readout electronics.

resistor R_q. In the progress of an avalanche the amplified photo current I through R_q increases, and with it the voltage drop $I \cdot R_q$ along the resistor increases as well. This leads to a decrease of the voltage along the G-APD. With a certain current the voltage along the G-APD drops beneath the breakdown voltage and the avalanche process stops. Subsequently, the initial voltage along the G-APD will be restored.
A different method is active quenching. Here, external electronics set the bias voltage below the breakdown voltage as soon as a photo current is detected. Afterwards, when the avalanche process is disrupted, the bias voltage is set to its nominal value, and the diode will revert to its initial state where it will be ready for its next breakdown.

With the Geiger-mode the proportionality of the output current of an APD to the absorbed radiant flux is lost. The signal will be of the same level irrespective of the number of absorbed photons, as long as the time between absorption is sufficiently small. Lets consider any number of photons greater than zero being absorbed at the same time in an ideal G-APD with a quantum efficiency of QE = 1 and a probability to trigger an avalanche of 1. The output current will be identical for all numbers of photons, except from some fluctuation due to the statistical nature of the avalanche process.

The gain G of a G-APD is proportional to the terminal capacitance of the device C and the difference between the bias voltage V_{bias} and the breakdown voltage V_{bd} [90]. The latter is called over-voltage $V_{ov} = V_{bias} - V_{bd}$.

$$G \sim \frac{C}{e} V_{ov} \tag{4.9}$$

with the elementary charge e. The terminal capacitance does not depend on the temperature T, but only on the width of the charge separation zone. At high reverse voltages, as it is the case for Geiger-mode operation, the width of the depletion zone does not depend on V_{ov}. Therefore, the gain will not vary with a variation of the temperature if the over-voltage is constant. However, the breakdown voltage will vary with changes of T. As discussed earlier, an increased temperature leads to increased crystal lattice vibrations which cause the charge carriers to lose more energy before they can create further eh-pairs. This leads to the need of a higher electric field strength to results in the same efficiency of triggering an avalanche. Thus, the breakdown voltage is higher for a higher temperature.
To keep the over-voltage (and the gain) constant with changes of the temperature the bias voltage has to be regulated according to changes of the breakdown voltage.

Silicon photomultipliers

A possibility to achieve a photosensor operated in Geiger-mode, and thus providing single photon detection, but also featuring an output current proportional to the absorbed radiant flux is provided by a silicon photomultiplier (SiPM). An SiPM is an array of G-APDs with their serial quenching resistors. The G-APD–resistor–pairs

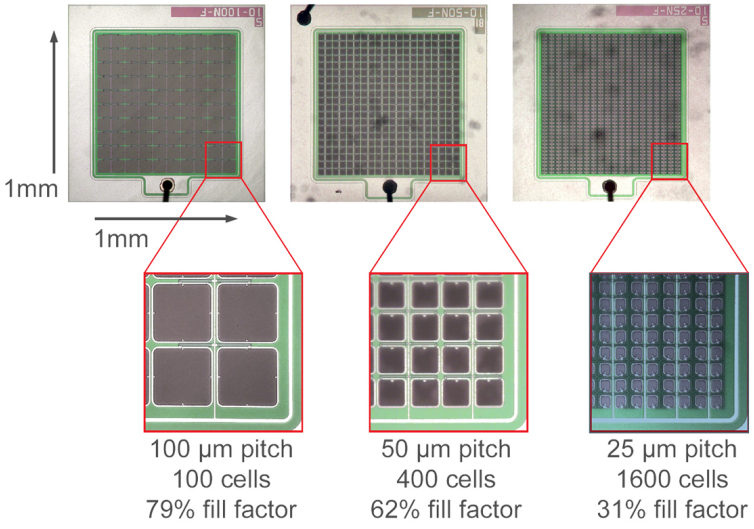

Figure 4.3: Photos of Hamamatsu SiPMs S10362-11-100C/-050C/-025C (from left to right). Taken from reference [95].

are connected in parallel and are referred to as a cells.[8] The arrays are well-visible in the photos shown in figure 4.3. A schematic of an SiPM is given in figure 4.4 (left). The output current is the sum of the currents of all cells. It can be measured by the voltage drop it evokes along a common load resistor. If a cell breaks down, it will generate a standard signal referred to as the 1 photon-equivalent (1 p.e.) signal, providing that the prior cell breakdown lies sufficiently in the past, so that the cell could completely recover from it.

It it obvious that the response of the SiPM can only be linear to the absorbed photon flux as long as the number of photons is small within a characteristic time compared to the number of cells, and as long as the photons are well distributed over the entire active area of the SiPM. Otherwise, saturation effects will distort the linearity of the response. We will have a closer look at these effects in section 4.2.
The characteristic time is the recovery time of the SiPM τ_{rec}. After a cell breakdown the capacitance of the G-APD will recharge with the time constant τ_{rec} and rebuild the charge separation region. If the cell breaks down before it has been fully recharged, the voltage drop V_{out} along the load resistor caused by the single cell will be smaller than the standard 1 p.e. signal $V_{1\,\text{p.e.}}$ according to the recharge process

$$V_{\text{out}}(t) = V_{1\,\text{p.e.}} \left(1 - e^{-t/\tau_{\text{rec}}}\right) \tag{4.10}$$

where t is the time after the initial cell breakdown. The equation might also take a potential dead time into account between the initial breakdown and the start of the recharge process.[9]

[8] Speaking of *cell*, the expression *pixel* is also frequently used in the literature. But since the telescopes we will discuss in the next chapters use cameras with pixels we will not use the same term for cell to avoid misunderstandings.

[9] However, in section 7.3 we will see that the dead time can often be neglected compared to the recovery time.

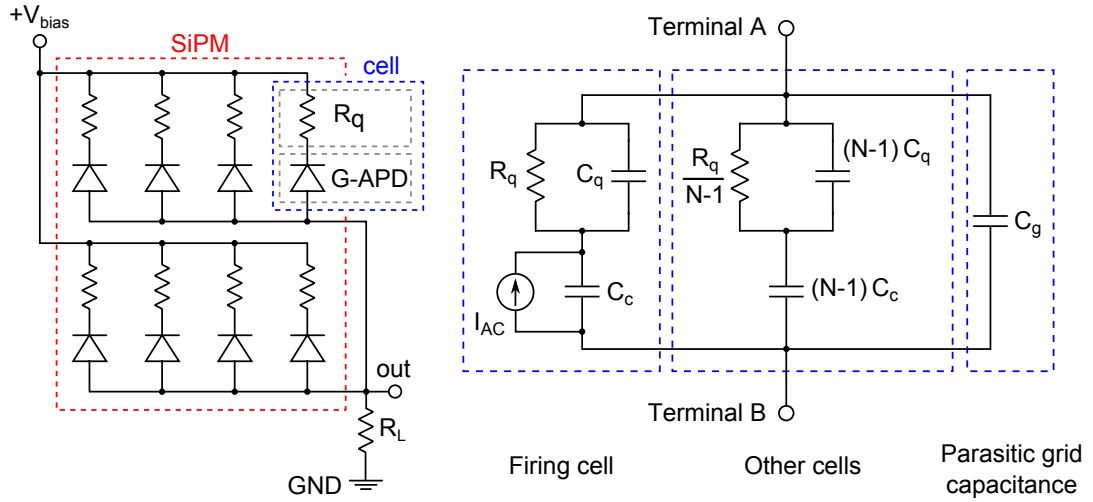

Figure 4.4: **Left:** Schematic of an SiPM with eight cells. Each cell consists of a Geiger-mode avalanche photodiode (G-APD) and its quenching resistor R_q. The cells are connected in parallel and biased with the voltage V_bias. The SiPM is terminated by a load R_L common to all cells. **Right:** Electric model of an SiPM with one cell breaking down according to reference [99]. See text for details.

Two photons being absorbed at the same time in the same cell both triggering an avalanche will lead to an output signal of $V_{1\,\mathrm{p.e.}}$. But as soon as the time between their absorption t is greater than zero, the output signal will be $V_{1\,\mathrm{p.e.}} + V_\mathrm{out}(t)$. It is a fact worth mentioning that this recovery time is not the recovery time of the SiPM itself but of a cell.[10] Each cell recovers individually after a breakdown. For our example with the two photons the question is if the voltage $V(t)$ and the time t can be resolved with the experimental setup to distinguish whether one or two photons have been detected. Novel SiPMs reach signal rise times of $\sim 100\,\mathrm{ps}$ and recovery time constants smaller than 1 ns [97].
The timing characteristics are also very good. The timing resolution of a single cell has been determined for instance in reference [98] to about 50 ps.[11]

Although an SiPM is a complex semiconductor device its electric behavior and the form of its output pulse can be described appropriately by a rather simple electronic model. Such a model as presented in reference [99] is shown in figure 4.4 (right). It is the equivalent circuit of an SiPM with N cells, where one cell is breaking down. This cell is depicted to the left of the equivalent circuit with its cell capacitance C_c and the quench resistance R_q in series. The quench resistor also possesses a capacitance C_q. The current source I_AC generates the current according to the cell breakdown which occurs at the time t_0. Its waveform is a Dirac delta pulse $Q\,\delta(t)$ with the

[10] A further recovery time constant exists which is probably not related to the cell capacitance but to the capacitance of the bulk (i.e. the substrate of the diode). It is relevant for the recharge if many or even all cells are triggered simultaneously. For more information please refer to reference [96].

[11] This value is the RMS of the histogram containing the response times of the cell after being triggered with a very fast laser. Contributions due to the timing of the laser and the electronics have been subtracted.

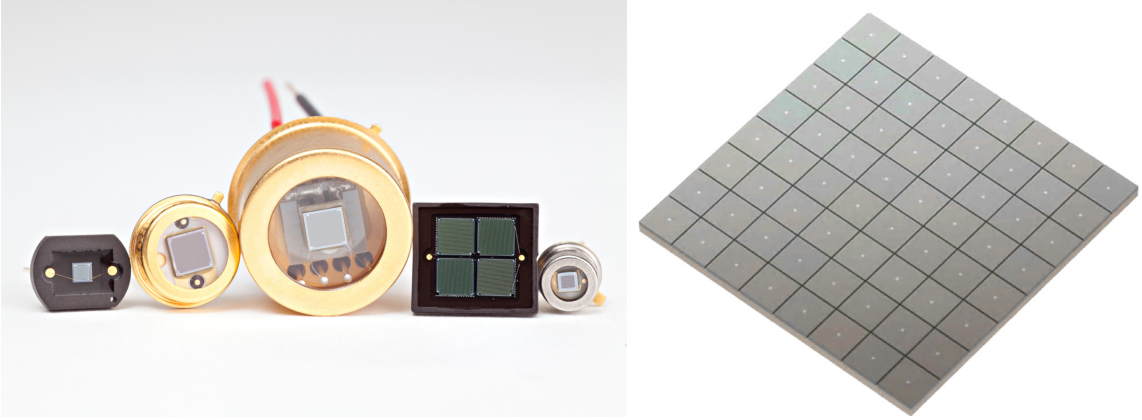

Figure 4.5: **Left:** Photo of a group of SensL MicroSL 100, 300, 600 series SiPMs. The sensor to the left has a sensitive area of $1\times1\,\mathrm{mm}^2$. Taken from reference [102]. **Right:** Array of 8×8 discrete SiPMs manufactured by Hamamatsu. Each SiPM has a size of $3\times3\,\mathrm{mm}^2$. Taken from reference [103].

charge $Q = V_{\mathrm{ov}}(C_{\mathrm{c}} + C_{\mathrm{q}})$. Connected in parallel to the cell we see the equivalent circuit of the $N-1$ cells which do not break down. Furthermore, a parasitic grid capacitance C_{g} is adopted.
In this model only the four parameters C_{c}, R_{q}, C_{q}, and C_{g} are needed to describe the SiPM.
Since the impedance Z of the model depends on these parameters, they can be accessed by measurements of Z using vector network analyzers or LCR meters. Extensive impedance measurements have been performed in the scope of reference [100] to determine the electric parameters of SiPMs manufactured by Hamamatsu and Ketek at different operating voltages. Comparisons of measurements with SPICE[12] simulations, which apply the pre-determined parameters, show a satisfactory agreement.
Such a model does not only contribute to our understanding of SiPMs, moreover it provides a great benefit to the development of front-end electronics designed for SiPMs. For instance, in the scope of reference [101] the model has been used to develop and manufacture front-end electronics for the characterization of SiPMs.

A huge variety of different designs and different types of SiPMs is already commercially available. If the customer considers the use of SiPMs for his or her application, the characteristics which might be regarded first are likely the spectral sensitivity of the device, its sensitive area, and the size of its cells. The spectral sensitivity has already been discussed qualitatively in the section on APDs. We will return to it quantitatively when we will discuss the photon detection efficiency of SiPMs in the next section.
The sensitive areas of SiPMs are typically in the range of $1\times1\,\mathrm{mm}^2$ to $6\times6\,\mathrm{mm}^2$. These are the areas where the cells are located. Depending on the type of SiPM

[12]SPICE (Simulation Program with Integrated Circuit Emphasis) — a popular software to simulate analog, digital, or mixed circuits

it might be surrounded by its package, connectors, sensors, etc. If larger detection areas are needed, arrays of SiPMs have to be considered. The reason for the rather small sizes of the devices is that different locations on an SiPM wafer show different gain characteristics. Thus, these locations need different bias voltages to have identical gain. Since all cells of an individual SiPM use the same bias voltage, a compromise has to be found between the tolerance regarding the gain and the size of the photosensors. Furthermore, as SiPMs feature rather high noise rates with dark count rates typically in the order of several $100\,\mathrm{kHz\,mm^{-2}}$, the noise rate per SiPM would increase to inappropriate values with larger sensitive areas.
The pitch of the cells ranges typically from $25\,\mu\mathrm{m}$ to $100\,\mu\mathrm{m}$. For a fixed size of the sensitive area, a smaller cell size leads to a greater total number of cells. Hence, the dynamic range is higher for SiPMs with a small cell pitch. On the other hand, there is some dead space between the individual cells. The ratio of the active area, i.e. the area where photons can enter the cells and thus trigger its breakdown, to the sensitive area is called fill factor. It is smaller for SiPMs with a smaller cell pitch, which is clearly visible in figure 4.3. Obviously, the photon detection efficiency of an SiPM has to depend on its fill factor. Hence, the customer has to choose whether he or she needs a device with high dynamic range, or high photon detection efficiency, or an appropriate compromise between these two features.

Photos of various SiPMs manufactured by SensL and Hamamatsu are shown in figure 4.5. The sensors are available in different packages, and also arrays of SiPMs sharing a common package are conventional. The right side of the figure shows a novel array of SiPMs where the dead spaces between the individual SiPMs is reduced drastically since the connectors are found on the backside of the photosensors. SiPMs are also offered in packages containing elements for thermoelectric cooling and/or temperature sensors. As discussed earlier, a rise in temperature leads to increased noise. Furthermore, with a constant temperature the regulation of the bias voltage to achieve a constant over-voltage can be omitted.
The sensitive areas of the SiPMs are typically covered with a layer of silicon dioxide, silicone, or epoxy resin to protect the silicon from external damage and to provide an anti-reflecting coating.

In the following section we will examine the properties of SiPMs. We will focus on characteristics important for the use of SiPMs in fluorescence telescopes intended to detect extensive air showers. For further features like for instance radiation hardness or insensitivity to magnetic fields please refer to the literature. A good starting point is reference [90]. Moreover, in this work at hand we will focus on devices manufactured by Hamamatsu since these are the sensors used for both telescopes we will discuss in the next chapters, the fluorescence telescope prototype FAMOUS and the telescope to measure the night-sky brightness.

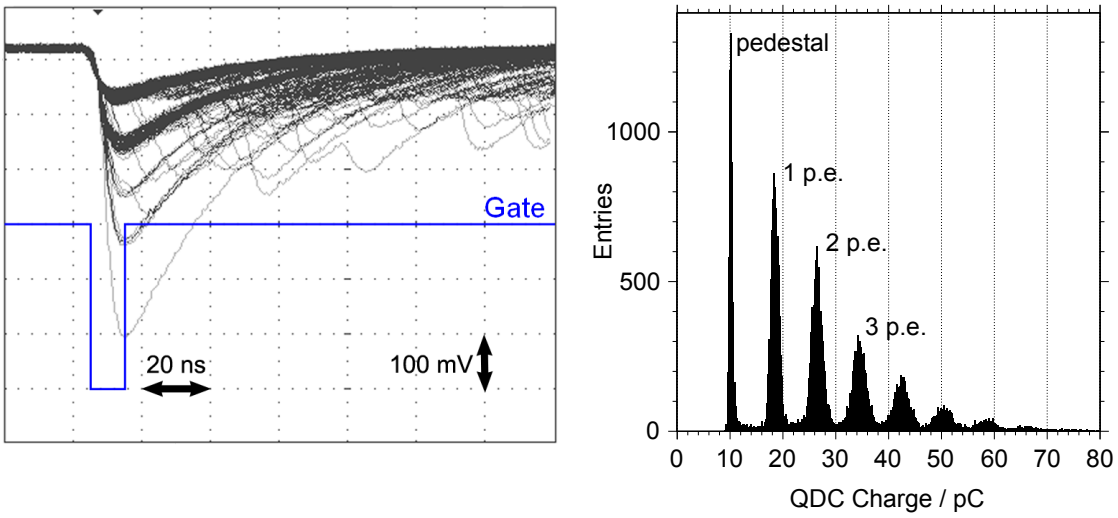

Figure 4.6: **Left:** Oscilloscope reading of amplified SiPM signals. The SiPM is operated in darkness, thus, the cell breakdowns which induced the signals are due to noise. Supplementary, a gate has been added for illustrative reasons. See text for details. **Right:** Charge spectrum of SiPM signals measured with a charge-to-digital converter (QDC). The peaks belonging to different numbers of cell breakdowns are clearly distinguishable. The gate time of the QDC is about 10 ns. See text for more details. Both plots first published in reference [104].

4.2 Properties of silicon photomultipliers

Single photon resolution

One great feature of SiPMs is their single photon resolution and photon counting ability due to their high internal gain (typically 10^5 to 10^6). The amplified output signals of an Hamamatsu S10362-11-100C measured with an oscilloscope are shown in figure 4.6 (left). The SiPM is operated in darkness, thus, the cell breakdowns which correspond to the displayed signals are due to noise. The signal levels of one cell breakdown (1 p.e.), two breakdowns (2 p.e.), 3 p.e., 4 p.e., and 6 p.e. are clearly distinguishable (a 5 p.e. signal is not visible in this particular oscilloscope reading). The right side of the figure shows a histogram of the charge Q the SiPM and its amplifier output for different events. To obtain this charge spectrum the SiPM has been illuminated with a pulsed LED. The width of the pulse, which has biased the LED, has been chosen to about 8 ns. The amplified signals of the SiPM are measured by a charge-to-digital converter (QDC). The QDC receives a gate which is triggered simultaneously to the flash of the LED. The width of the gate is about 10 ns. During this time the QDC measures the current at its input. A delay is used to shift the minima of the SiPM signals approximately to the time when the gate closes (cf. figure 4.6 (left)).
The different peaks in the charge spectrum belong to different numbers of cell breakdowns. As expected from the oscilloscope reading they are clearly separated, thus allowing to actually count photons. The spectrum also shows a pedestal peak. The

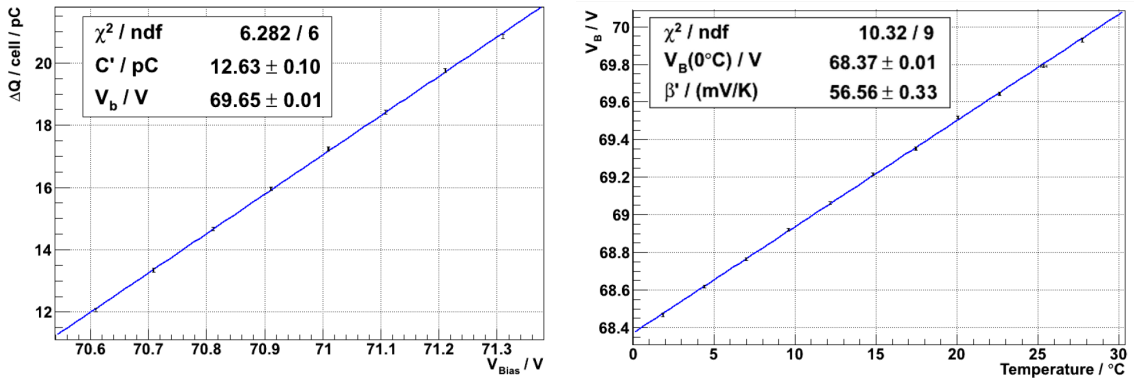

Figure 4.7: **Left:** Deposited charge ΔQ generated by a single cell breakdown of an SiPM as a function of the bias voltage V_{bias}. ΔQ/cell is proportional to the gain of the SiPM. Shown is a measurement of a Hamamatsu S10362-11-100C ($1\times1\,\text{mm}^2$, 100 µm cell pitch) at a temperature of about 23° C. The breakdown voltage V_{b} and the effective capacitance C' are obtained as parameters from the linear fit. **Right:** Breakdown voltage V_{b} of the same SiPM as a function of the temperature. The temperature progression factor β' is obtained from the linear fit. Both plots taken from reference [105].

charges in this peak are measured if no cell of the SiPM breaks down during the gate of the QDC. It differs from zero since the QDC provides an adjustable pedestal current which is added to its input current. In addition, the amplified output signal of the SiPM has a constant offset due to the amplifier circuit.
The width of the gate has been chosen to a very low value. Anyhow, charge spectra with clearly separated peaks are also measurable with gates which include the whole signal of the SiPM instead of just its falling edge. But since longer gates are more likely to collect also fractions of preceding or successive pulses, as well as afterpulses (see below) which can have signals smaller than the 1 p.e. signal, the peaks in the related charge spectrum will be broader and more asymmetric.
Similar to charge spectra are pulse height spectra, where typically the peak-to-baseline amplitude of individual pulses is filled into a histogram.

Temperature dependency of breakdown voltage and gain

The gain of SiPMs is typically in the range of 10^5 to 10^6. It is proportional to the over-voltage (cf. equation (4.7)).
As already discussed in section 4.1 the breakdown voltage V_{bd} of an SiPM increases with the temperature. Therefore, it is more convenient to express characteristics of SiPMs, like gain, photon detection efficiency, noise rates, etc., in terms of the over-voltage V_{ov} rather than the bias voltage $V_{\text{bias}} = V_{\text{bd}} + V_{\text{ov}}$. This way observables are independent of the temperature to a very good approximation.
The temperature dependency of the breakdown voltage also means that for applications which require constant characteristics of SiPMs, the bias voltage has to be regulated according to temperature changes to keep the over-voltage constant.

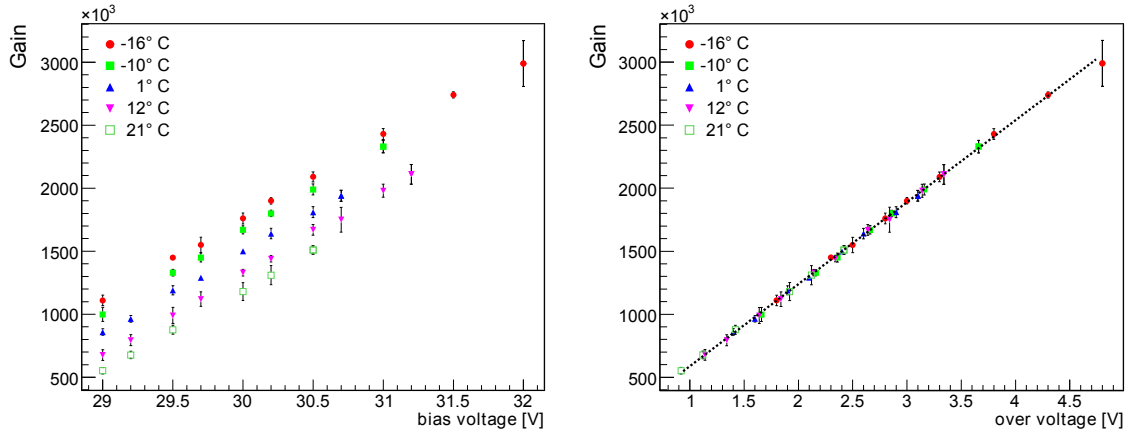

Figure 4.8: **Left:** Gain of an SensL CSI 0740 001 A20 HD prototype SiPM ($1\times1\,\mathrm{mm}^2$, 20 µm cell pitch, $\sim$ 1000 cells) depending on its bias voltage. The set of curves is for different temperatures ranging from -16° C to 21° C. **Right:** The same gain now plotted as a function of the over-voltage. The temperature dependency is eliminated. Both plots modified, originals taken from reference [106].

A common method to determine the breakdown voltage is by extrapolating the gain of an SiPM as a function of the bias voltage down to a value of zero. This method has been published for instance in reference [105]. The corresponding work has been carried out parallel to the work presented in reference [107]. In the scope of the latter, the breakdown voltage was determined by a measurement of the current–voltage characteristics of SiPMs. From these characteristics the breakdown voltage can be identified by the vast increase of the reverse current as soon as the breakdown voltage has been crossed. Both procedures have led to the same results. However, the determination of the current–voltage characteristics requires a reliable measurement of very small currents (down to $\sim$ 1 pA). Typically the measurement of the gain as a function of the bias voltage can be performed within applications of SiPMs without an additional picoammeter.

The gain of an SiPM is given by the charge a breakdown of a single cell produces divided by the elementary charge e. In the scope of reference [105] the charge of many SiPM signals, whose levels exceeded a 0.5 p.e. threshold, were measured with a QDC and filled to a histogram (cf. figure 4.6). This was performed for various bias voltages and temperatures. For each sweep of the bias voltage the temperature is kept constant. The charge a single cell produces is given by the difference of the positions of two neighboring peaks in the charge spectrum. This difference $\Delta Q/\mathrm{cell}$, obtained from the positions of the 1 p.e. and the 2 p.e. peak, is plotted in figure 4.7 (left) as a function of the bias voltage. This particular measurement is for a Hamamatsu S10362-11-100C ($1\times1\,\mathrm{mm}^2$, 100 µm cell pitch) at a temperature of 23° C.
However, $\Delta Q/\mathrm{cell}/e$ is not the gain of the SiPM since the signals of the SiPM are amplified. Furthermore, the gate of the QDC was chosen to 30 ns, a value too short

to include a whole SiPM pulse.[13] Anyway, ΔQ/cell is proportional to the gain. Thus, the breakdown voltage can be determined by an extrapolation of ΔQ/cell down to a value of zero. According to equation (4.9)

$$\Delta Q/\text{cell} = C' \cdot (V_{\text{bias}} - V_{\text{bd}}) \ . \tag{4.11}$$

C' is called the effective capacitance. It would equal the capacitance of a cell (plus parasitic capacitances) if the signals would not have been amplified and if the gate width would have been chosen to a value large enough to include the full SiPM pulses. A fit of equation (4.11) to the data yields the breakdown voltage. This fit and its parameters C' and V_{bd} are also shown in figure 4.7 (left).

This procedure can be performed for various temperatures T. In figure 4.7 (right) the linear dependency of the breakdown voltage on the temperature

$$V_{\text{bd}}(T) = V_{\text{bd}}(T = 0^\circ\,\text{C}) + \beta' \cdot T \tag{4.12}$$

is shown. The temperature progression factor β' is obtained from a fit of this relation to the data. With changes of the temperature the bias voltage has to be regulated according to this progression factor to keep the over-voltage constant. For this particular SiPM shown in figure 4.7 $\beta' = (56.6 \pm 0.3)\,\text{mV}/^\circ\,\text{C}$.
Since the gain G of the photosensor depends on the breakdown voltage, i.e. $G = G(V_{\text{bd}})$, and $V_{\text{bd}} = V_{\text{bd}}(T)$, it follows $G = G(T)$ for $V_{\text{bias}} = \text{const}$.

Subsequent to the determination of the breakdown voltage V_{bd}, the over-voltage can be directly calculated by subtracting V_{bd} from V_{bias}.[14] As expected the dependency of the gain of an SiPM on the temperature vanishes if it will be given as a function of the over-voltage. This can be seen in figure 4.8. It has been taken from reference [106] where various SiPMs of different manufacturers have been characterized. The figure shows the measurement of a SensL CSI 0740 001 A20 HD prototype SiPM ($1\times1\,\text{mm}^2$, 20 µm cell pitch, ~ 1000 cells).[15]

The elimination of the temperature dependency by stating the over-voltage instead of the bias voltage is a procedure which makes comparisons of different measurements much easier. Wherever it is possible it should be applied.

Photon detection efficiency

The photon detection efficiency (PDE) of an SiPM is the product of the probability that an incident photon creates an eh-pair with the charge carriers being separated

[13] The measurement discussed here has used the same type of SiPM and amplifier as the one shown in the oscilloscope reading in figure 4.6. From this figure you can see that the signal takes more than 100 ns to return to its baseline.

[14] The bias voltage V_{bias} is the potential difference along the SiPM. It does not have to be equal to the voltage provided by a (laboratory) voltage source V_{source}. There might be an additional voltage drop for instance due to the output current of the SiPM through a resistor in series to the SiPM. However, the difference between V_{bias} and V_{source} can be calculated from the actual circuit design and is typically negligible for small photo currents.

[15] stated in private communication by the author of the publication

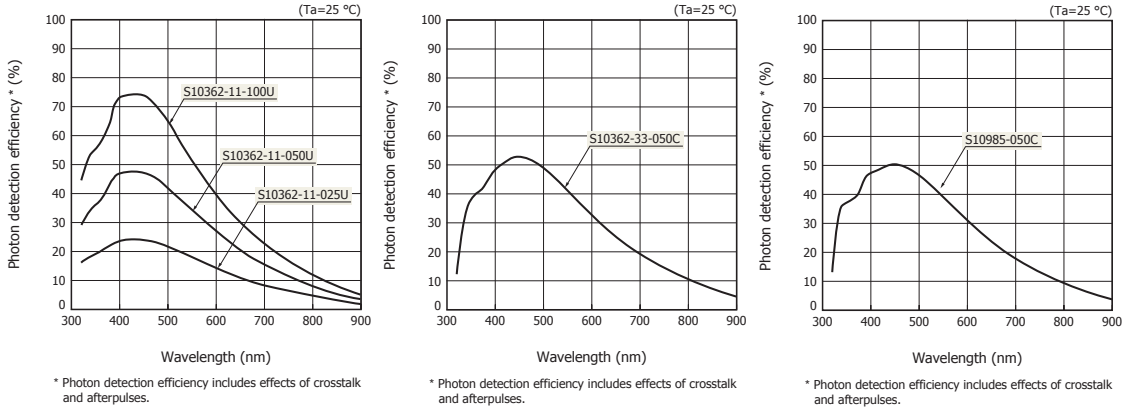

Figure 4.9: Photon detection efficiency as a function of the wavelength for various SiPMs manufactured by Hamamatsu at an ambient temperature of $T = 25°\,\mathrm{C}$. The values are overestimated since the measurements include effects of correlated noise (i.e. optical crosstalk and afterpulses). The first six characters of the type designation of an SiPM give its category, here: S10362 = single SiPM, S10985 = 2×2 SiPM array. For single SiPMs the two numbers in the middle give the pitches of the sensitive area in millimeters. The last three numbers give the cell pitch in micrometers, whereas the letter at the end denotes the type of package (U = metal type, C = ceramic type). The applied over-voltage is not specified. Taken from reference [108].

from each other, i.e. the quantum efficiency QE, its geometric fill factor ϵ, and the probability P_{trigger} that the created charge carriers trigger an avalanche.

$$\mathrm{PDE} = \mathrm{QE} \cdot \epsilon \cdot \mathrm{P}_{\mathrm{trigger}} \tag{4.13}$$

As discussed in section 4.1 the quantum efficiency depends on the wavelength. It can reach peak values of 80% to 90% [90]. The fill factor is the ratio of active area of the SiPM to its total (sensitive) area. The highest fill factors can be achieved for a small number of pixels with a large cell pitch. The avalanche trigger probability depends on the position where the eh-pair has been created. For eh-pairs being created at the same position, P_{trigger} increases with a rise of the over-voltage since the electric field strength in the G-APDs also rises.

The PDE as a function of the wavelength for various SiPMs manufactured by Hamamatsu is given in figure 4.9. These types of SiPMs are most sensitive to blue light (p-on-n structure, cf. section 4.1). The sensitivity peaks around 440 nm. However, with a thinner resin on top of the silicon the peak can be shifted to lower wavelengths and vice versa. Measurements without the resin show the maximum of the PDE at about 215 nm [109]. In the left plot of figure 4.9 the variation of the PDE due to different fill factors is shown. The corresponding SiPMs have cell pitches of (from top to bottom) 100 µm, 50 µm, and 25 µm. In the other two plots PDEs of different types of SiPMs with cell pitches of 50 µm are shown. It is hard to make a direct comparison of the three PDEs which belong to the SiPMs with cell pitches of 50 µm since the over-voltage is not specified. Furthermore, the number of data points is not evident. Hence, the feature below 400 nm might appear differently in

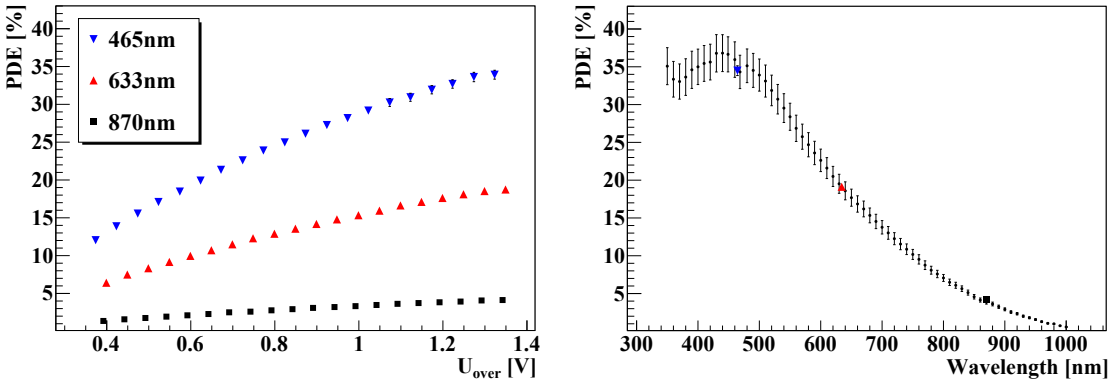

Figure 4.10: **Left:** Photon detection efficiency (PDE) of the Hamamatsu S10362-11-100C ($1\times1\,\mathrm{mm}^2$, 100 µm cell pitch) as a function of the over-voltage for three different wavelengths. **Right:** PDE of the same SiPM as a function of the wavelength at an over-voltage of $U_{\mathrm{over}} = (1.30 \pm 0.05)\,\mathrm{V}$ at room temperature $(25.0 \pm 1.5)^\circ\,\mathrm{C}$. Taken from reference [111].

the three plots due to measurements at different wavelengths and the subsequent smoothing of the plotted curves. Also, the entrance window of the SiPMs with the metal package (left plot, SiPM type designations end on U) differs from the window of the sensors with the ceramic package (plots to the middle and right).

With values up to 75% the PDEs of SiPMs seem to reach a stunning level for a fast device which features single photon resolution. For a comparison: the photomultiplier tubes of the fluorescence telescopes of the Pierre Auger Observatory discussed in chapter 3 have a peak quantum efficiency of about 30%.[16] But the PDE values of the SiPMs are overestimated, since their measurements include effects of correlated noise, i.e. optical crosstalk and afterpulses. We will discuss this noise later in more detail, for the moment it is sufficient to know that an initial cell breakdown can cause one or more further cell breakdowns. For the PDEs in figure 4.9 these noise events were interpreted as photon-generated cell breakdowns, and thus the efficiencies turn out to be too high.

Measurements of the PDE of Hamamatsu SiPMs with results corrected for correlated noise have for example been carried out in the scopes of references [105] and [111]. The applied photon counting method which eliminates contributions due to correlated noise will also be explained in chapter 6. It can be performed if the measured photon flux originates from a short-pulsed light source with a sufficiently low duty cycle.
The absolute PDE of a Hamamatsu S10362-11-100C at three different wavelengths as a function of the over-voltage, and the relative PDE as a function of the wavelength at an over-voltage of 1.3 V are shown in figure 4.10. The SiPM has a sensitive area

[16] The quantum efficiency of a photomultiplier tube equals almost its photon detection efficiency (although this term is usually not used for these devices) since typically all photo-electrons reach the first dynode. Novel types reach quantum efficiencies up to about 40% [110].

of $1\times1\,\mathrm{mm}^2$ and a cell pitch of $100\,\mu\mathrm{m}$. The measurements have been performed at a temperature of $(25.0 \pm 1.5)^\circ$ C. For the absolute PDE measurement, pulsed LEDs and laser diodes have been used as light sources (shown in the figure are results for the wavelengths 465 nm, 633 nm, and 870 nm). The pulsed light sources have yielded the real photon flux which has been compared to the flux measured with a calibrated reference sensor. For the relative PDE a xenon lamp in continuous wave mode together with a monochromator have been applied. Here, the photon flux could not be corrected for correlated noise. Thus, the relative PDE has been normalized to the absolute PDE at a wavelength of 633 nm. The normalized values agree with the absolute ones measured at 465 nm and 870 nm.
With values reaching about 35% the PDE of SiPMs is already comparable to the one of state-of-the-art photomultiplier tubes. As can be seen from the left plot in figure 4.10 the PDE has not yet reached its saturation at an over-voltage of about 1.35 V. But since the noise also increases with the over-voltage (see below), the operation of an SiPM is typically only reasonable at operating voltages where the PDE is not yet saturated.

In chapter 5 we will discuss the use of non-imaging light concentrators in front of SiPMs to increase their effective sensitive areas. These light concentrators will modify the incident angle Θ of photons hitting the SiPMs. As we will see, very high angles are possible even if the light enters the concentrator perpendicular to the surface of the SiPM. Therefore, it is of particular interest to know the PDE as a function of Θ. Its determination has been performed in the scope of reference [112]. In figure 4.11 the measured relative PDE of an Hamamatsu S10362-11-100C SiPM as a function of the incident angle of the light Θ is shown. It is normalized to have a value of 1 at $\Theta = 0^\circ$. The light has been produced by an LED with a wavelength of $\lambda = (465 \pm 22)$ nm. From the plot we see that the relative PDE stays above 90% for angles smaller than $\Theta \approx 70^\circ$. This has also been measured for further wavelengths in the range of 371 nm to 630 nm.
Shown in the figure is also a simulated relative PDE (blue curve) for unpolarized light entering silicon. The silicon is coated with a resin of a refractive index of 1.4 (like for the silicone resin the S10362-11-100C uses). The simulation accounts for reflections according to the Fresnel equations and considers multiple reflections inside the resin. Its comparison to the measured data leads to the conclusion, that the dependence of the PDE on the incident angle of light can be described sufficiently well by Fresnel reflections at the entrance window of the SiPM.

Noise

Even if an SiPM is operated in complete darkness, cell breakdowns will occur. The dark noise rate for currently available SiPMs manufactured by Hamamatsu is in the order of $100\,\mathrm{kHz\ mm^{-1}}$ to $1\,\mathrm{MHz\ mm^{-1}}$ at room temperature and a trigger level of 0.5 p.e., and depends on the over-voltage. In the scope of reference [107] the dark noise rate of a Hamamatsu S10362-11-100C ($1\times1\,\mathrm{mm}^2$, $100\,\mu\mathrm{m}$ cell pitch) has been measured as a function of the trigger threshold and the temperature for a nearly constant over-voltage. The noise rate drops by about a factor of two with a

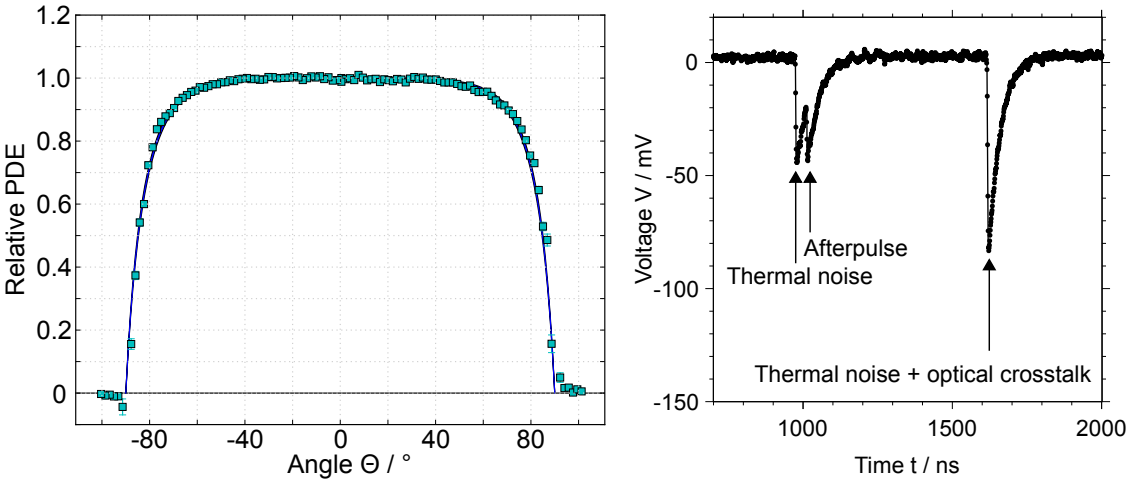

Figure 4.11: **Left:** Measured relative photon detection efficiency (PDE) of a Hamamatsu S10362-11-1000C SiPM ($1\times1\,\mathrm{mm}^2$, 100 µm cell pitch) depending on the incident angle of light Θ (data points). The PDE has been normalized to 1 at $\Theta = 0°$. The detected light has a wavelength of $(465 \pm 22)\,\mathrm{nm}$. Also shown is a simulation of the relative PDE (blue curve). See text for details. Modified, original taken from reference [112]. **Right:** Measured voltage trace of an SiPM operated in darkness. The first pulse relates most likely to a cell breakdown due to thermal noise, the second is due to afterpulsing. The third pulse relates to two simultaneous cell breakdowns, as for instance caused by thermal noise and optical crosstalk.

temperature reduction of 10° C.
The dark noise is caused by thermally generated eh-pairs which trigger avalanches (i.e. thermal noise) and correlated cell breakdowns. The correlated noise consists of cell breakdowns attributed to effects referred to as optical crosstalk and afterpulsing. In the following we will have a closer look at these effects.

The generation of photons inside semiconductors with high internal electric fields is known since the 1950s, and attributed to different causes (see e.g. reference [113] and those therein). However, the actual emission process is still under investigation. In figure 4.12 (left) a photo of an SiPM operated in darkness is shown. The exposure time was several hundred seconds. Pictured is an intensity map where the color denotes the intensity of the observed light from blue (low intensity) to red (high intensity). The picture is underlayed with a photo of the illuminated SiPM to easily assign the spots of the intensity map to the surface structure of the SiPM. Photons which are created during an avalanche process by recombination of electrons and holes (we will refer to them as crosstalk-photons) propagate through the semiconductor and can reach a neighboring cell. Here they can create eh-pairs which might trigger additional avalanches. This effect is referred to as optical crosstalk. It happens almost simultaneously to the initial cell breakdown, and is the reason why the oscilloscope reading in figure 4.6 shows numerous signals exceeding the 1 p.e. level. The intensity map shown in figure 4.12 is caused by those crosstalk-photons which leave the silicon and are detected by the camera.

By counting the number of events for which at least two cells break down simultaneously, the optical crosstalk probability can be calculated (as long as the probability to encounter two simultaneous thermal breakdowns is sufficiently small). We will apply this procedure in chapter 7 where it will be discussed in more detail. Previously it has been performed in the scope of reference [105] for various Hamamatsu SiPMs operated in darkness. The probability that more than one cell break down simultaneously has been measured as a function of the over-voltage for different temperatures. This probability does not show a dependency on the temperature and depends superlinear[17] on the over-voltage as can be seen in figure 4.12 (right). The superlinear behavior is attributed to a linear increase of the gain plus an increase of the avalanche trigger probability with a rising over-voltage.
For a fixed over-voltage an increase of crosstalk events occurs for larger sensitive areas and larger cell pitches. This is due to the fact that boundary effects are relatively big for small sensitive areas. Here, the probability that a crosstalk photon leaves the sensitive area is greater than for larger areas. SiPMs with small cell pitches have smaller fill factors compared to SiPMs with greater cell pitches. Thus, for the former crosstalk-photons are more likely to be absorbed in regions where they do not trigger a cell breakdown.
Typical choices of the over-voltage lie in the 1.2 V – 1.4 V range for Hamamatsu SiPMs with a cell pitch of 100 µm and in the 1.9 V – 2.2 V range for those with a cell pitch of 50 µm. Hence, a reference value to memorize is an optical crosstalk probability of roughly 20% for the considered SiPMs.

The incident of a cell breakdown shortly after a preceding breakdown without the involvement of incident photons or thermally generated eh-pairs is referred to as afterpulsing. It is believed to be caused by charge carriers which are stalled at impurities inside the silicon. When these charge carriers are released after a while they can trigger an avalanche. However, the exact process which generates afterpulses is still a topic of discussion.
The probability of afterpulse events, as well as the time constant with which the charge carriers are released, can be determined from an SiPM, which is operated in darkness, by measuring the time Δt between the breakdown of a cell due to thermal noise and its consecutive cell breakdown. This procedure will be performed in chapter 7 where it will be discussed in more detail. A histogram of time differences Δt is shown in figure 4.13 (left). This particular distribution is from a measurement of a Hamamatsu S10362-33-050C SiPM ($3\times3\,\mathrm{mm}^2$, 50 µm cell pitch) at an over-voltage of 2.1 V and a temperature of about 1° C.
For high values of Δt the distribution is dominated by events caused by thermal generation of eh-pairs. Thus, the thermal noise rate can also be extracted from this kind of measurements (see below). For small Δt the distribution exceeds the contribution of thermal noise. These events are due to afterpulsing.[18] The data can be described much better if two afterpulse contributions, one for fast afterpulses with the time constant τ_f, and one for slow afterpulses with the time constant τ_s are

[17] a superlinear function grows faster than a linear one

[18] As optical crosstalk happens in good approximation simultaneously to the cell breakdown which causes it (i.e. $\Delta t = 0$), the mentioned events are due to thermal noise and afterpulsing.

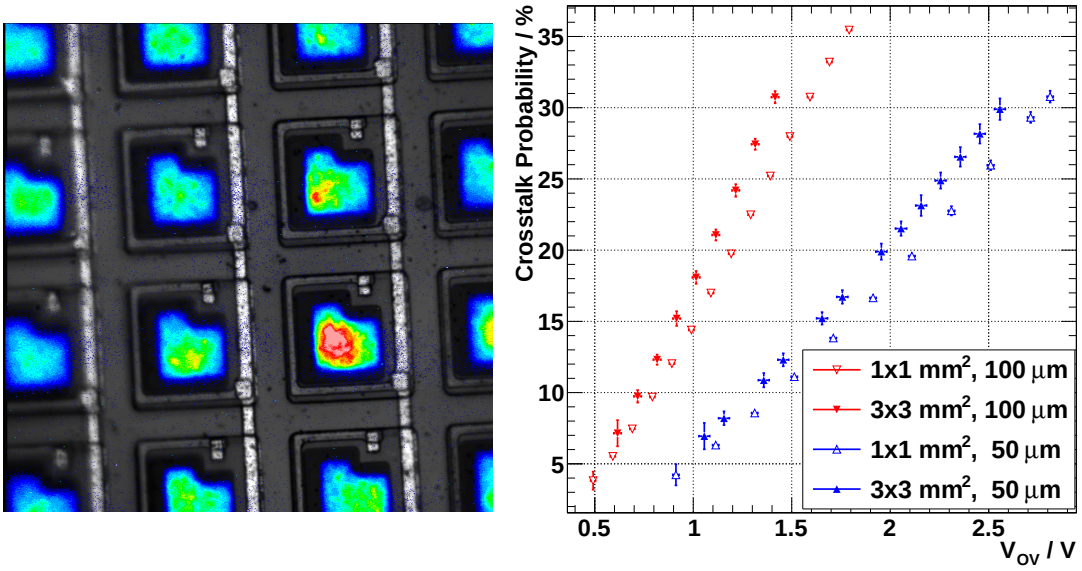

Figure 4.12: **Left:** Photo of an SiPM overlaid with a second photo taken in darkness and exposed for 300 s. The detected photons in the second photo are crosstalk-photons generated during the avalanche processes of the cells. The color denotes the light intensity from blue (low) to red (high). Taken from reference [114]. **Right:** Probability to encounter optical crosstalk after an initial cell breakdown for different SiPMs manufactured by Hamamatsu. Red, downwards pointing triangles are for a cell pitch of 100 µm, while blue, upwards pointing triangles are for 50 µm. Open markers are for a sensitive area of $1\times1\,\mathrm{mm}^2$ and filled markers are for $3\times3\,\mathrm{mm}^2$. Taken from reference [105].

considered. Depending on the time after the initial breakdown the output signal due to an afterpulse has a reduced level since the firing cell has to recharge after each break down according to equation (4.10). This is the reason for the cutoff in the Δt distribution for time differences smaller than about 40 ns. The afterpulses occurring this shortly after the initial pulse simply cannot be detected.
The data of the Δt distribution have been fitted with a superposition of three exponential functions — one accounts for the events due to thermal noise and the other two account for the events due to fast afterpulsing and slow afterpulsing. From this fit the time constants τ_f and τ_s, and the thermal noise rate can be determined. As already mentioned, we will discuss this procedure in more detail in chapter 7.
In reference [105] the time constants τ_f and τ_s have been measured to about 22 ns (44 ns) and 90 ns (125 ns), respectively, for Hamamatsu SiPMs with cell pitches of 50 µm (100 µm). The time constants do not depend on the over-voltage. However, they depend on the temperature. Reference [115] reports that a high time constant of about 110 ns at 300 K decreases to 95 ns at 200 K and to 40 ns at 77 K.

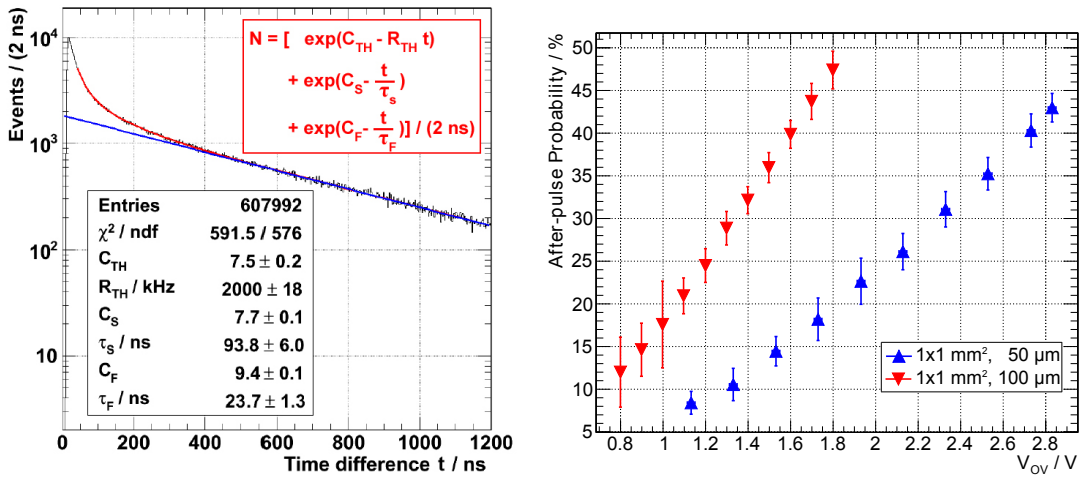

Figure 4.13: **Left:** Measured distribution of time differences between a cell breakdown caused by thermal generation of an eh-pair and the consecutive cell breakdown. The red line is a fit to the data according to the displayed function. The blue line relates to thermal noise. See text for more details. Modified, taken from reference [105]. **Right:** Afterpulse probability of Hamamatsu SiPMs with sensitive areas of $1\times1\,\mathrm{mm}^2$ as a function of the over-voltage. The blue data are for an SiPM with a cell pitch of 50 µm, whereas the red data are for an SiPM with a cell pitch of 100 µm. Modified, original taken from [105].

The probability that a single cell breakdown will cause one additional breakdown due to afterpulsing P_{AP} can be calculated from the Δt distribution by

$$P_{\mathrm{AP}} = \frac{N_{\mathrm{AP}}}{N_{\mathrm{AP}} + N_{\mathrm{th}}} \tag{4.14}$$

where N_{AP} and N_{th} are the numbers of the afterpulse events and the thermal noise events, respectively. P_{AP} is given as a function of the over-voltage for two Hamamatsu SiPMs with sensitive areas of $1\times1\,\mathrm{mm}^2$ in figure 4.13 (right). The blue data are for an SiPM with a cell pitch of 50 µm, whereas the red data are for an SiPM with a cell pitch of 100 µm. Larger cell pitches lead to increased afterpulse probabilities at a fixed over-voltage. This can be explained by the higher gain for the larger cells. The more or less quadratic dependence of the probability on the over-voltage can be explained by the linear dependence of the gain on the over-voltage (and thus of the number of charge carriers within an avalanche) if we assume that only a minority of trap levels is occupied, and the rise of the avalanche trigger probability with an increased over-voltage.
With the same typical over-voltages as stated above, a reference value of the afterpulse probability worth memorizing is roughly 25%.

For certain considerations it might be more appropriate to give the afterpulse probabilities for fast and slow afterpulses separately. We will refer to them as $P_{\mathrm{AP,f}}$ and

$P_{\mathrm{AP,s}}$. The determination of these probabilities will be needed and performed in chapter 7 as well. The combined afterpulse probability is given by

$$P_{\mathrm{AP}} = 1 - (1 - P_{\mathrm{AP,f}})(1 - P_{\mathrm{AP,s}}) \tag{4.15}$$

which is 1 minus the probability that neither a fast nor a slow afterpulse occurs.

Despite some statistical fluctuations of the avalanche process, all cell breakdowns develop identical for identical states of recharge of the cell, irrespective of their causes. Thus, all signals look the same irrespective of their causes. It is not possible to distinguish between thermal noise, optical crosstalk, afterpulsing, or the detection of signal-photons on an event-by-event basis. This principle also implies that each cell breakdown can cause correlated noise. For example, the mean number of afterpulse events after a thermally triggered avalanche process is not simply given directly by P_{AP}. An afterpulse event will cause further afterpulse events with the same probability as a thermal noise event does, provided that the considered cell is in the same state for both kinds of events. Moreover, an afterpulse event will also cause optical crosstalk with the related probability. And optical crosstalk events will also cause optical crosstalk events and afterpulses.
We will reconsider this evolution of correlated noise in a quantitative way in chapter 7 where we will distinguish between different causes of cell breakdowns on a statistical basis.

As mentioned above the thermal noise rate can be obtained from a fit to the Δt distribution (cf. figure 4.13 (left)). In reference [105] it has been shown that the thermal noise rate R_{th} depends linearly on the over-voltage U_{ov}.

$$R_{\mathrm{th}} = r_{\mathrm{th}} \cdot U_{\mathrm{ov}} \tag{4.16}$$

where $r_{\mathrm{th}} = r_{\mathrm{th}}(T)$ increases exponentially with the temperature T as discussed above.

Dynamic range

As already mentioned in the previous section the dynamic range of an SiPM is limited predominantly by its finite number of cells. But also noise is a cause for the limitation of the dynamic range. For a noise-less SiPM, featuring a total number of N_{tot} cells, the number of cells which fire according to the number of incident photons N_γ hitting the SiPM simultaneously is given by

$$N_{\mathrm{fire}} = N_{\mathrm{tot}} \left(1 - \exp\left(-\frac{\mathrm{PDE} \cdot \mathrm{N}_\gamma}{N_{\mathrm{tot}}}\right)\right) \tag{4.17}$$

assuming a uniform distribution of the photons on the sensitive area of the SiPM. However, for a noisy SiPM additional cells will fire. An expedient way to look at the saturation behavior of the photosensor is by means of simulations. They provide the possibility to distinguish between the cause of a cell breakdown on an event-by-event

basis. This is impossible for measured data. For these the distinction can only be performed on a statistical basis.

Simulations of SiPMs will be discussed in detail in the next section. For the moment a basic comprehension of the procedure is sufficient. We apply a phenomenological simulation which uses the characteristics of a specific SiPM as input parameters. These parameters include the total number of cells, the cell pitch, the fill factor, the breakdown voltage, the PDE, the thermal noise rate, the probabilities of optical crosstalk and afterpulsing, the afterpulse time constants, and the recovery time constant, which are all accessible by laboratory-based experiments. Whenever a cell breaks down the simulation dices according to the probabilities for correlated noise if further cell breakdowns are caused. For a crosstalk related breakdown a simultaneous breakdown of an appropriate cell is generated. For an afterpulse related breakdown the simulation dices the time after which the breakdown occurs according to the afterpulse time constants. For each breakdown the type of event (signal-photon, thermally generated, crosstalk, or afterpulse), the identification number of the cell, and the time of the breakdown are stored. In addition, a weight is stored for each event accounting for the recharge process of the cells. This weight is the fraction of the standard 1 p.e. signal the cell is intended to produce (cf. equation (4.10)).

The results of a simulation of an SiPM following the Hamamatsu S10362-11-100C type ($1\times1\,\mathrm{mm}^2$, 100 µm cell pitch) is shown in figure 4.14 (left). The photosensor has been simulated with an over-voltage of 1.3 V at a temperature of 23° C. In the figure the cell breakdown rate is plotted as a function of the rate with which signal-photons hit the SiPM. The simulation accounts for signal-photons with a wavelength of 450 nm, hitting the sensitive area of the SiPM normal to the surface, and uniformly distributed over the sensitive area and within the considered time. Hence, we consider a continuous light source.
The red curve is the cell breakdown rate for those breakdowns which correspond to signal-photons. The other curves are stacked graphs: the yellow one is for afterpulse-breakdowns plus signal-photons, the green one contains additionally the crosstalk-breakdowns, and the blue curve includes all four types of cell breakdowns. The latter corresponds to the measurable response of a real SiPM.
In the region where the curve of the signal-photons is linear, the cell breakdown rate equals the signal-photon rate multiplied by the PDE. The value of the total cell breakdown rate in this region can be calculated taking the thermal noise rate and the probabilities for correlated noise into account.

The dynamic range of an SiPM is not well defined in the literature. However, we can define some characteristic points in this plot to describe the response of the SiPM which are also of interest for measurements, since they all relate to the total cell breakdown rate which is directly accessible in measurements.
The point where the cell breakdown rate reaches twice the value of its noise floor is the *0 dB signal excess point*. Here, the cell breakdown rate due to signal-photons equals the breakdown rate due to thermal noise. For the correlated noise it does not make any difference which kind of event triggers a cell breakdown. Both kinds of

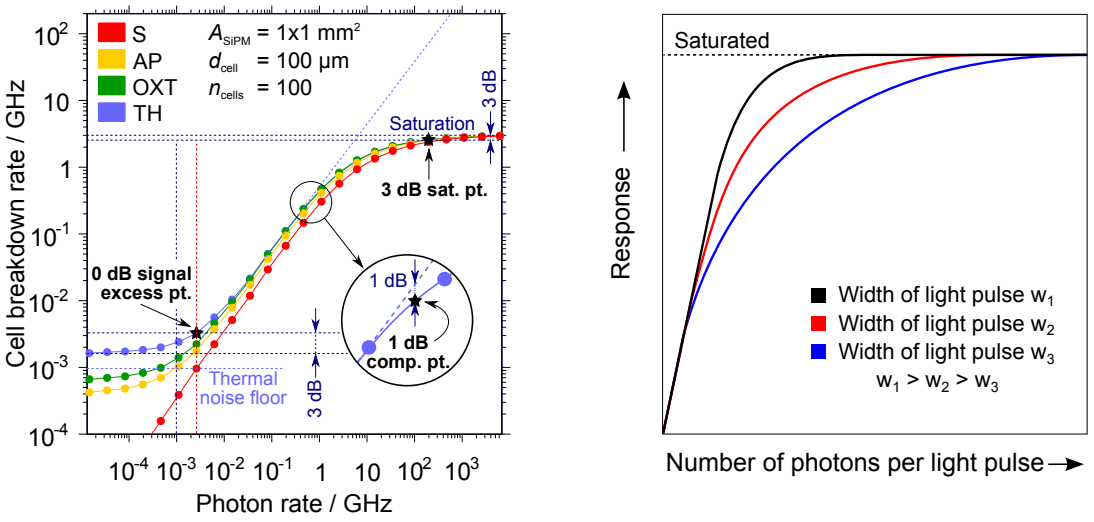

Figure 4.14: **Left:** Simulated cell breakdown rate of an Hamamatsu S10362-11-110C ($1\times1\,\mathrm{mm}^2$, 100 µm cell pitch) as a function of the incident photon rate produced by a continuous, monochromatic light source. The simulation allows to distinguish between different causes for cell breakdowns: signal-photons (S), afterpulses (AP), optical crosstalk (OXT), and thermal noise (TH). The graphs are stacked onto each other. Also plotted are some characteristic points and lines helping to identify them. See text for details. **Right:** Sketch of the response of an SiPM depending on the number of photons in a light pulse. The set of curves is for different widths of the light pulse.

breakdown lead to the same behavior of correlated noise. To describe the linearity of the response of the SiPM the *1 dB compression point* can be used as a reference. It is the point where the cell breakdown rate is reduced by 1 dB from the extrapolation of its linear curve. Another reference point is the *3 dB saturation point*, where the cell breakdown rate is 3 dB below the level of saturation. It can be considered as the end of the dynamic range of the SiPM.
The point where the dynamic range starts is not this easy to specify. It is not given by the 0 dB signal excess point. Even for signals smaller than the thermal noise the signal can be determined by subtracting the thermal contribution from the cell breakdown rate. This can be performed for example with a measurement of the response of the SiPM while the device is operated in the darkness, with the temperature and over-voltage kept constant. The question for the lower end of the dynamic range can only be answered properly with regard to the specific measurement the SiPM is used for. In theory the lower end of the dynamic range goes down to zero assuming a constant thermal noise rate, an assured single photon resolution, and an infinite measurement time.

With an increase of the signal-photon rate the fraction of cell breakdowns caused by correlated noise decreases. The simulation yields that the number of breakdowns caused by crosstalk N_{OXT} (afterpulses N_{AP}) divided by the sum of the numbers of

breakdowns evoked by thermal noise N_{th} and signal-photons N_{signal} decreases from 0.25 (0.45) at the 0 dB signal excess point to 0.02 (0.07) at the 3 dB saturation point. The reason for this is that the cells are busy with the avalanches triggered by signal-photons.

A plot as presented left in figure 4.14 can also be regarded as a calibration curve of an SiPM. The real photon flux, the SiPM is exposed to, can be taken under certain circumstances directly from the measured response of the SiPM. The latter does not have to be the cell breakdown rate. Anyway, it might be an observable not that easy to measure. Other quantities, for instance the mean output current of the SiPM, can also serve as the response.
The calibration can be used straightforward for monochromatic light applied to the calibration measurement as well as for the measurement where the photon flux is *a priori* unknown. Otherwise, corrections due to a different PDE (and related correlated noise) have to be taken into account. Furthermore, the over-voltage as well as the thermal noise rate should be identical during both measurements. If they are not, further corrections involving correlated noise have to be taken into account, and the simplicity of the photon flux determination by means of the calibration curve is lost.

The situation will be slightly different if a pulsed light source with a sufficiently low duty cycle is considered instead of a continuous light source. Such a pulsed light source might be for example an air shower passing through the field of view of a pixel of a fluorescence telescope. In this case we should no longer consider a photon rate, but the number of photons per pulse. A further parameter which has to be introduced is the pulse width. Let us consider two pulses of different widths containing both the same number of photons. As long as this number of photons is sufficiently high the response of the SiPM will be the same for both pulses since the photosensor will be saturated. Regarding the lower end of the linear region of the response curve, the response will also be identical if the number of photons is sufficiently small. With a very low photon flux the number of photons which hit a cell during recovery is negligible for both cases. This changes when the number of photons is increased: while for a large pulse width the effect of a reduced response due to the recovery of the cells is still negligible, this is not the case if the photons arrive during a significantly reduced time. Thus, the 1 db compression point of the curve representing the response to the shorter pulse will be at lower numbers of photons per pulse than the one of the curve representing the response to a broader pulse. This behavior is sketched in figure 4.14 (right).

Measurements of the response of Hamamatsu SiPMs have been performed in the scope of reference [116], where a single pulse width was applied. More sophisticated measurements have been carried out recently by S. Navas, M. Lauscher, *et al.* These measurements have been driven by the intention to provide a method which uses the response curves for calibrations of SiPMs predominantly in the application of an air shower fluorescence telescope. A related publication is in preparation.

4.3 Simulations

The simulation of the behavior of SiPMs used in the previous section, and which will be used in chapter 7 are performed with G4SiPM [117], a Monte Carlo-based simulation package developed by T. Niggemann *et al.* A predecessor of the code has been developed in the scope of the designing phase of the prototype fluorescence telescope FAMOUS and presented first in reference [118]. A dedicated publication on G4SiPM is in preparation.
G4SiPM provides a framework to simulate SiPMs within Geant4 [119]. Geant4 is a toolkit to simulate the passage of particles through matter and their interaction with it. It is widely used within the communities of high-energy, astroparticle, nuclear, and accelerator physics, but also for e.g. medical and space science. It is based on the programming language C++; its object-orientated programming paradigm provides the possibility of fast and facile adaptations, modifications, and enhancements of existing detector geometries.

A Geant4 simulation consists of at least one *run*. Each run includes at least one *event*, which contains at least one primary particle. The user specifies the kind of primary particles, their energies, their polarizations, their starting positions, and their directions of movement. These parameters do not have to be fixed. They can also be given in intervals together with the related distributions to dice a specific value for a specific primary particle. Within the event the primary particle, as well as secondary particles if produced, are tracked along their ways through a predefined detector geometry. To reduce computing time the user can specify the physical interaction processes to be omitted. The user has free choice to assign several parts of the detector as *sensitive detectors*. When a particle strikes a sensitive detector, a *hit* is created and the quantities which are of interest are stored within an output file. As soon as all particles have been absorbed, or have left the volume considered for the simulation, the event is completed. The detector and the primary particles are set back to their initial states to proceed with the next event.

G4SiPM provides a phenomenological model of SiPMs based on measurements. An SiPM is defined by its properties contained in its *properties file*. The properties are listed in table 4.1. They are the numbers of cells, the cell pitch, the fill factor, the breakdown voltage, the thermal noise rate, the probabilities and time constants of fast and slow afterpulsing, the probability of optical crosstalk, the spectral PDE, the angular PDE, and the recovery time constant. Apart from the geometrical attributes, these properties constitute a *set*. A set is defined for a specific temperature and over-voltage. By including more sets with different temperatures and over-voltages, the corresponding dependencies of the properties can be accounted for. G4SiPM uses linear interpolations between different sets. With respect to the absorption length of photons generated by optical crosstalk, the position of the cells where optical crosstalk can happen relative to the cell which genereated the crosstalk-photons can be specified.
G4SiPM allows also to specify a dead time t_{dead} of the cells of the SiPM. After a breakdown a cell will take the time t_{dead} until its recharge process commences.
In addition to the properties, a package of the SiPM including the resin on top of

Table 4.1: Properties of SiPMs simulated with G4SiPM. Performance properties depend on the temperature and over-voltage. See text for details.

Property	Symbol	Unit
Geometrical properties		
Number of cells	N_{cells}	-
Cell pitch	d_{cell}	µm
Fill factor	ϵ	-
Performance properties		
Breakdown voltage	V_{bd}	V
Thermal noise rate	R_{th}	Hz
Probability of fast afterpulse	$P_{\text{AP,f}}$	-
Probability of slow afterpulse	$P_{\text{AP,s}}$	-
Time constant of fast afterpulses	τ_{f}	s
Time constant of slow afterpulses	τ_{s}	s
Probability of optical crosstalk	P_{OXT}	-
Spectral photon detection efficiency	PDE(λ)	-
Normalized angular photon detection efficiency	PDE(Θ)	-
Recovery time constant	τ_{rec}	s

the silicon can be chosen, but this choice is not mandatory. If the simulation lacks the resin, the dependency of the PDE on the incident angle of the photons is also included in a set.
When a run is started the user specifies the bias voltage and the temperature.

A visualization of an SiPM simulated with G4SiPM is shown in figure 4.15.
In G4SiPM the photosensor is not modeled as an array of *sensitive detectors* which represent its cells, but its whole sensitive area is a *sensitive detector*. To account for the dead space between the individual cells which relates to the fill factor ϵ, the program calculates from the geometrical properties whether a hit is directly rejected or considered for acceptance. If the hit is not rejected, the simulation will dice according to the spectral PDE divided by the geometric fill factor (and its angular dependence if the resin is not included in the model) whether the hit is accepted. Each accepted hit is stored with its timestamp, cell identification number, and type (i.e. signal-photon, thermal noise, optical crosstalk, afterpulse) in a *priority queue* in which the individual hits are sorted in chronological order.

Besides the choice of the primary particles, which are typically photons in the spectral range of the acceptance of the SiPM, the user defines the duration of the simulation $t_{\text{sim}} = t_2 - t_1$, where t_1 and t_2 mark the start and end point of the simulation, respectively. Before an actual event starts and the primary particles approach the detector, $N_{\text{th}} = R_{\text{th}} \cdot t_{\text{sim}}$ hits are distributed uniformly between t_1 and t_2 and among the cells of the SiPM. These are the hits due to thermal noise, and R_{th} is the thermal

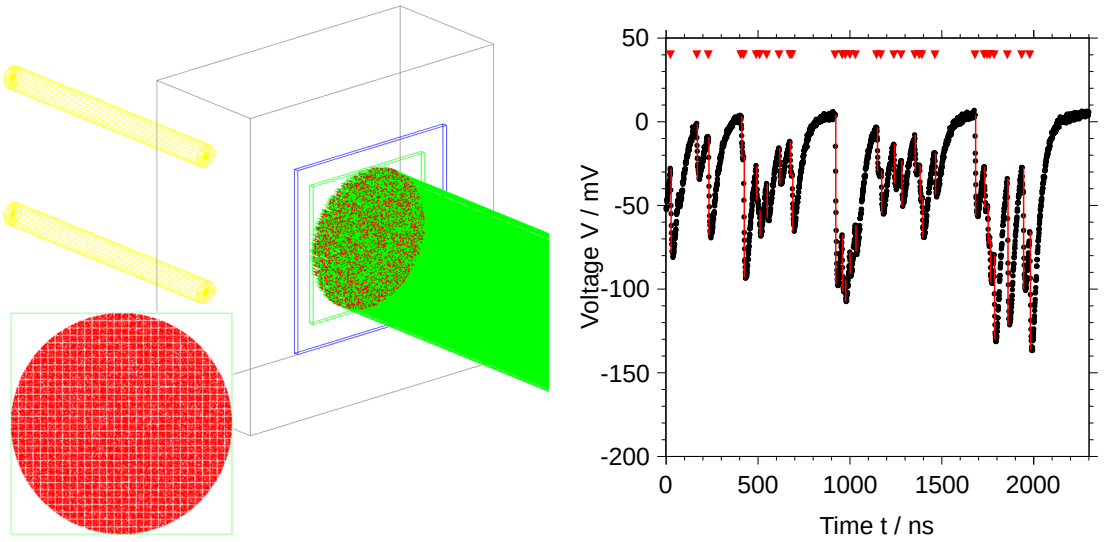

Figure 4.15: **Left:** Visualization of a Hamamatsu S10362-33-100C SiPM ($3\times3\,\mathrm{mm}^2$, 100 µm cell pitch) simulated with G4SiPM. The traces of 10000 photons are shown in green. The blue box shows the entrance window, the green one the silicon. The sensitive detector is on top of the silicon with red points denoting hits. The package is shown in gray, the electrical connectors in yellow. The inset is a front view of the sensitive area. Here, 500000 photons have been simulated to visualize the cell structure. **Right:** Voltage trace of an amplified Hamamatsu S10362-33-100C SiPM simulated with G4SiPM. The red triangles and lines denote the reconstructed times of cell breakdowns and pulse heights (cf. section 7.1).

noise rate.
To assure that afterpulses are not underrepresented at the beginning of the simulation, 100 additional thermal noise-hits, with the same noise rate as the other ones, and also uniformly distributed in time and and among the cells, are generated prior to t_1.[19] Hence, the simulation starts already at $t_0 = t_1 - 100/R_{\mathrm{th}}$, although the hits prior to t_1 are filtered and not saved in the output file.[20]

The priority queue is processed hit by hit to account for correlated noise. With regard to the probabilities of optical crosstalk and afterpulsing the random generator of the simulation program dices for each hit whether further hits due to correlated noise occur. A hit due to optical crosstalk obtains the same timestamp as its parent hit. Respecting the mean absorption length of crosstalk-photons, only cells in a predefined distance from the one with the parent hit are considered for optical crosstalk.
If the result of the random generator demands a hit due to afterpulsing, the time delay between the parent hit and the afterpulse-hit will be diced according to the ap-

[19] for typical thermal noise rates the time prior to t_0 is much larger than five times the time constant of slow afterpulses

[20] If the virtual digital-to-analog-converter is enabled (see below), falling edges of pulses with $t_{\mathrm{digi}} < t_1$ are present in the output data.

propriate time constant. The afterpulse-hit always owns the same cell identification number as its parent hit.

For each hit also a weight w is calculated which accounts for the recovery behavior of the cells of the SiPM. $w = V_{\text{out}}/V_{1\,\text{p.e.}}$ is calculated according to equation (4.10) as the fraction of the output signal V_{out} of the 1 p.e. standard signal $V_{1\,\text{p.e.}}$. It is also saved in the output file.

G4SiPM also features a module which can be regarded as a virtual digital-to-analog-converter. It uses the output file and creates a virtual voltage trace $V_{\text{sim}}(t)$ comparable to the ones which can be measured from real SiPMs. These virtual voltage traces can be handled in the same way as measured data, which makes a comparison of simulations and measurements very comfortable and insusceptible to mistakes, since the very same analysis procedure can be applied to both and used for cross checks.
The converter uses a pulse shaper which creates for each hit the virtual voltage

$$V_{\text{hit}}(t) = w \cdot A_0 \cdot \left[1 - \exp\left(-\frac{t - t_{\text{digi}}}{\tau_{\text{rise}}}\right)\right] \cdot \exp\left(-\frac{t - t_{\text{digi}}}{\tau_{\text{fall}}}\right) \tag{4.18}$$

with the constraint that $V_{\text{hit}}(t)$ has to be larger than zero. Here, A_0 is the amplitude parameter, t_{digi} is the timestamp from the digital hit, τ_{rise} and τ_{fall} are the time constants of the rising and falling edges of the pulse. For a good comparison of simulated and measured data, the pulse shape parameters can be determined from a fit of equation (4.18) to isolated 1 p.e. standard signal pulses found in the measured data. To account for fluctuations in the height of a simulated standard 1 p.e. signal A_0 can be smeared with a normal distribution according to the measured data.
The total output signal V_{sim} is then given as the sum of the virtual voltages of each hit.
In addition to the pulse shaper, the virtual digital-to-analog-converter features a noise generator to add virtual electronics noise to the voltage trace. A simulated voltage trace can be seen in figure 4.15 (right).

4.4 Recent developments

Frequently requested improvements of SiPMs are typically concerning higher PDEs, reduced noise rates, faster devices, increased sensitivities in the UV range, and larger detection areas.

For instance, with the M series manufactured by SensL, there are already SiPMs available which are very fast. The devices with the smallest cell pitch (20 µm) reach signal rise times of $\sim$ 100 ps and recovery times smaller than 1 ns [97].
Hamamatsu has also recently released a new generation of SiPMs, including high-speed devices with cell pitches of 10 and 15 µm [120]. According to the datasheets the standard devices of the new generation feature a significantly reduced dark count rate. At a 0.5 p.e. trigger level the dark count rate drops from a typical value of 8 MHz at 25° C for a 3×3 mm^2 SiPM with 100 µm cell pitch to a value of 1 MHz.

Recently Hamamatsu also presented a new surface mount SiPM type whose terminals are completely underneath the device [103]. This offers the possibility to build arrays of SiPMs with a minimum of dead space between the individual photosensors (cf. figure 4.5). The manufacturer also improved the UV sensitivity of a special series of SiPMs. New devices without resin show a PDE of about 18% at 175 nm which is the scintillation wavelength of liquid xenon. At this wavelength the standard devices with a removed resin reach only about 2% PDE. The improvement is still in progress, and a further goal is to reach also an appreciable PDE at 128 nm which is the scintillation wavelength of liquid argon [109]. Liquid xenon and liquid argon are for instance applied in experiments for a direct dark matter search.

A popular method to reduce the optical crosstalk of SiPMs is the use of trenches between the individual cells. They act as barriers for photons which otherwise would travel directly through the silicon to a neighboring cell. Typically the fill factor decreases compared to a similar type without trenches, but the crosstalk probability can be reduced significantly. For novel Hamamatsu SiPMs it is reduced by about one order of magnitude compared to the standard type. These novel SiPMs also feature a very reduced afterpulse probability. It stays below 3% for over-voltages up to 3 V [109]. The corresponding data are shown in figure 4.16 (left).

With reduced probabilities of correlated noise, the over-voltage can be raised without losing to much performance (still the thermal noise is rising with the over-voltage). This can lead to a compensation of the loss of PDE due to the trenches, or even exceed the sensitivity of standard devices at a reasonable operation voltage. The related data of Hamamatsu SiPMs with reduced a probability of optical crosstalk are still confidential. However, an SiPM with reduced crosstalk probability and high PDE has been presented in reference [121]: The 100B prototype with a sensitive area of $1\times1\,\mathrm{mm}^2$ and a cell pitch of 100 µm, manufactured by the Moscow Engineering and Physics Institute features a peak PDE of almost 60% at a wavelength of 400 nm and an over-voltage of $V_{\mathrm{ov}} = 4.7\,\mathrm{V}$. Its spectral PDE is shown in figure 4.16 (right). The crosstalk probability at $V_{\mathrm{ov}} = 4.7\,\mathrm{V}$ is about 4%.[21] Unluckily, with regard to the prototype fluorescence telescope FAMOUS, a serial model of the 100B is not yet commercially available.

Further enhancements of Hamamatsu SiPMs are due to new metal quenching resistors instead of standard ones made from poly-silicon. The resistance of the metal resistor changes significantly less with a variation of the temperature: while the poly-silicon resistor changes from a resistance of about $10\,\mathrm{k\Omega/mm}^2$ at 300 K to about $100\,\mathrm{k\Omega/mm}^2$ at 77 K, the metal resistor changes only from about $17\,\mathrm{k\Omega/mm}^2$ at 300 K to $22\,\mathrm{k\Omega/mm}^2$ [109]. Furthermore, higher fill factors for fixed cell pitches can be achieved.

A design going beyond the one of SiPMs discussed so far has been presented by Philips. It is called digital silicon photomultiplier (dSiPM) and includes integrated

[21] The afterpulse probability is not specified.

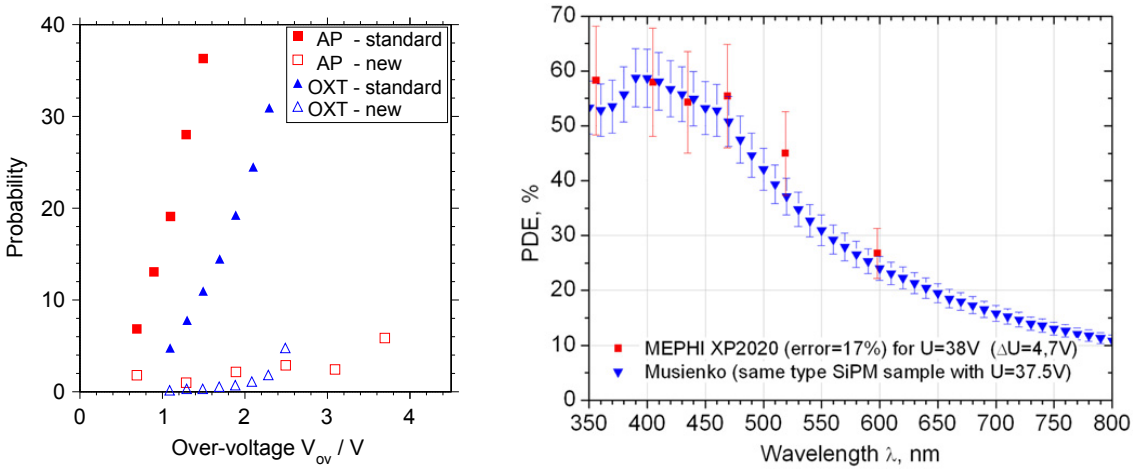

Figure 4.16: **Left:** Probabilities of optical crosstalk (OXT) and afterpulsing (AP) for new and standard SiPMs manufactured by Hamamatsu as a function of the over-voltage. The plot contains data which have been presented in reference [109]. **Right:** Spectral photon detection efficiency (PDE) of two samples (blue and red data points) of the 100B prototype SiPM ($1\times1\,\mathrm{mm}^2$, 100 µm cell pitch) developed by the Moscow Engineering and Physics Institute. U is the bias voltage, ΔU is the over-voltage. Taken from reference [121].

circuits within the die of the dSiPM. Each G-APD features its own readout circuit providing a slow data output signal, a fast trigger output connected to an on-chip time-to-digital-converter, and an active quenching and recharge circuit. A one-bit memory cell close to the diode can be used to enable or disable the respective cell [124]. The device is controlled via an FPGA.[22] Since the digitization of signals takes place directly within the chip of the photosensor, the dSiPM is less susceptible to temperature dependencies and electronic noise pickup compared to conventional SiPMs.

The dSiPM provides an internal trigger, which can be adjusted to a threshold of 1, ≥ 2, ≥ 3, or ≥ 4 detected photons. Except for the 1 photon trigger threshold, the first detected photon is rejected as thermal noise if a second photon is not detected within the next 10 – 15 ns. The data collection time can be set by the user to a value with a maximum of 20 µs. After photon collection the G-APDs are read out and set to their initial state. The minimum acquisition time of a demonstrator chip is 695 ns [124].

The design of the dSiPM features the possibility to identify the individual cells which break down. This provides interesting new measurements regarding the characterization of SiPMs. For example, maps of optical crosstalk events can be realized. Furthermore, individual cells can be turned off. Since some of the cells of an SiPM have a very high noise rate, the overall noise rate can be reduced significantly by disabling these hot cells.

Philips offers two designs which differ in the size of the cells ($59.4\times32\,\mu\mathrm{m}$ and

[22] FPGA = Field Programmable Gate Array

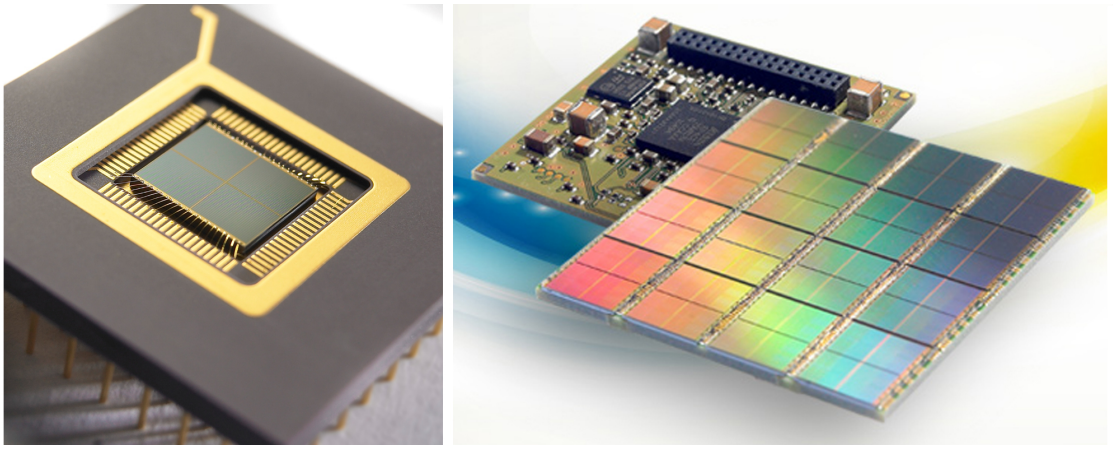

Figure 4.17: **Left:** Photo of a digital silicon photomultiplier (dSiPM) manufactured by Philips. Taken from reference [122]. **Right:** Photos of a four-side tileable 8×8 dSiPM array manufactured by Philips (top and bottom view). The shown structure has a size of about 33×33 mm^2. Modified, original taken from reference [123].

59.4×64 µm) [123]. Both designs are four-side tileable 8×8 dSiPM arrays with a size of 32.6×32.6 mm^2. The devices have peak sensitivities of 30% and 40%, respectively, at a wavelength of 420 nm. The fill factor of the 8×8 dSiPM tile is 75%. Photos of a dSiPM and a dSiPM array are shown in figure 4.17.

Commercially available SiPMs possess sensitivities which are comparable to state-of-the-art photomultiplier tubes (PMTs). Wherever their high noise rates can be tolerated and small detection areas are needed, already now SiPMs offer an interesting alternative to PMTs. Their potential for even higher photon detection efficiencies has led to the decision to study the feasibility of fluorescence detection of air showers with an SiPM telescope prototype. This prototype named FAMOUS will be discussed in the next chapter.

5. FAMOUS - Fluorescence Telescope Prototype

The direct observation of the longitudinal development of air showers by means of fluorescence light detection is a powerful and straightforward technique in the physics of ultra-high-energy cosmic rays. Its major drawback compared to ground arrays is the reduced number of detected air shower events since clear and moonless nights are essential for observation. This necessity leads to significantly reduced duty cycles of fluorescence telescopes. For example, the duty cycle of the fluorescence detector of the Pierre Auger Observatory is 15%. An increase of the event statistics cannot only be achieved by an increased duty cycle, but also by larger effective detector areas. Here, not the aperture of the telescope is meant, but the area in the ground plane above which air showers can be appropriately detected by a telescope. On the one hand, the field of view of a telescope can be increased to result in a larger effective area. This is similar to operate additional telescopes facing into different directions. On the other hand, a single telescope with a fixed field of view will benefit from an increased effective detection area if it is able to see more distant air showers. Hence, the light sensitivity of a telescope is a crucial parameter regarding event statistics. Not only can a more sensitive detector see fluorescence light produced in a farther distance, it might also be able to detect closeby air showers of lower energy which would not have been detected by a less sensitive detector, since they produce less light.

Silicon photomultipliers (SiPMs), which have been discussed extensively in the previous chapter, seem to be an excellent choice to replace photomultiplier tubes (PMTs) in fluorescence telescopes. Examples of both photodetectors are shown in the photo of figure 5.1. SiPMs are small semiconductor devices with sensitive areas in the order of square millimeters. Several types feature a high photon detection efficiency in the wavelength region of blue and UV light. Furthermore, SiPMs are capable of single photon detection and resolution, and possess excellent timing performances. However, their application evokes also new challenges like correlated noise and strong temperature dependencies.
Another interesting point is the fact that SiPMs do not suffer from high illumination unlike PMTs. This could be of interest if the uptime of a fluorescence detector can be extended into the twilight of dusk and dawn to achieve a higher duty cycle. This is typically not performed for fluorescence telescopes with PMT-instrumented cameras. In addition, the small sizes of SiPMs, their possibility to mass production, and their non-existent need for high-voltage power supplies might direct to the cost-

Figure 5.1: Photo of a 3 inch photomultiplier tube (left) and a silicon photomultiplier (right). The active area of the silicon photomultiplier is 1 mm^2. Taken from reference [125].

efficient construction of small, unconventional telescope designs to increase both the duty cycle and the effective detection area.

FAMOUS (First Auger Multi-pixel-photon-counter[1] camera for the Observation of Ultra-high-energy air Showers) is a small fluorescence telescope prototype to study the feasibility of fluorescence detection of air showers with SiPMs. FAMOUS will answer the question whether SiPMs are a serious alternative to PMTs in fluorescence telescopes and might be the first step towards a new fluorescence detector design. In this chapter we will discuss the design of FAMOUS and its current status. At its end we will also have a look at the imaging air Cherenkov telescope FACT (First Geiger-mode Avalanche-photodiode Cherenkov Telescope) which uses an SiPM-based camera for γ-ray astronomy.

5.1 Prototype baseline design

The baseline design of the optical components of FAMOUS has been developed in the scope of reference [118] and presented in references [104, 127–129]. FAMOUS uses a simple refractive design with a Fresnel lens which focuses the light on a camera with 64 pixels. The field of view (FOV) per pixel is 1.5°, which follows the design of the fluorescence telescopes of the Pierre Auger Observatory, and leads to a total FOV of approximately 12°. Each pixel consists of four SiPMs providing a sensitive area of $4 \times 3 \times 3\,\mathrm{mm}^2$. To enlarge the effective sensitive area, non-imaging light concentrators, referred to as Winston cones, are mounted in front of the SiPMs. To achieve a better signal-to-noise ratio, UV band-pass filters between the light concentrators

[1] Multi-pixel-photon-counter (MPPC) is another frequently used expression for SiPM introduced by the manufacturer Hamamatsu.

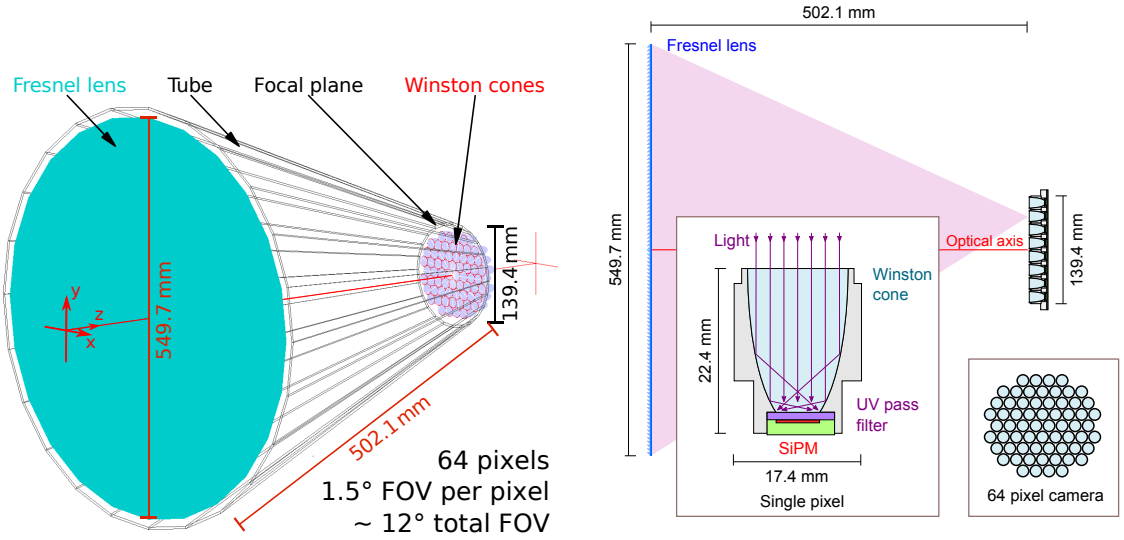

Figure 5.2: **Left:** Geant4 visualization of the FAMOUS fluorescence prototype telescope. The z–axis is identical to the optical axis of the telescope (FOV = field of view). Modified, original taken from reference [118]. **Right:** Schematic view of FAMOUS in the y–z–plane. The inset to the bottom right shows the camera in the focal plane with its 64 pixels in a frontal view (x–y–plane). The inset to the left shows the cross section of a single camera pixel (y–z–plane). Modified, original taken from reference [126].

and the SiPMs prevent most of the background light to be detected by the photosensors. The baseline design of FAMOUS is shown in figure 5.2. The following sections will discuss the individual components in more detail. The choice of the overall size of the prototype was driven by the requirements to have an aperture as wide as possible, but also provide easy transport of the instrument between laboratory and observational sites.

Fresnel lens

A Fresnel lens can be obtained from a conventional lens by dividing it into concentric rings, and reducing the thickness of the bulk material of these rings. The surface of the resulting lens reminds of a saw tooth tread design, and the fragmentation of the original lens into rings is typically stated as grooves per unit of length. The advantages of a Fresnel lens compared to conventional lenses are a reduced absorption and less weight. The disadvantage is a reduced imaging quality. However, the imaging quality of the Fresnel lens used for FAMOUS is sufficient for its application [130]. It is manufactured by Reflexite,[2] has a diameter of $D = 549.7\,\text{mm}$, a focal length of $f = 502.1\,\text{mm}$, and 10 grooves per millimeter in a *grooves out* configuration. The latter denotes that the planar side of the lens is facing towards the focal surface, whereas the groves face towards the sky. The lens is made of UV-transparent PMMA (polymethyl methacrylate, sometimes also referred to as acrylic glass). The internal

[2]Reflexite is now a product brand acquired by ORAFOL Europe GmbH.

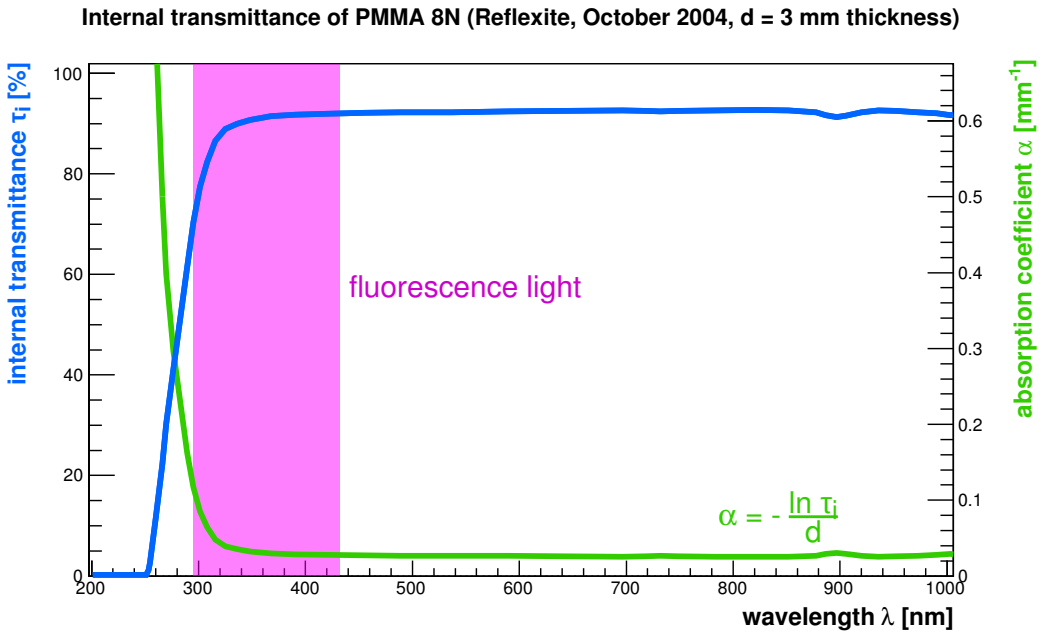

Figure 5.3: Internal transmittance (blue) and absorption coefficient (green) of 3 mm of PMMA as a function of the wavelength. Shown is also the wavelength interval in which the UV fluorescence light of air showers is contained. The data are according to private communication with Reflexite. Picture credit: T. Niggemann.

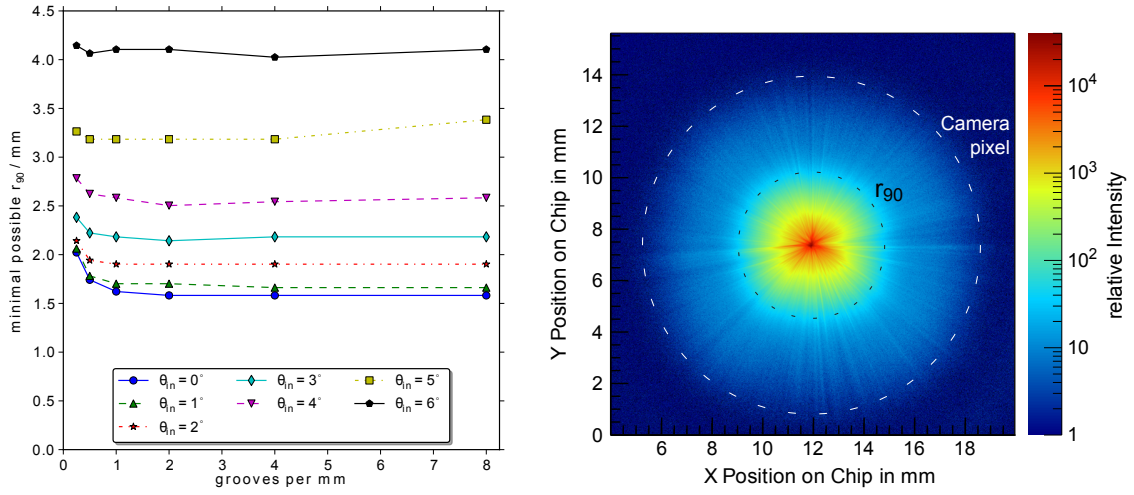

Figure 5.4: **Left:** Simulated minimal possible r_{90} for ideal Fresnel lenses with different numbers of grooves per millimeter. The set of functions is for different incident angles of the parallel light on the lens θ_{in}. Taken from reference [128]. **Right:** Measured distribution of photons in the focal plane (x-y-plane) of the Fresnel lens used for FAMOUS. Coordinates are given as the position on the applied photosensor which is a CCD chip. The light source has a diameter of about 1 mm and is placed along the optical axis of the lens in a distance of about 22 m. The black dashed circle contains 90% of the photons and has a radius of $r_{90} = 2.89$ mm. The white dashed circle denotes the size of a camera pixel of FAMOUS. Taken from reference [130].

transmittance of UV-transparent PMMA as a function of the wavelength is shown in figure 5.3. It does not consider effects due to reflections. Taking also reflections into account simulations yield that the overall transmission for wavelengths corresponding to the fluorescence light signals (cf. its spectrum in figure 2.11) is about 70% [131].
A common quantity to express the imaging quality of a lens is the radius r_{90}. It is the radius of the circle within the focal plane of the lens, which contains 90% of the refracted photons. In figure 5.4 (left) the simulated r_{90} is shown as a function of the number of grooves of the lens per millimeter. The set of functions is for various incident angles of the light θ_{in}. For the Fresnel lens of FAMOUS the minimal r_{90} is found for $\theta_{\text{in}} = 0°$ and its value equals 1.88 mm. It becomes larger with increasing θ_{in}, meaning that the imaging quality gets worse. However, for all relevant incident angles the r_{90} are smaller than the radius of the camera pixel size, which is 6.7 mm as it will be discussed in the next paragraph.
The r_{90} of a lens identical to the one used for FAMOUS has been measured in the scope of reference [130]. An exemplary measurement of the point spread function is shown in figure 5.4 (right). The point spread function is the distribution of photons in the focal plane, which originate from a point light source and which have been refracted by the lens. The r_{90} is given by the black dashed circle, whereas the size of the camera pixel is given by the white dashed one. For a light source with a diameter of about 1 mm located along the optical axis in a distance of about 22 m from the lens, the measured r_{90} equals 2.89 mm. It is larger than the corresponding simulated value of the left plot of figure 5.4 since the simulations account for an ideal lens featuring angled grooves. The real grooves are more likely round-shaped at the edges, and lead to a higher value of r_{90}.
For $\theta_{\text{in}} \leq 6°$, which corresponds to the 12° field of view of FAMOUS, the measured r_{90} are smaller than the radius of the size of the camera pixel. Thus, the imaging quality of the lens is sufficient for its intended application.
The total transmittance of the Fresnel lens has also been measured in reference [130]. Unlike the internal transmittance it takes reflections of light into account. For light with a wavelength of 400 nm which illuminates the full lens approximately parallel to its optical axis (0.7° divergent cone) the transmittance is $(50.2 \pm 2.0)\%$. For more information on the Fresnel lens please refer to reference [130].

Winston cones

To increase the effective area of a camera pixel, a special kind of non-imaging light concentrators referred to as Winston cone [132] is used. An ideal Winston cone will collect all light, which enters at its entrance aperture, at its exit aperture, provided that the incident angle of the light does not exceed a certain characteristic angle θ_{max}. To realize this principle we first define a circular entrance aperture with a radius r_1 and a circular exit aperture with a radius $r_2 < r_1$. These apertures are parallel to each other, and their centers are located in a distance l from each other along an axis of symmetry (which will be the optical axis of the completed Winston cone). A cross section of this construction is given in figure 5.5 (left). In this cross section the outer-most point of the entrance at one side of the axis is connected by

a parabola with the outer-most point of the exit on the same side of the axis. The parabola is tilted with respect to the axis by an angle of $\theta_{\max} = \arcsin(r_2/r_1)$, and its focal point is located at the outer-most point of the exit at the opposite side of the axis. The reflecting surface of the three-dimensional Winston cone is now given by a rotation of the parabola around the axis of symmetry.
With the choice of r_1 and r_2 and the requirements to the parabola, its shape is fixed and the distance of the entrance aperture to the exit aperture is not free to choose, but given by $l = (r_1 + r_2)/\tan\theta_{\max}$. Generally speaking, a Winston cone will be completely described by the choice of two of the four parameters r_1, r_2, $\theta_{\max}$, and l if at least one of them is r_1 or r_2. The shape of the parabola is given by

$$r(\theta) = 2\,r_2\,\frac{1+\sin\theta_{\max}}{1-\cos(\theta+\theta_{\max})} \tag{5.1}$$

with $\theta \in [\theta_{\max},\, \pi/2]$ $\big($cf. figure 5.5 (right)$\big)$ [133].
Light which enters the Winston cone with angles greater than $\theta_{\max}$ will be reflected more than once and will leave the cone through the entrance aperture.
Imagine a light sensor whose acceptance does not depend on the incident angle of the light. Its field of view Ω would be the hemisphere above it, thus, $\Omega = 2\pi\,\mathrm{sr}$. A Winston cone in front of it reduces the field of view by rejecting light with incident angles greater than $\theta_{\max}$. In this case $\Omega = 4\pi\sin^2(\theta_{\max}/4)\,\mathrm{sr}$.

The previous discussion of Winston cones was implicitly performed for cones which have the same medium between the reflecting surface and in front of entrance and exit aperture. In many practical cases (as for FAMOUS) this medium is air. Thus, the discussed Winston cone is a hollow cone, e.g. manufactured by lathing the shape into a solid block of aluminium. But also solid cones are possible, e.g. manufactured by injection molding of an appropriate material into a negative form. In this case the reflection inside the cone is due to total reflection at the transition from a medium of higher optical density to a medium of lower optical density. For the solid cone also refraction of light at the entrance and exit apertures have to be taken into account. This refraction at the entrance aperture leads to greater $\theta_{\max}$ compared to the hollow cone. But additional material also leads to higher absorption. For FAMOUS where we have to deal with UV light, this point becomes crucial and makes the hollow cone the preferred choice. A more detailed comparison of hollow and solid Winston cones is given in reference [118].

For FAMOUS the parameters of the Winston cone are given by the size of the light sensor (see below) which defines $r_2 = 3.0\,\mathrm{mm}$, and by the parameters of the lens (diameter D, focal length f). During the design phase a lens with $D = f = 511.0\,\mathrm{mm}$ has been considered. Light refracted by this lens reaches the center of the focal plane with angles $\theta_{\mathrm{in}} \leq \arctan(0.5 \cdot D/f) \approx 26.6°$. Hence, $\theta_{\max} = 26.6°$ was chosen. This leads to $r_2 = 6.7\,\mathrm{mm}$ and $l = 19.4\,\mathrm{mm}$. The shape for this Winston cone is given in figure 5.5 (right). The light concentrator increases the effective area by a factor of

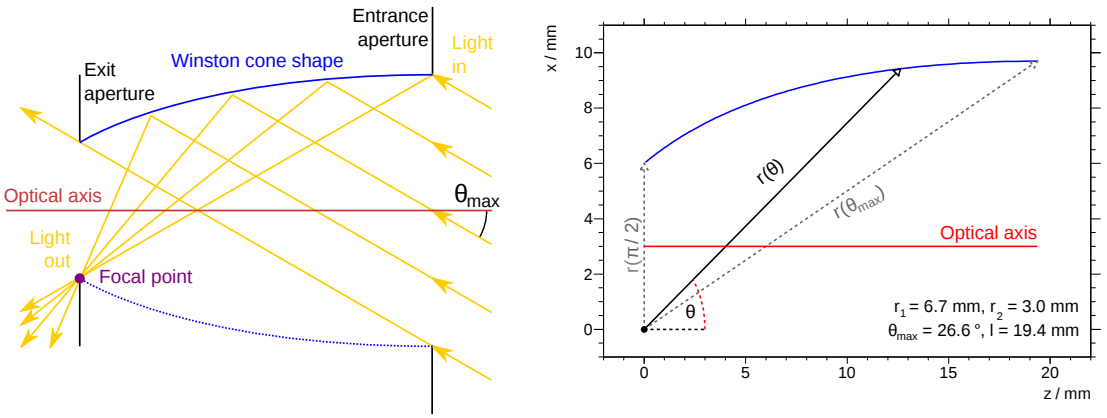

Figure 5.5: Schematics to demonstrate the construction of a Winston cone, (**left**) with light paths for photons with the maximum incident angle $\theta_{\max}$, and (**right**) with the dimensions of the Winston cone used for FAMOUS. The shape of the cone $r'(\theta)$ is given by equation (5.1). See text for more details. Modified, originals taken from reference [118].

$r_1^2/r_2^2 \approx 5$.[3]
The parameters of the lens eventually acquired for FAMOUS differ from $D = f = 511.0\,\text{mm}$. With $D = 549.7\,\text{mm}$ and $f = 502.1\,\text{mm}$, we find $\theta_{\text{in}} \leq 28.7°$ at the center of the focal plane. The 64 pixel camera has a diameter of 139.4 mm. At its outermost point the maximum of θ_{in} even gets higher and reaches a value of approximately 34.5°.[4] This mismatch of Fresnel lens and Winston cone design leads to a reduced light collection efficiency which can be determined by analytical calculations or ray-tracing simulations. By these means it can be evaluated which maximum photon collection efficiency of the optical system can be achieved by an optimum design. However, it is not the goal of the FAMOUS prototype to feature the optimum design regarding the photon collection efficiency, but to study the feasibility of fluorescence light detection of air showers with SiPMs. As long as the causes for reductions of the photon collection efficiency are well known, possible successors to FAMOUS can counteract these causes.

Another reduction of the light collection efficiency is due to the round design of the Winston cones which leads to dead space between the individual camera pixels. Other designs, for instance with a hexagonal or squared entrance aperture, would provide a better fill factor. These designs have also been studied in reference [118]. Even more complicated designs are possible, like the combination of a hexagonal entrance and a squared exit aperture.[5] The main reason to use the round Winston cone design for FAMOUS is its simplified manufacturing process: the individual cones for FAMOUS are lathed with high precision from solid aluminium and their

[3] Since the four SiPMs at the exit of a Winston cone provide a squared sensitive area of $4 \times 3{\times}3\,\text{mm}^2$, but the exit aperture of the cone is circular, the increase in effective area regarding the SiPMs is only of a factor of approximately 4.

[4] Note that the diameter of the camera will also change if $\theta_{\max}$ is set to another value.

[5] Such a design is used for the γ-ray telescope FACT, which will be presented in section 5.5.

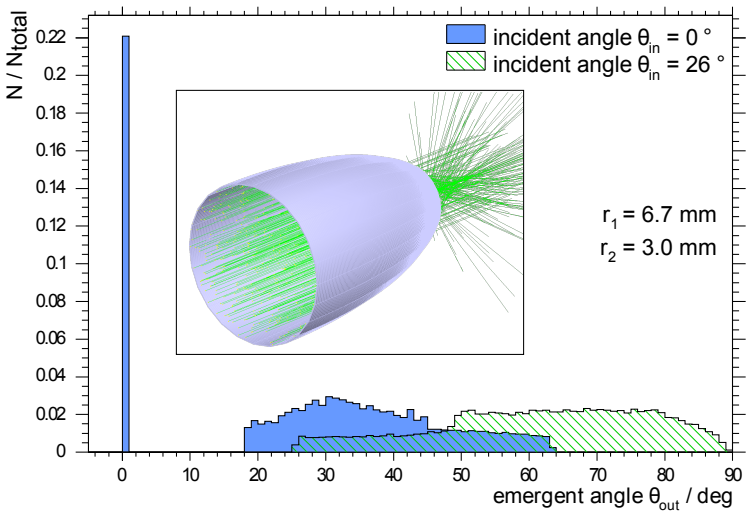

Figure 5.6: Simulated distributions of emergent angles θ_{out} of light concentrated by the Winston cone of FAMOUS. The blue histogram is for light entering the Winston cone parallel to its optical axis ($\theta_{\text{in}} = 0°$). The green shaded histogram is for light with an incident angle of $\theta_{\text{in}} = 26°$. Modified, original taken from reference [118]. **Inset:** Geant4 visualization of a Winston cone. Light (green) enters it with an incident angle of $\theta_{\text{in}} = 0°$ and leaves it under emergent angles $\theta_{\text{out}} \geq 0°$. Taken from reference [104].

reflecting surface is polished afterwards. The reflectivity of polished aluminium is greater than 90% for light with a wavelength of 400 nm as can be seen for example in reference [134]. In this reference also measurements regarding the reflectivity of aluminium in different stages of oxidation have been presented. It has been found that the reflectivity does not decrease significantly with oxidation of the aluminium for wavelengths around 400 nm.

An additional interesting feature of Winston cones is the fact that the angles under which the light leaves the cone are typically higher than the ones under which it enters the cone. This is visualized in figure 5.6. Simulated distributions of emergent angles for the Winston cone of FAMOUS are shown for light entering the cone parallel to its optical axis ($\theta_{\text{in}} = 0°$, blue histogram) and for parallel light entering it with $\theta_{\text{in}} = 26°$ (green shaded histogram). The peak at 0° is for light passing right through the cone without any reflection. As soon as the light is reflected at the surface of the cone, relatively large emergent angles appear. For $\theta_{\text{in}} = 26°$ they can reach values close to 90°.
For high emergent angles the photon detection efficiency of the silicon photomultipliers is reduced. The dependence of this efficiency on the emergent angle has been discussed in section 4.2.

The combined, simulated photon transmission efficiency of lens and Winston cone is about 38% for a full illumination of the lens with light parallel to its optical axis

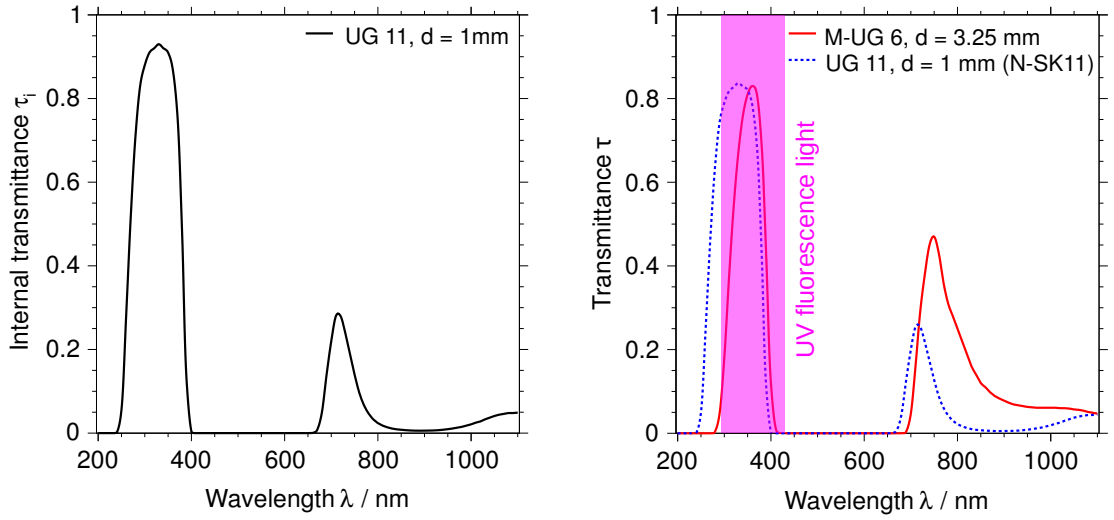

Figure 5.7: **Left:** Internal transmittance τ_i of Schott UG 11 UV band-pass filter as a function of the wavelength according to the datasheet [136]. The filter has a thickness of 1 mm. **Right:** Transmittance τ of Schott UG 11 and Schott M-UG 6 UV band-pass filters. The thickness of the UG 11 is 1 mm, whereas the thickness of the M-UG 6 is 3.25 mm. The transmittance of the UG 11 filter has been calculated from its internal transmittance with the assumption that it is identical to the one of N-SK11 glass. The transmittance of the M-UG 6 is according to its datasheet [136]. See text for more details. Also shown is the region of the UV fluorescence light.

at a wavelength of 400 nm.[6] The value of the photon transmission efficiency of the fluorescence telescopes of the Pierre Auger Observatory to compare to is about 64% at 370 nm [135].[7]

UV band-pass filters

At the exit aperture of the Winston cones, just in front of the SiPMs, UV pass-band filters are mounted. The choice of this position is discussed at the end of this section. The UV filters are ionically colored glasses manufactured by Schott with the type designation UG 11. They have a thickness of 1 mm. The internal transmittance τ_i of 1 mm of UG 11 is given in figure 5.7. Also shown is the transmittance τ of the UV band-pass filter M-UG 6 also produced by Schott and used for the fluorescence telescopes of the Pierre Auger Observatory. The data correspond to M-UG 6 with a thickness of 3.25 mm, which is the same thickness as for the filters of the observatory. In contrast to the transmittance τ, the internal transmittance τ_i does not consider reflection losses at the transitions of the glass to its surrounding medium.[8] The internal transmittance thus refers to the absorption of light inside the filter. Light of the intensity I_0 will be reduced to an intensity of $I = I_0 \cdot \exp(-\alpha \cdot d)$ according

[6] not included is the UV filter discussed in the next subsection

[7] In the reference a value of 54% is stated but the corresponding simulation includes the UV band-pass filter.

[8] These and the following quantities are according to the definitions given by Schott [137, 138].

to the Beer–Lambert law, where α is the absorption coefficient of the filter material, and d is the traveled distance. The internal transmittance is given by $\tau_\mathrm{i} = 1 - I/I_0$. The manufacturer states τ_i for the UG 11 and τ for the M-UG 6. For a direct comparison of both glasses we have to calculate τ for the UG 11 from its internal transmittance.

The starting point are the Fresnel equations which describe the reflectivity of light traversing the boundary of two media of differing refractive indices. The Fresnel reflectivities for parallel (p) and perpendicular (s, German *senkrecht*) polarized light moving from a medium with refractive index n_1 to a medium with refractive index n_2, hitting the boundary surface with an angle of ϑ_1 to the normal are given by

$$R_\mathrm{s} = \left| \frac{n_1 \cos\vartheta_1 - n_2 \cos\vartheta_2}{n_1 \cos\vartheta_1 + n_2 \cos\vartheta_2} \right|^2 \quad , \tag{5.2}$$

$$R_\mathrm{p} = \left| \frac{n_1 \cos\vartheta_2 - n_2 \cos\vartheta_1}{n_1 \cos\vartheta_2 + n_2 \cos\vartheta_1} \right|^2 \quad . \tag{5.3}$$

Here, ϑ_2 is the angle relative to the surface normal under which the light propagates after refraction at the transition of the two media. It can be calculated from n_1, n_2, and ϑ_1 using Snell's law

$$n_1 \sin(\vartheta_1) = n_2 \sin(\vartheta_2) \, . \tag{5.4}$$

For unpolarized light the Fresnel reflectivity is given by

$$R = \frac{1}{2} \left(R_\mathrm{s} + R_\mathrm{p} \right) \, . \tag{5.5}$$

For our consideration we regard light approaching the transition of the two media perpendicular to the boundary surface. Hence, $\vartheta_1 = \vartheta_2 = 0$, and the reflectivity of the light, moving from air (refractive index set to 1) to glass (refractive index $n > 1$) and moving from glass to air is identical. Hence, the relation between the reflectivity and the refractive index of the glass simplifies to

$$R = \left(\frac{n-1}{n+1} \right)^2 \, . \tag{5.6}$$

Light which passes plane-parallel glass surrounded by air is sketched in figure 5.8. Different from the consideration in the text an incident angle ϑ_1 larger than zero has been chosen in favor of a clear illustration. The light which passes directly through has encountered two transmissions at the edges of the glass — one transmission while entering the glass, and one while leaving it. Its intensity is thus reduced by a factor of $(1 - R)^2$. The amount of light which is reflected at the exit surface of the glass moves backwards to the entrance surface. There again some light leaves the glass and some is reflected back into its original direction. These multiple reflections continue until the light leaves the glass or is absorbed. In addition to the light which passes directly through the glass, we find the first order of multiple reflection giving a factor of R^2 (back and forth) to the intensity. The second order of multiple reflection

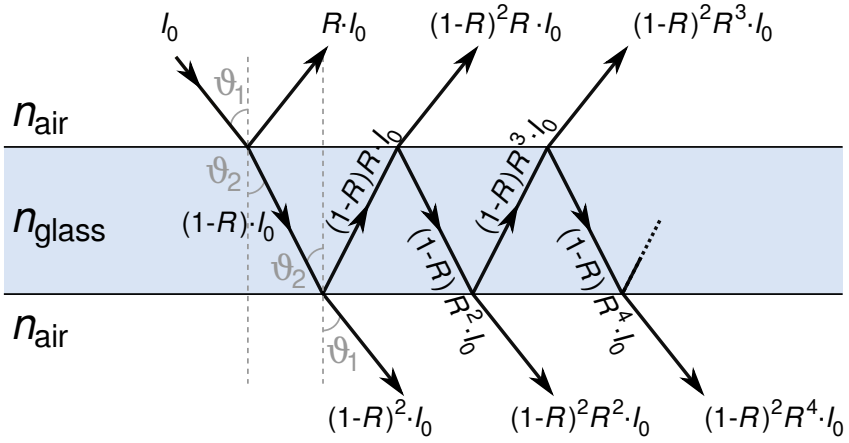

Figure 5.8: Schematic of multiple reflection of light in glass surrounded by air. The light has an intensity of I_0 upon entrance into the glass. The labels indicate the intensities of the refracted and reflected light with R being the reflectivity. See text for details.

gives a factor of R^4 (back and forth, and again, back and forth). Thus, the reflection factor taking all orders of multiple reflections (including the zero order, which is the light passing directly through the glass), as well as the transmission *into* and *out of the glass* into account is given by

$$\begin{aligned} P &= (1-R)^2 \cdot \left(1 + R^2 + R^4 + \mathcal{O}(R^6)\right) \\ &= (1-R)^2 \cdot \sum_{i=0}^{\infty} R^{2i} \\ &= \frac{(1-R)^2}{1-R^2} = \frac{1-R}{1+R}\,, \qquad \text{since } \sum_{i=0}^{\infty} a^k = \frac{1}{1-a} \text{ for } a < 1\,. \end{aligned} \tag{5.7}$$

The reflection factor describes the loss of the intensity of the light while passing through the glass caused exclusively by reflections. Absorption processes are not considered. Equations (5.6) and (5.7) yield the reflection factor as a function of the refractive index of the glass n, which itself depends on the wavelength of the light λ:

$$P = \frac{2\,n(\lambda)}{n(\lambda)^2 + 1}\,. \tag{5.8}$$

Per definition given by Schott the relation between transmittance τ and internal transmittance τ_i is given by [137]

$$\tau = P \cdot \tau_i\,. \tag{5.9}$$

Unluckily, Schott published the refractive index of UG 11 only for two wavelengths (cf. datasheet [136] and figure A.2 (right)). Using the Schott product catalog [138] and a comprehensive online database of refractive indices [139] the glass found to be closest to UG 11 regarding n is Schott N-SK11. Its refractive index can be found in

the appendix in figure A.2 (right). Also shown in this figure is the linear extrapolation of the two data points of the UG 11 given by the manufacturer. The refractive index of N-SK11 is only known for wavelengths greater than 300 nm, hence, for $\lambda < 300$ nm an extrapolation is used in this case as well.
Calculating the transmittance of the UV band-pass filter with these two approximations of the actual refractive index of UG 11 leads to very similar results. The one which uses the refractive index of N-SK11 is shown in figure 5.7 (right). The result from the linear extrapolation of the refractive index is not displayed since its difference to the other approach is too small to be recognized in the plot. The differences are smaller than 1.6% for each considered wavelength.

Already from figure 5.7 we can conclude that the UG 11 features a good transmittance in the wavelength region interesting for fluorescence light detection of air showers (i.e. 290 nm to 430 nm). The transmittance has its maximum very close to the position of the line of the fluorescence spectrum which has the highest intensity. This line is located at 337 nm. For the wavelength interval from 290 nm to 430 nm the UG 11 filter has a transmission efficiency[9] of 53.4% (for both the N-SK11 and the linear approach to approximate the refractive index), whereas the M-UG 6 filter has 47.8%. The UG 11 absorbs most of the visible light and has a smaller transmittance for red and infra-red light than the M-UG 6 filter. The transmission efficiency for wavelengths between 430 nm to 1100 nm is 3.3% for the UG 11 and 8.9% for the M-UG 6. A higher absorption of these wavelengths increases the signal-to-noise ratio of a fluorescence telescope, since the spectrum of the night-sky at dark and solitude observational sites is typically dominated by emissions above 700 nm (see for instance reference [140]).

The position of the UV filters within FAMOUS have been chosen originally to avoid a transition from air to the filter and back to air, and the involved reflections of light. With the filters being coupled to the SiPMs by a refractive index matching liquid, a smoother transition from air to the silicon is provided. The entrance window of the SiPM is made from epoxy resin. It protects the silicon from external influences and provides itself a smoother transition from the air to the photo-sensitive material. There is a huge variety in epoxy resins from different manufactures and a reference value for the refractive index is 1.58 at about 589 nm [141].[10] Assuming similar dispersion characteristics for epoxy resin, as well as for polystyrene (PS) and polycarbonat (PC), we, the FAMOUS group, have assumed the refractive index of the epoxy resin to be greater than 1.61 for wavelengths smaller than 436 nm with an increase of this value going to smaller wavelengths.[11] These values have been obtained from a comparison of data given in reference [141] and an online database of refractive indices which contains PS and PC, but no epoxy resin [139]. Hence, the optical density of the resin is greater than the one of the UV filter, which is 1.59 at 365 nm, and its position in front of the SiPM is well-chosen. Recent private

[9] given as the integral of the spectral transmittance

[10] The standard reference wavelength for refractive indices is $\lambda_D \approx 589.3$ nm which is the center of the natrium spectral line dublett D_1 and D_2 (see e.g. NIST Atomic Spectra Database).

[11] There are no entries for wavelengths smaller than 436 nm in the considered databases.

communication with the manufacturer of the SiPMs has led to the awareness that the resin has a refractive index of 1.5 to 1.6 at a wavelength of 589 nm, thus, our assumptions seem justified. However, the spectral progression of the refractive index is still an unknown characteristic and worth to be determined in the future.
If it turns out that the actual optical density of the resin is smaller than the one of the UV filter, total reflection of light, which occurs at the transition surface, should be prevented. In this case it becomes necessary to mount the filter somewhere at the opposite side of the Winston cone. Here, the angles between the light and the optical axis of the telescope have not yet been increased by the reflections inside the Winston cone. However, to answer the questions where the filter has to be mounted in an optimal way, measurements of the refractive index of the epoxy resin have to be performed in the future.
Should the position of the filter at the exit of the Winston cone turn out to be the optimal way, the knowledge of the refractive indices of the filter and the resin can be used to choose an appropriate index matching liquid, to couple both elements to each other and avoid small inclusions of air between the two materials.
Alternative possibilities like the production of the Fresnel lens or the entrance windows of the SiPMs from glass, which acts as a UV band-pass filter, can be discussed with the manufacturers for future upgrades of FAMOUS to a large fluorescence detector design.

Silicon photomultipliers

The four SiPMs of a single camera pixel are located behind the UV pass-band filter (cf. figure 5.2). They have a sensitive area of $3\times3\,\mathrm{mm}^2$ each and are housed in the same ceramic package, leading to a total sensitive area of $6\times6\,\mathrm{mm}^2$. Since the Winston cone has a circular exit aperture, the SiPM array provides a sensitive area of approximately $28\,\mathrm{mm}^2$ to the detection of light entering the telescope.

The SiPM arrays are manufactured by Hamamatsu and possess the type designation S10985-100C. A technical drawing is given in figure 5.9 and a photo is shown in figure 5.10. The individual SiPMs show the same characteristics as the ones of the S10362-33 series, which also have an active area of $3\times3\,\mathrm{mm}^2$. These characteristics are summarized in table 5.1. Hamamatsu has stated in private communication that the entrance window of the array is made from epoxy resin with a thickness of about 450 µm and a refractive index of 1.5 to 1.6 at 589 nm. The cell pitch of the SiPMs is 100 µm and their monolithic structure eliminates gaps between the four individual SiPMs. An array can be connected via five pins, four of them are connected to the anodes of the individual channels, whereas the remaining pin is connected to the common cathode. The latter leads to a common bias voltage of all four SiPMs within an array. Since the breakdown voltage among individual SiPMs may vary, the recommended bias voltage is determined by the manufacturer individually for each SiPM or SiPM array before shipment, and data are attached to each product. Hamamatsu has stated in private communication that the variation of the recommended bias voltage between the four channels of the S10985-100C is 0.2 V or less. This means that for a nominal over-voltage of for instance 1.3 V this leads

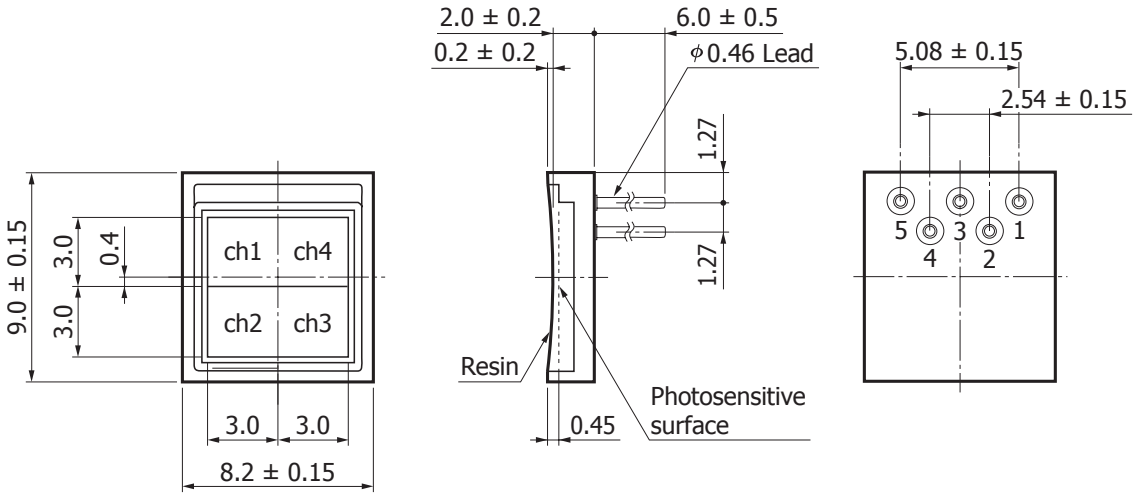

Figure 5.9: Technical drawing of Hamamatsu S10985 series SiPM. All values are given in millimeters. From left to right: top view, side view, bottom view. The pin configuration for pins in the order from 1 to 5 is: anode ch1, anode ch2, common cathode, anode ch3, anode ch4. Taken from the datasheet [108].

to a maximum difference of about 15%. This 15% variation is directly transfered to the gain of the SiPMs. Thus, for a summed signal of all four SiPMs within the array the single photon resolution is affected in an unfavorable way by the variation of the over-voltage if the anodes share a common ground. This could be prevented with floating grounds which provide different electric potentials to the anodes in a way, that they counteract the variation of the breakdown voltage. The feasibility of this procedure in consideration of the light fluxes involved in the operation of FAMOUS will be studied. Besides, Hamamatsu offers a service to select arrays with a reduced tolerance of breakdown voltages which is liable to charge.

Another very interesting service is a custom resin at the entrance window of the array. A thinner resin means less material to traverse for incoming photons, thus, the device becomes more sensitive to shorter wavelengths (cf. section 4.1). With its peak sensitivity shifted towards lower wavelengths (which is located at 440 nm for standard devices), the photosensors become even more attractive to the fluorescence light detection of air showers.

Recent achievements of Hamamatsu have led to SiPMs with significantly reduced correlated noise. These achievements have been discussed briefly in section 4.4. After a positive evaluation of these new devices, a replacement of the currently implemented SiPMs of FAMOUS might be arranged.

5.2 Performance evaluation

An evaluation of the optical baseline design of FAMOUS is performed by means of a full detector simulation. It has been developed in the scope of reference [118] and latest results have been presented in reference [126]. We will only discuss it

Table 5.1: Characteristics of Hamamatsu S10985-100C SiPM. Except from the first entry, all values are identical to the one of the Hamamatsu S10362-33-100C SiPM. Adapted, original found in reference [108].

Parameter	Value	Unit
Number of channels	4 (2×2)	–
Effective sensitive area/channel	3×3	mm^2
Number of pixels/channel	900	–
Pixel size	100×100	μm^2
Fill factor [*1]	78.5	%
Spectral response range	320 to 900	nm
Peak sensitivity wavelength	440	nm
Operating voltage range	70 ± 10 [*2]	V
Dark counts/channel [*3]	8000	kcps
Dark counts max./channel [*3]	12000	kcps
Terminal capacitance/channel	320	pF
Temperature coefficient of reverse voltage	56	mV/°C
Gain	2.4×10^6	–

[*1] Ratio of the active area of a pixel to its sensitive area (cf. section 4.2)
[*2] For the recommended operating voltage of each device, refer to the data attached to each device
[*3] 0.5 p.e. (threshold value)

very briefly at this point. For further information please refer to the mentioned publications.

Vertical extensive air showers have been simulated with the program CONEX (see section 2.4) using EPOS 1.99 as the hadronic interaction model for high energies. The CONEX output includes the particle density of the air shower as well as the energy deposit as a function of the atmospheric depth.
The subsequent simulation steps are performed with Offline. Offline is the software package of the Pierre Auger Observatory [142]. It consists of a detector description, an event data model, and a collection of processing modules, among which the data model is relayed within a module chain. For our purpose the core positions of the simulated showers are randomized within the field of view of a fluorescence telescope. Afterwards, the amount of produced fluorescence light is calculated from the energy deposit obtained from CONEX. To account also for the lateral stretch of the air showers, the positions of the sources of the fluorescence light are smeared along the shower axis according to a parametrization of the lateral shower profile. The simulated fluorescence photons are then propagated through the atmosphere by means of a ray-tracing simulation. This propagation includes molecular and aerosol scattering of the light.

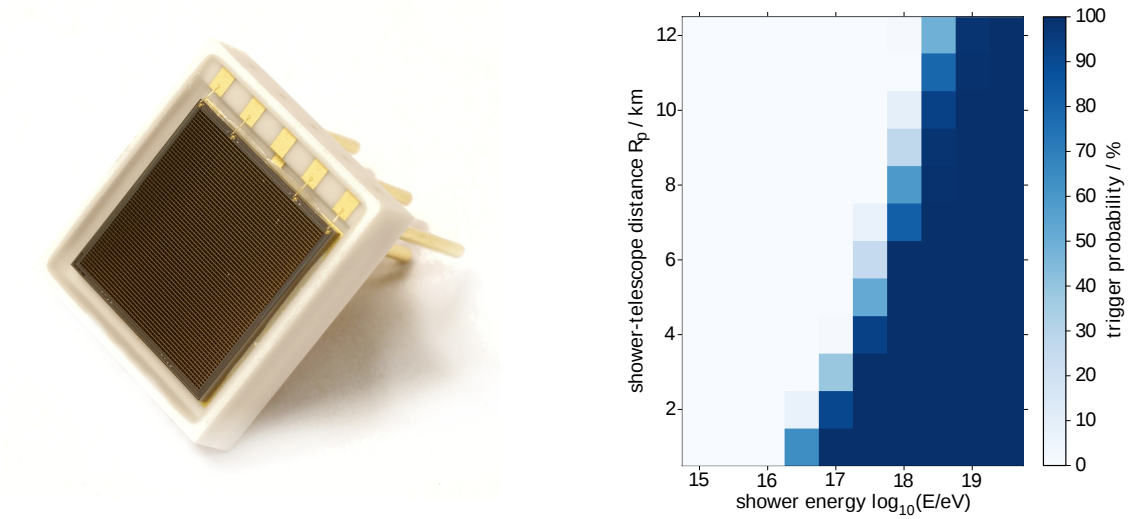

Figure 5.10: **Left:** Photo of a Hamamatsu S10985-100C SiPM (4 channels, $4 \times 3{\times}3\,\mathrm{mm}^2$, 100 µm cell pitch). **Right:** Simulated trigger probability of FAMOUS for vertical air showers with different distances to the telescope R_p and different energies E. Taken from reference [126].

Photons arriving at the aperture of one of the Auger fluorescence telescopes are transferred to a custom-made detector simulation of FAMOUS realized within Geant4 (cf. section 4.3). In this simulation the optical axis of FAMOUS has the same orientation as the one of the fluorescence telescope, which is at 15° elevation. A visualization of the simulated FAMOUS telescope is shown in figure 5.2 (left). The simulation of the photosensors is realized with G4SiPM which has been discussed in section 4.3.
Aside from the signals which the SiPMs generate when they detect fluorescence photons, they also generate noise. This noise includes the intrinsic noise of the SiPM, as well as a response of the sensors to photons from the continuously luminous night-sky. The intrinsic noise of the SiPM has been measured in the laboratory. The measurement of the night-sky photon flux will be described in detail in the following chapters. To obtain an early, and thus preliminary evaluation of the optical design of FAMOUS, the night-sky photon flux has been determined with a tentative experimental setup and analysis routine. The result has been the upper limit $\phi^{\mathrm{UV}}_{\mathrm{max}}$ of the photon flux in the 300 nm to 400 nm band measured in a rural environment close to Aachen, Germany. This limit $\phi^{\mathrm{UV}}_{\mathrm{max}} = 1.9 \cdot 10^{12}\,\mathrm{photons\,m^{-2}\,s^{-1}\,sr^{-1}}$, as well as its measurement and the associated analysis have been reported in reference [104].

FAMOUS has an aperture area of $A \approx \pi \cdot (550\,\mathrm{mm}/2)^2 = 0.24\,\mathrm{m}^2$. The field of view per pixel of 1.5° defines the solid angle of a single pixel of $\Omega = 4\pi{\cdot}\sin^2(1.5°/4) \approx 5.4{\cdot}10^{-4}\,\mathrm{sr}$. Thus, the maximum number of night-sky photons arriving at the aperture from a region of the sky seen by a single pixel is given by $\phi_1 = A{\cdot}\Omega{\cdot}\phi^{\mathrm{UV}}_{\mathrm{max}} \approx 2.4{\cdot}10^8\,\mathrm{s}^{-1}$. The combined transmission efficiency of Fresnel lens and Winston cone is about 45%. With a transmittance of the UV filter of about 85% and a photon detection efficiency

of the SiPMs of about 30%, the SiPMs of a single camera pixel have a night-sky photon detection rate of about $0.45 \cdot 0.85 \cdot 0.30 \cdot \phi_1 \approx 30\,\mathrm{MHz}$. Not included is correlated noise due to the detection of night-sky photons. At an over-voltage of 1.3 V the SiPMs have optical crosstalk and afterpulse probabilities of about 25% each. We will not include the optical crosstalk since it happens instantaneously to the cell breakdown which triggers it. Thus, it does not add new pulses to the output signal of the SiPM but increases the level of certain already existent pulses. Therefore, it will not affect a trigger rate primarily. The trigger rate at a 0.5 p.e. level due to night-sky photons and associated correlated noise is thus very roughly 40 MHz. For comparison, the tigger rate of the four SiPMs of a single camera pixel due to intrinsic SiPM noise at room temperature, also at a level of 0.5 p.e., is about $4 \cdot 8\,\mathrm{MHz} = 32\,\mathrm{MHz}$.

Of course this was just an estimate with very simplified assumptions. The simulation of FAMOUS determines not only the noise in a much more sophisticated way, but also the signal-photons from air showers detected by the photosensors. It accounts for reflection and absorption processes which might occur, and it includes the dependencies on the wavelength of all relevant parameters. Furthermore, the response of the SiPMs is realized in a complex and advanced way. Results of these simulations are given in figure 5.10 (right). The dependence of the trigger probability of FAMOUS on the distance of the telescope to the air shower and on the energy of the shower is shown. This trigger probability should be considered as a benchmark quantity. A trigger will be generated if the simulated amplitude of the output signal of the SiPMs in one pixel exceeds a certain threshold above the simulated noise level. For the simulation results shown in figure 5.10 a threshold of approximately 10 p.e. (p.e. = photon-equivalent) was applied. The simulation uses the limit of the night-sky photon flux $\phi_{\mathrm{max}}^{\mathrm{UV}}$ and the noise rates of SiPMs as measured in reference [105]. With these input parameters vertical air showers with for instance an energy of $E = 10^{18}\,\mathrm{eV}$ can be detected at full efficiency up to a distance of 6 km. But let us keep in mind, that the trigger probability does not include effects associated with any of the electronics of the telescope, and that it acts only on a single pixel base.

Regarding the results shown in figure 5.10 the sensitivity of the telescope can be increased not only by higher photon detection efficiencies of the SiPMs or higher transmittance/lower absorption of the components of FAMOUS, but also by a darker observational site and reduced intrinsic noise rates of the SiPMs. The latter can be achieved by employing the latest SiPM types or by cooling the photosensors.

The optical performance of large aperture fluorescence telescopes which feature the FAMOUS technology has been studied in the scope of reference [143] by means of simulations. As the imaging quality of a Fresnel lens becomes worse with an increasing diameter ($r_{90} \approx 25\,\mathrm{mm}$ for an optimized lens with a diameter of 2 m), a reflecting design is favored, and reference [143] presents a Schmidt telescope (cf. section 3.2) for an SiPM-based camera which features an optimized and custom Fresnel corrector plate. This telescope has a diameter of 2.2 m and r_{90} is estimated to 8 mm. With the

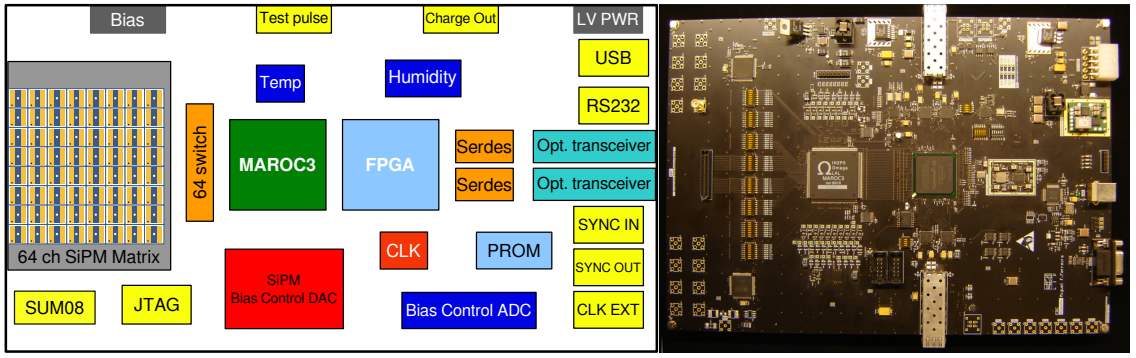

Figure 5.11: Layout and photo of the front-end electronics of FAMOUS. (LV PWR: low voltage power input – MAROC3, FPGA: see text – SERDES: serializer/deserializer – SUM08: analog sum outputs – JTAG: joint test action group (test port) – CLK: internal clock – PROM: programmable read only memory – CLK EXT: external clock) – Temp: Temperature – DAC: digital-to-analog-converter). Layout reprinted from reference [129].

small size of SiPMs compared to conventional photomultiplier tubes smaller fields of view per pixel, and thus, higher spatial resolutions can be achieved. Successive studies can answer the question whether SiPM-based cameras can consequently lead to improved reconstructions of air shower parameters.
A different question to be investigated by successive studies is whether a multitude of small aperture telescopes which feature the FAMOUS technology are an appropriate alternative to a large aperture fluorescence telescope.

5.3 Readout electronics

With 64 pixels and a total field of view of about 12°, FAMOUS is a very small fluorescence telescope. Since possible successors are expected to feature larger cameras with a significantly increased number of pixels, the readout electronics of FAMOUS follows a modular design, which allows easy extension of the number of readout channels. The front-end electronics of FAMOUS provide this modularity as will be described below. A front-end board which handles 64 input channels is referred to as Elementary Readout Cell (ERC) and has been developed at the Laboratório de Instrumentação e Física Experimental de Partículas (LIP), Lisbon, Portugal.
To avoid long wiring between the photosensors and the front-end electronics, and to avoid the related increased noise pickup, the electronics aim at an early digitization. A base printed circuit board which carries the SiPMs can be piggyback connected to the ERC using a high-speed and high-density SEARAY pin array connector. The summed signals of each four SiPMs, which constitute a single camera pixel, are then digitized by a MAROC3 chip [144] (see footnote[12] for meanings of technical abbreviations in this section). The MAROC3 is a 64 channels readout ASIC with a power

[12]MAROC = Multi-Anode ReadOut Chip, ASIC = Application-Specific Integrated Circuit, DAC = Digital-to-Analog Converter, ADC = Analog-to-Digital Converter, FPGA = Field Programmable Gate Array, DAQ = Data AcQuisition

consumption of 3.5 mW per channel. It provides one low-impedance amplifier with adjustable gain per channel which features different pulse shapers. Two thresholds per channel are defined by in-core DACs. The signals are digitized by Wilkinson ADCs. In addition to its digital signals, the MAROC3 outputs eight configurable analog sums of up to eight input channels per sum signal.
The serial data stream of the MAROC3, as well as the trigger information are relayed to an Altera Cyclone III [145] FPGA which handles digital functions. These functions include a trigger algorithm to decide whether the received signals might be due to the detection of an air shower or should be rejected as a noise event. The FPGA also receives signals from temperature and humidity sensors and is able to adjust the 64 bias voltages individually according to changes of the temperature.
The ERC can be connected to the off-detector DAQ electronics by an optical link at 3.125 Gbps maximum transmission rate. The off-detector electronics can implement further trigger levels and connect more than one ERC, if more than 64 readout channels are desired. The layout of the ERC and a photo are shown in figure 5.11. For further information on the electronics of FAMOUS please refer to reference [146].

5.4 Current status

The Elementary Readout Cell discussed in the last section has been recently manufactured and is currently in the stage of firmware programming and testing. To perform tests of the prototype telescope already before its completion, a seven pixel camera of FAMOUS has been built. Photos of the telescope are given in figure 5.12. The camera (together with the aluminium backplane of the telescope) can be replaced later by the 64 pixel camera. Unlike the original FAMOUS design, the seven pixel camera outputs not the summed signal of the four SiPMs of one pixel, but the four individual signals. This ensures a more detailed evaluation of the pixel design in this early phase. The signals can be summed in the off-camera electronics.

The output currents of the SiPMs are amplified by a one-stage transimpedance amplifier with a gain of 0.5 mV/µA. The amplified signals are summed by two identical custom-made linear FAN-IN/OUTs. They are realized in the VME standard, and each one features four independent sections, each of them with four inputs accepting SiPM pulses with negative polarity, four outputs providing the input signals 1:1, and two outputs providing the sum of the four inputs. The seven summed signals of the seven camera pixels are then relayed to a 16 channel CAEN V965 QDC (Charge-to-Digital Converter). According to the choice of a specific evaluation measurement the signals can alternatively be connected to an oscilloscope or a four channel CAEN V1729 FADC (Flash Analog-to-Digital Converter).
The amplifier as well as temperature sensors are mounted on printed circuit boards inside the camera close to the SiPMs (cf. figure 5.12). To keep the over-voltage of the SiPMs constant, microcontrollers which are housed in a custom-made NIM module communicate with the temperature sensors and provide the appropriate bias voltage to the SiPMs. The NIM module also supplies the amplifiers and temperature sensors with their bias voltages.
Test measurements have confirmed the single photon resolution of the individual

Figure 5.12: Photos of FAMOUS (preliminary design with a seven pixel camera). **Top left:** Telescope on an altitude-azimuth mount. View on the aperture with the Fresnel lens. **Top right:** Small focal plane array with seven Winston cones. **Middle:** Mounting of the seven pixel camera. The SiPMs (not visible) are soldered onto the green printed circuit board (PCB). **Bottom left:** Camera compartment with detached cylindrical housing. The vertically orientated PCB carries the SiPMs and the temperature sensors. The piggyback connected PCBs hold the amplifiers (up to eight channels per PCB). Each SiPM has its own output channel (7 x 4 channels, gray cables and small connectors, signals of one camera pixel are not summed up at the focal plane electronics). Communication and bias voltages are provided via the big connectors and the colored cables. **Bottom right:** View onto the seven pixel camera. At the exit apertures of the Winston cones the UV band-pass filters are mounted in front of the SiPMs (not visible).

SiPMs with this preliminary setup [126], thus, providing a determination of the combined gain of SiPMs and electronics to calibrate the setup.

The usage of a Raspberry Pi mini computer for the data acquisition of FAMOUS has been presented in reference [147]. It runs a Debian GNU/Linux 7.1 operating system and is connected to the readout electronics via USB and to the network via LAN/WLAN. The mini computer hosts a web server, which allows to operate the readout electronics remotely via a web interface. With this web interface also the acquired data can be accessed. Reference [147] also presents the use of an Arduino microcontroller to operate a GPS receiver and run sensors for the measurements of ambient light, temperature, pressure, and humidity. The Arduino board is connected to the computer via USB.

The seven pixel version of FAMOUS has been commissioned recently. First measurements are presented in reference [148]. Even though the actual camera with its $\sim 4.5°$ total field of view is still too small to be used for the detection of extended air showers in a meaningful way, the seven pixel version of FAMOUS can already be used to measure passages of stars and measure the night-sky photon flux in the same way as described in the following chapters.

In parallel to the development and construction of FAMOUS, a telescope instrumented with a single FAMOUS-like pixel has been established to perform photometric measurements of the night-sky brightness. This photometer will be discussed in the next chapter. But prior to this the following excursus will briefly discuss the application of SiPMs in a field of astroparticle physics different from the fluorescence detection of ultra-high-energy cosmic rays.
Although FAMOUS is generally able to detect direct and scattered Cherenkov light from air showers, its rather large field of view per pixel is essentially intended for the detection of fluorescence light from showers which are typically observed more or less from the side. This large field of view per pixel leads to large uncertainties in the reconstruction of the arrival direction of an air shower if predominantly its direct Cherenkov light is observed.
Telescopes used for the imaging air Cherenkov technique typically feature higher spatial resolutions than fluorescence telescopes. With FACT the first SiPM-based imaging air Cherenkov telescope has started operation in γ-ray astronomy.

5.5 Excursus: FACT - First G-APD Cherenkov Telescope

FACT [149] is the first telescope applying SiPMs in an imaging air Cherenkov telescope (cf. section 2.4). It is shown in the left photo of figure 5.13. FACT uses the refurbished HEGRA CT3 telescope [151] and is mounted close to the MAGIC [152] telescopes on the Roque de los Muchachos on La Palma, Canary Islands, Spain. It started its operation in October 2011.

The mirror of FACT has a diameter of $D \approx 3.5\,\mathrm{m}$ and a focal length of $f \approx 4.9\,\mathrm{m}$. The camera consists of 1440 pixels, each with a field of view of $0.11°$ leading to a

Figure 5.13: **Left:** Photo of the FACT telescope at the Observatorio del Roque de los Muchachos on La Palma, Canary Islands, Spain. **Right:** Photo of the assembled sensor compartment of FACT. From bottom to top: the front flange with the entrance window, the Winston cones, the SiPMs (white packaging), the printed circuit boards (green) for the co-axial cables (white), and the insulation plate. The black connectors on top are for the signals of the SiPMs, the three-pole cables (white-black-orange) for the bias supply. Other colored cables (yellow-purple and red-green-white) connect the temperature and humidity sensors. Both photos taken from reference [149].

total field of view of 4.5°.
A single pixel consists of a Hamamatsu S10362-33-50C SiPM and a solid Winston cone.[13] The SiPM has an active area of $3\times3\,\mathrm{mm}^2$ and 3600 cells with a pitch of 50 µm. The Winston cone is made from UV-transparent PMMA by injection molding, featuring a hexagonal entrance aperture with its parallel sides being at a distance of 9.5 mm. The exit aperture is quadratic to fit the shape of the photosensor and has an area of $2.8\times2.8\,\mathrm{mm}^2$. In contrast to the light concentrators discussed in section 5.1, the shape of the reflecting surface of the one used for FACT is not a tilted parabola, but a non-tilted one. This design leads to higher light transmission efficiencies for a solid Winston cone (see e.g. figure 4.2.5 in reference [118]). The length of the cones used for FACT is $l = 20\,\mathrm{mm}$.
The light concentrators are glued to the SiPMs by a two-component glue which matches the refractive index of the entrance windows of the SiPMs. On the opposite side they are glued to the entrance window of the camera which is also made from PMMA.

The camera pixels are arranged in groups of nine pixels. The signals of the SiPMs are amplified by amplifiers with a gain of $0.45\,\mathrm{mV/\mu A}$. The sum of the signals of the nine pixels is processed to a trigger board, whereas the individual signals are relayed to 160 DRS4 ring-sampling chips which feature nine input channels each. A DRS4 chip continuously stores data in a ring buffer until a trigger is received. With the reception of a trigger in standard data taking mode, the chip is set to have 300

[13] The design of the light concentrator described here is not the original Winston cone design, since it makes use of a non-tilted parabola as the reflecting surface. However, we will call this light concentrator also Winston cone.

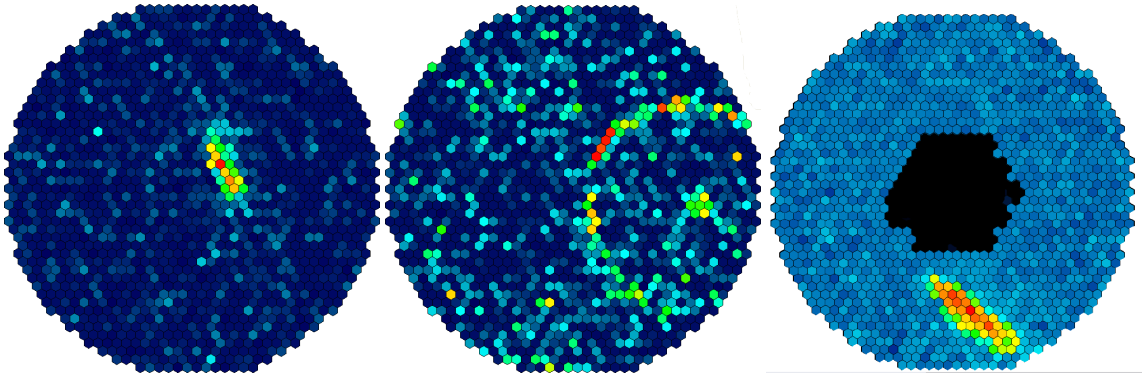

Figure 5.14: Shower images recorded with FACT. Each hexagon corresponds to one of the 1440 camera pixels. The different colors denote the amplitudes of the signals within the pixels from dark blue (low) to red (high). **Left:** Example of a gamma event candidate. **Middle:** Example of a muon event. See text for details. Both taken from reference [149]. **Right:** An event which was recorded while the telescope tracked the full Moon on June 23, 2013. The power for the central pixels (black) was disabled. Taken from reference [150].

values being read out at a sampling frequency of 2 GHz. FACT shows single photon resolution and has a total time jitter between different channels of about 600 ps.

Each group of nine pixels is again arranged in two groups of four and five pixels. The SiPMs of these groups share the same bias voltage provided by 320 bias voltage channels. To have a minimum variation of characteristics of SiPMs within one group, the sensors have been sorted according to their recommended operating voltage. The bias voltages of the individual channels is regulated according to changes in the temperature at the SiPMs and according to changes of the output current of the photosensors. Both quantities are monitored by the electronics of the FACT camera.

The FACT collaboration has reported first air shower event candidates. A gamma air shower candidate is shown in figure 5.14 (left). Also shown in this figure (middle) is a muon event. Muon events are due to single muons of air showers induced by cosmic rays. Especially striking is the ring-shaped signal structure caused by a narrow Cherenkov light cone. Muon events can be used to study the time jitter between the readout channels of individual camera pixels. The collaboration has also reported on the long term stability of the photosensors and their use during nights with strong moonlight [150]. It was even possible to detect air shower events while the telescope was tracking the full Moon. A corresponding event display is given in figure 5.14 (right). However, the central pixels, which had the Moon in their fields of view, have been turned off.

The facts presented in this section have been obtained from reference [149]. Please consider this reference for further information on FACT.

6. The Night-Sky Photometer

In this chapter we will discuss the motivation for the measurement of the night-sky brightness, the basic principle to determine this quantity from SiPM-based observations, and the experimental setup to which we refer to as the night-sky photometer (NSPM). The presented setup as well as the raw data acquired with this setup are the same as presented by my colleague R. Meißner in her Bachelor thesis *Brightness Measurements of Stars and the Night-Sky with a Silicon-Photomultiplier-Telescope* given as reference [153]. The corresponding measurements have been performed by R. Meißner and me.

The night-sky brightness (NSB) is a generic term for the photon flux originating from celestial light sources being observed during night.
For most urban environments it is dominated by light of bright stars[1] and a diffuse background mainly due to light pollution. Depending on its phase and relative position the Moon can also contribute strongly to the NSB.
For observational sites where light pollution becomes less important, the most intense contribution to the diffuse background is airglow.[2] Airglow-photons are caused by the de-excitation of atoms and molecules in the upper atmosphere which have been excited beforehand by solar UV radiation. From its high orbit, the International Space Station (ISS) offers a spectacular view on the airglow. A photo taken from aboard of the ISS is shown in figure 6.1. The airglow is well-visible as the glowing band above the horizon.
A further contribution to the NSB is the zodiacal light which is sunlight scattered by interplanetary dust. This dust is essentially located along the ecliptic plane. Thus, at Earth the scattered light is predominantly visible in the zodiac, which is the region around the ecliptic with a spread of about 20°. Under good conditions the zodiacal light is visible to the naked eye soon after sunset and soon before sunrise. In addition, it can be observed in anti-sun direction where it is called *Gegenschein* (German for "counter shine"). A photo of the zodiacal light observed after sunset is shown in figure 6.2.
A small contribution to the diffuse NSB is also due to starlight of faint stars between the bright ones. Their light is scattered by interstellar dust along the galactic plane and produces a weak glow, similar to the zodiacal light. Even weaker is the NSB due to extra-galactic light.
For observational sites with a latitude whose absolute value exceeds 40° also auroral

[1] and other bright objects, e.g. planets

[2] For a classification of sources of the NSB according to their intensity, and for a more detailed discussion of contributions to the NSB see for instance reference [156].

Figure 6.1: Photo of the slightly overcast Iberian peninsula facing towards east-north-east direction taken from the International Space Station. The picture was taken on December 4, 2011 by the Expedition 30 crew. In the center of the peninsula the location of Madrid is visible by the large, brightly lit area. The brightest area at the coast to the bottom of the picture is the Lisbon region. The diffuse glow of the higher regions of the atmosphere is the air glow. Picture credit: NASA/JSC [154]

light (i.e. light caused by the aurora borealis or the aurora australis also referred to as northern and southern lights, respectively) has to be taken into account [156].

The purpose of this work at hand is the determination of the NSB with a detector which applies a FAMOUS-like camera pixel design.
Since the diffuse glowing night-sky background defines the sensitivity of air shower measurements by means of the fluorescence detection technique, the knowledge of the nightly photon flux is crucial for the performance evaluation of the considered fluorescence telescope (cf. section 5.2).
Instead of providing a catalog of NSB data for various observational sites and times, or studying the light flux as a function of celestial coordinates, this work studies a method based on photon counting to determine the light flux of a continuous light source measured with SiPMs.

The measurements with the NSPM have been performed in parallel to the design and construction phases of FAMOUS. The NSB could also have been measured with a light sensor different from an SiPM, but for three reasons the SiPM is the detector of choice. The first reason is the benefit of simplicity: The question which has to be answered is how many NSB photons a camera pixel detects. By applying a FAMOUS-like pixel to the NSPM, both FAMOUS and the NSPM have the same spectral acceptance. Imagine for an instant two different acceptances. To give an answer to our question we would need to unfold the spectral acceptance of the NSPM from the measured photon flux of the night-sky. This procedure would require the measurement of the spectrally resolved irradiance of the night-sky. Afterwards, the unfolded photon flux would have to be folded with the spectral acceptance of

Figure 6.2: Photo of the zodiacal light observed at Roque de las Muchachos Observatory, La Palma, Canary Islands, Spain. The zodiacal light is visible as the wedge-shaped glow spreading from the center of the picture to the upper left corner. The photo was taken on the evening of June 27, 2011. By courtesy of Alex Cherney [155].

FAMOUS. The use of identical acceptances simplifies the experimental and analytic procedures significantly.
The second reason is the re-usability of the applied method to determine the photon flux of the night-sky: at the corresponding time FAMOUS has not yet been constructed, and therefore could not be have been used for the measurements. Nevertheless, the analysis of the NSPM data has always been intended to be applicable to FAMOUS data with as few modifications as possible.
The third reason is less of a practical nature: A reliable reconstruction of the photon flux measured with SiPMs requires a deeper understanding of the behavior and characteristics of this kind of photosensor. Thus, cross-checks of results of the photon counting technique with independent measurements, as well as the comparison of the reconstructed photon flux from well-known stars with their literature values can reveal whether our understanding of SiPMs is correct. This demand on the experimental challenge excludes the use of a reference sensor to calibrate the SiPM as discussed for instance in section 4.2. By means of the photon counting technique, exclusively the SiPM itself shall answer our purpose.

6.1 Basic principle of photon counting and light flux reconstruction

A major role in the reconstruction of light fluxes measured with SiPMs is the correction of the response of the photosensor for cell breakdowns due to thermal and correlated noise.
The correction for thermal noise can be performed by means of *dark measurements*: In addition to the main measurement a second measurement is performed where

the SiPM is operated in darkness. This measurement only includes cell breakdowns due to thermal noise as well as the subsequent correlated noise. If the over-voltage and the temperature do not differ between the main measurement and the one performed in darkness, the latter can be subtracted from the former. The remaining cell breakdowns are due to signal-photons and their subsequent correlated noise.

The correction for correlated noise can often be performed by means of photon counting.[3] Photon counting can be performed in different ways. In section 4.2 we discussed the measurement of SiPM signals with a charge-to-digital converter (QDC) resulting in a charge spectrum (cf. figure 4.6). Each event in such a charge spectrum is a single measurement of the charge flowing into the input of the QDC during a user-specific gate time t_{QDC}.
Due to the single photon resolution of an SiPM, the charge spectrum can be directly used to determine the level of the 1 p.e. standard signal (p.e. = photon-equivalent) if the light flux is low enough to acquire a sufficient number of 1 p.e. signals. This can be used to calibrate the measurement and calculate the amount of photon-equivalents from the charge. Thus, we can now refer to the spectrum as a *photon-equivalent spectrum* (cf. figure 6.3). The total number of cell breakdowns within it is given by $N_{\mathrm{bd}} = \sum_{i=1}^{\infty} i \cdot N_i$, where N_i is the number of events in the ith p.e. peak. For an ideal SiPM with no noise the number of cell breakdowns equals the number of detected photons. For a real SiPM this number equals the number of photon-equivalents. Also signals with amplitudes smaller than the 1 p.e. signal can appear due to the reduced output caused by avalanches occurring during the recharge process of the corresponding cells.
The mean number of cell breakdowns per time t_{QDC} is given by the mean of the spectrum. But these cell breakdowns include the ones due to correlated noise. A correction for the noise can be performed by calculating the mean of the spectrum which would have been measured if the SiPM would have been an ideal device. We will discuss this procedure now in more detail.

Let us assume an ideal SiPM being operated in total darkness. This device features neither thermal noise nor correlated noise and has no dead time. We illuminate this SiPM with a pulsed light source. The duty cycle of the light source is low enough that the SiPM is fully recharged before the next light pulse occurs. Also the time between two pulses is much greater than the time constant of slow afterpulsing $\tau_{\mathrm{AP,s}}$.[4] The optical output of the light source is low enough that for some light pulses the SiPM does not detect any photons. In addition, the photons generated by the light source are distributed uniformly within the duration of a pulse. Furthermore, effects

[3] Technically speaking the expression *photon counting* is not always correct since in many photon counting applications not only photons are counted but also cell breakdowns due to noise. Since these breakdowns can look exactly like being caused by a signal-photon, the term *photon-equivalent counting* would be more correctly. However, since the method which will be applied to the data finally yields the number of signal-photons, we retain the expression photon counting.

[4] Apparently an ideal SiPM does not feature afterpulsing. Hence, assigning a time constant to afterpulses, which happen with the probability of zero, does not seem very convenient. However, we will need this time constant in the further course of the discussion when we will consider an SiPM which produces afterpulses.

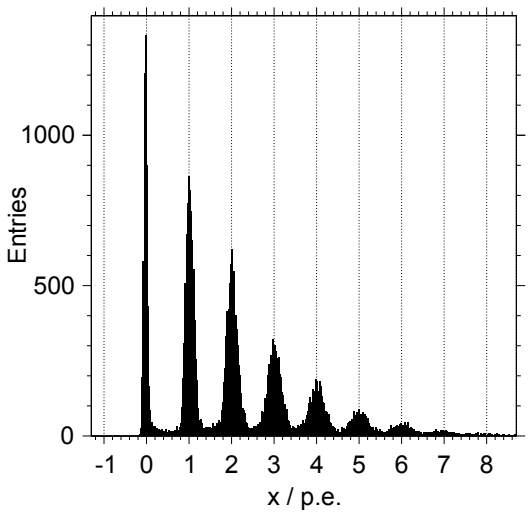

Figure 6.3: A photon-equivalent spectrum. The data are the same as shown in figure 4.6 (right), but the x-axis is expressed in photon-equivalents (p.e.).

due to saturation of the SiPM are negligible. The response of the SiPM is measured appropriately to result in a photon-equivalent spectrum assuring that the number of events in the spectrum equals the number of light pulses. For illustrative reasons a spectrum similar to the one discussed is shown in figure 6.3, though the applied SiPM is apparently not an ideal SiPM.
For the ideal SiPM, which features exclusively cell-breakdowns due to signal-photons with signal amplitudes at the 1 p.e. level, the events in the spectrum are Poissonian distributed. Their photon-equivalent values are given by x. The corresponding probability mass function[5] of the random variable *measured photon-equivalent per light pulse* X is thus given by

$$P_\mu(X = x) = \frac{\mu^x}{x!} \exp(-\mu) . \tag{6.1}$$

The mean of the distribution μ can be calculated from any probability to measure a certain outcome of the random experiment $P_\mu(0)$, $P_\mu(1)$, $P_\mu(2)$, etc. Here we will use the probability that no photon has been detected

$$P_\mu(0) = \exp(-\mu) = \frac{N_{\text{ped}}}{N_{\text{tot}}} \tag{6.2}$$

where N_{ped} is the number of events where no photon has been detected (i.e. the pedestal events) and N_{tot} is the total number of events in the spectrum. The mean is thus given by

$$\mu = -\ln\left(\frac{N_{\text{ped}}}{N_{\text{tot}}}\right) \tag{6.3}$$

[5]For the ideal SiPM x is an integer. Thus, P_μ is no probability density function but the discrete analogon which is referred to as probability mass function.

and its statistical uncertainty is given by the binomial error to

$$\sigma_\mu = \frac{1}{N_{\text{tot}}} \sqrt{N_{\text{tot}} \cdot P_\mu(0) \cdot (1 - P_\mu(0))} \tag{6.4}$$

since we only distinguish whether an event is a pedestal event or not.

Now let us assume that the SiPM features correlated noise but no thermal noise. The measurement is identical to the yet discussed one, and we assure to have the same number of light pulses ($= N_{\text{tot}}$). If the SiPM detects at least one photon, optical crosstalk and afterpulses will occur with certain probabilities depending on the over-voltage of the photosensor. The acquired spectrum will thus be different from the one of the ideal SiPM since the mean will be shifted to a higher value. How far it will be shifted depends on the actual probabilities of correlated noise.
However, if the SiPM *does not* detect a photon during a light pulse, no correlated noise will occur. This leads to the same number of pedestal entries N_{ped} as for the case with the ideal SiPM. Here the assumption that the time between two light pulses is much larger than the time constant of slow afterpulses $\tau_{\text{AP,s}}$ is of relevance. Without it we might detect an afterpulse from the previous light pulse which could lead to a decrease of N_{ped}.
We see, although the SiPM outputs signals due to correlated noise, the calculation of μ by means of equation (6.3) yields the mean number of detected signal-photons per light pulse under certain assumptions. Deviations from these assumptions lead to systematic biases which can be corrected by means of a calibration if the number of signal-photons is known. Such a calibration will be discussed and performed later in section 7.5.

Now let us assume that the SiPM also features thermal noise. As mentioned in the beginning of this section we can perform a measurement in darkness simply by turning off the light source but measuring the output of the SiPM exactly as before. The recorded spectrum will contain $N_{\text{tot}}^{\text{dark}}$ events with $N_{\text{ped}}^{\text{dark}}$ pedestal entries. The mean number of cell breakdowns due to thermal noise per measurement time t_{meas} is given by

$$\mu^{\text{dark}} = -\ln\left(\frac{N_{\text{ped}}^{\text{dark}}}{N_{\text{tot}}^{\text{dark}}}\right), \tag{6.5}$$

thus, the number of detected photons per light pulse for the SiPM which features thermal and correlated noise is

$$\tilde{\mu} = \mu - \mu^{\text{dark}} = -\ln\left(\frac{N_{\text{ped}}}{N_{\text{tot}}}\right) + \ln\left(\frac{N_{\text{ped}}^{\text{dark}}}{N_{\text{tot}}^{\text{dark}}}\right). \tag{6.6}$$

The mentioned measuring time t_{meas} is the time during which the data acquisition system records the signals. It has to be short enough to assure that there are pedestal events. If the value of t_{meas} is chosen too high, there will always be pulses due to thermal noise within the considered time. t_{meas} has to be the same for both measurements, the one with the light source turned on and the one with the light

source turned off. Otherwise equation (6.6) must not be applied. In the case of our measurement device being a QDC as discussed above, t_{meas} would equal t_{QDC}.

In fact, the described method does not even require the knowledge of the spectrum to determine μ. For each of the N_{tot} events the only information which is needed is whether the SiPM outputs a pulse or not.

Basically the same procedure can be performed also for a continuous light source. It can be considered as a pulsed one with a duty cycle of 100%. The only difference is that $\tilde{\mu}$ is no longer the mean number of detected photons per t_{meas} but also contains afterpulses. This is due to the fact that the requirement for a time between two light pulses being much larger than the time constant of slow afterpulsing $\tau_{\mathrm{AP,s}}$ is violated.
To correct $\tilde{\mu}$ for afterpulses we can calculate the mean number of afterpulses from the afterpulse probability P_{AP}. This requires the knowledge of the actual over-voltage, which was not required so far. Furthermore, also the knowledge of the probability of optical crosstalk P_{OXT} has to be taken into account. Indeed, $\tilde{\mu}$ does not contain cell breakdowns due to optical crosstalk, though there have been some occurring in the SiPM. These breakdowns have also caused afterpulses, and not just the ones caused by signal-photons.[6]

To account for a realistic SiPM also effects related to the dead time of the SiPM should be considered. Furthermore, effects due to the recovery time, the limited dynamic range of the SiPM, and the non-linear response beyond a certain photon flux could also lead to an underestimated result of $\tilde{\mu}$. All these effects will be studied in detail in chapter 7.
Another feature of the analysis method is that the temperature is a quantity which does not have to be known. However, it has to be constant while measuring μ and μ^{dark}. All we need to know is the actual over-voltage V_{ov}, which can be determined from a gain measurement. As we have seen in chapter 4 the gain plotted as a function of the over-voltage does not depend on the temperature (cf. figure 4.8).

The procedure outlined in this section will be performed on data in the next chapter.

6.2 Measurement setup

The NSPM consists of a commercial Newton reflector with a single FAMOUS-like pixel mounted instead of an eye-piece. The signals of the SiPM are acquired by a commercial analog-to-digital converter.
The following list gives a short summary of the individual components. Some of them have already been discussed in the previous chapters. Additional information is given in the text below the list.

[6] Afterpulses initiated by cell breakdowns due to thermal noise are removed from $\tilde{\mu}$ by equation (6.6).

Bresser Messier PN-203 203/800
The commercial Newton reflector manufactured by Meade Europe/Bresser has an aperture diameter of $D = 203\,\text{mm}$ and a focal length of $f = 800\,\text{mm}$. The semi-minor axis of the secondary mirror has a diameter of 70 mm. The focuser features a 1:10 micro transmission. The PN-203 is mounted on an LXD-75 GoTo which includes an equatorial mount, a tripod, servomotors, a hand-held GoTo Computer, and a polar alignment finder. Picture credit: Meade Europe/Bresser [157]

UV band-pass filter
The filter is made from the same glass as the ones used for FAMOUS, i.e. Schott UG 11 (cf. section 5.1). It has a thickness of 1 mm and a diameter of 1.25 inch.

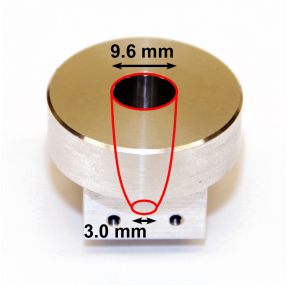

Winston cone
A round, hollow Winston cone as discussed in section 5.1. The entrance aperture has a diameter of $(9.6 \pm 0.3)\,\text{mm}$, the exit aperture has a diameter of $(3.0 \pm 0.1)\,\text{mm}$. The reflecting surface is made from polished aluminium. The aluminium has a diameter of 1.25 inch at its upper end, to fit into the focuser of the PN-203.

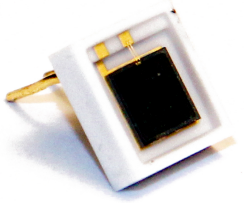

Silicon photomultiplier (SiPM)
Hamamatsu S10362-33-100C SiPM — it has a sensitive area of $3{\times}3\,\text{mm}^2$ and a cell pitch of 100 µm. Its characteristics are the same as for a single channel of the S10985-100C SiPM used for FAMOUS. See table 5.1 for specifications.

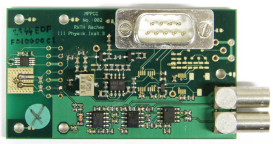

Transimpedance amplifier
Charge sensitive three-stage SiPM amplifier prototype (PCB revision 902) developed at III. Phys. Inst., RWTH Aachen University by F. Beißel. Two analog output channels INT and FAST feature gains of 6.7 V/mA and 2.9 V/mA, respectively. Fixed operating voltage of SiPM, adjustable by potentiometer.

CAEN ADC V1729
Analog-to-digital converter (ADC) manufactured by CAEN. 4 channels, 12 bit resolution, 1 or 2 GS/s sampling frequency, 300 MHz bandwidth, ±0.5 V full scale range, 2520 usable sampled points. Picture credit: CAEN S.p.A. [158]

LeCroy Wavejet 354A Oscilloscope
Digital oscilloscope manufactured by Teledyne LeCroy. 4 channels, 8 bit resolution, 1 GS/s sampling frequency (2 GS/s interleaved), 500 MHz bandwidth. Picture credit: Teledyne LeCroy [159]

A photo and a schematic view of the complete NSPM are shown in figures 6.4 and 6.5, respectively. The SiPM is mounted at the exit aperture of the Winston cone. The amplifier is directly attached to the SiPM and housed in an aluminium box to shield it from radio interference. These components form a firm unit to which we refer to as the camera. The Winston cone of the camera can be mounted at the focuser of the telescope. With a distance of 26.5 mm the UV band-pass filter can be attached in front of the entrance aperture of the Winston cone. This distance is fix, since the filter will move in the same manner as the camera if the focuser is adjusted.

The amplifier is an early version prototype of the front-end electronics used for the seven pixel version of FAMOUS (cf. section 5.4). Some solder pads of the printed circuit board are not populated since the board and the connector are already designed for follow-up versions of the amplifier. These versions[7] also feature a third output channel with a comparator generating NIM output signals, as well as an active regulation of the bias voltage of the SiPM. This regulation is performed by a microcontroller receiving data from a temperature sensor mounted close to the SiPM. In the version used for the NSPM the bias voltage can be adjusted by a potentiometer. The amplifier receives an operating voltage of +80 V to bias the SiPM, as well as +5 V and -5 V to bias the amplifier circuits. The voltages are provided by a voltage source integrated into a custom-made NIM module especially designed for the amplifier.
In this work only signals of the FAST output channel are used. This channel has been designed initially for timing measurements, whereas the integrating channel INT has been intended for energy measurements. The outputs of both channels are AC coupled.

[7] none of them is the one of FAMOUS, for FAMOUS a different printed circuit board layout is used

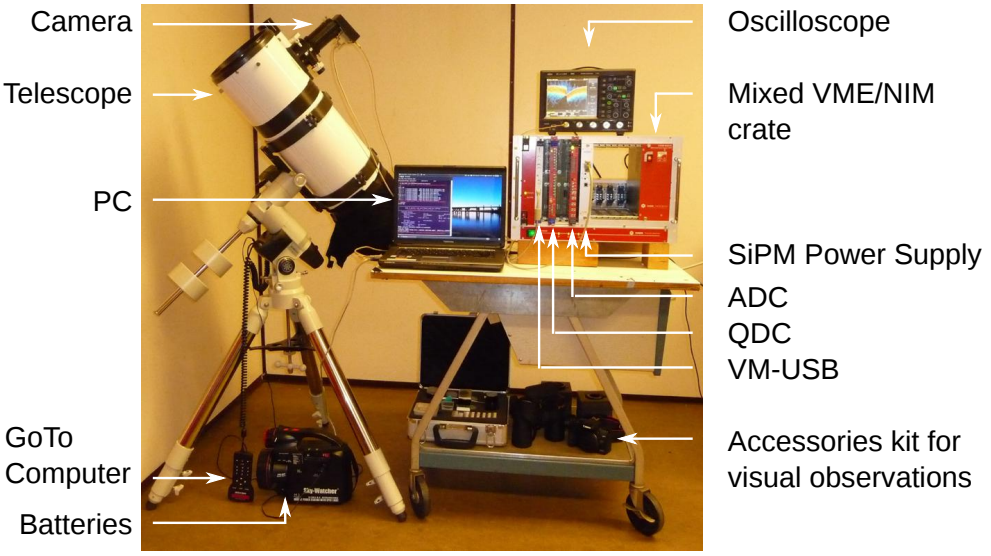

Figure 6.4: Photo of the complete measurement setup. (The QDC is not required for the measurements of the night-sky brightness.)

As we will see in the next chapter, a great benefit of the applied photon counting method is that it can be performed with signals processed by such very rudimentary front-end electronics.

The amplified signals of the SiPM are recorded by the V1729 ADC. Its analog input is continuously sampled in a circular memory which can store 2520 valid values. Once the ADC receives a trigger these values are read, digitized with 12 bits, and stored in a digital memory buffer. Unluckily the programming of the ADC has a bug. The starting point of the recorded voltage trace is randomly placed within the digitized data. A temporary solution is to place the starting point at a defined position in the buffer, provided that the random trigger of the ADC is used. This solution leads to a reduced number of 2300 valid values.
All measurements in this work performed with the V1729 are randomly triggered and use a sampling frequency of 1 GS/s with a timing precision of 15 ps to result in lengths of the voltage traces of 2300 ns. A trigger is generated automatically after the readout and processing of the data of the preceding event.
The ADC is a VME module. It is accessed via the VME controller VM-USB manufactured by Wiener. Both devices as well as the power supply for the amplifier are placed in a NV8020 mixed VME/NIM crate manufactured by CAEN.

The V1729 as well as the digital oscilloscope are controlled from a PC using the LibLAB. The LibLAB is a library containing modules for various laboratory instruments which can be remotely accessed. It aims at offering its users an easy access to devices by an object-orientated C++ interface. The LibLAB is developed and maintained by D. Terhorst *et al.* No further reference can be given at this moment since the access to the LibLAB is currently restricted to members of the III. Phys. Inst., RWTH Aachen University. However, the developers aim at a prospective public access.

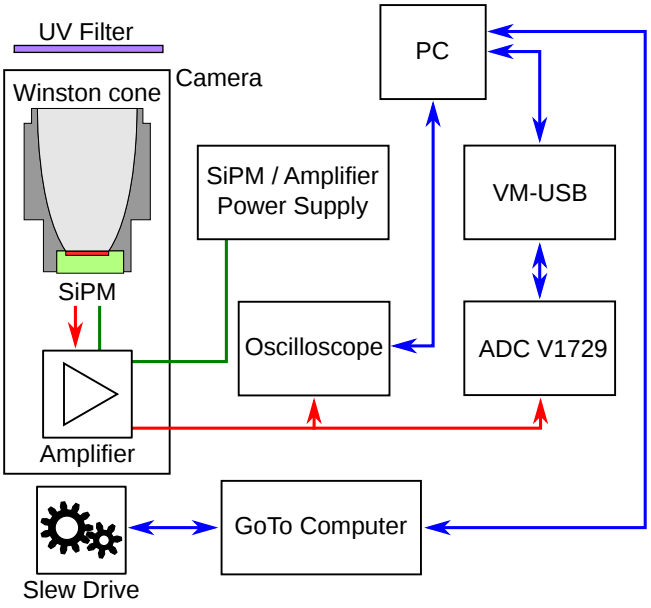

Figure 6.5: Schematic view of the night-sky photometer. The (amplified) signal of the SiPM is illustrated in red. For the measurements presented in this chapter it is provided to the oscilloscope. For the measurements presented in the following chapters it is provided to the V1729 ADC. Communication signals run along the blue connections. The green lines represent power lines to bias the SiPM and its amplifier.

The GoTo Computer of the PN-203 telescope can be accessed by the PC via the Instrument-Neutral-Distributed-Interface (INDI). INDI is an XML-like communications protocol for interactive and automated remote control of diverse instrumentation [160]. The INDI Library supports a variety of astronomical instruments, including the AutostarLX driver of the GoTo Computer of the PN-203. The open source library offers server software and C++ classes which have been used to program a custom-made client controlling the slew drive of the PN-203 and the data acquisition of the V1729 ADC or oscilloscope simultaneously.

During data acquisition pulses of radio interference are occasionally superpositioned to the signal. To assure an offline discrimination between this noise and SiPM pulses by means of a threshold scan, the bias voltage of the SiPM is adjusted to a rather high level, resulting in about 35 mV for a 1 p.e. signal.

For upcoming calculations we will need the optical efficiency of the PN-203 as well as the field of view of the NSPM. The optical efficiency of the PN-203 telescope is determined by measurements with a CMOS[8] active pixel sensor ($22.3 \times 14.9\,\mathrm{mm}^2$, ~19 Megapixel) behind a Bayer filter. A Bayer filter is a matrix of red, green, and blue filters on a squared grid. The filter pattern is 50% green, 25% red, and 25% blue. It is used to create a color image from photosensors which do not feature

[8] complementary metal-oxide-semiconductor

information on the wavelengths of the detected photons. The active pixel sensor is placed at a certain distance from a light source and measures the received intensity. The surface normal of the sensor is facing towards the light source. Measurements are performed (a) in a dark laboratory with a green LED (558 nm) behind a diffuser and a pin diaphragm at a distance of 22.3 m from the sensor and (b) in the field at night with the Moon acting as the light source ($\sim 70\%$ lit disc). In case (b) a cylindrical hood protects the sensor from being illuminated by terrestrial stray light. After the measurement of the intensity the telescope aperture is placed at the position where the active pixel sensor has been located, with the light source being along the optical axis of the PN-203. The active pixel sensor is mounted at the focuser of the telescope, and the image of the light source is located in the center of the sensor. By comparing the intensities measured by the sensor with the two different setups, and by taking the two different effective aperture areas (i.e. aperture area of the telescope and the size of the sensor) and the corresponding exposure times into account, the optical efficiency of the PN-203 is determined. The optical efficiency is given by the normalized intensity measured with the telescope divided by the normalized intensity measured directly by the sensor. The analysis is performed on the raw data of the sensor and a subtraction of dark counts is performed before the quotient of the two intensities is calculated. The dark counts are determined from masked pixels located at the border of the sensor. For sanity checks the measurements are performed for various exposure times, and in the case of the direct illumination of the active pixel sensor in experiment (a), the sensor is operated at various positions by shifting it parallel to its surface to check for inhomogeneities of the intensity. The measurements agree with each other within their uncertainties. The optical efficiency of the PN-203 is $\epsilon_{\mathrm{PN-203}} = 0.40 \pm 0.02$. The data acquired from experiment (b) are analyzed in the red, green, and blue channels individually. The efficiency is constant within the three channels.

In figure 6.6 (left) a schematic of a telescope is shown. For the sake of clarity a refractive design instead of a reflective one is displayed. The telescope is axially symmetric relating to its optical axis. The sensor in the figure, which is the entrance aperture of the Winston cone for the NSPM, is located in the focal plane of the lens. The diameter of the sensor is d_{sens}. Parallel light which enters the telescope with an angle of α_{max} with respect to the optical axis is just focused on the outermost region of the sensor. α_{max} is thus given by $\alpha_{\mathrm{max}} = \arctan\left(d_{\mathrm{sens}}/(2\,f)\right)$, where f is the focal length. Thus, for the NSPM where $d_{\mathrm{sens}} = 9.6\,\mathrm{mm}$ and $f = 800\,\mathrm{mm}$ the field of view (FOV) equals $2\,\alpha_{\mathrm{max}} \approx 0.69°$. The solid angle

$$\Omega = 2\,\pi\,(1 - \cos\alpha_{\mathrm{max}}) = 4\,\pi\sin^2\left(\frac{\alpha_{\mathrm{max}}}{2}\right) \tag{6.7}$$

given by the field of view of the NSPM has thus a value of $\Omega \approx 1.1 \cdot 10^{-4}\,\mathrm{sr}$. For comparison, as observed from Earth, the full diameter of the Moon has a mean size of about 0.5°.

The field of view of the NSPM is also determined by means of a Geant4 simulation (cf. section 4.3). Parallel light with a wavelength of 330 nm is simulated to enter

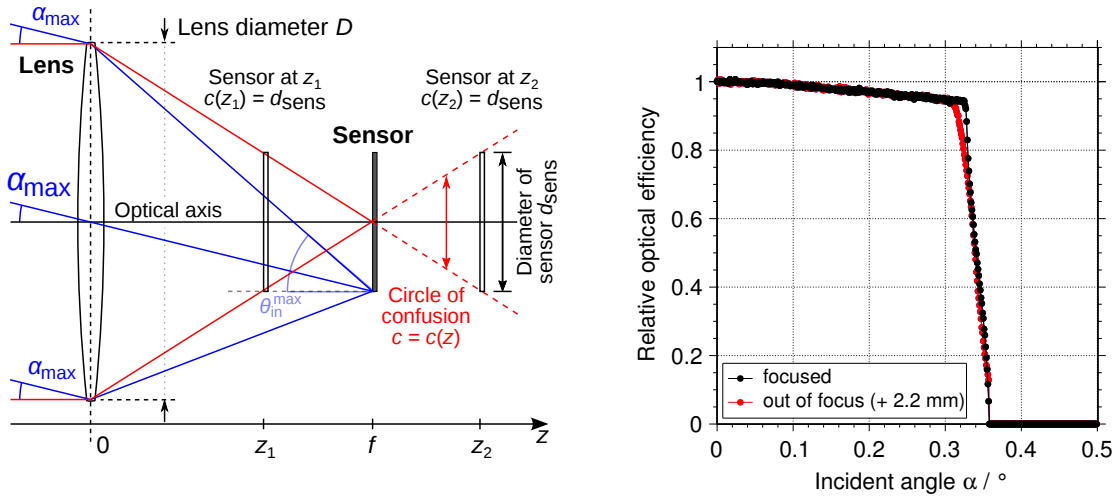

Figure 6.6: **Left:** Schematic of a telescope. Parallel light enters the telescope and is focused on a sensor with diameter d_{sens} at the position $z = f$. Alternative positions of the sensor z_1 and z_2 are drawn where d_{sens} equals the diameter of the circle of confusion c. See text for further details. **Right:** Simulated relative optical efficiency of the PN-203 telescope as a function of the incident angle of the light α. The black data points are for a sensor in the focus of the telescope. The red data points are for a sensor which is moved by 2.2 mm out of focus to a position farther away from the secondary mirror. See text for details.

the telescope. For each run of the simulation the incident angle α is increased by 0.001° starting at 0° and running up to 0.5°. Upon entrance the photons are distributed uniformly over the whole diameter of the tube of the telescope. For each run 50000 photons enter the tube. Filter, Winston cone, and SiPM are omitted for the simulation of the field of view. The sensitive detector is placed in the focus of the telescope and has the same diameter as the entrance aperture of the Winston cone. The relative optical efficiency for an incident angle α is defined as the number of photons arriving at the sensitive detector normalized to an incident angle of $\alpha = 0°$. The result of the simulation is shown in figure 6.6 (right) by the black data points. The relative optical efficiency decreases linearly from 1 at $\alpha = 0°$ to about 0.94 at $\alpha = 0.33°$. There it drops rapidly to zero with the half height of the cutoff being at about 0.34°. As expected there is a good agreement of the simulated FOV with the analytically determined one. For the case where the sensitive detector is in the focus of the telescope, we find FOV $= (0.68 \pm 0.02)°$ and $\Omega = (1.1 \pm 0.1)$ sr.
It is also worth noticing that all angles, under which the photons hit the sensitive detector, are smaller than the angle $\theta_{\text{max}} = \arcsin(r_2/r_1) \approx 18.2°$ of the Winston cone[9] (cf. section 5.1). This means that the camera of the NSPM will accept all photons with respect to their incident angles. This is also clear from an analytical consideration regarding the schematic in figure 6.6 (left): the maximum angle under

[9] θ_{max} is determined analytically from the geometry of the Winston cone as the cone is not featured in the simulation

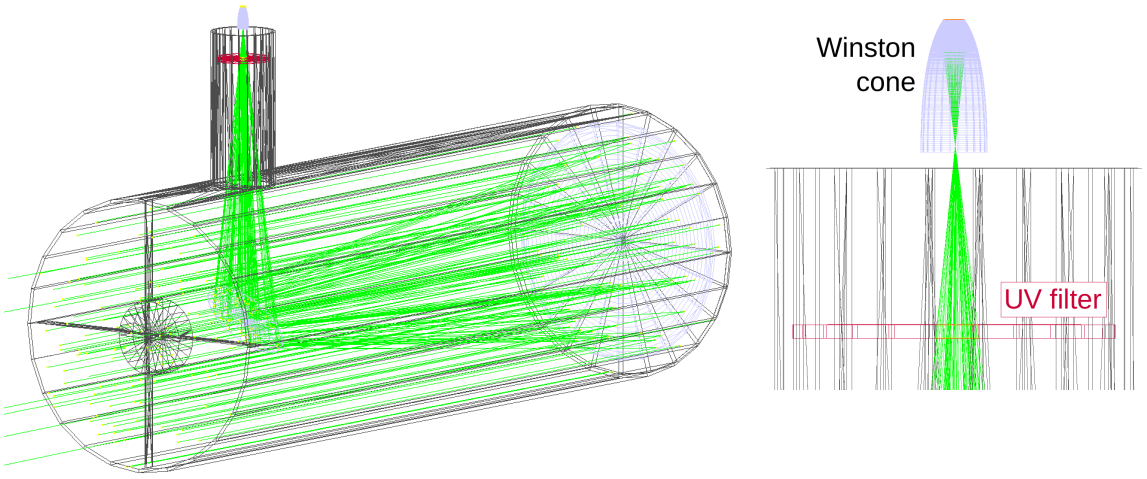

Figure 6.7: Geant4 visualization of the PN-203 telescope. Reflecting surfaces are shown in gray (main mirror, secondary mirror, Winston cone). The UV band-pass filter is shown in red. The sensitive detector at the exit of the Winston cone is depicted in red. 100 photons enter the telescope from the left parallel to the optical axis. Their traces are given in green. The right side of the figure shows a zoom to the filter and Winston cone. The entrance of the cone will be exactly in the focus of the telescope if the filter is removed.

which a photon can enter the Winston cone is $\theta_{\text{in}}^{\max} = \arctan\left((D + d_{\text{sens}})/(2\,f)\right) \approx 7.6°$.

A visualization of a Geant4 simulation of the PN-203 telescope is shown in figure 6.7. The green lines are the traces of 100 photons which enter the telescope parallel to its optical axis. In contrast to the just discussed simulation, the one shown in figure 6.7 also includes the UV band-pass filter and the Winston cone. Here, the sensitive detector is located at the exit aperture of the cone. Its entrance aperture is still at the position given by f, but the focal point is shifted slightly into the cone due to the refracting characteristics of the filter.

It might come to mind that it is not very crucial to have the entrance aperture of the Winston cone exactly in the focal plane. Since the cone is a non-imaging light concentrator, all light which enters it will be collected at its exit aperture.[10] It is not required that the light has to be focused. This is illustrated in the schematic in figure 6.6 (left). In addition to the sensor at the position f, two further sensors at the positions z_1 and z_2 are drawn. At these positions the circles of confusion of the light entering the telescope with $\alpha = 0°$ have the same size as the sensor. Thus, the complete light still reaches it. The distances of z_1 and z_2 to f are identical and given by $z_{1,2} = f \cdot (d_{\text{sens}}/D)$. For the NSPM this is more than 37 mm! Collecting all the light which enters the telescope from a star in the direction of the optical axis in the Winston cone should therefore not be a challenge. This is correct, but

[10] at least if it has a perfect reflecting surface

Table 6.1: Optics-related parameters of the night-sky photometer

Parameter	Symbol	Value	Unit
Focal length	f	800	mm
Aperture diameter	D	203	mm
Aperture area	A	$3.24 \cdot 10^{-2}$	m^2
Optical efficiency of PN-203 telescope	ϵ_{PN-203}	0.40 ± 0.02	–
Pixel diameter	d_{sens}	9.6 ± 0.3	mm
Field of view [*1]	FOV	0.68 ± 0.04	°
Field of view [*1]	Ω	1.1 ± 0.1	sr
Uncertainty of camera position [*2]	–	2.2	mm
Distance UV filter – camera	–	26.5	mm

[*1] including the uncertainty of camera position (i.e. uncertainty on focusing)
[*2] as discussed in section 6.3

nonetheless great attention must be paid to a careful focusing of the NSPM, since we are not only interested in the light parallel to the optical axis but also in light with larger angles α. This light will only reach the entrance aperture of the Winston cone appropriately if it is located in the focal plane.

The parameters discussed in this section are summarized in table 6.1. The next section will describe how the NSPM is actually focused in the field prior to the measurements of the night-sky photon fluxes. Furthermore, it addresses the question whether the detector is able to distinguish between stars and the diffuse NSB.

6.3 Focusing and aiming at stars

When placed at a suitable position beneath the night-sky, the polar axis of the mount of the telescope is made parallel to the Earth's axis of rotation by aligning it towards the direction of the celestial north pole. Subsequently, the computer of the telescope is set to the actual geographical coordinates and time. If not stated differently, the telescope will move constantly to compensate the rotation of the Earth.
During the initial orientation of the telescope all electronics are already switched on to heat up to their operational temperature.

The focusing of the NSPM is performed by eye. The camera is removed from the focuser and another Winston cone is placed exactly at its position. This cone has a piece of tracing paper at its entrance aperture which acts as a screen. The additional Winston cone is also a hollow one made from aluminium. At its upper end it has the same geometry as the one of the camera to allow an exchange of both with a high accuracy. In contrast to the light-concentrator of the camera, the one used for focusing has wider apertures. Its entrance aperture has a diameter of 13.4 mm and its exit aperture has a diameter of 6.0 mm. These are the same dimensions as for the Winston cones of FAMOUS. The reason to choose the bigger Winston cone for focusing is a practical one: it is easier to watch the image of a celestial object

projected onto the screen through the wider exit aperture. The UV band-pass filter is not used for the focusing, since the eye is not able to see starlight sufficiently well through it.
A bright star is brought to the center of the field of view of the telescope and the focuser is adjusted to result in a sharp image of the star on the screen. The precision is estimated to be about 2.2 mm with respect to the line of movement. This appears to be a large value compared to the precisions achieved with eye-pieces which are in the sub-millimeter region. However, due to the pixel design of the NSPM a given inaccuracy in focusing does not affect the results too much. For a quantitative evaluation the Geant4 simulations, which result in the relative optical efficiency of the telescope, and which have been discussed in the previous section, are performed with the sensitive detector being ± 2.2 mm out of focus. The results are shown in the plot of figure 6.6 (right) by the red data points, which correspond to the sensitive detector being 2.2 mm farther away from the secondary mirror of the telescope. Differences of these data to the simulation results for the sensitive detector being moved out of focus into the opposite direction, are not apparent in the presented display. Therefore, the related data points are not drawn. Compared to the nominal simulation with the sensitive detector being in the focus (shown by the black data points) the simulated optical efficiency does not change significantly if the sensor moves out of the focus. However, the cutoff of the optical efficiency is not as sharp in the case of the simulations of an unfocused setup. This leads to a slightly increased uncertainty in the field of view of the telescope due the uncertainty of focusing. In the following we will thus use the field of view FOV $= (0.68 \pm 0.04)^\circ$. According to the simulations the total optical efficiency, determined by an integration over the angle α_f under which the light enters the telescope, will only be reduced by about 0.8% if the sensor is out of focus by ± 2.2 mm.

To test the communication between the PC and the telescope, and also to test whether the NSPM has the sensitivity to distinguish between bright stars and the diffuse NSB, an automated measurement program is executed which scans the sky. The field of view will successively move to different positions where the signals of the SiPM are subsequently measured.
The user can specify a region of interest by defining its center, the angular distance between two neighboring positions the field of view will move to, and the total number of steps into the two orthogonal directions of the equatorial coordinate system which are declination (DEC) and right ascension (RA). This coordinate system does not rotate with the Earth but remains fixed with respect to the stars. After each movement of the telescope, to look at a different position in the sky, the program waits a few seconds before the data acquisition is started. This is necessary since the telescope oscillates a little bit after its movement has stopped. The program can be set to ask the user before each individual measurement whether the data acquisition shall be started. This is useful since single clouds can pass through the field of view and the user might want to wait for a clear sight. A single measurement takes about 20 s. Hence, the complete scan of the region of interest can become time consuming depending on the choice of the initial settings.
The data are acquired by the Wavejet 354A oscilloscope. Its *edge trigger* generates

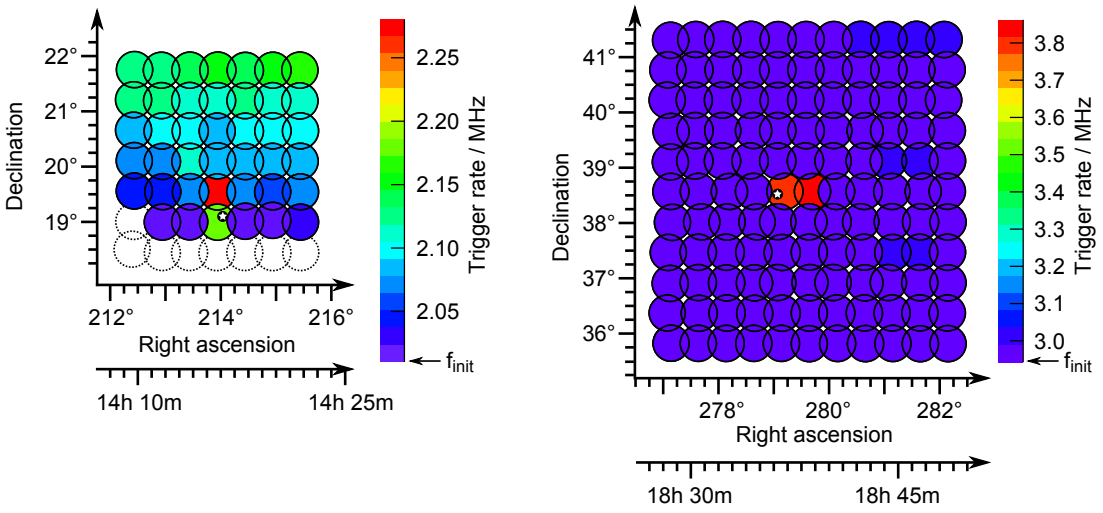

Figure 6.8: Regions of the sky given in equatorial coordinates declination and right ascension around the bright stars Arcturus (left) and Vega (right). The circles denote the field of view of the telescope. Data corresponding to the circles with the dashed contours are doubtful and therefore not displayed. For the other circles the color code indicates the trigger rate of the oscilloscope measuring signals of the SiPM. The rate is a measure of the detected photon flux in an arbitrary scale. See text for further details. The reference positions of the stars are shown by the black circles with the white star symbols in their centers.

a trigger when the amplified SiPM signal, whose pulses have a negative polarity, falls below a certain threshold. The threshold is adjusted by the program to a level resulting in the configurable initial trigger rate f_{init}. This rate is measured while the NSPM is detecting the light flux from a region of the sky without bright stars. The trigger rate for each individual measurement, corresponding to the different positions within the region of interest, is stored. The program can be configured to move the telescope at the end of the scan to the position with the highest measured trigger rate.

The chosen regions of interest are centered around the bright stars Arcturus (α Boötis) and Vega (α Lyrae). Arcturus has an apparent magnitude[11] of V = -0.05 mag and Vega of V = 0.03 mag [161]. The step size from measurement to measurement is

[11] The apparent magnitude is a logarithmic scale of the light intensity relating to the logarithmic visual perception of the human eye. The lower the value of the magnitude is, the brighter the object appears. Per definition a difference in five magnitudes corresponds to a difference in brightness of 1:100. Thus, with m_1 and m_0 being the magnitudes of two objects with the measured photon fluxes ϕ_1 and ϕ_0, the difference in magnitudes is given by $m_1 - m_0 = -5/\log(100) \cdot \log(\phi_1/\phi_0)\,\text{mag} = -2.5 \cdot \log(\phi_1/\phi_0)\,\text{mag}$. The fluxes depend on the band in which they are measured. A widely used photometric system (i.e. a set of well-defined filters) is the UBV systems, where U stands for ultra-violet, B for blue and V for visual. As a reference point of the apparent magnitude scale Vega had been chosen to have a value of 0 mag. With more modern instruments the apparent magnitude of Vega in the V band has been determined to V = 0.03 mag.

0.55° in DEC and 0.50° in RA.[12] The scan of the region of interest starts with the lowest values for DEC and RA. Then the RA value is increased by on step keeping the value of DEC fixed. After the RA has reached its maximum value, it is reset to its lowest one, and the value of DEC is increased by one step. This continues until the scan is completed. In other words, the sky is scanned line by line of constant DEC.
With FOV = 0.68° for each of the individual measurements within a region of interest, this specific choice of step sizes leads to an overlap of the fields of view of two neighboring lines of sight of $\delta_{\mathrm{DEC}} = 0.16°$ in DEC and $\delta_{\mathrm{RA}} = 0.21°$ in RA. There is a small blind spot between the individual fields of view. Its width is $\delta_{\mathrm{blind}} = 0.03°$ along the line which connects the centers of two diagonally neighboring fields of view.

The sky maps in figure 6.8 show the measured trigger rates for the scanned coordinates. The left plot is for a scan around Arcturus, and the right one for a scan around Vega. The measurements into the direction of Arcturus were performed without the UV band-pass filter. For the measurements into the direction of Vega the UV filter was applied. They were performed in the mornings of May 31, 2012 (Arcturus) and July 24, 2012 (Vega) under a rather bright night-sky on top of the Physikzentrum in Aachen, Germany[13] which is located in an urbanized region.[14] The first complete scan took about one and a half hours, the second one took about 45 minutes. The scan around Arcturus covers less regions towards which the telescope had to move, but the sky was partly clouded during the scan so that the data acquisition had to be paused several times.

Since the output of the SiPM amplifier is AC coupled, an overshoot of the signal of the SiPM occurs whenever a pulse is caused by a cell breakdown. For high cell breakdown rates the signal does not fully revert to its baseline until the next breakdown takes place. Hence, the overshooting leads to an effective shift of the baseline to higher voltages. The value of this shift depends on the cell breakdown rate. But the trigger level of the oscilloscope is kept constant. Thus, without further calibration of the SiPM, the trigger frequencies shown in figure 6.8 can only be regarded as a measure of the cell breakdown rate of the SiPM on a non-linear and unknown scale. The cell breakdown rate can be regarded as a measure of the detected photon flux on a non-linear and unknown scale. The initial trigger rate f_{init} was set to values of about 2 MHz and 3 MHz for the scans around Arcturus and Vega, respectively.

Hotspots are clearly visible in both sky maps. Thus, the NSPM can distinguish between bright stars and the diffuse NSB with and without the UV filter. Though, it

[12] This asymmetry was introduced by mistake by means of a typing error. Though, it has no consequences regarding analysis results.

[13] coordinates: N 50° 46′ 53″, E 6° 02′ 55″

[14] The position of Aachen is marked in the brightness map in figure A.4 which is shown in appendix A.3. In this figure the artificial night-sky brightness is given for Europe. The data are for the astronomical V band and are measured with the Operational Linescan System aboard the DMSP satellites [162]. The brightness map can be regarded as a reference to qualitatively evaluate Aachen as an observational site.

cannot distinguish between the diffuse NSB and the fainter stars nearby. Regarding the sky scan into the direction of Arcturus, the brightest objects aside from Arcturus ($V = -0.05\,mag$) in the considered region of the sky have apparent magnitudes of $V = 5.97\,mag$ and $V = 6.25\,mag$. This relates to a light intensity of less than 1% of the one of Arcturus. Regarding the other sky scan, Vega is also by far the brightest object in the considered region. The next brightest objects provide each about $\sim 3\%$ of the light intensity of Vega.[15]
The diameter of the circles in the sky maps of figure 6.8 correspond to the FOV of the NSPM. They are centered around the positions which were identified by the telescope during the measurements. They fluctuate slightly around the positions which were preset in the measurement program, since the driver of the telescope features a certain tolerance between the requested coordinates and the one the telescope is moved to. The values of the intersecting regions of the circles are set to the minimum value of the two overlapping regions, since the goal is to identify a star which is expected to be observed as a point in the sky. From the data we can conclude that the stars are in the directions of the overlapping regions with the highest photon flux, assuming that the NSPM was perfectly focused.[16]

In the sky map around Arcturus the data points with the lowest value in RA as well as the next one with respect to the time are missing due to initial problems with the data acquisition. With increasing time (which means going to higher values in RA and DEC) an increase of the measured photon flux is visible. This is due to the advancing dawn. The positions of Arcturus and Vega are also displayed in the maps by the black dots with the white star symbols. They differ by about 0.3° and 0.4°, respectively, from the measured ones. The difference between the actual position of a star and the position where the star was identified can be regarded as the accuracy of the process of the orientation of the telescope prior to all measurements beneath the night-sky. Inaccuracies in the initial orientation process will also lead to tracking errors, i.e. an object will gradually move out of the field of view, even with an enabled tracking control. Since such an inaccuracy will not affect the results in the further course of this work, the scans of the sky have not been performed again with a higher accuracy regarding the orientation of the telescope.

[15] The objects are identified with the Hipparcos and Tycho star catalogs [161] and the Simbad astronomical database [163] by use of the planetarium software Stellarium [164]. For the region around Arcturus: star V* CN Boo at (RA/DEC (of date)) 14 h 16 m 39 s / +18° 51′ 17″, angular distance to Arcturus: ∼15′, apparent magnitude (V): 5.97 mag; binary star HIP 69751 at 14 h 17 m 07 s / +20° 03′ 52″, angular distance to Arcturus: ∼1°, apparent magnitude: 6.25 mag. For the region around Vega: binary star ζ Lyrae at 18 h 45 m 12 s / +37° 37′ 08″, angular distance to Vega: ∼2°, apparent magnitudes: 4.07 mag; multiple star ε Lyrae (i.e. four stars form the two binary stars ε^1 and ε^2) at 18 h 44 m 45 s / +39° 41′ 02″, angular distance to Vega: ∼2°, apparent magnitude: 3.88 mag. As for the measurements into the direction of Vega the UV filter has been applied it is worth noticing that Vega and the two star systems in Lyra have similar spectral classes (Vega has the spectral class A, both star systems consist of stars with spectral classes A and F).

[16] An unfocused setup does not significantly affect the field of view of the NSPM and its optical efficiency. However, if the star is not in the center of the field of view, an unfocused setup may lead to the detection of the star in two neighboring regions of the sky maps shown in figure 6.8.

Regarding the hotspot in the sky map around Arcturus, the rather high difference in the measured trigger rates for the two individual measurements close to the actual position of the star (i.e. the red and the green ones), might suggest that the telescope was not perfectly focused. On the other hand, as already noted above, the sky was partly clouded. Also with a perfect focusing some clouds, which might not have been recognized by the eyes of the experimenters, could have lead to the difference in the trigger rates. Additional scans with overlapping fields of view of more than just two individual measurements could answer the question regarding the accuracy of the focusing. However, for the further course of the analysis the precision of the focusing as discussed previously is sufficient.

For a better resolution and the prevention of the blind spots in the sky maps, the step sizes of the DEC and RA can be decreased. However, the goal of this measurement is already achieved. The remote control of the telescope works properly and the NSPM can distinguish between bright stars and the diffuse NSB.
For all further measurements of the light of stars the telescope is brought visually into the line of the star, since this procedure provides a higher accuracy especially if only a reasonable amount of time is intended for the alignment of the telescope. Furthermore, frequent visual checks counteract tracking errors.

During the further discussion we will be interested in the absolute light flux measured with the NSPM. The next chapter will discuss the analysis of data recorded with the V1729 ADC in detail. It follows the basic principle of the reconstruction of light fluxes presented in section 6.1 and yields the absolute number of detected photons originating from the diffuse NSB and the stars.

7. Data Analysis

The procedure to analyze the data measured with the V1729 ADC of the night-sky photometer (NSPM) will be discussed in this chapter. The raw data are the voltage traces containing the output signal of the SiPM. At the end of the analysis chain the number of detected signal-photons per unit of time will be determined. This detection rate can be transformed to the flux of detected signal-photons in terms of radiance.

Before we go into details, this paragraph gives a brief summary of the procedure. First of all a waveform analysis searches the voltage traces recorded with the ADC for pulses which correspond to cell breakdowns of the SiPM. Once the pulses are identified the photon counting method introduced in section 6.1 is applied. It results in the cell breakdown rate R_{wa} according to the waveform analysis. The consideration of the efficiency of the pulse search algorithm and the photon counting method yields the cell breakdown rate R_{pc}. Per construction of the photon counting method the rates do not contain counts due to cell breakdowns caused by optical crosstalk. Subsequently, R_{pc} has to be corrected for afterpulses and thermal noise to obtain the rate of the detected signal-photons R_{γ}. The correction for afterpulses requires the knowledge of the actual over-voltage, the probabilities of afterpulsing and optical crosstalk, and the recovery time of the cells of the SiPM. These characteristics are also required to study the efficiency of the waveform analysis algorithm and the photon counting method, and have thus to be determined beforehand. The correction for thermal noise can be performed with data measured in darkness.[1]

7.1 Waveform analysis

As discussed in the previous chapter all measurements considered in the following of this work are performed with the V1729 ADC. All recorded data are voltage traces with a length of 2300 ns and a sampling interval of 1 ns. The device stores data upon the reception of random triggers.
In figure 7.1 (left) a section of a voltage trace is shown. The black points are the recorded data. The section contains several pulses due to cell breakdowns of the SiPM. To the right side of the figure one of the pulses is displayed in greater detail.

[1] The analysis at a glance: In figure 7.22 the complete analysis chain is summarized in a block diagram. It is presented not before the end of this chapter since some quantities will not yet be defined until then. However, an early glance will not cause harm and might turn out to be worthwhile in relating details to the big picture.

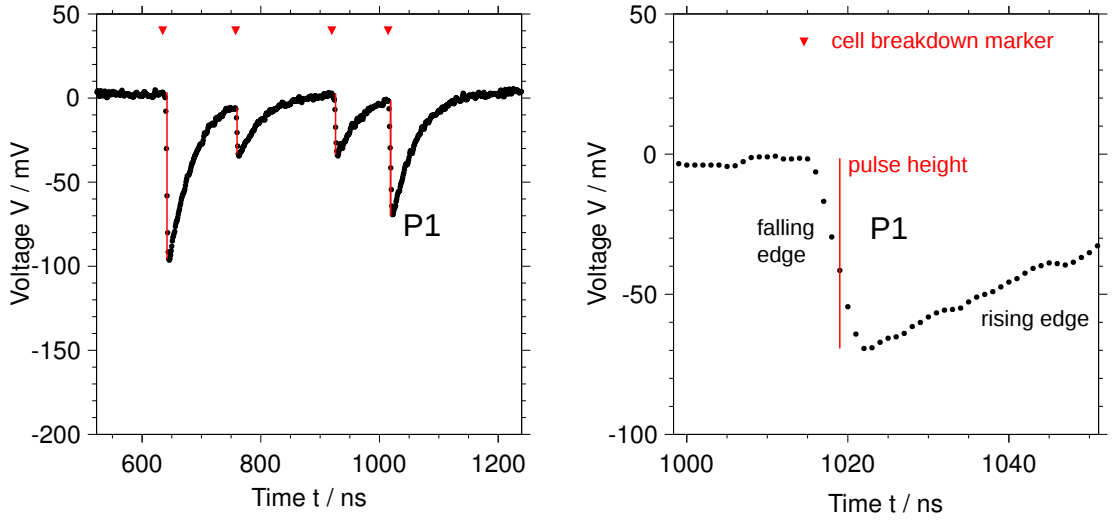

Figure 7.1: **Left:** A section of a measured SiPM voltage trace to demonstrate the waveform analysis. Red triangles mark the time of the cell breakdowns. Red lines indicate the amplitude of the pulse. **Right:** Zoom to the region of the last pulse (called P1) of the left plot.

We are interested in the number of cell breakdowns within a trace, in the times when these breakdowns occur, as well as in the pulse heights of the individual pulses. The shape of the pulses makes the use of a simple threshold scan to identify them inappropriate. Since the rising edges of the pulses have a rather high time constant, which is the recovery time τ_{rec}, pulses can pile up while cells are still recovering. This is especially, but not exclusively, the case for fast afterpulses.[2] These pulses on the recovering edges of their preceding pulses could be unrecognized by a threshold scan. Thus, here we identify the cell breakdowns in the voltage traces by a search algorithm which scans the data points of the trace point by point looking for local minima.[3] Basically this waveform analysis algorithm checks whether the voltage is decreasing or not.

In figure 7.2 the same pulse[4] which is highlighted in figure 7.1 is shown to illustrate the principle of the search algorithm. A start marker is initially set to the first data point. The following N_{wa} data points are included in a search window of fixed width in time. In the figure the start marker is displayed as the blue arrow, while the search window is depicted as the blue box. More than one of each are displayed in the example since the algorithm is shown at different steps.
As long as the last data point within the search window has a smaller voltage than

[2] cf. for instance top-right plot in figure 7.4

[3] The algorithm is a modified version of the one applied in reference [105].

[4] The voltages of some data points in the right plot of figure 7.1 differ only very little from the voltages of neighboring data points. Hence, sometimes it is hard to distinguish by eye whether the voltage is varying from a data point to the subsequent one or whether it is constant. For the sake of clarity, in figure 7.2 the concerned data points are mildly shifted vertically from their original positions to make the change of the voltage clearer.

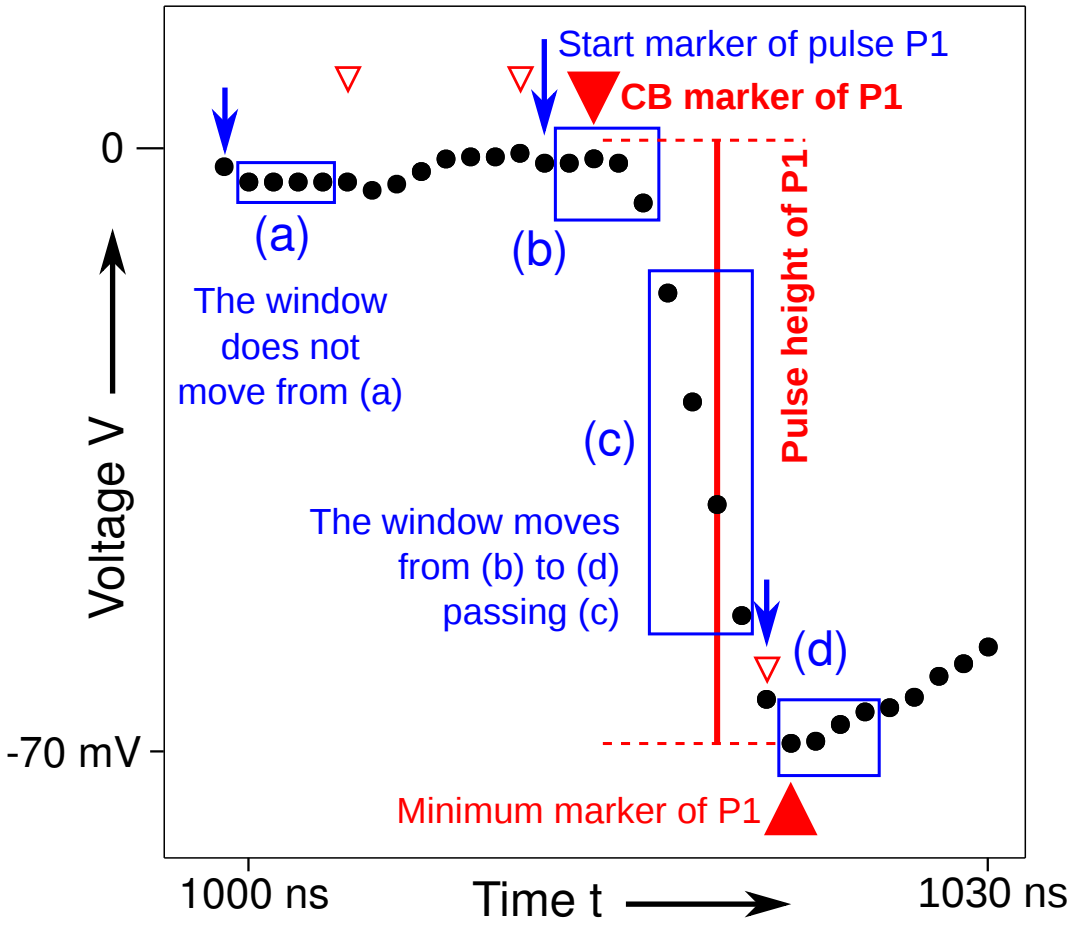

Figure 7.2: The waveform analysis algorithm to identify cell breakdowns illustrated for the pulse P1 (cf. figure 7.1) — see text for a description of the algorithm. The blue arrow is the *start marker*. It is displayed at different positions. The blue box is the *search window*, also shown at different positions (a) to (d). Only three of the many positions where the window actually starts are shown. These are (a), (b), and (d). Position (d) is also the final position for the window starting at position (b). The red downwards pointing triangles are the *cell-breakdown(CB)-markers*. The small open triangles tag pulses which are rejected from being regarded as SiPM pulses. The upwards pointing triangle is the *minimum marker* of the pulse P1. The red vertical line is the pulse height of P1.

the first one, the window will move one position to the right. N_{wa} can be set to values greater than 2 to account for fluctuations of the voltage due to electronics noise, which can be identified spuriously as cell breakdowns. If the window does not move at all (as it is for instance the situation at the position (a) in figure 7.2), the position of the start marker will be increased by one data point. Every time the start marker is moved the algorithm starts over and the window is again placed to the N_{wa} data points following the start marker.
When the window has reached a final position (e.g. position (d) in figure 7.2 for its

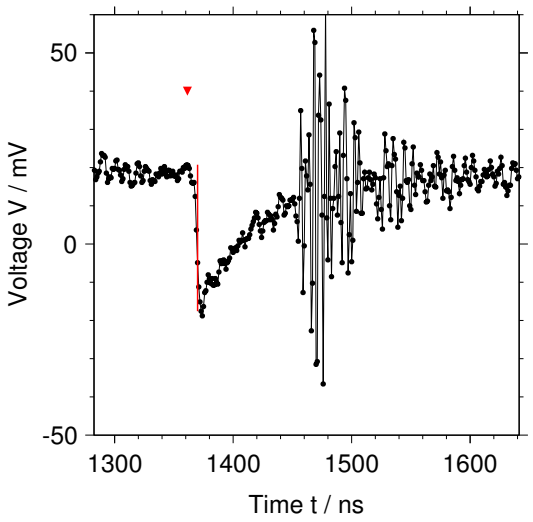

Figure 7.3: A section of a measured voltage trace containing an SiPM pulse and a subsequent oscillation of the voltage due to the rare event of radio interference.

start at position (b)) the first data point in the window is tagged with a minimum marker. Afterwards the voltage maximum of the N_{wa} consecutive data points starting with the one of the start marker is identified. The corresponding data point is tagged with a cell-breakdown(CB)-marker. Since so far it is possible that the minimum marker is located at a position earlier than its corresponding CB-marker, it is required that the minimum distance of the two markers exceeds N_{wa} data points. In addition, this requirement rejects noise due to radio interference (see below).
The voltage difference of the two points at the CB-marker and the minimum marker is defined as the pulse height of the identified pulse. If it exceeds a certain threshold V_{th}, the pulse is regarded as an SiPM pulse. Subsequently, the start marker is moved to the data point just left of the current search window position.

For pulses which are regarded as SiPM pulses the CB markers are drawn in the voltage traces. They are the red downwards pointing triangles which can be seen in many voltage traces throughout this work, e.g. in figure 7.1. Also the pulse heights are drawn as red vertical lines. Their position in time is the same as for the data point where the pulse amplitude exceeds 50% of its full level.

For this work $N_{\mathrm{wa}} = 4$; thus, per construction the minimum time between two identified, consecutive pulses cannot be smaller than $\Delta t_{\mathrm{min}} = (N_{\mathrm{wa}} + 1)\,\mathrm{ns} = 5\,\mathrm{ns}$. Many pulses due to fluctuations of the signal are found, but they are rejected from being regarded as SiPM pulses by the threshold $V_{\mathrm{th}} = 14\,\mathrm{mV}$ and by the requirement of the minimum distance between CB marker and minimum marker. In the data shown in figure 7.2 there are three pulses due to fluctuations of the signal, i.e. true-negatives. Their CB-markers are drawn as the red, open triangles.
The rather high value of V_{th}, with respect to the RMS of the electronics noise (~ 1 to $2\,\mathrm{mV}$) and the small amplitudes of some of the fast afterpulses, is necessary to reject pulses due to radio interference which are visible in the voltage traces on

occasion. An example of such a rare event is shown in figure 7.3 where an oscillation of the measured signal due to radio interference is visible. At the beginning of these oscillations the positions of the maxima and minima are too close for the waveform analysis algorithm to consider the signal as SiPM pulses. However, if V_{th} was not set to a rather high value, there would be quite a number of radio interferences whose signals would be interpreted as several SiPM pulses as the oscillations decrease and larger distances between the extrema occur. The actual value of 14 mV has been determined by studying voltage traces without SiPM pulses.
Apparently, there are SiPM pulses in the data which are not recognized since their signal levels do not exceed the threshold (e.g. fast afterpulses). In the further course of this analysis, the results will be corrected for these false-negatives.

The question how efficient the waveform analysis algorithm identifies SiPM pulses is addressed in section 7.5 in the context of the photon counting method. But before this method is discussed, key characteristics of the SiPMs have to be determined. In the following section we will attend to the determination of the over-voltage of the SiPM. There, the waveform analysis algorithm will be used to determine the gain of the photosensor.

7.2 Determination of the over-voltage

The electronics of the NSPM do not feature an automated control of the bias voltage. This will cause the over-voltage of the SiPM to change during measurements if the temperature changes. To account for different over-voltages in the analysis of the night-sky brightness (NSB) data, the gain of the SiPM is determined as a function of the over-voltage. From this linear relationship (cf. section 4.2) the over-voltage of the individual NSB measurements will be determined.

The calibration measurement discussed in this section is performed in the laboratory with the SiPM and its amplifier being in a light-tight box. Operated in darkness the SiPM will only have cell breakdowns due to thermal and correlated noise. Different bias voltages are provided to the SiPM, and for each bias voltage the amplified signals of the photosensor are recorded by the V1729 ADC. The temperature is monitored. It increases with the proceeding measurement time from 26.6° C to 27.9° C. The systematic uncertainty of the temperature is irrelevant since we are only interested in temperature differences. The statistical uncertainty of the temperatures is smaller than 0.1° C. The experimental procedure starts with the lowest bias-voltage of 70.14 V. It is monotonically increased until the highest bias-voltage of 70.80 V is reached.

Voltage traces for the bias voltages $V_{\mathrm{b}} = 70.34\,\mathrm{V}$ and 70.68 V are shown in figure 7.4 (top row). Also shown are the cell breakdown-markers and the pulse heights found by the waveform analysis algorithm. For a higher bias voltage the cell break down rate increases. This is due to an increase in the thermal noise rate, the optical crosstalk probability, as well as the afterpulse probability. Also visible is the increase of the height of the 1 p.e. signal (p.e. = photon equivalent). Another feature worth noticing

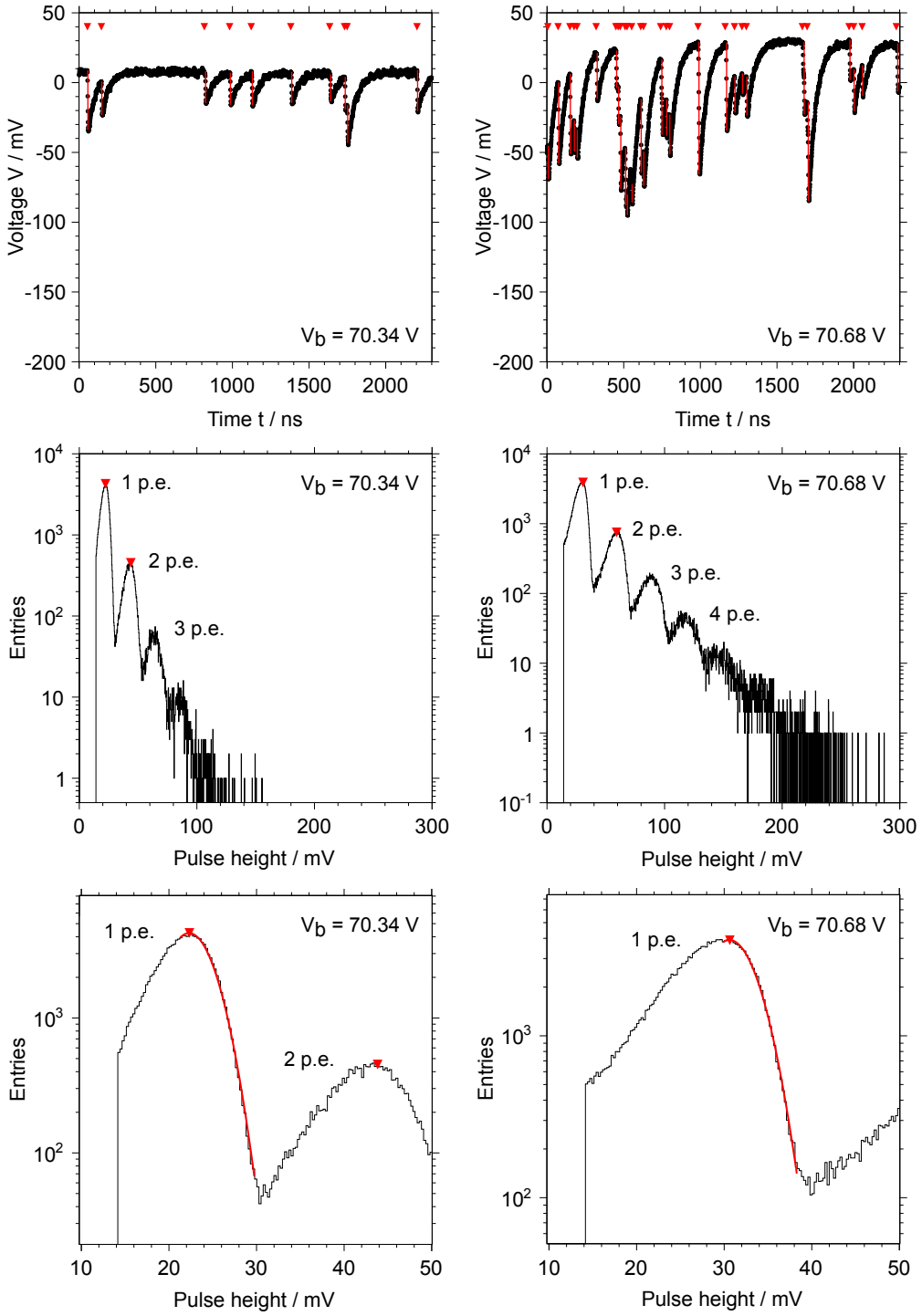

Figure 7.4: Voltages traces and pulse height spectra of the SiPM of the night-sky photometer operated in the laboratory in complete darkness (exemplary). The left column is for a bias voltage of $V_\mathrm{b} = 70.34\,\mathrm{V}$, the right one for $V_\mathrm{b} = 70.68\,\mathrm{V}$. The top row shows voltage traces with pulse heights (red lines) and points of cell breakdowns (red triangles) identified by the waveform analysis. Charge spectra of the entire sets of voltage traces for the specific bias voltages are shown in the middle row. The bottom row contains zoomed displays of the charge spectra and right-sided Gaussian fits to the 1 p.e. peaks. See text for more details.

is the shift of the effective baseline of the signal to higher voltages for an increased bias-voltage. As explained in section 6.3 this is due to the AC coupling of the output of the amplifier which results in an overshoot of the signal after a pulse.

The distributions of the pulse heights found by the waveform analysis are shown in the middle row of figure 7.4. The two plots are for the same bias voltages as stated above. Please note the logarithmic scale. Each of the pulse height spectra results from about 11000 voltage traces. The spectra allow to distinguish clearly between the peaks corresponding to the 1 p.e., 2 p.e., etc. levels. The peaks are of Gaussian shape with an additional contribution on their left edges. This additional contribution is due to the afterpulses with reduced signal levels compared to the 1 p.e. signal level. They can also contribute to pulse heights larger than 1 p.e. since the waveform analysis algorithm might not identify a pulse followed by an afterpulse as two individual pulses, but regards them as just one pulse.
A further contribution to the left edges of the peaks arises from a misinterpretation by the waveform analysis algorithm. It may happen on occasion that, within a voltage trace, a data point on the right side of a pulse minimum has the very same voltage value as a data point on the left side of the minimum. If these data points happen to be the first and the last data points in the search window of the waveform analysis algorithm, misleadingly the first one is identified as the pulse minimum. This leads to reduced pulse heights compared to pulses where the minimum was identified correctly. This minor effect does not influence the further course of this analysis. In fact, the important effect is the incapacity of the algorithm to find certain pulses in the first place. This effect will be addressed in section 7.5.

Disregarding these two effects the peaks are Gaussian and their widths are attributed to fluctuations of the signal due to electronics noise (RMS $\sim$ 1 to 2 mV) and a non-uniform breakdown-voltage among the individual cells of the SiPM. The latter leads to a cell-to-cell variation of the gain for a constant over-voltage. If these are the only significant contributions to the width of the peaks, the breakdown-voltage varies by about 10% over the sensitive area of the SiPM. In reference [111] the gain of Hamamatsu SiPMs has been measured for each individual cell. The authors report a variation of the gain by about 10% to 20%. A variation of the output signal of the SiPM due to the statistical nature of the avalanche process is expected to be smaller than 0.1%.[5]

Fits to the right edges of the 1 p.e. peaks are shown in the bottom row of figure 7.4. The red triangle highlights the position of the Gaussian function. This position of the 1 p.e. peak, $V_{1\,\mathrm{p.e.}}$, is proportional to the gain and should thus depend linear on the over-voltage for a constant temperature (cf. section 4.2). The choice of $V_{1\,\mathrm{p.e.}}$ is arbitrary to some extend. For instance, also the position of the 2 p.e. peak or the distance between the 1 p.e. and the 2 p.e. peaks can serve the purpose to calibrate the SiPM. All these choices lead to consistent results.

[5] Even if — for a constant temperature — the breakdown voltage is not constant over the entire sensitive area of the SiPM we keep the expression *breakdown voltage*, although it is effectively a mean breakdown voltage. The same applies for the over-voltage.

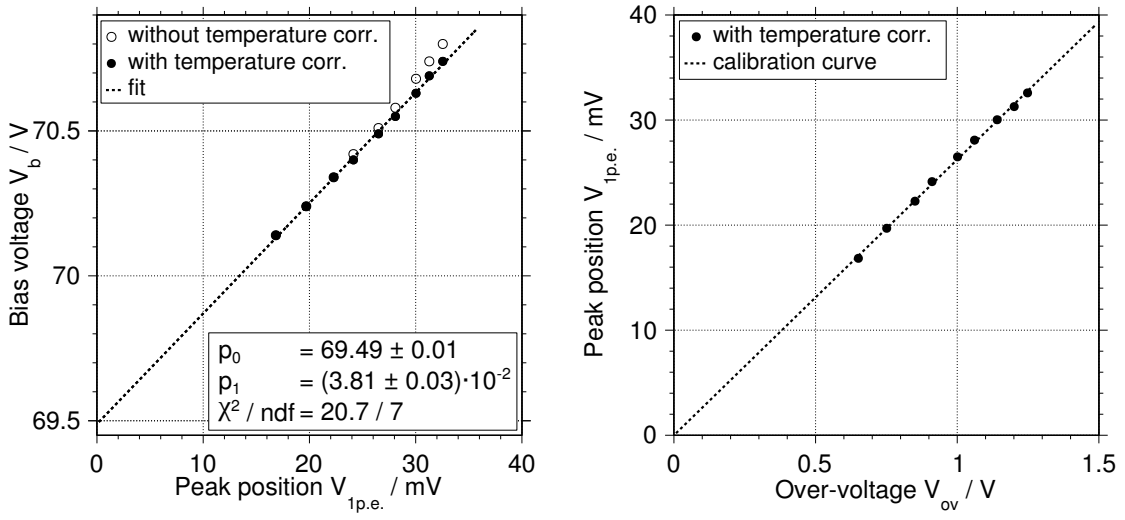

Figure 7.5: **Left:** Functional relation between the position of the 1 p.e. peak $V_{1\,\mathrm{p.e.}}$ and the bias voltage V_b. The open and filled data points show data without and with corrections for a change of the temperature, respectively. The dashed line is a fit to the temperature corrected data. The y-intercept of the fit (i.e. p_0) equals the breakdown voltage V_bd. **Right:** Same temperature corrected data as left but shown is the inverse function, while the determined breakdown voltage has been subtracted from the bias voltage to result in the over-voltage V_ov. The transformed fit reveals the calibration curve (dashed line).

The relation of $V_{1\,\mathrm{p.e.}}$ to the measured bias voltage is shown in figure 7.5 (left) by the open circles. The statistical uncertainty of $V_{1\,\mathrm{p.e.}}$ is taken as the uncertainty of the mean resulting from the fit. The one of the bias voltage has been determined from the data acquired with the voltmeter.[6] The uncertainties are smaller than the size of the markers. The gain features a non-linear behavior: with an increase of the bias voltage the gain, and thus $V_{1\,\mathrm{p.e.}}$ decreases. As discussed in section 4.2 this is expected with a rise of the temperature. To compensate this effect the bias voltage has been corrected for the temperature changes according to the progression factor $\beta' = 56\,\mathrm{mV\,K^{-1}}$ $\big($cf. equation (4.12)$\big)$ as stated by the manufacturer of the SiPM and confirmed in reference [105]. Actually, for the time being the progression factor is expressed in terms of the breakdown voltage. But it can be transfered to the bias voltage. On this account let us remember the fact that the bias voltage V_b is the sum of the breakdown voltage V_bd and the over-voltage V_ov:

$$V_\mathrm{b} = V_\mathrm{bd} + V_\mathrm{ov} \tag{7.1}$$

For a constant bias voltage an increase of the temperature leads to an increased breakdown voltage (and a decreased over-voltage and gain). But considering the purpose of the calibration of the gain of the SiPM, we desire a constant breakdown-voltage. Keeping the breakdown voltage fixed, and increasing the temperature, will

[6] Fluke 8845A precision multimeter

lead to a decreased bias voltage if a constant gain, and thus constant over-voltage is required. Hence, the progression factor can be applied directly for a correction of the bias-voltage. The temperature corrected data are shown as the filled data points in figure 7.5.

The breakdown voltage V_{bd} can be determined from an extrapolation of the data to $V_{1\,\mathrm{p.e.}} = 0\,\mathrm{V}$. A linear fit to the temperature corrected data results in $V_{\mathrm{bd}} = (69.49 \pm 0.01)\,\mathrm{V}$. Subtracting V_{bd} from the bias voltage transfers the latter into the over-voltage V_{ov}. The mean of the 1 p.e. pulse height is shown as a function of V_{ov} in the right plot of figure 7.5. The appropriately transformed fit result also displayed in the plot serves as a calibration curve for the SiPM. In the following we will determine $V_{1\,\mathrm{p.e.}}$ from the data obtained by the measurements of the NSB, and the calibration curve will yield the applied over-voltage. As discussed in section 4.2 the gain as a function of the over-voltage does not depend on the temperature. Thus, the knowledge of the temperature during the following NSB measurements is not required to determine the over-voltage.

7.3 Recovery time and dead time

The recovery time of the cells of the SiPM can lead to reduced pulse heights of the response of the photosensor. Only if all pulse heights exceed the threshold V_{th} of the waveform analysis algorithm, the finally determined photon flux does not not contain a bias due to recovery time effects. Since especially signal levels which correspond to fast afterpulses are smaller than the threshold, the recovery time has to be determined and accounted for. The determination of the recovery time will be performed in this section, whereas its effect regarding the determination of the photon flux will be discussed in section 7.5.
The intrinsic dead time of the cells can lead to signal-photons which are absorbed in the drift region of the silicon but do not cause a signal. In analogy the dead time can prevent cell breakdowns due to the other three causes, i.e. thermal excitation of the silicon, optical crosstalk, and afterpulsing. The measured night-sky photon flux can be corrected for effects of the intrinsic dead time if the dead time is known.

To determine the intrinsic dead time and the recovery time we study the signal levels of the afterpulses of the SiPM as a function of the time Δt which elapsed since the preceding pulses. The determination of the time difference Δt is illustrated in figure 7.6 and will be explained in an instant. As discussed in section 4.2 the distribution of Δt can also be used to determine the afterpulse probability. This will be performed in the following section. The analyses use voltage traces of the SiPM operated in complete darkness which have been recorded with the V1729 ADC. The traces are handled by the waveform analysis algorithm which identifies the SiPM pulses. If a pulse is found at a time smaller than 1200 ns, which is roughly half the trace length, it could serve as a start pulse. In addition, it has to feature a level smaller than the 1.5 p.e. level, and lack further pulses 300 ns prior to it. If these requirements are fulfilled, the pulse is regarded as a start pulse, and the time difference Δt to its subsequent pulse is determined. This pulse is referred to as the

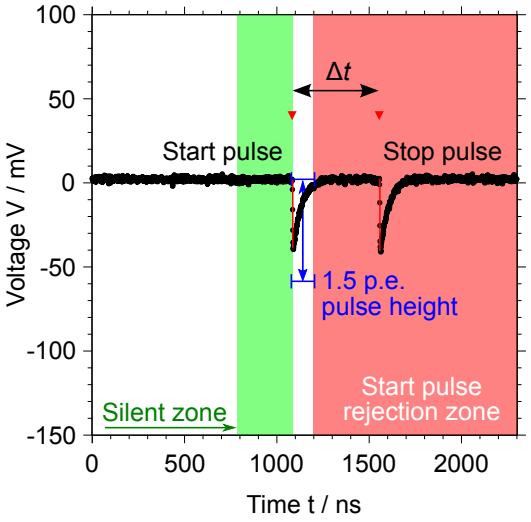

Figure 7.6: Measured voltage trace containing SiPM pulses to demonstrate the determination of time difference Δt between a 1 p.e. start pulse and the consecutive stop pulse. Pulses with a cell-breakdown-marker (red triangle) in the red shaded region are rejected from being a start pulse. See text for more details.

stop pulse. Δt is defined as the distance of the cell-breakdown markers of start and stop pulse. Per construction of the waveform analysis algorithm the minimum time difference is $\Delta t_{\text{min}} = 5\,\text{ns}$ (cf. section 7.1). In addition to the time difference also the pulse height of the stop pulse is determined. The values are filled into a two-dimensional histogram. The stop pulse can again serve as a start pulse if the three demands on start pulses are fulfilled.

The constraints on the start pulse ensure already a correct consideration of the afterpulse probability: The one on the time window in which the start pulse may be located accounts for the finite length of the voltage trace. If the start pulse could be anywhere in the trace, the analysis would suffer from a bias since there would be an excess for small values of Δt. For a start pulse located at the end of a trace, afterpulses with small Δt can still be detected while afterpulses with greater Δt will not be included in the trace.
A signal level of the start pulse smaller than the 1.5 p.e. level rejects pulses with more than one cell breaking down. This will be of importance for the study of the afterpulse probability since we would like to observe what happens after *one* cell breaks down. Omitting this cut would lead to start pulses caused by the breakdown of more than just one cell due to optical crosstalk. This would lead to a bias in the resulting afterpulse probability. The same reason requires the 300 ns without a pulse prior to the start pulse. If the voltage trace would be longer this value could be raised,[7] but greater values lead to reduced statistics regarding Δt. Also a high cell breakdown rate will reduce the statistics significantly. Thus, the SiPM is operated in complete darkness. With its sensitive size of $3\times3\,\text{mm}^2$ the SiPM of

[7] As we will see in section 7.4 the time constants of fast and slow afterpulsing are $\tau_{\text{f}} = 55\,\text{ns}$ and $\tau_{\text{s}} = 175\,\text{ns}$, respectively.

the NSPM has a thermal noise rate at room temperature which is still too high to result in appropriate statistics. Thus, measurements of the same type of SiPM, from the same production charge, operated in a light-tight box and cooled to a temperature of $\left(1.0 \pm 0.5\,(\text{sys.})\right)^\circ$ C are employed to determine the characteristics of interest. The temperature is constant within 0.2 to 0.5° C. The signals of the SiPM are also amplified with a transimpedance amplifier of the same revision as the one of the NSPM. The raw data have been recorded in the scope of reference [105]. In contrast to the data measured with the NSPM, here the threshold of the waveform analysis algorithm could be reduced to $V_{\text{th}} = 6\,\text{mV}$. This is possible since the data do not feature signals due to radio interference, and the lower threshold is favored since more fast afterpulses can be detected.
Since the recovery time τ_{rec} depends on the cell capacitance C_{c} and the resistance of the quenching resistor of the cell R_{q} (i.e. $\tau_{\text{rec}} = R_{\text{q}}\,C_{\text{c}}$, cf. subsection *Silicon photomultipliers* in section 4.1), and since the quenching resistor is made from polysilicon whose resistance rises with a decreasing temperature, the recovery time constant also rises with a decrease of the temperature. According to measurements of the manufacturer of the SiPM the recovery time constant is about 7% higher at 1° C than it is at a room temperature of 23° C [109]. During the measurements of the night-sky brightness the temperatures ranged from 10° C to 15° C and a recovery time constant which is 3% to 5% lower than measured in the laboratory has to be taken into account.

The two-dimensional histograms containing the determined time differences Δt and the pulse heights of the stop pulses are shown in the top and middle rows of figure 7.7. The left column is for an over-voltage of 0.8 V, whereas the right column is for an over-voltage of 1.2 V. There are no data for pulse heights smaller than 6 mV due to the detection threshold V_{th}. For $\Delta t < 80\,\text{ns}$ a discrimination of pulses due to thermal noise and due to afterpulsing can be made very clearly. The events in the histogram corresponding to afterpulses are the ones whose pulse heights increase significantly with a rise in Δt until they reach the same level as the ones due to thermal noise. In terms of the pulse height distributions these events are well-visible for pulse heights smaller than the mean of the 1 p.e. peaks (at about 24 mV and 36 mV for the over-voltages 0.8 V and 1.2 V, respectively) and slightly visible for pulse heights smaller than the mean of the 2 p.e. peaks. This kind of plot makes the reason for the asymmetry of the peaks in the pulse height spectra, which we already discussed after regarding them in figure 7.4, more obvious.

To perform a fit to the data, which yields the recovery time of the SiPM, a quantitative discrimination between the pulse heights, which correspond to thermal noise, and those, which correspond to afterpulses, has to be achieved. A cut to the data is applied leaving only pulse heights smaller than the 1.5 p.e. level for the further consideration (these are roughly the events shown in the zoomed displays in the middle row of figure 7.7). Subsequently, the mean pulse height of each Δt bin is calculated. The dashed curves in the middle row of figure 7.7 connect the individual mean values. This curve will act as a cut discriminating between afterpulses and thermal noise for time differences $\Delta t < 80\,\text{ns}$. For larger time differences the differ-

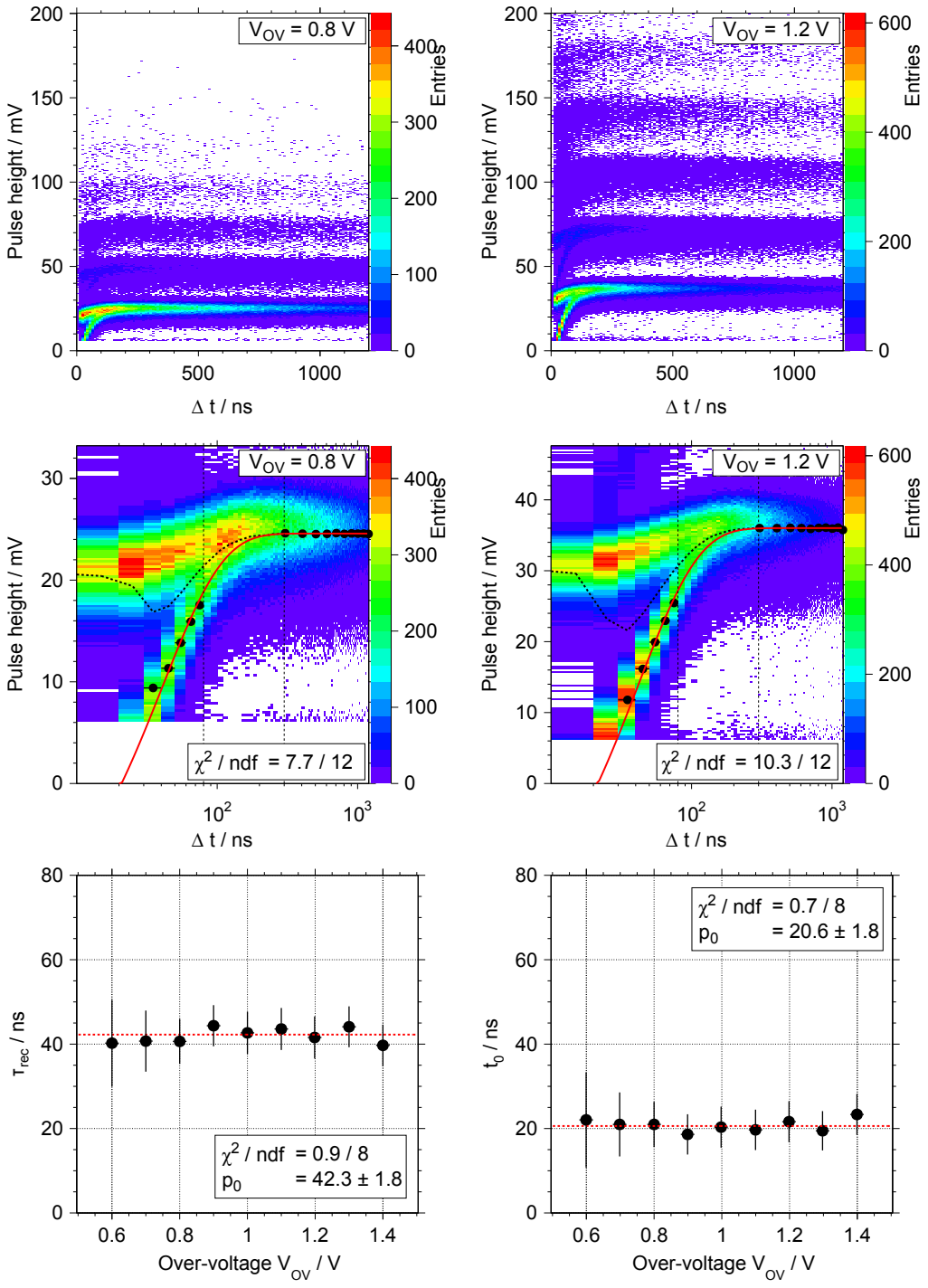

Figure 7.7: **Top row:** Distribution of time differences Δt between a 1 p.e. pulse and the consecutive pulse, and the pulse height of the consecutive pulse for a Hamamatsu S10362-33-100C SiPM. The left plot is exemplary for an over-voltage of $V_{\mathrm{ov}} = 0.8\,\mathrm{V}$, the right one for $V_{\mathrm{ov}} = 1.2\,\mathrm{V}$. Only pulse heights above a detection threshold of $V_{\mathrm{th}} = 6\,\mathrm{mV}$ are considered. **Middle row:** Zoom of top row. The dashed lines are the mean pulse heights for pulses smaller than the 1.5 p.e. level. The black data points are the mean pulse heights for $\Delta t \leq 80\,\mathrm{ns}$ below the dashed line. For $\Delta t \geq 300\,\mathrm{ns}$ they equal the values of the dashed line. The red curves are fits to the data points according to the recharge behavior given by equation (7.2). See text for more details. **Bottom row:** Recovery time constant τ_{rec} and effective dead time t_0 resulting from the mentioned fits as functions of the over-voltage V_{ov}. The red dashed lines are fits of constants to the data.

ent causes of cell breakdowns cannot be discriminated. For $\Delta t > 300\,\text{ns}$ the cells are in good approximation fully recovered and the pulse heights of the afterpulses are approximately identical to the ones of the pulses caused by thermal noise.
Again the mean pulse height of the Δt bins is calculated, but for $\Delta t < 80\,\text{ns}$ only entries of the histogram beneath the dashed curve are considered. As the waveform analysis algorithm cannot find the afterpulses with pulse heights smaller than $V_{\text{th}} = 6\,\text{mV}$, the first two bins are omitted. The same holds for the transition region between $\Delta t = 80\,\text{ns}$ and $\Delta t = 300\,\text{ns}$. For $\Delta t > 300\,\text{ns}$ the mean of ten bins is calculated, resulting in a value each 100 ns. The resulting values are displayed by the black data points. The statistical uncertainty is given by Poisson statistics. A fit according to

$$V_{\text{ph}} = V_{\text{1p.e.}} \cdot \left(1 - \exp\left(-\frac{\Delta t - t_0}{\tau_{\text{rec}}}\right)\right) \tag{7.2}$$

is performed to these data points, where V_{ph} is the pulse height, and t_0 is the time between a cell breakdown and the subsequent start of the recovery process. The fit is shown as the red curve in the histograms. For the considered range the resulting recovery time τ_{rec} and t_0 do not depend on the over-voltage as can be seen from the plots in the bottom row of figure 7.7. We find

$$\tau_{\text{rec}} = (42.3 \pm 1.8)\,\text{ns} \qquad \text{and} \qquad t_0 = (20.6 \pm 1.8)\,\text{ns}\,. \tag{7.3}$$

The recovery time constant is in the expected range, since it is given by $\tau_{\text{rec}} = R_{\text{q}}\, C_{\text{c}}$, with the quenching resistance R_{q} and the cell capacitance C_{c}. In reference [100] these values have been determined for the considered type of SiPM to about $120\,\text{k}\Omega$ and $0.4\,\text{pF}$, respectively.

A question which remains is whether t_0 can be identified as the intrinsic dead time of the cells of the SiPM. It does not seem very convincing, that a cell of the SiPM is dead for about 20 ns. Certainly the cell will be dead for the time of the avalanche process. When the avalanche is initiated the corresponding current de-charges the capacitance of the cell. The current and the voltage along the cell decrease exponentially until the avalanche process is quenched. The time constant of the de-charge of the charge separation zone within the cell is $\tau_{\text{av}} = R_{\text{c}}\, C_{\text{c}}$ and determined by the cell resistance R_{c} and the cell capacitance C_{c}.[8] The diode resistance is in the range of a few hundred ohms to several kiloohms [165], and as mentioned C_{c} is about $0.4\,\text{pF}$. According to these values τ_{av} would be $\mathcal{O}(10 - 100\,\text{ps})$. Therefore, the intrinsic dead time of the cells should not be the reason for the rather high value of t_0. However, the measured timing of the leading edges of the output voltages of the SiPM is different from the timing of the avalanche process, since the grid capacitance of the SiPM C_{g}, which is in parallel to its cells, together with the input impedance of downstream electronics, acts as a low pass. In our case this input impedance is given by the first stage of the amplifier and is $\mathcal{O}(10\,\Omega)$. In addition, further parasitic capacitances in parallel to the SiPM, for instance due to the connection of the photosensor, also affect the timing performance. The total parasitic capacitance is two to three orders of magnitude

[8] The electrical model of an SiPM was presented in figure 4.4. In this model the cell resistance R_{c} is the internal resistance of the current source I_{AC}.

higher than the cell capacitance C_c [100]. Altogether, the leading edge of the voltage output is expected to have a timing in the (sub-)nanosecond range. The measured voltage traces reveal that the majority of pulses take indeed several nanoseconds starting at the baseline to reach their minima (cf. for instance figure 7.1). However, the timing of the trailing edge is given by the recovery time constant.

A critical view at the distributions of Δt and pulse heights in figure 7.7 indicates that the pulse heights of the afterpulses are not sufficiently well approximated by the model of the recovery behavior given by equation (7.2). The model describes the output voltage V_{ph} which an individual cell contributes to the common output signal. The latter is given as the sum of all the individual signals of all cells. In contrast, the data plotted in the histograms are the pulse heights of pulses in the output signal as determined by the waveform analysis algorithm, i.e. the voltage difference between local minima and maxima. These pulse heights are typically smaller than the corresponding voltage V_{ph} of an individual signal, due to the shape of the pulses in the output voltage. Since the minimum of an individual pulse B is not reached instantaneous but after several nanoseconds, a previous pulse A, if not yet fully recovered, will reduce the height of B determined by the waveform analysis. The reduction equals the voltage which the individual pulse A changes from the time of the breakdown corresponding to pulse B, to the time when the minimum corresponding to B in the output voltage is reached. An example of such a reduction of the pulse height of B is shown in figure 7.8 (left). Two cells break down simultaneously leading to a 2 p.e. pulse followed by a pulse caused by the breakdown of another single cell. The first two breakdowns lead to the individual signal displayed by the red dashed line. The last one leads to the individual signal shown by the blue dashed lines, a 1 p.e. signal.[9] However, the output of the SiPM is the sum of these individual signals as given by the black solid curve. Since the second pulse of the output signal happens before the first pulse is sufficiently recovered to the baseline, its amplitude is significantly smaller than the 1 p.e. level.
Such a reduction of the amplitudes can be observed in the distributions of Δt and pulse heights of figure 7.7: If the plotted pulse heights were the ones of the individual pulses, those of the pulses due to thermal noise would not depend on the time difference Δt. But, as expected, they decrease for small Δt as the time difference further decreases. The same must hold for the afterpulses.

An additional effect, which leads to a deviation from the measured pulse heights of the afterpulses to the ones given by the model stated in equation (7.2), is due to a temporary drop of the over-voltage of a single cell after a breakdown. The current which restores the charge separation zone after the breakdown leads to a voltage drop V_q along the quenching resistor of the cell R_q. Thus, the effective over-voltage of the cell is $V_{ov} - V_q$, where V_{ov} is the nominal over-voltage of the SiPM. The effective gain of the cell will be reduced, especially during the beginning of the recharge process when the recharging current is high, and the functional relation between the pulse heights of afterpulses and Δt will be modulated in contrast to the one of the model. Unluckily, the afterpulses with small Δt cannot be observed since their

[9] see equation (4.18) or appendix A.2 for the functional form of these pulses

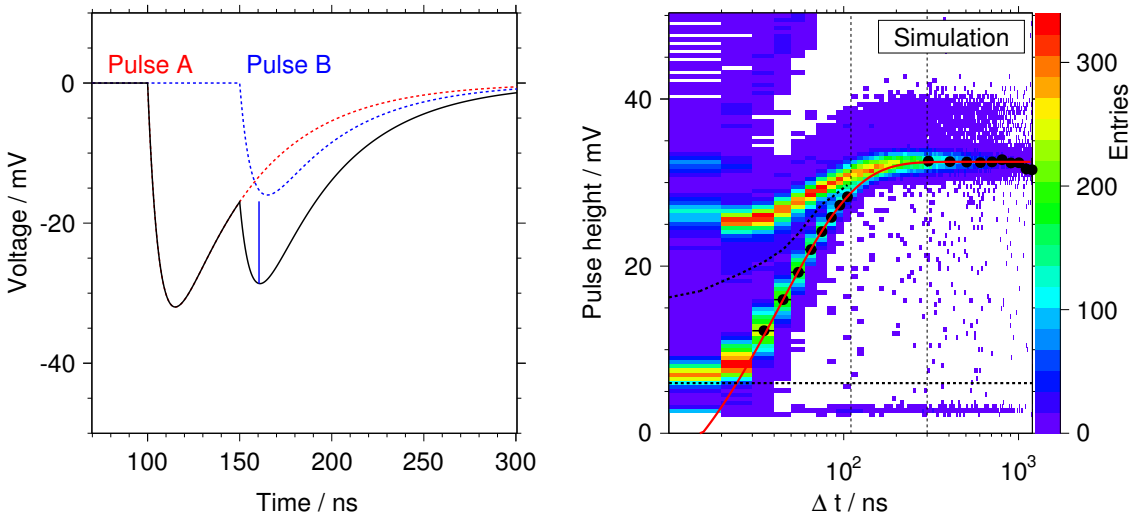

Figure 7.8: **Left:** Sketch of a voltage trace to illustrate the pile-up of pulses. A 2 p.e. pulse (pulse A, red dashed curve) and a consecutive 1 p.e. pulse (pulse B, blue dashed curve) sum up to the output signal given by the black solid curve. Due to the pile-up of the pulses the height of the second pulse, shown by the blue solid line, is smaller than the amplitude of an isolated 1 p.e. pulse. **Right:** Simulated distribution of time differences Δt between a 1 p.e. pulse and the consecutive pulse, and the pulse height of the consecutive pulse. The black data points denote the mean pulse heights of afterpulses. The red solid line is a fit according to equation (7.2) to these data points. Fit results: $V_{1\,\mathrm{p.e.}} = (32.48 \pm 0.08)\,\mathrm{mV}$, $\tau_{\mathrm{rec}} = (43.5 \pm 3.5)\,\mathrm{ns}$, $t_0 = (15.5 \pm 4.6)\,\mathrm{ns}$, $\chi^2\,/\,\mathrm{ndf} = 4.0\,/\,15$. See text for more details.

signal levels are too small.
By means of a simulation this modulation can be visualized. 150000 voltage traces are simulated with the SiPM simulation toolkit G4SiPM (cf. section 4.3) and analyzed in the same manner as the measured voltage traces. Simulated is an SiPM presenting the one of the measurements. It also has 900 cells with a cell pitch of 100 µm, is operated at an over-voltage of 1.2 V, and features thermal noise, afterpulsing, and optical crosstalk. Its recovery time is set to $\tau_{\mathrm{rec}} = 42.3\,\mathrm{ns}$ and the intrinsic dead time of its cell is very small with a value of 1 ps. The simulation accounts for the reduction of the effective over-voltage of the cells after a breakdown, caused by the voltage drop along quenching resistors with $R_{\mathrm{q}} = 120\,\mathrm{k\Omega}$. The pulse shaper module of G4SiPM leads to simulated output pulses similar to the measured ones. However, the simulation features reduced electronics noise compared to the measurements. This allows, in contrast to the measured data, to detect also pulses of smaller amplitude since the detection threshold of the waveform analysis can be reduced to $V_{\mathrm{th}} = 2\,\mathrm{mV}$. Details on the simulation input parameters are summarized in table A.2 given in appendix A.3.
The results of the simulation are shown in figure 7.8 (right) for pulse heights up to about the 1.5 p.e. level. As for the measured data the pulse heights of thermal noise-pulses decrease as Δt decreases. Also the mentioned deviation of the pulse heights

of afterpulses from the behavior described by equation (7.2) is clearly visible for very small Δt. The mean pulse heights of the afterpulses are shown by the black data points. The cut values to separate the afterpulses from the pulses due to thermal noise have been determined manually, and only values above a pulse height of 6 mV have been considered to determine the mean signal levels of the afterpulses. (The cut values and the pulse height threshold are depicted in the histogram of figure 7.8 by the thick, dashed curve and the horizontal, dashed line, respectively.) A fit according to equation (7.2) is performed to the pulse heights of the afterpulses. As for the measured data, bins with $\Delta t \leq 30$ ns and within the transition region, here between 110 ns and 300 ns, are not considered. The fit yields $V_{1\,\mathrm{p.e.}} = (32.48 \pm 0.08)$ mV, $\tau_{\mathrm{rec}} = (43.5 \pm 3.5)$ ns, and $t_0 = (15.5 \pm 4.6)$ ns (χ^2 / ndf = 4.0 / 15).
Indeed, equation (7.2) describes the recovery behavior only well for Δt greater than several ten nanoseconds. However, the recovery time resulting from the fit agrees reasonably well with the one used for the simulation.

Nevertheless, the effect of the reduced pulse heights due to the pile-up of pulses should lead to a small systematic bias in the determination of the recovery time constant τ_{rec} towards smaller values. To verify this, the measured voltage traces which contain only a start pulse are selected and an exponential function of the form

$$V(t) = V_0 \cdot \exp\left(-\frac{t - t_{\mathrm{trig}}}{\tau_{\mathrm{rec}}}\right) + V_{\mathrm{base}} \tag{7.4}$$

is fitted to the tails of the pulses. V_0 accounts for the amplitude of a pulse, t_{trig} for the time when the pulse occurs, and V_{base} for a shift of the baseline to values different from zero. The fits yield that τ_{rec} does not depend on the over-voltage, and we find

$$\tau_{\mathrm{rec}} = (46.2 \pm 2.7)\,\mathrm{ns}\,. \tag{7.5}$$

Although the values of the recovery time constant determined with the two different approaches agree with each other within their uncertainties, the last mentioned value is higher by about 9% than the other one over the complete considered range of over-voltages. Within the further course of the analysis we will use $\tau_{\mathrm{rec}} = (46.2 \pm 2.7)$ ns at a temperature of $(1.0 \pm 0.5)^\circ$ C.
The recovery time constant has also been measured in the scopes of references [96] and [100]. The reported values are in agreement with the one determined in this work.

Besides the intrinsic dead time of the cells, a *system dead time* also exists which is caused by the detection threshold V_{th} of the waveform analysis algorithm. The system dead time is given by the time difference Δt when the signal level of the afterpulses exceeds V_{th}. The modes of actions of these two dead times differ essentially from each other. During the intrinsic dead time a cell is insensitive to any event which normally can trigger an avalanche breakdown. Thus, such events during the dead time do not affect the course of the avalanche and recharge process. But if a cell breakdown occurs before the system dead time is reached, the cell will again be de-charged and the recharge process starts over.
The effect of the system dead time to the measured night-sky photon flux will be

studied by means of Monte Carlo methods in section 7.5. Within the next paragraphs we will evaluate how the intrinsic dead time t_{dead} affects a measured cell breakdown rate assuming all signals are detectable.
The live time of a measurement is given by

$$t_{\mathrm{live}} = t_{\mathrm{tot}} - t_{\mathrm{dead}}^{\mathrm{tot}} \tag{7.6}$$

where t_{tot} is the total time the measurement has been running and $t_{\mathrm{dead}}^{\mathrm{tot}}$ is the total dead time. The latter depends on the cell breakdown rate of the SiPM R_{cb}. It is given by

$$t_{\mathrm{dead}}^{\mathrm{tot}} = t_{\mathrm{dead}} \cdot \frac{R_{\mathrm{cb}}}{N_{\mathrm{cells}}} \cdot t_{\mathrm{tot}} \,. \tag{7.7}$$

The division by the number of cells of the SiPM N_{cells} accounts for the fact that the intrinsic dead time is related to the single cells and not to the entire SiPM. The cell breakdown rate corrected for the intrinsic dead time is given by

$$R_{\mathrm{corr}} = \frac{t_{\mathrm{tot}}}{t_{\mathrm{live}}} \cdot R_{\mathrm{cb}} = \frac{R_{\mathrm{cb}}}{1 - t_{\mathrm{dead}} \cdot R_{\mathrm{cb}}/N_{\mathrm{cells}}} \,. \tag{7.8}$$

To evaluate the significance of the dead time correction we choose $R_{\mathrm{cb}} = 50\,\mathrm{MHz}$ which exceeds the corresponding rates we will encounter in the data of the NSB measurements. Moreover, since the intrinsic dead time could not be resolved with the discussed method, we further choose $t_{\mathrm{dead}} = t_0 = 20.6\,\mathrm{ns}$ to result in a maximum limit. With $N_{\mathrm{cells}} = 900$ we find $(R_{\mathrm{corr}} - R_{\mathrm{cb}})/R_{\mathrm{corr}} = 1.1 \cdot 10^{-3}$. The uncorrected cell breakdown rate differs only by about 0.1% from the corrected rate. The difference is even smaller for reduced cell breakdown rates, and smaller by orders of magnitude for an intrinsic dead time in the range of tens to hundreds of picoseconds.

7.4 Correlated noise

To determine the effect of the system dead time on the measurement of the night-sky photon flux, the probabilities of afterpulsing and optical crosstalk have to be known. In addition, also the timing constants of afterpulsing are needed to study the effect. The studies themselves will be performed in the following section by means of a Monte Carlo method. Within the section at hand the probabilities and timing constants of correlated noise will be determined.
If the probabilities of the correlated noise are known we can also calculate how many of the breakdowns contributing to a measured cell breakdown rate are due to afterpulsing and crosstalk on average. The remaining rate will only be attributed to signal-photons and thermal noise.

To determine the afterpulse probability we reconsider the Δt distributions discussed in the previous section. In figure 7.9 the distributions of figure 7.7 are shown again, but this time the additional information on the pulse heights are disregarded. The left plot is again for an over-voltage of 0.8 V, whereas the right one is for 1.2 V. Let

us briefly recall: Δt is the time between an initial 1 p.e. pulse and its consecutive pulse. The SiPM is operated in darkness. If there was no afterpulsing at all, all pulses, the initial ones as well as the consecutive ones, would be caused by thermal excitation of the silicon. In this case the Δt distributions would be of the form

$$f(\Delta t) = A_0 \cdot \exp(-R_{\mathrm{th}} \cdot \Delta t) \tag{7.9}$$

with $R_{\mathrm{th}} = 1/\tau_{\mathrm{th}}$ being the thermal noise rate and the scaling factor $A_0 = N_{\mathrm{th}}/\tau_{\mathrm{th}}$, where N_{th} is the number of thermally generated pulses. Fits of exponential functions to the data are shown in figure 7.9 as the blue dashed lines. For these fits only data points with $\Delta t > 800\,\mathrm{ns}$ have been considered. The excess of the data for smaller Δt is due to afterpulsing. From the plots it is already visible by eye that a higher over-voltage results in a higher thermal noise rate as well as in a higher afterpulse probability. The steep cutoff at very small time differences is caused by the threshold of the waveform analysis algorithm: afterpulses which occur very fast after the initial pulse have significantly reduced pulse heights since the cell is only slightly recharged; thus, these pulses are not identified by the analysis.

Afterpulses are caused by charge carriers in the silicon being stalled at trap levels and released on average after a characteristic time τ_{AP}. If we consider only afterpulses, the probability density function (p.d.f.) of time differences $\Delta t \geq 0$ for afterpulsing is given by

$$\mathrm{p.d.f.}_{\mathrm{AP}}(\Delta t) = \frac{1}{\tau_{\mathrm{AP}}} \exp\left(-\frac{\Delta t}{\tau_{\mathrm{AP}}}\right). \tag{7.10}$$

Since the p.d.f. of thermal noise has the same structure we introduce

$$\mathrm{p.d.f.}_i(\Delta t) = \frac{1}{\tau_i} \exp\left(-\frac{\Delta t}{\tau_i}\right), \qquad i = 1, 2, \ldots \tag{7.11}$$

as the probability density functions for different causes i of the consecutive pulses. In this p.d.f. only consecutive pulses due to one specific cause i are considered. The probability that such a pulse occurs later than δt is given by

$$\begin{aligned} P_i(\Delta t > \delta t) = \int_{\delta t}^{\infty} \mathrm{p.d.f.}_i(\Delta t')\ \mathrm{d}(\Delta t') &= 1 - \int_0^{\delta t} \mathrm{p.d.f.}_i(\Delta t')\ \mathrm{d}(\Delta t') \\ &= \exp\left(-\frac{\delta t}{\tau_i}\right). \end{aligned} \tag{7.12}$$

Now let there be two different causes 1 and 2 which can provide the consecutive pulses. The p.d.f. for a pulse at the time δt being due to cause 1 and being earlier than a pulse due to cause 2 is given by $\mathrm{p.d.f.}_1(\delta t)$ multiplied by the probability that no pulse due to cause 2 occurred until δt. Since we can interchange the two causes we find the combined p.d.f. to be

$$\begin{aligned} \mathrm{p.d.f.}_{1,2}(\Delta t = \delta t) &= \mathrm{p.d.f.}_1(\delta t) \left(1 - \int_0^{\delta t} \mathrm{p.d.f.}_2(\Delta t')\ \mathrm{d}(\Delta t')\right) \\ &\quad + \mathrm{p.d.f.}_2(\delta t) \left(1 - \int_0^{\delta t} \mathrm{p.d.f.}_1(\Delta t')\ \mathrm{d}(\Delta t')\right) \\ &= \left(\frac{1}{\tau_1} + \frac{1}{\tau_2}\right) \exp\left(-\frac{\delta t}{\tau_1}\right) \exp\left(-\frac{\delta t}{\tau_2}\right). \end{aligned} \tag{7.13}$$

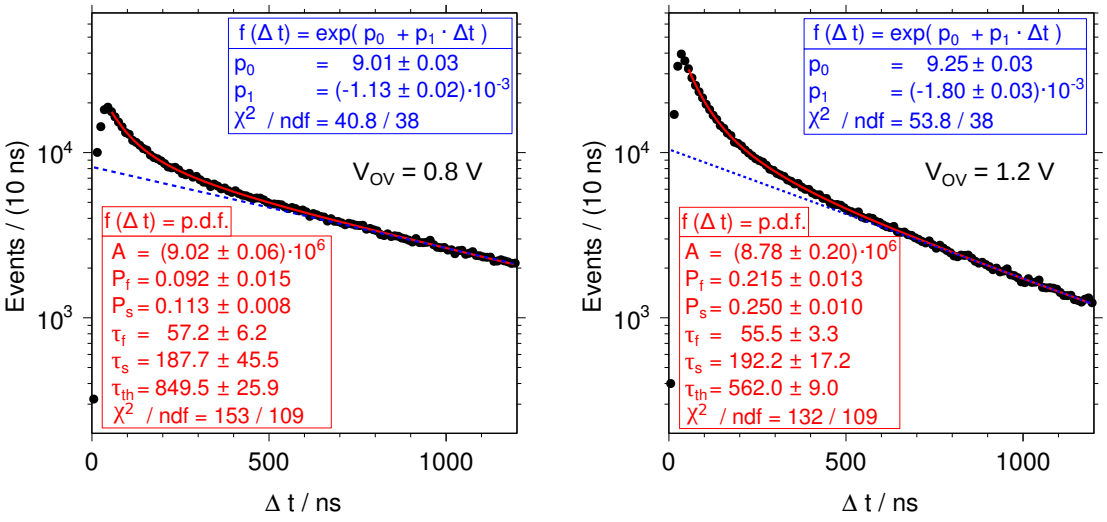

Figure 7.9: Measured distributions of time differences Δt between a 1 p.e. start pulse and the consecutive pulse (cf. figure 7.6). Left for an over-voltage of $V_{\mathrm{ov}} = 0.8\,\mathrm{V}$, right for $V_{\mathrm{ov}} = 1.2\,\mathrm{V}$. The solid red curves are fits to the data for $\Delta t > 50\,\mathrm{ns}$ following equation (7.16). The blue dashed curves are exponential fits for $\Delta t > 800\,\mathrm{ns}$ revealing the contribution due to thermal noise.

In analogy, the p.d.f. for three causes is given by

$$\text{p.d.f.}_{1,2,3}(\Delta t = \delta t) = \left(\frac{1}{\tau_1} + \frac{1}{\tau_2} + \frac{1}{\tau_3}\right) \exp\left(-\frac{\delta t}{\tau_1}\right) \exp\left(-\frac{\delta t}{\tau_2}\right) \exp\left(-\frac{\delta t}{\tau_3}\right). \quad (7.14)$$

The data favor three causes. Taking only two causes into account results in a worse agreement between the theory and the measured data. If a fourth cause is introduced, the fourth time constant equals one of the others within their uncertainties, and the fourth cause is thus unnecessary. We interpret the three essential causes as thermal noise, slow afterpulsing, and fast afterpulsing and refer to their time constants as τ_{th}, τ_{s}, and τ_{f}, respectively.

Not every initial pulse is followed by pulses of all three causes. If the time after the initial pulse is sufficiently long, a thermal noise pulse will occur in all cases. This does not apply for afterpulses: some cell breakdowns will evoke an afterpulse (or more than one), others will not. Thus, regarding just one initial pulse there is a certain possibility that no afterpulse will occur at all. Let $P_{\mathrm{AP,f}}$ and $P_{\mathrm{AP,s}}$ be the probabilities that one cell breakdown causes one further cell breakdown due to a fast or a slow afterpulse, respectively. The probability of afterpulsing in general is then given by

$$P_{\mathrm{AP}} = 1 - (1 - P_{\mathrm{AP,f}})(1 - P_{\mathrm{AP,s}}) \quad (7.15)$$

which is 1 minus the probability that neither a fast nor a slow afterpulse occurs. After an initial breakdown the following cases can take place

- no afterpulsing with the probability: $(1 - P_{\mathrm{AP,f}})(1 - P_{\mathrm{AP,s}})$

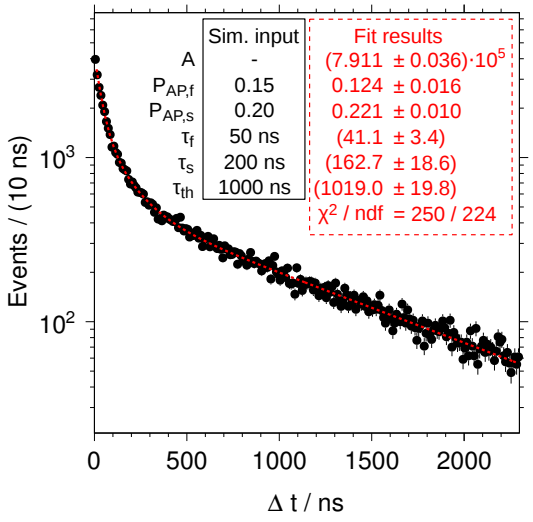

Figure 7.10: Simulated distributions of time differences Δt between a first pulse and the consecutive pulse. The simulation uses the input parameters as stated in the left box. The red curve is a fit to the data following equation (7.16). See text for more details.

- fast but no slow afterpulsing with the probability: $P_{\mathrm{AP,f}}\,(1 - P_{\mathrm{AP,s}})$
- slow but no fast afterpulsing with the probability: $(1 - P_{\mathrm{AP,f}})\,P_{\mathrm{AP,s}}$
- fast and slow afterpulsing with the probability: $P_{\mathrm{AP,s}}\,P_{\mathrm{AP,f}}$

This leads to the combined probability density function

$$\begin{aligned}
\text{p.d.f.}(\Delta t) = {} & (1 - P_{\mathrm{AP,f}})(1 - P_{\mathrm{AP,s}})\ \frac{1}{\tau_{\mathrm{th}}}\ \exp\left(-\frac{\Delta t}{\tau_{\mathrm{th}}}\right) \\
& + P_{\mathrm{AP,f}}(1 - P_{\mathrm{AP,s}})\left(\frac{1}{\tau_{\mathrm{f}}} + \frac{1}{\tau_{\mathrm{th}}}\right)\ \exp\left(-\frac{\Delta t}{\tau_{\mathrm{th}}}\right)\exp\left(-\frac{\Delta t}{\tau_{\mathrm{f}}}\right) \\
& + (1 - P_{\mathrm{AP,f}})P_{\mathrm{AP,s}}\left(\frac{1}{\tau_{\mathrm{s}}} + \frac{1}{\tau_{\mathrm{th}}}\right)\ \exp\left(-\frac{\Delta t}{\tau_{\mathrm{th}}}\right)\exp\left(-\frac{\Delta t}{\tau_{\mathrm{s}}}\right) \\
& + P_{\mathrm{AP,f}}\,P_{\mathrm{AP,s}}\left(\frac{1}{\tau_{\mathrm{f}}} + \frac{1}{\tau_{\mathrm{s}}} + \frac{1}{\tau_{\mathrm{th}}}\right)\ \exp\left(-\frac{\Delta t}{\tau_{\mathrm{th}}}\right)\exp\left(-\frac{\Delta t}{\tau_{\mathrm{f}}}\right)\exp\left(-\frac{\Delta t}{\tau_{\mathrm{s}}}\right).
\end{aligned} \tag{7.16}$$

As required for probability density functions

$$\int_0^\infty \text{p.d.f.}\ \mathrm{d}(\Delta t) = 1\,.$$

To test this model a Monte Carlo-like simulation is performed. 230000 points in time t_1, t_2, …, t_{230000} are distributed uniformly over 230 ms. These times represent initial pulses of thermal noise with a rate of 1 MHz, i.e. $\tau_{\mathrm{th}} = 1000$ ns. The times are stored and for each $t_i, i = 1, 2, \ldots, 230000$, the simulation dices whether a fast or a slow afterpulse occurs. Both events are diced independently, so both fast and

slow afterpulsing may take place. The probability for fast and slow afterpulsing are set to $P_{\mathrm{AP,f}} = 0.15$ and $P_{\mathrm{AP,s}} = 0.20$, respectively. If afterpulsing occurs, the simulation dices a time distance t_d according to a choice of time constants $\tau_\mathrm{f} = 50\,\mathrm{ns}$ and $\tau_\mathrm{s} = 200\,\mathrm{ns}$. At $t_i + t_\mathrm{d}$ a further point in time is stored. For every new stored time the routine of dicing afterpulses is performed again to account for the fact that afterpulses can trigger further afterpulses. When the simulation is terminated in the sense that no further time differences have to be diced, the simulated times are sorted chronologically and inspected afterwards. To make use of the terminology previously introduced, we will treat the simulation result as if there was a pulse at each of the stored times. If such a pulse does not have a preceding pulse 1000 ns prior to it, it will be regarded as a start pulse. In contrast to the procedure in the previous section this *silent time* can be set to a higher value without decreasing the statistics to unreasonable values, since the inspected overall time is not limited to the trace length $t_\mathrm{trace} = 2300\,\mathrm{ns}$. For each start pulse the time difference Δt to its consecutive pulse is determined. The distribution of these time differences is shown in figure 7.10. The simulation results in a total number of about 330000 pulses, including the 230000 initial ones. About 80000 pulses are identified as start pulses. Taking an additional normalization factor A into account, the function of equation (7.16) can be fitted to the data as shown in figure 7.10 by the red curve. The additional factor has no physical meaning but is necessary since unlike the p.d.f. the data are not normalized. The fit results are also stated in the figure. They agree well with the input parameters of the simulation.

Fits according to equation (7.16) are also applied to the measured data and are given exemplary for over-voltages of 0.8 V and 1.2 V in figure 7.9 by the red curves. These fits use data with $\Delta t > 50\,\mathrm{ns}$, since pulses which result in a small Δt are typically fast afterpulses which have significantly reduced pulse heights. These pulses cannot be detected due to the detection threshold. The afterpulse probabilities P_AP, $P_\mathrm{AP,f}$, and $P_\mathrm{AP,s}$, the time constants τ_f and τ_s, as well as the thermal noise rate $R_\mathrm{th} = 1/\tau_\mathrm{th}$ resulting from the fits are shown for all regarded over-voltages in figures 7.11 and 7.12.
Within the considered range of over-voltages the afterpulse probabilities $P_\mathrm{AP,f}$ and $P_\mathrm{AP,s}$ appear to be power functions. Thus, fits according to $P(V_\mathrm{ov}) = a \cdot (V_\mathrm{ov})^x$ are performed to the data. The resulting exponents x agree with 2 within their uncertainties.[10] Hence, for simplicity and since it represents the data very well, these probabilities will be parametrized for the further course of the analysis by functions of the form $P_\mathrm{AP,f,s}(V_\mathrm{ov}) = a_\mathrm{f,s} \cdot (V_\mathrm{ov})^2$ with the free parameters a_f and a_s for fast and slow afterpulsing, respectively. The corresponding fits and their results are displayed in figure 7.11 (left). We find

$$a_\mathrm{f} = (0.143 \pm 0.004)\,\mathrm{V}^{-2} \qquad \text{and} \qquad \mathrm{a_s} = (0.172 \pm 0.003)\,\mathrm{V}^{-2}\,. \tag{7.17}$$

Following equation (7.15) the overall afterpulse probability P_AP is given by

$$\begin{aligned} P_\mathrm{AP}(V_\mathrm{ov}) &= (a_\mathrm{f} + a_\mathrm{s}) \cdot V_\mathrm{ov}^2 - a_\mathrm{f} \cdot a_\mathrm{s} \cdot V_\mathrm{ov}^4 \\ &= p_2 \cdot V_\mathrm{ov}^2 - p_4 \cdot V_\mathrm{ov}^4\,. \end{aligned} \tag{7.18}$$

[10] corresponding fits are shown in figure A.3 in appendix A.3

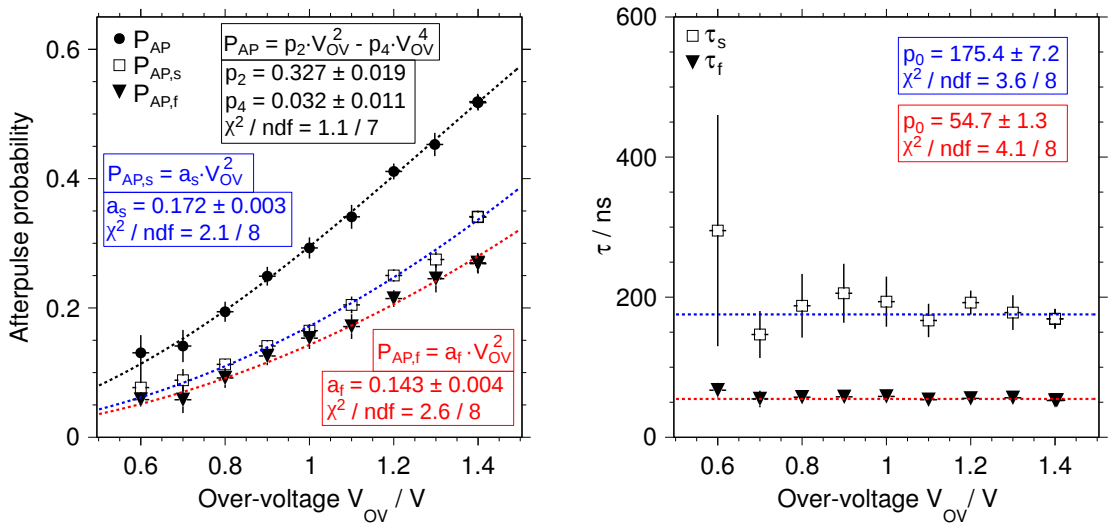

Figure 7.11: **Left:** Afterpulse probabilities determined by the fit to the Δt distributions as functions of the over-voltage V_{ov}. The squares are the probability $P_{\mathrm{AP,s}}$ of slow afterpulses. The triangles are the probability $P_{\mathrm{AP,f}}$ of fast afterpulses. The circles are the combined probability P_{AP}. The lines are fits of the form $P = a \cdot V_{\mathrm{ov}}^2$. **Right:** Time constants of fast and slow afterpulsing τ_{f} and τ_{s} determined by the fit to the Δt distributions as a function of the over-voltage V_{ov}. The lines are zero order polynomials.

Analytically we find

$$p_2 = (0.315 \pm 0.007)\,\mathrm{V}^{-2} \qquad \text{and} \qquad \mathrm{p}_4 = (0.025 \pm 0.001)\,\mathrm{V}^{-4}\,. \tag{7.19}$$

A function according to equation (7.18) is fitted to the data and displayed in figure 7.11 (left). The fit results agree well with the analytically derived parameters. Within the further course of this analysis we will use the analytically derived values for a parametrization of P_{AP}.

The determined time constants τ_{f} and τ_{s} are shown in figure 7.11 (right). Within their statistical uncertainties they are constant for the considered over-voltage range. Their values are

$$\tau_{\mathrm{f}} = (54.7 \pm 1.3)\,\mathrm{ns} \qquad \text{and} \qquad \tau_{\mathrm{s}} = (175.4 \pm 7.2)\,\mathrm{ns}\,. \tag{7.20}$$

The thermal noise rate is expected to depend linearly on the over-voltage and to be zero for $V_{\mathrm{ov}} = 0$ (cf. chapter 4). The determined values are shown in figure 7.12 (left). The results of a linear fit to the data demonstrate that the measurement is in agreement with the expectations. The fit and its results are also depicted in figure 7.12 (left).

To reconstruct the measured night-sky photon flux we will apply the photon counting method as discussed in section 6.1. Let us briefly recall that a key feature of the method is that it corrects already for counts due to optical crosstalk. The cell

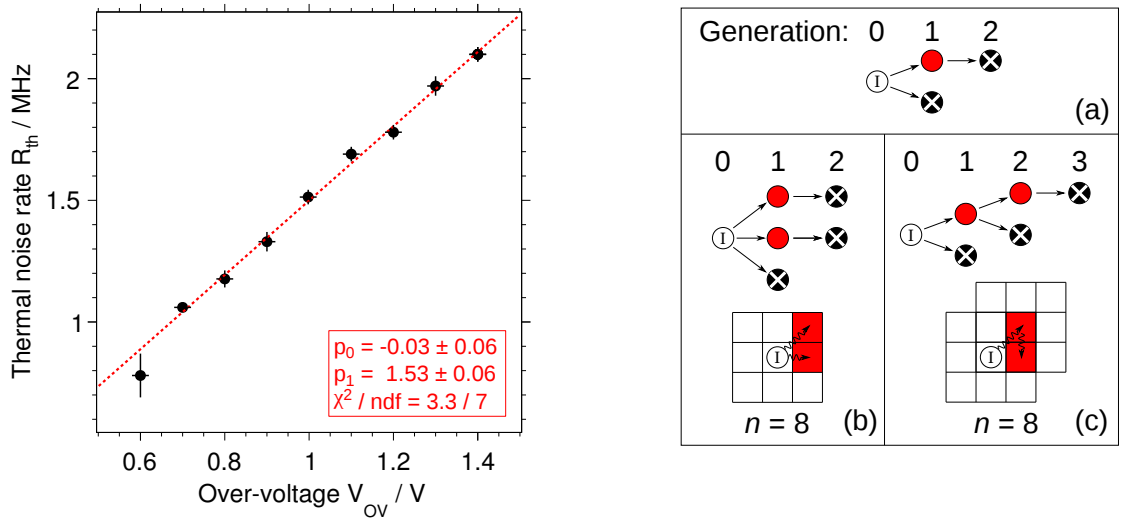

Figure 7.12: **Left:** Thermal noise rate determined by the fit to the Δt distributions as a function of the over-voltage V_{ov}. The red line is a linear fit to the data. **Right:** Schematic of optical crosstalk (OXT). (a) An initial cell breakdown (I) causes one additional cell breakdown due to OXT (red circle). This is a first generation OXT breakdown. The X are the $n-1$ neighboring cells which do not break down. (b) The initial breakdown causes two OXT breakdowns in the first generation. Below the $n = 8$ neighbors of the cell causing the OXT breakdown are shown. Curly arrows denote the OXT-photons which trigger the additional breakdowns. (c) The initial breakdown causes one OXT breakdown in the first generation, which itself causes another OXT breakdown in the second generation.

breakdown rate determined with the photon counting method R_{pc} thus approximately equals the cell breakdown rate exclusively due to signal-photons, afterpulses, and thermal noise. To correct this rate for counts due to afterpulsing, the afterpulse probability can be used. Yet, it has to be handled with caution if we want to apply it for the reconstruction of a measured signal-photon flux. It tells us on a statistical basis how many cell breakdowns will occur due to afterpulsing. However, the experimental setup is typically not able to detect and identify all these afterpulses. In our case we will miss quite a number of (especially fast) afterpulses since their signal levels do not exceed the detection threshold. Anyhow, since we know which pulses we miss, we can correct the afterpulse probability appropriately. We will come back to this later. For the moment we assume that we can detect each afterpulse and address a further fact.

Even with this ideal pulse detection efficiency it is not sufficient to correct the cell breakdown rate R_{pc} by a factor of $1/(1 + P_{\mathrm{AP}})$ to remove the cell breakdowns due to afterpulsing. This is by the reason that afterpulses can again act as the initial pulse for further afterpulses. But also the correction factor $1/(1 + \sum_{n=1}^{\infty} (P_{\mathrm{AP}})^n)$, which accounts for a series of afterpulses, is not sufficient either since also cell breakdowns due to optical crosstalk can act as the initial breakdown for afterpulses. These crosstalk-breakdowns are already removed from R_{pc}, but nevertheless they happen

in the SiPM. To get the appropriate factor for the correction for afterpulses we need the probability of optical crosstalk as well.

If a cell of the SiPM breaks down, crosstalk-photons are created which can propagate to a different cell and trigger a further breakdown there. This additional breakdown happens approximately simultaneously due to the very fast evolution of the avalanche process and the short distances which the crosstalk-photons have to propagate. The emission spectrum ranges from about 400 nm to values beyond 1100 nm [166] around where the silicon becomes transparent for the photons. Crosstalk-photons which trigger cell breakdowns have propagated directly through the semiconductor or have left and subsequently being reflected at the coating backwards into the silicon. Due to the short absorption length of the photons (e.g. 10 µm at a wavelength of 800 nm, cf. figure 4.1), optical crosstalk is preferred in cells close to the one of the initial breakdown. This has been demonstrated in reference [167] where the application of a digital SiPM (cf. section 4.4) allowed to identify the cells which fired due to crosstalk.
Let n be the number of cells in which a breakdown can be triggered by cross-talk photons. We will refer to these n cells and the one with the initial breakdown as *neighbors*. The initial cell is called *cell A*. Let further p be the probability that a cell will break down due to optical crosstalk, if its neighbor has a breakdown. For our model we assume that p is identical for all cells. The probability $P(k)$ that in total k breakdowns due to optical crosstalk are triggered is assumed to be approximated by the binomial distribution[11]

$$P_n(k) = \left(\begin{array}{c} n \\ k \end{array} \right) p^k \, (1-p)^{n-k} \, . \tag{7.21}$$

In this model, the absorption of more than one crosstalk-photon in a particular cell will lead to only one breakdown of the cell, due to the fast evolution of the process of optical crosstalk. The equation is only valid for the breakdowns due to crosstalk-photons originating from cell A. But the neighbors of A can also produce crosstalk-photons if they brake down. Thus, it is reasonable to arrange the breakdowns in generations. Cell A can cause crosstalk-breakdowns of the first generation, its neighbors can cause crosstalk-breakdowns of the second generation in their neighbors (not all of them are also neighbors of cell A), and so on (cf. figure 7.12).
The probability that no optical crosstalk occurs after an initial breakdown is given by

$$\widetilde{P}_n(0) = P_n(0) = (1-p)^n = 1 - P_{\mathrm{OXT},\geq 1} \tag{7.22}$$

where $P_{\mathrm{OXT},\geq 1}$ is the probability that at least one additional cell fires due to crosstalk after the initial breakdown.
Although we introduced the expression *generation*, we should keep in mind that the development of optical crosstalk is virtually simultaneous. This implies that cells which have broke down in a certain generation cannot be triggered to break down in a successive generation.
Hence, the probability that exactly one cell fires after the initial breakdown $\widetilde{P}_n(1) \equiv$

[11] this approach has also been discussed in reference [168]

P_{OXT} is given by the product of the probability that exactly one cell breaks down in the first generation $P_n(1)$ and the probabilty of no breakdown in the second generation $P_{n-1}(0)$:

$$\widetilde{P}_n(1) = P_n(1)\, P_{n-1}(0) = n\, p\, (1-p)^{2n-2} = P_{\mathrm{OXT}} \tag{7.23}$$

Here the index $n-1$ indicates that the cell which breaks down in the first generation has only $n-1$ neighbors which could break down due to optical crosstalk in the second generation, since its neighbor cell A is already busy with the initial breakdown. For numbers of crosstalk-breakdowns $k > 1$ no simple expression for the probability $\widetilde{P}_n(k)$ to have k further breakdowns after the initial one can be realized if it shall provide for a free choice of the number of neighbors n. For geometric and combinatorial reasons n has to be chosen prior to identifying all the possible combinations which can lead to k crosstalk-breakdowns after an initial one. The sum of all the individual probabilities for these combinations will lead to $\widetilde{P}_n(k)$. With increasing n and k the vastly growing number of possible combinations leads to more and more complex analytic expressions for $\widetilde{P}_n(k)$. Since within the further course of this analysis we will only need the analytic expressions for $k \leq 1$ given by equations (7.22) and (7.23), we will not discuss further details here. Where $k > 1$ will be needed, numerical simulations taking advantage of the SiPM simulation software G4SiPM (cf. section 4.3) will be performed. However the interested reader might refer to reference [168] to find analytic expressions for higher k and several choices of n.

Experimentally the crosstalk probabilities $P_{\mathrm{OXT},\geq 1}$ and P_{OXT} can be obtained by studying the distribution of events in a pulse height spectrum. The same raw data as for the determination of the afterpulse probabilities are exploited. In contrast to the determination of the afterpulse probabilities where we studied pairs of pulses, this time we consider the distribution of pulse heights for single pulses which have no pulse 935 ns prior to them.[12] Since the SiPM is operated in darkness these pulses are most likely caused by thermal breakdowns and thermal breakdowns combined with optical crosstalk. The amount of events due to afterpulses or multiple simultaneous thermal breakdowns is negligible.
The probability that a cell breakdown causes at least one additional cell breakdown due to optical crosstalk is then given by the number of events with two or more cells breaking down $N_{\geq 2}$ divided by the total number of events N_{tot}.

$$P_{\mathrm{OXT},\geq 1} = \frac{N_{\geq 2}}{N_{\mathrm{tot}}} \tag{7.24}$$

[12] The *silent zone* (cf. figure 7.6) prior to the pulse could be increased in contrast to the analysis of the afterpulse probabilities since we do not need a consecutive pulse here. The statistics are therefore sufficient even with the high silent time. The actual value of 935 ns derives from a preliminary analysis of afterpulses and equals about five times of the preliminary value of the time constant of slow afterpulses.

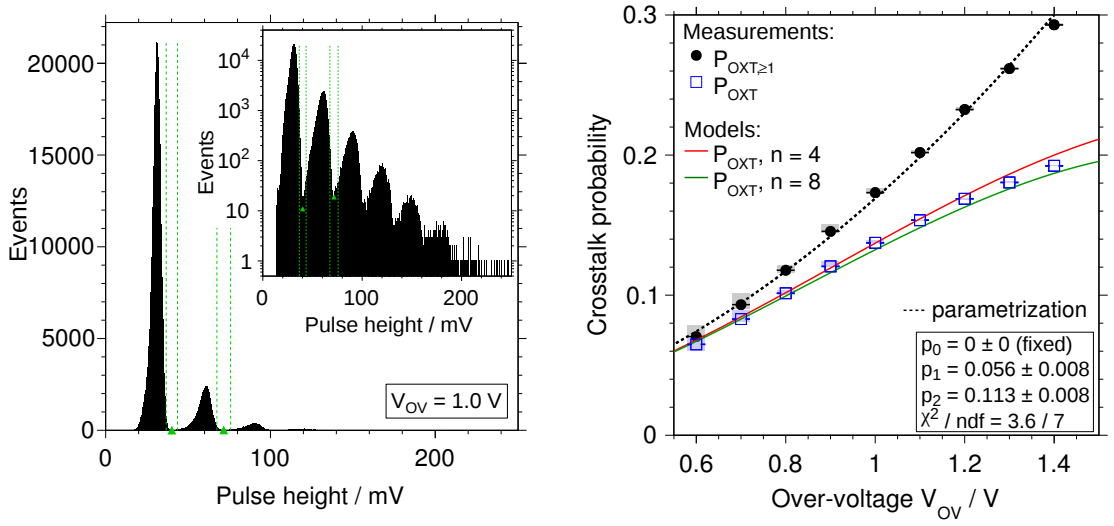

Figure 7.13: **Left:** Exemplary pulse height spectrum at an over-voltage of 1.0 V applied for the analysis of the crosstalk probability. The inset shows the same data on a logarithmic scale. See text for further details. **Right:** Probabilities of optical crosstalk as functions of the over-voltage V_{ov}. The blue, open squares are the probability P_{OXT} that an initial cell breakdown triggers exactly one additional cell breakdown. The black points are the probability $P_{OXT,\geq1}$ that an initial cell breakdown triggers one or more additional cell breakdowns. The black dashed curve is a fit of a second order polynomial fitted to the $P_{OXT,\geq1}$ data. The green and red solid lines are predictions for P_{OXT} derived from the model of optical crosstalk. See text for further details.

The probability that a cell breakdown causes exactly one additional breakdown due to optical crosstalk is given by the number of events with two cell breakdowns N_2 divided by N_{tot}.

$$P_{OXT} = \frac{N_2}{N_{tot}} \tag{7.25}$$

$$= \frac{N_{\geq2}}{N_{tot}} - \frac{N_{\geq3}}{N_{tot}} = P_{OXT,\geq1} - \frac{N_{\geq3}}{N_{tot}} \tag{7.26}$$

where $N_{\geq3}$ is the number of events with at least three cell breakdowns.

An exemplary pulse height spectrum for an over-voltage of 1.0 V is shown in figure 7.13 (left). The green triangles mark the minima which separate the individual peaks from each other. Since the peaks are not perfectly separated the systematic uncertainty on the choice of the borderline between two peaks is determined by varying it by 0.2 p.e. The varied borders are shown by the green dashed lines.
The crosstalk probabilities determined from the pulse height spectra according to equations (7.24) and (7.26) are shown in figure 7.13 (right). $P_{OXT,\geq1}$ is given by the black data points, whereas P_{OXT} is given by the blue squares. The statistical uncertainties are shown by the error bars (almost completely hidden by the size of

the markers), while the systematic uncertainties on the probabilities are shown by the vertical size of the gray areas. They are asymmetrical due to the asymmetrical shape of the peaks in the pulse height spectra. Furthermore, they decrease for an increasing over-voltage since the gain of the SiPM increases and the peaks become more separated.
The dashed line is a fit to the $P_{\mathrm{OXT},\geq 1}$ data of a second order polynomial. Its results are given in the corresponding figure.

From this fit the values of p are calculated following equation (7.22) with the choice of $n = 8$ and $n = 4$. Apparently, the choice of n is not restricted to 8 and 4. Though, these values might be *a priori* of special interest since they represent crosstalk-photons reaching the eight adjacent cells of the initial cell and the four cells side-to-side of the initial cell, respectively. The latter might be of interest due to the quadratic structure of the cells. But one might also consider different values of n, for instance $n = 24$ representing crosstalk-photons reaching all up to the next-to-the-next cells of the initial one.
Subsequently, P_{OXT} is calculated from p according to equation (7.23). The obtained values are over-estimated since the discussed model of optical crosstalk does not account for the effect of the limited number of cells $N_{\mathrm{cells}} = 900$. Thus, the values have to be corrected by a factor of κ_n. We find

$$\begin{aligned}\kappa_8 &= \frac{4 \cdot (n-5) + 4 \cdot (\sqrt{N_{\mathrm{cells}}} - 2) \cdot (n-3) + (\sqrt{N_{\mathrm{cells}}} - 2)^2 \cdot n}{N_{\mathrm{cells}} \cdot n} \\ &\approx 0.951 \qquad \text{for } n = 8\,.\end{aligned} \tag{7.27}$$

The denominator gives the hypothetical total number of neighbors if each of the 900 cells had $n = 8$ of them. The numerator gives the actual total number of neighbors. There are the 4 cells in the corner which have only 3 neighbors. Then there are the $4 \cdot 28$ cells at the four borders of the sensitive area which have only 5 neighbors. The remaining 28^2 cells are completely surrounded by cells, and thus have 8 neighbors. Similarly, the correction factor can be determined for $n = 4$.

$$\begin{aligned}\kappa_4 &= \frac{4 \cdot (n-2) + 4 \cdot (\sqrt{N_{\mathrm{cells}}} - 2) \cdot (n-1) + (\sqrt{N_{\mathrm{cells}}} - 2)^2 \cdot n}{N_{\mathrm{cells}} \cdot n} \\ &\approx 0.967 \qquad \text{for } n = 4\,.\end{aligned} \tag{7.28}$$

The values of P_{OXT} derived from the model of optical crosstalk for $n = 8$ and $n = 4$ and corrected for the corresponding κ_n are shown in figure 7.13 (right) by the solid green and red lines, respectively. They show a good agreement with the data derived directly from the pulse height spectra. However, the agreement for $n = 4$ seems slightly better, and the data appear to favor a higher value of n with an increasing over-voltage. This can explained by the growth of the region within the cells in which the avalanche process takes place, and where thus the crosstalk-photons are created and can be absorbed to trigger further avalanches (cf. the photo in figure 4.12). With a larger area, which emits and absorbs photons, it becomes more likely that the emitted photons will reach also the four cells to the corners of the initial cell and trigger a breakdown there.

Optical crosstalk can also lead to afterpulses which again can lead to optical crosstalk and afterpulses. As discussed earlier in this section the cell breakdown rate determined by the photon counting method R_{pc} is already corrected for counts due to optical crosstalk. To obtain the rate of detected signal-photons, the counts caused by afterpulses have to be removed from R_{pc}.
To determine the mean number of detectable afterpulses which occur after an initial breakdown (i.e. a thermal breakdown or one caused by a signal-photon) a simulation with G4SiPM is performed. The performance parameters of the simulation are set to the values determined in the section at hand and the previous one to represent the SiPM applied for the measurements of the night-sky brightness. The geometric properties are set appropriately. All these parameters are summarized in table A.2 given in appendix A.3. Before the mean number of detectable afterpulses will be determined a crosscheck is performed to compare the simulated data with measured data. For various over-voltages in the range from 0.6 V to 1.5 V G4SiPM generates 100000 voltage traces per over-voltage, each with a length of 2300 ns. The simulated traces are then analyzed with the same procedure as discussed previously in this section. The afterpulse probability P_{AP} as well as the probability of optical crosstalk $P_{\mathrm{OXT},\geq 1}$ determined by the analysis of the simulated data are shown as functions of the over-voltage in figure 7.14 (left). Also shown are the corresponding measured quantities and their parameterizations as they have been presented in figures 7.11 (left) and 7.13 (right). A comparison of the measured and the simulated data shows a very good agreement.
For our objective to determine the mean number of detectable afterpulses after an initial cell breakdown, G4SiPM simulates one trace per considered over-voltage with a length of 500 ms. Within a trace $N_{\mathrm{init}} = 100000$ initial cell breakdowns are uniformly distributed. The length of the trace assures sufficient time between the initial breakdowns to avoid a pile-up of individual correlated noise series. For each run the total number of detectable afterpulses N_{AP} is determined. An afterpulse is *detectable* if the corresponding signal in the simulated output voltage exceeds the detection threshold of $V_{\mathrm{th}} = 14\,\mathrm{mV}$ as introduced in section 7.1. To check wheter a pulse is detectable, not the waveform analysis algorithm is used, but the amplitudes of the pulses are calculated analytically from the output of the simulation.[13] This procedure prevents a possible bias introduced by the efficiency of the waveform analysis in finding all pulses of interest. As discussed in the previous section the simulations account for the fact that the effective over-voltage of a single cell is temporarily reduced after its breakdown. The probability that a detectable pulse within the output voltage is caused by afterpulsing is given by

$$P'_{\mathrm{AP}} = \frac{N_{\mathrm{AP}}}{N_{\mathrm{tot}}} = \frac{N_{\mathrm{AP}}}{N_{\mathrm{init}} + N_{\mathrm{AP}}} \tag{7.29}$$

with N_{tot} being the total number of detectable pulses. All initial pulses are detectable since their pulse heights has a minimum at the 1 p.e. level. Since P'_{AP} depends on the detection threshold, which is determined by the experimental setup and the analysis method, we will refer to it as the *application specific afterpulse*

[13] these calculations are provided in appendix A.2

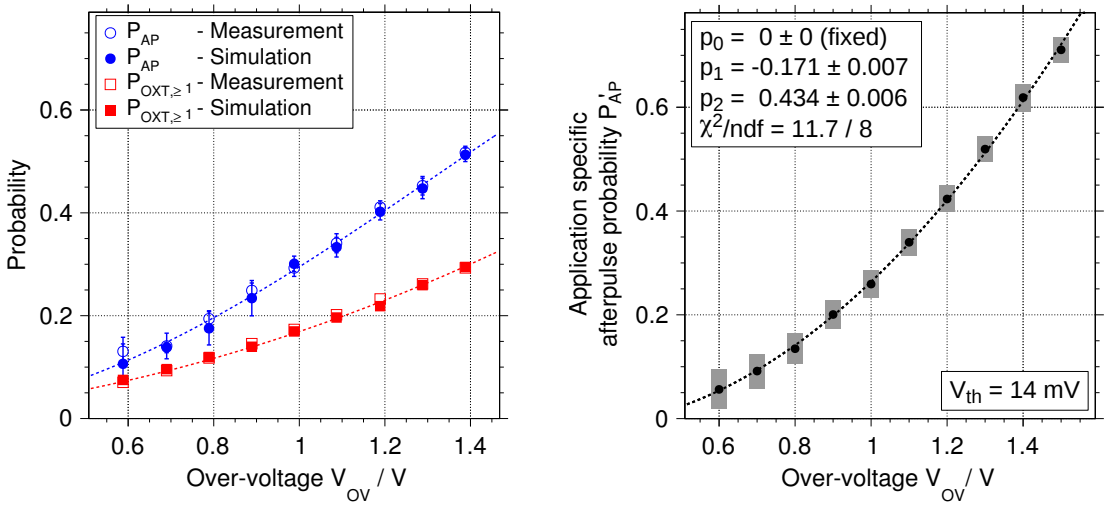

Figure 7.14: **Left:** Probabilites of afterpulsing (AP, blue markers) and optical crosstalk (OXT, red markers) as functions of the over-voltage V_{ov}. The open markers depict the same measured data as in figures 7.11 (left) and 7.13 (right). The dashed lines are the parametrizations of these data also shown in the mentioned figures. The filled markers depict simulated data. **Right:** Simulated, application specific probability P'_{AP} that a cell breakdown is caused by afterpulsing, and that its pulse height exceeds the detection threshold $V_{\mathrm{th}} = 14\,\mathrm{mV}$, shown as a function of the over-voltage V_{ov}. The vertical size of the gray squares denote the systematic uncertainties. The dashed curve is a fit of a polynomial of second order to the data. Please do not confuse P'_{AP} with P_{AP} (shown for instance in the left plot) which is the probability that a cell breakdown will cause an afterpulse.

probability. The simulated P'_{AP} is shown in figure 7.14 (right) as a function of the over-voltage. The statistical uncertainties are hidden by the size of the markers. The systematic uncertainties are indicated by the vertical size of the gray boxes. They are determined by varying the performance parameters of the simulation according to their uncertainties and performing further N_{init} runs for each over-voltage. The plotted uncertainties are the standard deviations of the outcome of these additional simulation runs. P'_{AP} is parametrized by a fit of a polynomial of second order with its constant fixed to zero. The fit results are also shown in figure 7.14 (right).

The cell breakdown rate R_{pc} determined by the photon counting method equals approximately the cell breakdown rate exclusively caused by signal-photons, thermal excitation of the silicon, and afterpulses. With the knowledge of P'_{AP} we can correct this rate for the afterpulses:

$$R_{\mathrm{AP}} = (1 - P'_{\mathrm{AP}}) \cdot R_{\mathrm{pc}}\,. \tag{7.30}$$

R_{AP} equals approximately the rate of detectable cell breakdowns exclusively triggered by signal-photons and thermal excitation of the silicon.

A bias could be included in the correction for afterpulses due to the different temperatures at which the SiPMs are operated. The one of the night-sky photometer is

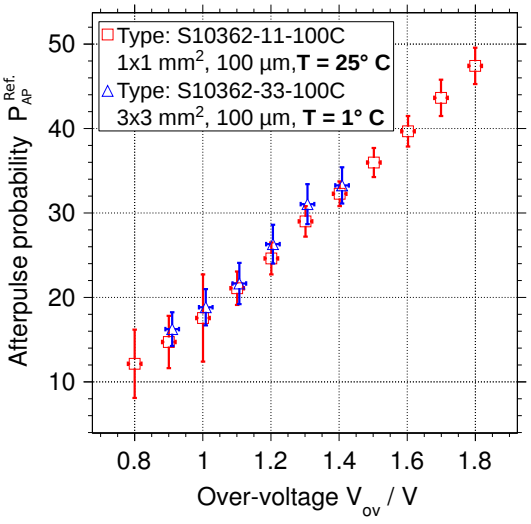

Figure 7.15: Afterpulse probability as a function of the over-voltage for Hamamatsu SiPMs measured within the scope of reference [105]. Considered are only afterpulses which can be detected with the corresponding experimental setup. The SiPMs have the same cell pitch (100 µm) but different sensitive areas. The small one ($1\times1\,\mathrm{mm}^2$, red squares) is operated at a temperature of about 25° C. The other one ($3\times3\,\mathrm{mm}^2$, blue triangles) at about 1° C. Data assembled from different figures of reference [105].

operated at ambient temperatures of summer nights (ranging from about 10° C to 15° C for the acquired data). The one of the auxiliary measurement to determine the probabilities of correlated noise and the timing constants is operated at about 1° C. This is necessary since at higher temperatures the SiPMs feature too much noise to result in Δt distributions which can be used for a reliable determination of the afterpulse probability. However, the bias is assumed to be insignificant compared to other systematic uncertainties: In figure 7.15 the afterpulse probability $P_{\mathrm{AP}}^{\mathrm{Ref.}}$ as measured in the scope reference [105] is shown for the SiPM type discussed in this chapter, as well as for a similar type with identical cell pitch but a smaller sensitive area, which is $1\times1\,\mathrm{mm}^2$ instead of $3\times3\,\mathrm{mm}^2$. The afterpulse probability $P_{\mathrm{AP}}^{\mathrm{Ref.}}$ is defined slightly different from P_{AP}, which is the one used in the analysis at hand.[14] The difference is that P_{AP} accounts for all afterpulses, while $P_{\mathrm{AP}}^{\mathrm{Ref.}}$ only regards afterpulses which can be detected by the experimental setup and the applied analysis method used in the scope of reference [105]. Hence, especially fast afterpulses with small pulse amplitudes are disregarded by the latter. A direct comparison of the two measured probabilities is thus not reasonable. However, both afterpulse probabilities depend on the cell pitch of the corresponding SiPM (cf. figure 4.13) and might depend on the temperature. Yet, they are not expected to depend on the overall size of the SiPM which justifies the comparison of the two different types for our intention. Since for identical temperatures the thermal noise rate of the small SiPM is reduced by about one order of magnitude compared to the large SiPM, measurements leading to its afterpulse probability can also be performed at comparatively high temperatures.

[14] please do not confuse P_{AP} with P'_{AP}

The plot shows $P_{\mathrm{AP}}^{\mathrm{Ref.}}$ of the two types at 25° C and 1° C for the small and the large SiPM, respectively.
Although, the results agree within their statistical uncertainties, there is a very small trend to higher afterpulse probabilities for reduced temperatures. For future analyses the dependence of the afterpulse probability on the temperature could be studied, but this would require the determination of the temperature during the measurements of the night-sky brightness. In the analysis at hand, this temperature does not have to be known. An alternative for upcoming measurements applying the photon counting technique would be to keep the temperature of the SiPM at a level at which the afterpulse probability has been measured.

7.5 Photon counting

The previous sections of this chapter discussed how to analyze the measured voltage traces regarding cell breakdowns and how to determine the operational parameters of interest of the SiPM. Within this section we will use these parameters and the waveform analysis to reconstruct the rate of detected signal-photons from the measured raw data.

Once the pulses have been identified in the voltage traces, the photon counting technique discussed in section 6.1 can be applied. Let us briefly recall the basic quantity: for a continuous light source, which we assume the night-sky to be, the mean number of cell breakdowns per measurement time t_{meas} due to signal-photons, thermal noise, and afterpulses is given by

$$\boxed{\mu = -\ln\left(\frac{N_{\mathrm{ped}}}{N_{\mathrm{tot}}}\right)}, \tag{7.31}$$

with N_{tot} being the total number of measurements, each with a duration of t_{meas}, and N_{ped} being the number of measurements where no cell breakdown occurs. Breakdowns due to optical crosstalk are not included in μ. Not every *cell breakdown* will cause a *pulse* in the output signal of the SiPM: since optical crosstalk happens almost instantaneously, the corresponding cell breakdowns do not add new pulses to the signal of the SiPM, but increase the pulse height of some of the pulses which are generated by the other three causes. Thus, we can also say that μ is the number of pulses per t_{meas}. The pulse rate is thus given by[15] $R_{\mathrm{wa}} = \mu / t_{\mathrm{meas}}$. Consequently, this pulse rate is composed of pulses due to signal-photons, thermal noise, and afterpulses. If the number of observed events without a pulse is sufficiently high ($N_{\mathrm{ped}} \gtrsim 10$), the statistical uncertainty of μ is approximated well by (cf. equation (6.4))

$$\sigma_\mu = \sqrt{\frac{1}{N_{\mathrm{tot}}}\left(\frac{N_{\mathrm{ped}}}{N_{\mathrm{tot}}} - \left(\frac{N_{\mathrm{ped}}}{N_{\mathrm{tot}}}\right)^2\right)}. \tag{7.32}$$

As previously discussed in section 6.1 the characteristics of the SiPM are idealized with equation (7.31) by the assumption, that the number of counted SiPM pulses

[15] The index 'wa' is chosen in dependence on the waveform analysis algorithm.

is Poissonian distributed. Deviations from this idealization will lead to a systematic bias which has to be accounted for. For this reason the pulse rate will be calibrated later.

The measurement time t_{meas} can be regarded for instance as the length of the voltage traces which is $t_{\mathrm{trace}} = 2300\,\mathrm{ns}$. μ is then determined by counting the total number of traces N_{tot} and the number of traces without pulses N_{ped}.
But since the photon counting method relies on a value of $N_{\mathrm{ped}} > 0$, it is obvious that this choice of t_{meas} will only lead to practical values of μ if the cell breakdown rate is very low. For a sufficiently high cell breakdown rate there will not be a single trace without a pulse, and μ together with its uncertainty will diverge. However, we can sub-divide the voltage traces into consecutive intervals of equal width and choose t_{meas} to be this width. In the following we will refer to this width as t_{gate} in the sense of each interval being a gate within which we check whether pulses are found or not.
For t_{gate} tending to smaller values, μ converges in the manner that the pulse rate R_{wa} converges to the mean number of pulses in a trace divided by the trace length. To illustrate this behavior figure 7.16 shows a measured voltage trace which has been inspected by the waveform analysis algorithm. The red triangles are the cell breakdown markers and display the positions of the pulses which are identified. There are $N_{\mathrm{cb}} = 14$ pulses, and we thus expect the pulse rate to be $14/2300\,\mathrm{ns} \approx 6.1\,\mathrm{MHz}$. The trace is divided into $N_{\mathrm{tot}} = 23$ gates of the width $t_{\mathrm{gate}} = 100\,\mathrm{ns}$. Let N_{occ} be the number of gates which are occupied by at least one cell breakdown marker. The number of gates without pulses is then given by $N_{\mathrm{ped}} = N_{\mathrm{tot}} - N_{\mathrm{occ}} = 23 - 11 = 12$. According to equation (7.31) we find the number of pulses per gate $\mu = 0.65$ and the pulse rate $R_{\mathrm{wa}} = 6.5\,\mathrm{MHz}$.
If we take the same voltage trace but choose $t_{\mathrm{gate}} = 1\,\mathrm{ns}$, we find $N_{\mathrm{tot}} = 2300$ and $N_{\mathrm{ped}} = N_{\mathrm{tot}} - N_{\mathrm{occ}} = 2300 - 14 = 2286$ since the 14 individual pulses are separated by more than 1 ns from another. Here, N_{occ} will equal N_{cb}. Hence, $\mu = 6.1 \cdot 10^{-3}$ and $R_{\mathrm{wa}} = 6.1\,\mathrm{MHz}$.
The convergence of μ with t_{gate} tending to smaller values introduces a bias to the method which depends on the actual choice of t_{gate}.

To study the photon counting method quantitatively in more detail, the SiPM simulation toolkit G4SiPM is applied to simulate voltage traces of SiPM signals for various pulse rates. In contrast to measured data, the actual pulse rate of the SiPM is known for the simulation. The simulation is performed with a model of the Hamamatsu S10362-33-100C SiPM, which is the same type of SiPM as applied to the camera of the night-sky photometer. It owns 900 cells. The simulation uses an over-voltage of 0.6 V. Further technical details of the simulations are given in table A.2 in appendix A.3.
For each of the simulated pulse rates 1000 voltage traces are simulated. Like the measured data, these traces also feature a length of 2300 ns and a sampling interval of 1 ns. The pulse shaper module of G4SiPM is used to result in an approximately identical pulse shape of measured and simulated data. The input parameters of the module are determined from fits of the pulse shape according to equation (4.18) to

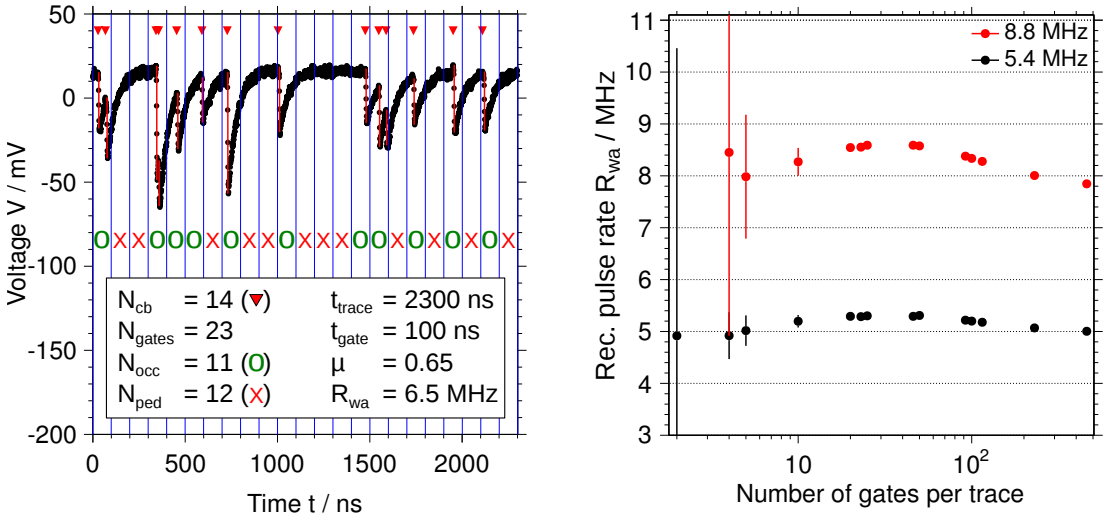

Figure 7.16: **Left:** A measured voltage trace divided into consecutive time intervals referred to as *gates*. Shown is a rather high gate width of $t_{\mathrm{gate}} = 100\,\mathrm{ns}$ for illustrative reasons. The green circles and red crosses denote whether a gate contains at least one cell-breakdown-marker (red triangles) or not, respectively. **Right:** Pulse rate R_{wa} reconstructed by the waveform analysis as a function of the number of gates per trace. A higher number of gates corresponds to a shorter gate width t_{gate}. The red data points are for a simulated pulse rate of 8.8 MHz, the black ones for a rate of 5.4 MHz.

the measured data.
The simulated traces are analyzed by the waveform analysis algorithm to identify the individual cell breakdowns. Afterwards the traces are sub-divided into a variable number of gates, with gate widths t_{gate} reaching from 2300 ns to 5 ns. Only gate widths with $t_{\mathrm{trace}}/t_{\mathrm{gate}}$ being an integer are considered. The choice of the minimum value of t_{gate} is motivated by the fact, that the minimum distance between two consecutive cell breakdowns, which the waveform analysis is able to resolve, is $\Delta t_{\mathrm{min}} = 5\,\mathrm{ns}$ (see section 7.1). Subsequently, the number of gates without cell breakdowns $N_{\mathrm{ped}} = N_{\mathrm{gates}} - N_{\mathrm{occ}}$ is counted and μ is determined according to equation (7.31).
The resulting pulse rate depending on the number of gates per voltage trace is shown in figure 7.16 (right). A higher number of gates corresponds to a shorter gate width. The displayed data are for simulated pulse rates of 5.4 MHz and 8.8 MHz.
Generally speaking, for a sufficiently high number of gates per voltage trace, and thus a sufficiently short gate width, N_{occ} will equal the number of pulses found by the waveform analysis N_{cb}. With $N_{\mathrm{occ}} = N_{\mathrm{cb}}$ the pulse rate R_{wa} will tend to $N_{\mathrm{cb}}/t_{\mathrm{trace}}$ for t_{gate} tending to smaller values. Then again, for a sufficiently small number of gates per trace N_{occ} will be smaller than N_{cb}, and its value will further decrease with a falling number of gates. For very small numbers of gates the fact that N_{ped} will be close to zero (or actually will be zero) will lead to large statistical uncertainties.

The expected behavior, especially the convergence for small gate widths, is visible in the right plot of figure 7.16. (Please note the logarithmic scale of the x-axis.) For high numbers of gates per voltage trace the data might still be significantly different from the value it is tending to, but the smallest possible gate width is limited by the waveform analysis algorithm.[16] This issue has to be incorporated in the further course of the analysis, otherwise the determined pulse rates would be biased.
From the same figure it is also visible that the value, to which the data converge, is significantly smaller than the simulated pulse rate. Thus, the waveform analysis algorithm is not fully efficient in finding the SiPM pulses. To account for this inefficiency the simulated data are analyzed for $t_{\mathrm{gate}} = 5\,\mathrm{ns}$, and the reconstructed pulse rate is compared to the simulated pulse rate.
Within the simulations the rate of cell breakdowns due to signal-photons and thermal excitation of the silicon can be set directly. The rates of cell breakdowns due to afterpulses and optical crosstalk can only be set indirectly by setting the probabilities of afterpulsing and optical crosstalk. Indeed the rates can be calculated from these probabilities, but since we are only interested in the rate of pulses which exceed the detection threshold of $V_{\mathrm{th}} = 14\,\mathrm{mV}$, the determination becomes less straightforward due to the reduced pulse heights of those pulses which pile up. This is not only of interest at high pulse rates but also at low rates for (especially fast) afterpulses. Such a pile-up has been illustrated in figure 7.8 (left) and discussed in section 7.3. The effect of reduced pulse heights, caused by the pile-up, has to be accounted for if the simulated rate of pulses above the detection threshold has to be calculated.
For each cell breakdown the simulation outputs a timestamp and a weight corresponding to the individual signal of the cell. From these information the actual pulse heights of the pulses in the simulated output signal can be calculated analytically. This is discussed in detail in appendix A.2. By subsequently counting the number of pulses, whose pulse heights exceeded the detection threshold $V_{\mathrm{th}} = 14\,\mathrm{mV}$, the simulated rate of detectable pulses $R_{\mathrm{sim}}^{\mathrm{thr.}}$ can be determined.
As the probabilities of afterpulsing and optical crosstalk, and with them the simulated pulse rates, depend on the over-voltage, simulations as described above are also performed for further over-voltages to cover the range of 0.6 V to 1.4 V.

The pulse rates R_{wa}, as reconstructed by the waveform analysis algorithm and the photon counting method for a gate width of $t_{\mathrm{gate}} = 5\,\mathrm{ns}$, are shown in figure 7.17. They are plotted as a function of the rate of simulated pulses above the detection threshold $R_{\mathrm{sim}}^{\mathrm{thr.}}$.[17] Apparently the corresponding total rate of simulated pulses is higher. Within the simulation results it reaches values up to almost 5 GHz for the highest over-voltage of 1.4 V. Since such high rates exceed by far the rates which

[16] Apparantly, for any measured data the sampling frequency of the measurement device will set an ultimate limit for the minimum gate width.

[17] With all operational characteristics of the real SiPM determined, and after validation of the underlying models, the simulations described in this section could also be advanced in future works to a *Real Monte Carlo* which simulates the actual state of an SiPM and gives thus a functional relation between the detected pulse rate and the signal-photon flux. A similar thought has been raised at the very end of subsection *Dynamic range* in section 4.2. There the calibration of SiPMs has been discussed in the sense of determining the response of the sensors to a known incident light flux by means of measurements.

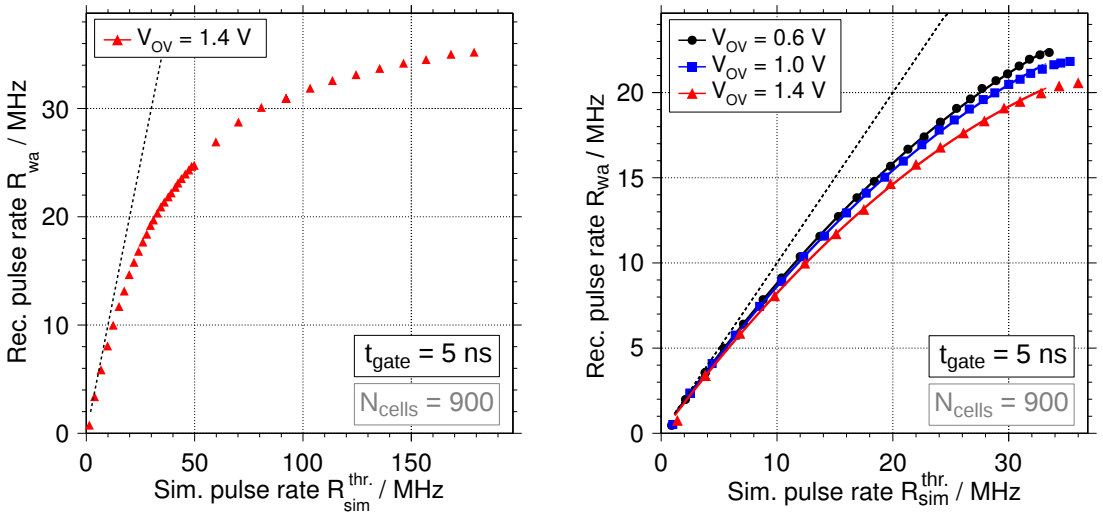

Figure 7.17: **Left:** Rate of SiPM pulses reconstructed by the waveform analysis R_{wa} as a function of the simulated rate of SiPM pulses above the detection threshold $R_{\mathrm{sim}}^{\mathrm{thr.}}$. The simulated SiPM features 900 cells and is operated at an over-voltage of 1.4 V. The analysis uses a gate width of $t_{\mathrm{gate}} = 5\,\mathrm{ns}$. The black dashed line is the identity transformation. **Right:** Zoomed display to the data of the left plot. Also shown are data for the over-voltages 0.6 V (black data points) and 1.0 V (blue squares). The solid curves are fits to the data according to equation (7.33) up to simulated pulse rates of 33 MHz. See text for more details.

are contained within the measured data of the night-sky brightness (which are up to several 10 MHz), the simulations of the lower over-voltages cover only the range of interest, and the resolution of the simulated rates is increased in contrast to the high rates.

As discussed in section 7.3, the recovery time of a cell of the SiPM is $\mathcal{O}(10\,\mathrm{ns})$. Thus, with 900 cells, the cell breakdown rate of the entire SiPM is expected to saturate at a value of $\mathcal{O}(10\,\mathrm{GHz})$ (cf. figure 4.14).

The compression of R_{wa} which is visible in figure 7.17 is predominantly caused by the inefficiency of the waveform analysis algorithm of finding all pulses of interest, and by the systematics introduced by the photon counting method. For a fixed value of $R_{\mathrm{sim}}^{\mathrm{thr.}}$ the reconstructed pulse rate R_{wa} is lower for higher over-voltages, since the relative number of afterpulses increases with higher over-voltages. By increasing the amount of afterpulses the mean distance of two consecutive pulses in the output signal of the SiPM decreases. Thus, it happens more frequently that the waveform analysis algorithm will regard two pulses, which are close to each other, as just one pulse.

The individual runs of the simulation, each corresponding to an individual data point in the right plot of figure 7.17, are performed for equidistant numbers of initial cell breakdowns per time (i.e. breakdowns caused by signal photons and thermal excitation of the silicon). For higher numbers of these breakdowns, the pile-up of the pulses in the simulated output voltage leads to the compression in $R_{\mathrm{sim}}^{\mathrm{thr.}}$ which is

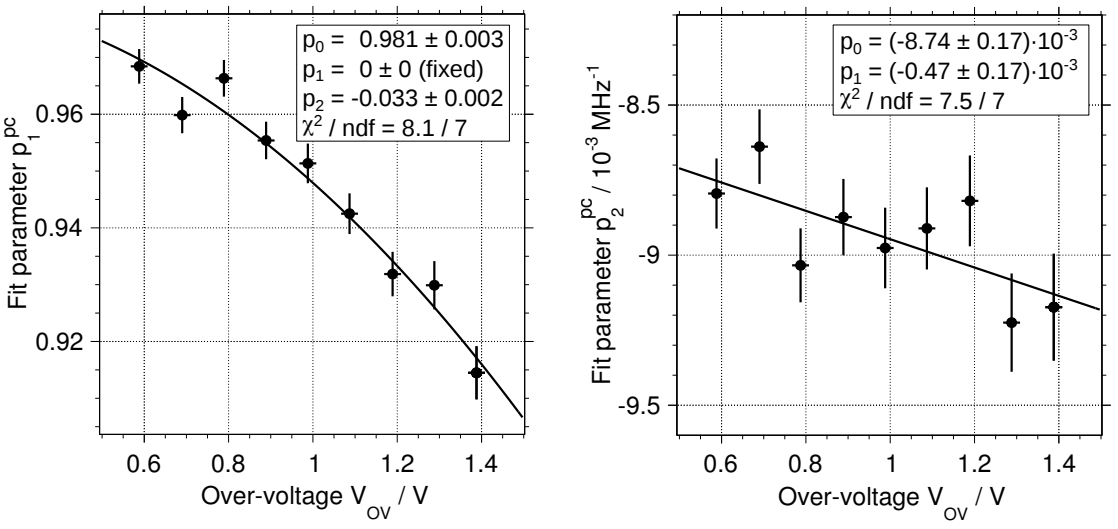

Figure 7.18: The parameters p_1^{pc} (left) and p_2^{pc} (right) of the functions to parametrize the data of figure 7.17. The black lines to the data are fits of second and first order polynomials, respectively.

visible in the plot: the more intense pile-up causes significantly more reduced pulse-heights, and the number of pulses which exceed the detection threshold decreases. The highest numbers of initial pulses corresponding to the data shown in the right plot of figure 7.17 are identical for the different over-voltages. But since the number of pulses due to correlated noise increases with the over-voltage, $R_{\mathrm{sim}}^{\mathrm{thr.}}$ reaches higher values for higher over-voltages.

To account for the systematics caused by the inefficiency of the waveform analysis and the photon counting method, we will use the simulation results for a calibration of the measured pulse rates within the further course of the analysis. For this reason R_{wa} is parametrized according to

$$R_{\mathrm{wa}}(R_{\mathrm{sim}}^{\mathrm{thr.}},\, V_{\mathrm{ov}}) = p_1^{\mathrm{pc}}(V_{\mathrm{ov}}) \cdot R_{\mathrm{sim}}^{\mathrm{thr.}} + p_2^{\mathrm{pc}}(V_{\mathrm{ov}}) \cdot R_{\mathrm{sim}}^{\mathrm{thr.}\,2}\,. \tag{7.33}$$

As can be seen in figure 7.17 (right) these polynomials describe the data very well for detectable simulated pulse rates $R_{\mathrm{sim}}^{\mathrm{thr.}}$ of up to 33 MHz. This limit is high enough for those rates we will encounter in the measured data. For future works, where higher rates might occur, different parameterizations should be considered.
The resulting fit parameters p_1^{pc} and p_2^{pc} are shown in figure 7.18 as functions of the over-voltage. They themselves are parametrized by second[18] and first order

[18]The parameter of the linear term is set to zero, since this leads to a satisfying result, and since the parameter is compatible with zero within its uncertainties anyway if it is left free.

polynomials, respectively. The corresponding fits are also given in the figure. They yield

$$\begin{aligned} p_1^{\mathrm{pc}}(V_{\mathrm{ov}}) = \quad & (0.981 \pm 0.003) \\ & - (0.033 \pm 0.002) \cdot V_{\mathrm{ov}}^2 \ \mathrm{V}^{-2} \\ p_2^{\mathrm{pc}}(V_{\mathrm{ov}}) = & - (8.74 \pm 0.17) \cdot 10^{-3} \ \mathrm{MHz}^{-1} \\ & - (0.47 \pm 0.17) \cdot 10^{-3} \cdot V_{\mathrm{ov}} \ \mathrm{MHz}^{-1}\,\mathrm{V}^{-1}\,. \end{aligned} \tag{7.34}$$

From the measured pulse rate

$$\boxed{R_{\mathrm{wa}} = \frac{\mu}{t_{\mathrm{gate}}}}\,, \tag{7.35}$$

which has been determined after the analysis of the raw data by the waveform analysis algorithm, we will calculate the measured rate of detectable SiPM pulses R_{pc} in the further course of this analysis by means of the inverse of the parametrization given by equation (7.33) which acts as a calibration for R_{wa}. For measurements we can replace $R_{\mathrm{sim}}^{\mathrm{thr.}}$ by R_{pc}.

$$\boxed{R_{\mathrm{pc}} = \left(-\frac{p_1^{\mathrm{pc}}}{2 \cdot p_2^{\mathrm{pc}}} - \sqrt{\left(\frac{p_1^{\mathrm{pc}}}{2 \cdot p_2^{\mathrm{pc}}} \right)^2 + \frac{R_{\mathrm{wa}} \cdot \mathrm{MHz}^{-1}}{p_2^{\mathrm{pc}}}} \right)} \tag{7.36}$$

R_{pc} is the pulse rate corrected for the systematics introduced by the waveform analysis and the photon counting method. As explained at the beginning of this section the rate R_{wa} is caused by cell breakdowns due to signal-photons, thermal excitation of the silicon, and afterpulses, but not due to optical crosstalk. Hence, R_{pc} does not contain contributions of pulses caused by optical crosstalk either, and thus the rate of detectable pulses R_{pc} equals approximately the rate of detectable cell breakdowns caused by signal-photons, thermal noise, and afterpulses.
The systematic uncertainty of applying equation (7.36) is determined by varying the parametrization according to the uncertainties of the fit results. The relative difference of the outcome compared to the nominal cell breakdown rate ranges from 0.7% at an over-voltage of 0.6 V to 1.2% at 1.4 V.

From here on all determinations of μ and the corresponding cell breakdown rates are performed with $t_{\mathrm{gate}} = 5\,\mathrm{ns}$. Regarding all further pulse height spectra, the individual pulses within a gate will be summed up before they contribute to a spectrum.[19] This assures that a pulse height spectrum contains as many events as there are gates in the total number of considered traces. In addition to the pulse heights, the spectra will also feature an entry at zero which gives the number of gates without pulses, i.e. the number of pedestal events N_{ped}. Since the bin widths of the spectra are typically too small to identify the first bin in the plots well enough, a red star will mark N_{ped}. An example is given in figure 7.19.

[19] A pulse belongs uniquely to the specific gate in which its cell breakdown marker is set.

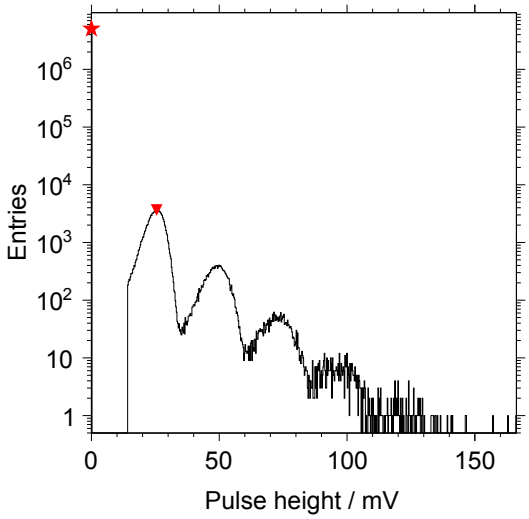

Figure 7.19: A pulse height spectrum resulting from about 11000 measured voltage traces divided into gates with a width of $t_{\text{gate}} = 5\,\text{ns}$. The red star marks the number of gates without cell breakdowns, i.e. N_{ped}. The red triangle marks the 1 p.e. voltage $V_{1\,\text{p.e.}}$. See text for details.

The recovery behavior of the cells of the SiPM together with the detection threshold of the waveform analysis raise the *system dead time* as introduced in section 7.3. The simulations discussed above account already for a compression of the detected rates caused by the system dead time.
They also allow to determine the total rate of cell breakdowns caused by signal-photons, thermal excitation of the silicon, afterpulses, and optical crosstalk. With this rate determined a correction for the *intrinsic dead time* of the cells of the SiPMs can be performed as presented in section 7.3.[20] However, the intrinsic dead time is not known, but only its upper limit. In section 7.3 we concluded that within this limit, the effect of the intrinsic dead time to the cell breakdown rates encountered in the measurements of the night-sky photon flux is marginal. It will thus here not be accounted for.

Correction for afterpulses

The procedure to correct the cell breakdown rate R_{pc} for cell breakdowns due to afterpulsing has been explained in detail in section 7.4. With the application specific probability P'_{AP} that a detectable cell breakdown is caused by afterpulsing, the rate

$$\boxed{R_{\text{AP}} = (1 - P'_{\text{AP}}) \cdot R_{\text{pc}}} \tag{7.37}$$

equals approximately the rate of detectable cell breakdowns exclusively caused by signal-photons and thermal excitation of the silicon. As discussed previously in section 7.4, P'_{AP} depends on the over-voltage.

[20] Referring to a footnote found previously in this section, a *Real Monte Carlo* is a very convenient way to perform the correction for the effect of the intrinsic dead time. Appropriate methods are already provided by G4SiPM, and once the intrinsic dead time has been measured it can be included directly in the simulations.

Correction for thermal noise

In general, the procedure discussed so far to correct the measured cell breakdown rates for correlated noise can be applied to the data of the nigh-sky brightness (NSB) as well as to data acquired in darkness. For instance, the latter can be achieved by closing the aperture of the PN-203 telescope. In case of the NSB measurements $R_{\mathrm{AP}}^{\mathrm{NSB}}$ includes cell breakdown due to signal-photons as well as thermal breakdowns. The dark measurements lack the first kind. Thus, its rate corrected for afterpulses $R_{\mathrm{AP}}^{\mathrm{dark}}$ is only caused by thermal breakdowns.
Dark measurements are performed frequently throughout a night in which the NSB is measured. The data acquisition starts with a dark measurement. It is followed by typically four measurements of the NSB before the next dark measurement is performed. This series continues. Typically each measurement lasts 90 s. Additional time is arranged for a quick survey of the acquired data and for closing the aperture of the telescope. Typically dark measurements are performed roughly every ten minutes. If the time between two dark measurements does not exceed 30 minutes, the mean variation of the corrected detection rate $R_{\mathrm{AP}}^{\mathrm{dark}}$ to the preceding one is smaller than 2%. Hence, we assume that the temperature is approximately constant for an NSB measurement and its corresponding dark measurement. In this case the rate of cell breakdowns caused by signal-photons is given by

$$R_{\gamma} = R_{\mathrm{AP}}^{\mathrm{NSB}} - R_{\mathrm{AP}}^{\mathrm{dark}} \,. \tag{7.38}$$

However, for the actual experimental setup of the NSPM two issues remain which have to be considered.

The first one is caused by the fact that the mean current through the SiPM is different for NSB and dark measurements due to different mean cell breakdown rates. The amplifier board, which also provides the bias voltage of the SiPM, features a resistance of 20 kΩ in series to the photosensor on the power supply line. A schematic of the equivalent circuit is shown in figure 7.20 (left). A different current through the SiPM leads to a different voltage drop along the serial resistor, and with it to a different over-voltage V_{ov} for a constant operating voltage supplied by the electronics. Therefore, the thermal noise rate is lower for NSB measurements than for the dark measurements. But since the thermal noise rate depends linearly on the over-voltage and is zero for $V_{\mathrm{ov}} = 0$, the dependence of the thermal noise rate of an NSB measurement on the over-voltage can be expressed as

$$R_{\mathrm{th}}^{\mathrm{NSB}}(V_{\mathrm{ov}}) = \frac{R_{\mathrm{AP}}^{\mathrm{dark}}}{V_{\mathrm{ov}}^{\mathrm{dark}}} \cdot V_{\mathrm{ov}} \tag{7.39}$$

where $V_{\mathrm{ov}}^{\mathrm{dark}}$ is the over-voltage of the dark measurement. Considering this change of the over-voltage with a variation of the cell breakdown rate equation (7.38) changes to

$$\boxed{R_{\gamma} = R_{\mathrm{AP}}^{\mathrm{NSB}} - R_{\mathrm{th}}^{\mathrm{NSB}}} \,. \tag{7.40}$$

Let I^{light} and I^{dark} be the current through the SiPM for the case of an illuminated SiPM and an SiPM in darkness, respectively. Let further $V_{\mathrm{s}}^{\mathrm{light}}$ and $V_{\mathrm{s}}^{\mathrm{dark}}$ be the

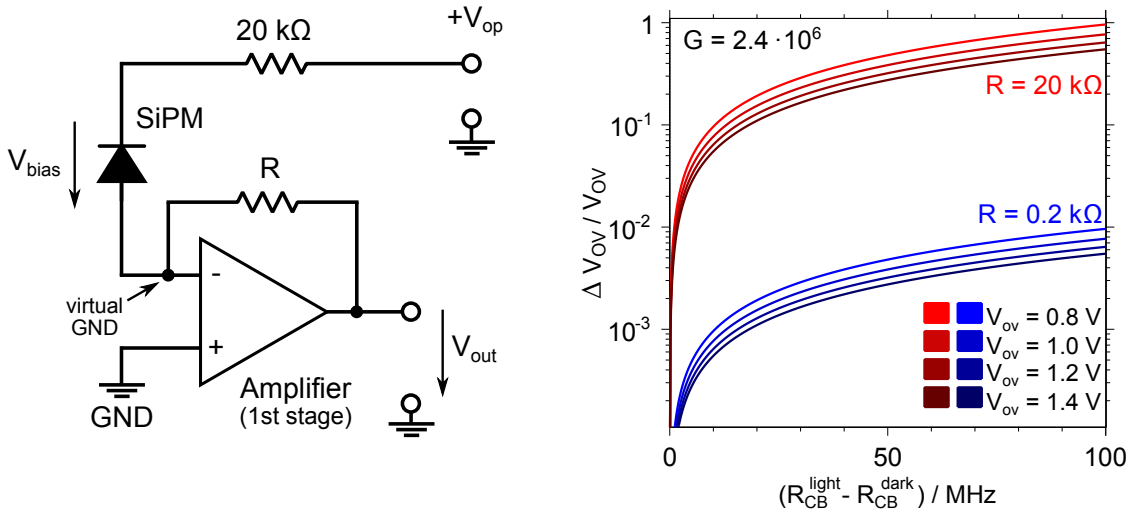

Figure 7.20: **Left:** Equivalent circuit of the loop of the transimpedance amplifier containing the SiPM. In series to the SiPM is a 20 kΩ resistor and the inverting input of the charge sensitive operational amplifier (opamp). The high gain of the amplifier together with the feedback along the resistance R cause a very small potential difference between the inputs of the opamp. This leads to a virtual ground (GND) at its inverting input. A current through the SiPM I_{SiPM} will lead to a voltage drop along the 20 kΩ resistor, which causes the bias voltage V_{bias} to be different from the operational voltage V_{op}. $V_{\mathrm{bias}} = V_{\mathrm{op}} - I_{\mathrm{SiPM}} \cdot 20\,\mathrm{k\Omega}$. The output voltage of the opamp V_{out} is provided to the second stage amplifiers. **Right:** Relative change of the over-voltage $\Delta V_{\mathrm{ov}}/V_{\mathrm{ov}}$ as a function of the cell breakdown rate $R_{\mathrm{cb}}^{\mathrm{light}}$ minus the dark noise rate $R_{\mathrm{cb}}^{\mathrm{dark}}$ following equation (7.41). The gain has been set to $G = 2.4 \cdot 10^6$. The red set of curves is for a serial resistor with $R = 20\,\mathrm{k\Omega}$, the blue one for $R = 0.2\,\mathrm{k\Omega}$. Different shades of a color are for different over-voltages ranging from 0.8 V (light color) to 1.4 V (dark color).

corresponding voltage drops at the serial resistor with the resistance R_{s}. The change of the over-voltage from the illuminated state to darkness is given by

$$\begin{aligned} \Delta V_{\mathrm{ov}} &= V_{\mathrm{s}}^{\mathrm{light}} - V_{\mathrm{s}}^{\mathrm{dark}} \\ &= \left(I^{\mathrm{light}} - I^{\mathrm{dark}}\right) \cdot R_{\mathrm{s}} \\ &= (R_{\mathrm{cb}}^{\mathrm{light}} - R_{\mathrm{cb}}^{\mathrm{dark}}) \cdot G\, e\, R_{\mathrm{s}}\,. \end{aligned} \tag{7.41}$$

Here, $R_{\mathrm{cb}}^{\mathrm{light}}$ and $R_{\mathrm{cb}}^{\mathrm{dark}}$ are the cell breakdown rates for the illuminated and non-illuminated SiPM, respectively, G is the intrinsic gain of the photosensor, and e is the elementary charge. In figure 7.20 (right) two sets of functions representing the relative change of the over-voltage $\Delta V_{\mathrm{ov}}/V_{\mathrm{ov}}$ with a variation of the cell breakdown rate according to equation (7.41) are shown for the choice of $G = 2.4 \cdot 10^6$. For the one set displayed by the red curves $R_{\mathrm{s}} = 20\,\mathrm{k\Omega}$. For the other one (blue curves) $R_{\mathrm{s}} = 0.2\,\mathrm{k\Omega}$. The curves are for different over-voltages ranging from 0.8 to 1.4 V. Certainly, the gain changes with the over-voltage, but the message is clear also with

this rough approximation of a constant gain; a reduced resistance of the serial resistor results in a significantly reduced variation of the over-voltage with different cell breakdown rates. Due to the linear structure of equation (7.41) the reduction of R_s by two orders of magnitude reduces the relative change of the over-voltage by two orders of magnitude as well.
Accordingly, the seven pixel version of FAMOUS features serial resistors with resistances of 0.15 kΩ. With night-sky photon rates of several ten megahertz, the relative change of the over-voltage from the illuminated state to an operation in darkness is $\mathcal{O}(0.1\%)$. A further approach to take care of varying over-voltages with varying cell breakdown rates is the monitoring of the current through the resistor and an appropriate regulation of the bias voltage.

The second issues mentioned above arises from the fact that the probabilities of optical crosstalk initiated by thermal breakdowns or breakdowns due to signal-photons are slightly different. This is caused by the circular aperture of the light concentrator on top of the sensitive area of the SiPM. While signal-photons can only trigger cell breakdowns on the corresponding circular area, thermal breakdowns can trigger avalanche processes over the entire sensitive area. The initial cells of optical crosstalk triggered by signal-photons have therefore more *neighbors* (cf. section 7.4) on average than the ones triggered by thermal excitation of the silicon. Technically speaking, the crosstalk probability of the signal-photons needs a correction factor. However, as we will see this correction factor is very small, therefore it will be omitted. A schematic view of the sensitive area of the SiPM is shown in figure 7.21. In addition, the circular area which can be reached by signal-photons is illustrated. With a cell pitch of 100 µm and a number of neighbors $n = 4$ there are 48 cells within the circular area which do not have four neighbors. They are the 12 centered cells at each of the four borders of the SiPM.
Let us consider the following three possibilities: (a) each cell of a squared SiPM can act as an initial cell for optical crosstalk, indexed *squa*, (b) each cell of a squared SiPM within a circular area, as given for instance by the exit aperture of the light-concentrator, can act as an initial cell, indexed *circ*, and (c) all cells of an ideal SiPM, i.e. with no borders, and thus each cell having n neighbors, can act as an initial cell, indexed *ideal*. As discussed in the previous section the corresponding crosstalk probabilities relate according to $P_\mathrm{OXT}^\mathrm{squa} = \kappa_4 \cdot P_\mathrm{OXT}^\mathrm{ideal}$ where $\kappa_4 \approx 0.967$ is the correction factor given in equation (7.28). Furthermore, $P_\mathrm{OXT}^\mathrm{circ} = \kappa_\mathrm{NSPM} \cdot P_\mathrm{OXT}^\mathrm{ideal}$ with

$$\kappa_\mathrm{NSPM} = \frac{4 \cdot 12 \cdot (n-1) + (N_\mathrm{cells} - 4 \cdot 12) \cdot n}{N_\mathrm{cells} \cdot n} = 0.987 \qquad \text{for } n = 4\,. \tag{7.42}$$

This leads to

$$P_\mathrm{OXT}^\mathrm{circ} = \frac{\kappa_\mathrm{NSPM}}{\kappa_4} \cdot P_\mathrm{OXT}^\mathrm{squa} \approx 1.021 \cdot P_\mathrm{OXT}^\mathrm{squa}\,. \tag{7.43}$$

Since (b) describes the SiPM only correctly for crosstalk breakdowns of the first generation[21] the value of 1.021 has to be interpreted as an upper limit. The true value taking further generations into account is closer to 1.

[21] for the reason that cells which generate crosstalk-photons causing crosstalk of higher generations do not necessarily have to lie within the circular area

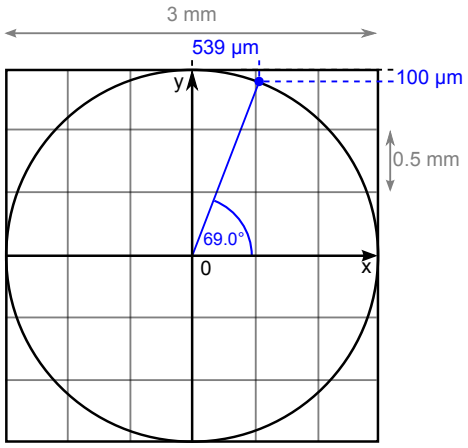

Figure 7.21: Schematic view of the sensitive area of the SiPM (big square) mounted in the night-sky photometer and the exit aperture of the Winston cone in front of it (circle). A Cartesian coordinate system with its origin in the center of the circle is superimposed. At an angle of 69.0° the circle has the coordinates $x \approx 539\,\mu\text{m}$ and $y = 1500\,\mu\text{m} - 100\,\mu\text{m}$. See text for details.

A correction on the crosstalk probability of 2% leads to a variation of the rate R_γ smaller than 0.8% (0.2%) at an over-voltage of 1.4 V (1.0 V).[22]

7.6 Reconstruction of the night-sky photon flux

To make a comparison of the measured night-sky photon flux with results of different experiments more convenient, and to provide a simplified implementation of the NSB data within the detector simulations of FAMOUS, the signal-photon rate R_γ given by equation (7.40) is normalized according to

$$\boxed{\phi_\gamma = \frac{R_\gamma}{\Omega\, A\, \epsilon}} \tag{7.44}$$

where $\Omega = (1.1 \pm 0.1) \cdot 10^{-4}\,\text{sr}$ is the solid angle of the field of view of the night-sky photometer (NSPM), $A = (3.24 \pm 0.01) \cdot 10^{-2}\,\text{m}$ is the aperture area of the PN-203 telescope, and $\epsilon = 0.40 \pm 0.02$ is its optical efficiency (cf. chapter 6). Please note, that this efficiency is the one of the Newton reflector. It does not include the optical efficiencies of the camera pixel, i.e. of the UV filter, Winston cone, and SiPM.

The detected photon flux ϕ_γ is the final result of the analysis method discussed in this chapter. For the sake of clarity the full method is summarized in a block diagram in figure 7.22.
Three exemplary pulse height spectra and the corresponding over-voltages, cell breakdown and photon detection rates, as well as probabilities of correlated noise are given in figure 7.23. Data acquired while the NSPM has been pointing at a bright

[22] With $n = 8$ we find $\kappa_{\text{NSPM}}/\kappa_8 \approx 1.030$. A correction on the crosstalk probability of 3% leads to a variation of the rate R_γ smaller than 1.3% (0.3%) at an over-voltage of 1.4 V (1.0 V).

Table 7.1: Systematic uncertainties of the measurements of the night-sky brightness (NSB). If an uncertainty depends on the over-voltage, its value is stated for the minimum and maximum over-voltage occurring in the NSB data. These over-voltages are 1.13 V and 1.45 V. See text for details.

Waveform analysis	0.3%
Photon counting	1.0% ÷ 1.2%
Afterpulsing	6.8% ÷ 3.9%
Field of view	9.1%
Optical efficiency [*1]	5.0%
Aperture area	0.3%
Total	**13.9% ÷ 12.7%**

[*1] of the PN-203 telescope

star, at a region without bright stars, and while the aperture of the telescope has been closed are shown in the top, middle, and bottom row, respectively.

Reconsidering the subtraction of the dark measurements from the NSB measurements by means of equation (7.40), the individual systematic uncertainties of the former are subtracted from the corresponding ones of the latter, assuming correlation coefficients of 1. The timing accuracy of the V1729 ADC leads to a small uncertainty of the waveform analysis algorithm ($< 1\%$). The correction for the systematics of the waveform analysis and the photon counting method introduce a further small uncertainty ($\sim 1\%$) which depends slightly on the over-voltage. A more significant contribution, also depending on the over-voltage, is raised by the correction of the detected pulse rates for afterpulses ($\sim 5\%$).[23] In table 7.1 the systematic uncertainties are summarized. If an uncertainty depends on the over-voltage, its value is given for 1.13 V and 1.45 V which are the minimum and maximum over-voltages occurring in the NSB data. Only very few measurements have been performed at rather high over-voltages close to 1.45 V. Most of the measurements have been carried out in the range of 1.20 V to 1.35 V (cf. table A.4 in appendix A.3).
Further systematic uncertainties are introduced by the telescope parameters. The highest contribution is due to the uncertainty of the field of view ($\sim 9\%$), followed by the one of the optical efficiency of the PN-203 telescope ($\sim 5\%$). The uncertainty of the aperture area has only a minor contribution ($< 1\%$). The uncertainty of the field of view is raised by the fact that the pixel of the NSPM might be out of focus (cf. section 6.3). In this case there is no sharp cutoff in the light flux sensed by the pixel when the star moves out of the field of view. The uncertainty can be reduced by a factor of two if focusing can be provided.
Regarding the statistical uncertainties of the measured photon fluxes, there are two contributions. One derives from the counting of the number of gates in the voltages traces which do not contain an SiPM pulse, while the other one derives from the

[23] The asymmetry of the systematic uncertainty of the correction for afterpulses, which is raised by the determination of the probability of optical crosstalk (cf. figure 7.13 (right)), is not significant within the considered precision of the uncertainty.

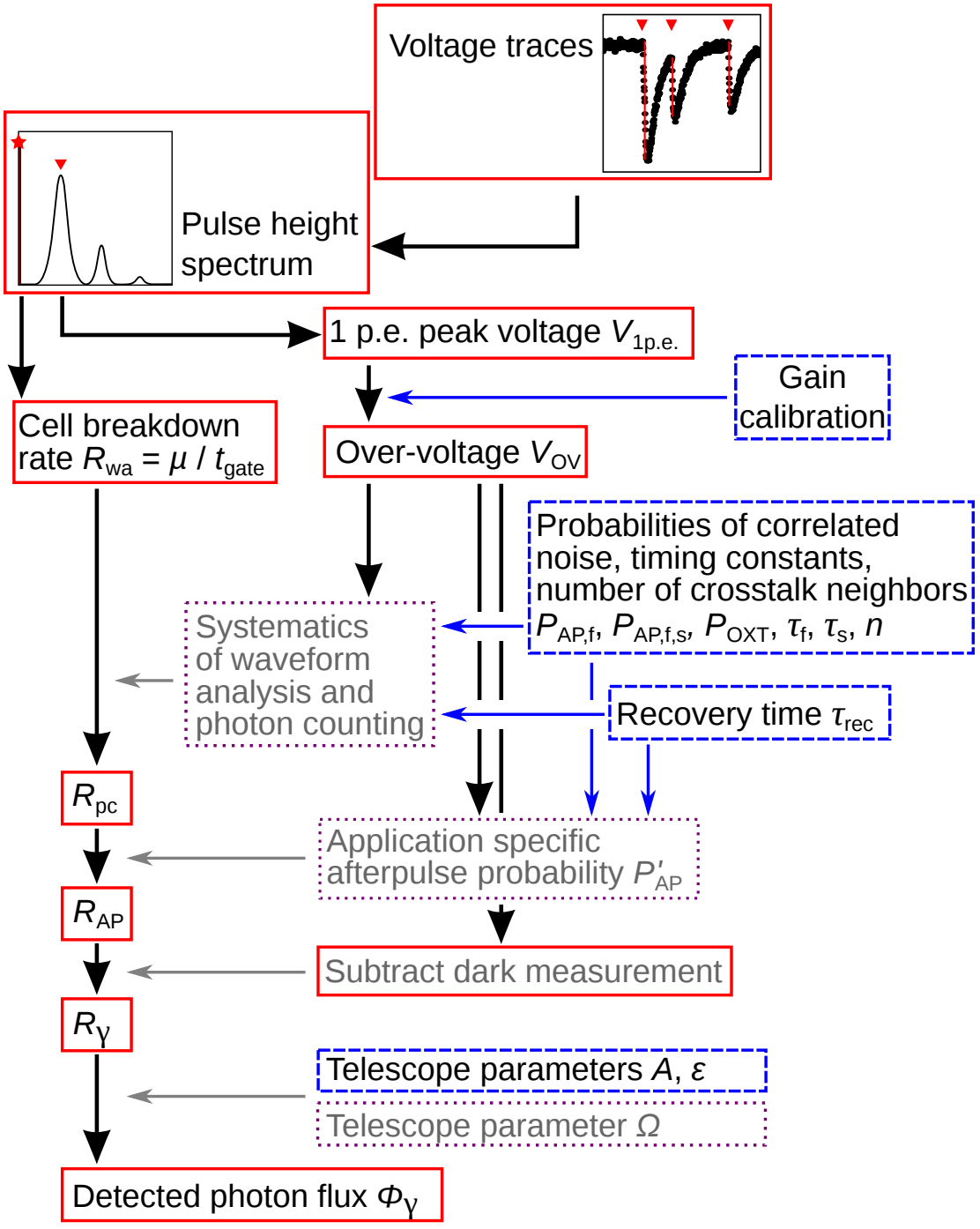

Figure 7.22: Block diagram summarizing the analysis discussed in this chapter. The arrows denote the work flow of the analysis chain. Quantities in red boxes are determined for each individual measurement of the night-sky brightness. Quantities in blue dashed boxes are determined from the auxiliary measurements. The ones in magenta-colored dotted boxes are determined by Monte Carlo methods based on measurements.

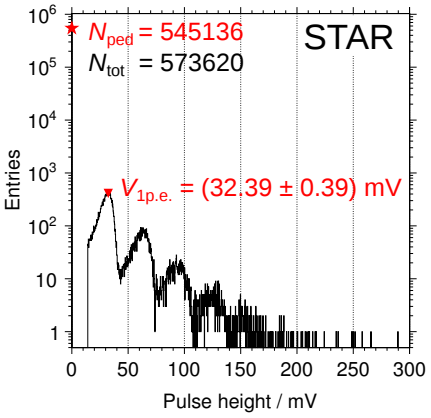

duration of measurement: 10 s
N_{traces} = 1247

V_{OV} = (1.23 ± 0.02 (stat.) ± 0.02 (sys.)) V

$P_{OXT,\geq 1}$ = 0.240 ± 0.007 (stat.) ± 0.017 (sys.)
P_{AP} = 0.419 ± 0.012 (stat.) ± 0.016 (sys.)
P'_{AP} = 0.446 ± 0.018 (stat.) ± 0.024 (sys.)

μ = 0.05093 ± 0.00029 (stat.)
R_{wa} = (10.19 ± 0.06 (stat.) ± 0.03 (sys.)) MHz
R_{pc} = (12.51 ± 0.08 (stat.) ± 0.13 (sys.)) MHz
R_{AP} = (6.93 ± 0.28 (stat.) ± 0.39 (sys.)) MHz
R_γ = (3.98 ± 0.22 (stat.) ± 0.24 (sys.)) MHz
Φ_γ = (2.78 ± 0.15 (stat.) ± 0.37 (sys.)) · 10^{12} m^{-2} s^{-1} sr^{-1}

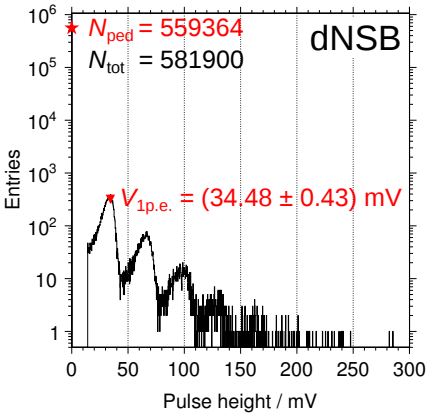

duration of measurement: 10 s
N_{traces} = 1265

V_{OV} = (1.31 ± 0.02 (stat.) ± 0.02 (sys.)) V

$P_{OXT,\geq 1}$ = 0.267 ± 0.007 (stat.) ± 0.019 (sys.)
P_{AP} = 0.467 ± 0.012 (stat.) ± 0.017 (sys.)
P'_{AP} = 0.521 ± 0.019 (stat.) ± 0.025 (sys.)

μ = 0.03950 ± 0.00025 (stat.)
R_{wa} = (7.90 ± 0.05 (stat.) ± 0.02 (sys.)) MHz
R_{pc} = (9.45 ± 0.07 (stat.) ± 0.11 (sys.)) MHz
R_{AP} = (4.53 ± 0.17 (stat.) ± 0.22 (sys.)) MHz
R_γ = (1.40 ± 0.10 (stat.) ± 0.07 (sys.)) MHz
Φ_γ = (0.98 ± 0.07 (stat.) ± 0.12 (sys.)) · 10^{12} m^{-2} s^{-1} sr^{-1}

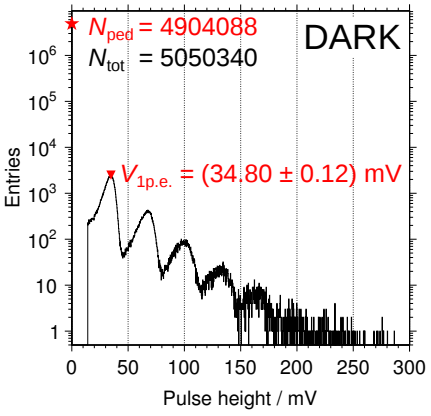

duration of measurement: **90 s**
N_{traces} = 10979

V_{OV} = (1.33 ± 0.01 (stat.) ± 0.02 (sys.)) V

$P_{OXT,\geq 1}$ = 0.274 ± 0.004 (stat.) ± 0.019 (sys.)
P_{AP} = 0.479 ± 0.006 (stat.) ± 0.018 (sys.)
P'_{AP} = 0.540 ± 0.010 (stat.) ± 0.025 (sys.)

μ = 0.02939 ± 0.00007 (stat.)
R_{wa} = (5.88 ± 0.02 (stat.) ± 0.02 (sys.)) MHz
R_{pc} = (6.85 ± 0.02 (stat.) ± 0.07 (sys.)) MHz
R_{AP} = (3.15 ± 0.07 (stat.) ± 0.15 (sys.)) MHz
R_γ = 0 (per definition)
Φ_γ = 0 (per definition)

N_{ped}	pedestal entries	P_{AP}	afterpulse probability	R_{pc}	CB rate corr. for systematics of WA and photon counting
N_{tot}	total entries	P'_{AP}	application specific afterpulse prob. (accounts for cascades of afterpulses)	R_{AP}	CB rate corr. for afterpulses
$V_{1p.e.}$	position of 1 p.e. peak	μ	number of cell breakdowns (CB) per t_{gate} = 5 ns	R_γ	CB rate corr. for thermal noise
N_{traces}	number of traces	R_{wa}	CB rate determined by waveform analysis (WA)	Φ_γ	detected photon flux
V_{ov}	over-voltage				
$P_{OXT,\geq 1}$	crosstalk probability				

Figure 7.23: Exemplary pulse height spectra and the resulting quantities of interest measured on July 3rd, 2012 (cf. following figures). The top row is for a measurement into the direction of the bright star Arcturus. The middle row is for a line of sight of the night-sky photometer into a direction without bright stars, thus measuring the diffuse night-sky brightness (dNSB). For the bottom row the aperture of the telescope was closed.

statistical uncertainty in the determination of the applied over-voltage. They are propagated through the entire analysis chain by means of a Monte Carlo method. The statistical uncertainty of the rates of detected signal-photons is $\sim 2\%$ for a nominal measurement duration of 90 s.

The detected light flux ϕ_γ measured with the NSPM as a function of time is shown in figure 7.24. The time is stated in seconds elapsed since the beginning of July 3, 2012 for the left plot of the figure and the beginning of July 24, 2012 for the other one. The first data points in both plots refer to measurements into the directions of bright stars. For the left plot this is Arcturus and for the right one this is Vega. The telescope tracked the stars up to a certain time, where its movement stopped. This time is denoted by the red lines in the plots. From there on the sky moved relatively to the NSPM through its field of view.
Shown by the black error bars are the statistical uncertainties. The vertical size of the boxes around the data points are the systematic uncertainties. In the plots they are linearly stacked onto each other to distinguish between the different causes of the systematics. Aside from plots, the systematic uncertainty is given as the quadratic sum of the individual contributions. The horizontal size of the boxes indicates the duration of the individual measurements. Unlike all other NSB measurements performed with the V1729 ADC the two shown in figure 7.24 consist of individual measurements which took 10 s each instead of 90 s. Also dark measurements were not performed after each four individual NSB measurements. This choice is motivated to resolve the decrease in the photon flux after the slew control of the telescope is switched off and the stars will leave the field of view.

On a first guess one might be tempted to assume that, providing perfect focusing, there should be a very sharp cutoff of the detected photon flux at the moment when the star leaves the field of view since it is just a point in the focal plane of the telescope. However, even with the assumption of perfect focusing this is not the case. On the one hand, the optical efficiency of the PN-203 telescope does not feature a very sharp cutoff (cf. figure 6.6). On the other hand, the design of the camera pixel will lead to a reduction of the detected photon flux if the light of the star enters the telescope with an angle $\alpha_\mathrm{f} > 0°$. As the image of a star moves from the border of the exit aperture of the Winston cone radially along its reflecting surface, the incident angles of the light on the SiPM will increase (cf. figures 5.5 and 5.6). For higher incident angles the photon detection efficiency of the SiPM is reduced (cf. figure 4.11).
By means of the planetarium software Stellarium [164] the angular velocities of Arcturus and Vega are determined to $(4.25 \pm 0.05) \cdot 10^{-3}\,°s^{-1}$ and $(4.00 \pm 0.05) \cdot 10^{-3}\,°s^{-1}$, respectively. Assuming perfect focusing and alignment of the telescope, the stars will need (80 ± 5) s and (85 ± 5) s, respectively, to move $(0.34 \pm 0.02)°$ from the center of the field of view to its border.
For the data concerning Arcturus the timescale of the decrease of the measured light flux agrees very well with this calculation. However, Vega needs less than 60 s to move out of sight. This corresponds to an angular distance of 0.24°. Vega might not have been centered in the field of view when the movement of the telescope stopped.

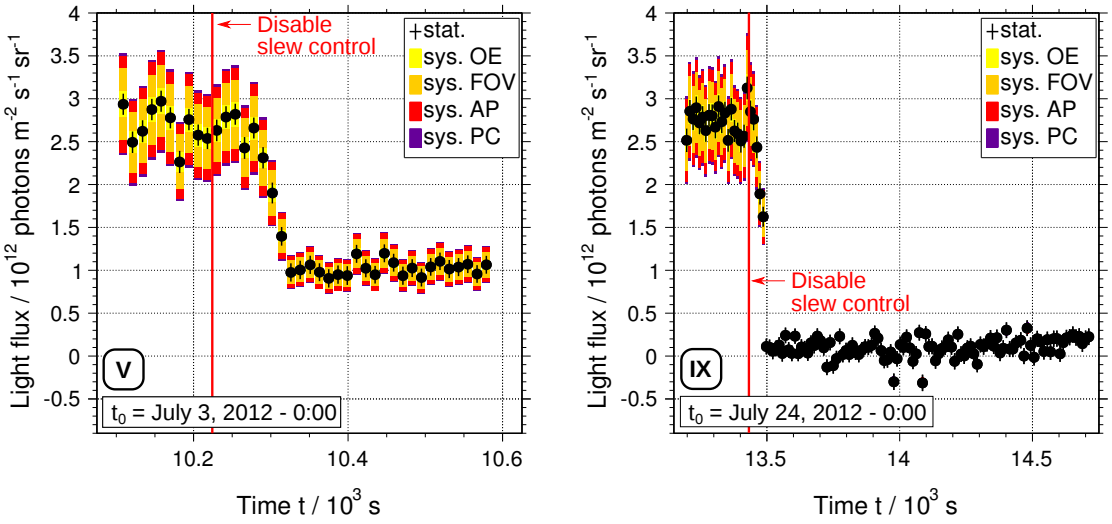

Figure 7.24: Measured night-sky light flux as a function of the time since t_0. The data do not include dark counts of the SiPM. Left plot for the star Arcturus, right plot for Vega. The telescope is tracking the stars up to the times denoted by the solid red lines. Afterwards the slew control of the telescope is disabled. Bars indicate statistical uncertainties, the vertical size of the boxes the systematic ones (optical efficiency of the PN-203 telescope (OE), field of view (FOV), afterpulsing (AP), systematics of waveform analysis and photon counting (PC)). The horizontal size of the boxes indicates the duration of the individual measurements. The boxes of the systematic uncertainties are stacked upon each other. The Roman numbers in the boxes are the identification numbers also given in figure 7.25 and table 7.2.

The detected light flux ϕ_γ is in the order of 10^{11} to 10^{12} photons per square meter per second per steradian. It is obvious from the data that the diffuse NSB is much more intense in the measurements on July 3, 2012 compared to the ones on July 24, 2012. Both measurements were performed at the same observational site, which is on the roof of the Physikzentrum in Aachen, Germany.[24] The reason for the difference is the Moon. On July 3 it was full Moon. The Moon was visible and had an angular distance to Arcturus of about 69°. On July 24 it was waxing Moon, two days before half Moon, and the Moon was about 40° below the horizon.
A slight increase in the data of the diffuse NSB for the measurements on July 24 is visible. This is due to the advancing dawn. The astronomical dawn[25] was at 2:44 a.m., while the nautical dawn was on 4:12 a.m. This corresponds to $9.8 \cdot 10^3$ s and $15.1 \cdot 10^3$ s past midnight, respectively.

Similar plots to those of figure 7.24 can be found in figure 7.25. The first four measurements on June 23, 2012 were performed without the UV filter while the subsequent ones during this night were performed with the standard setup including

[24] coordinates: N 50° 46′ 53″, E 6° 02′ 55″

[25] At the astronomical dawn the Sun is 18° below the horizon. It is the beginning of the astronomical twilight, followed by the nautical twilight. At the nautical dawn the Sun is 12° below the horizon. At 6° below the horizon the civil twilight commences.

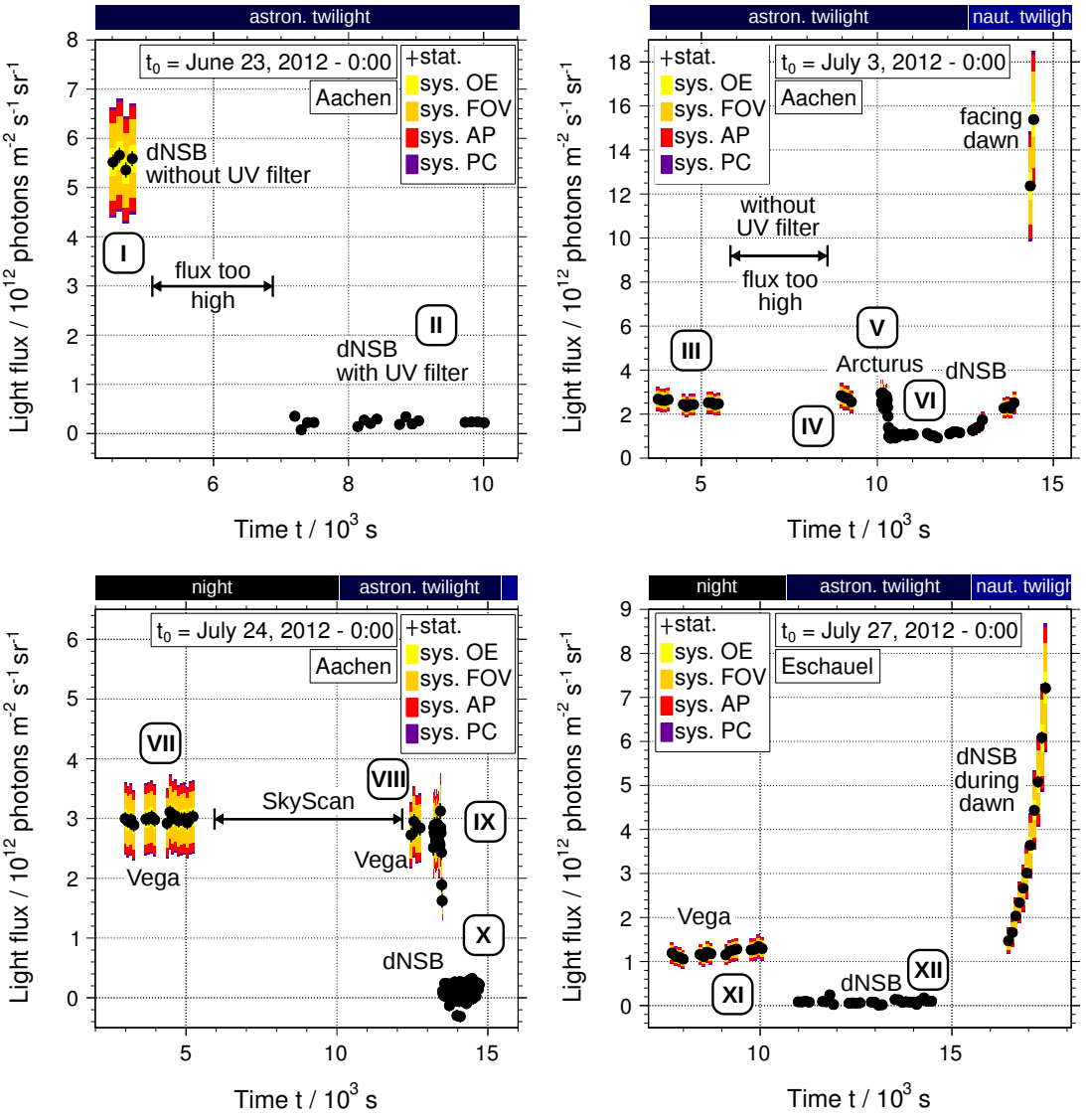

Figure 7.25: Measured night-sky light flux as a function of the time since t_0 for four different nights in summer 2012 at two different observational sites (Aachen and Eschauel). The data do not include dark counts of the SiPM. Bars indicate statistical uncertainties, the vertical size of the boxes the systematic ones (optical efficiency of the PN-203 telescope (OE), field of view (FOV), afterpulsing (AP), systematics of waveform analysis and photon counting (PC)). The horizontal size of the boxes indicates the duration of the individual measurements. The boxes of the systematic uncertainties are stacked upon each other. The bars above the plots denote different phases of dawn (astronomical twilight and nautical twilight). Text indicates into which direction the night-sky photometer was pointing (dNSB = diffuse night-sky brightness,i.e. no bright star into this direction) and why there were apparent breaks in the data acquisition. If not stated differently, the UV band-pass filter was applied. The Roman numbers in the boxes are the identification numbers also given in table 7.2 where the mean light fluxes for different time intervals are summarized. See text for further details.

the filter. More than 95% of the radiance of the night-sky brightness can be suppressed by applying the UV filter to the detector.
On June 23 and July 3 the star Arcturus has been observed with the NSPM without applying the UV filter. The corresponding time intervals are marked in figure 7.25 with the label *flux too high*. The cell breakdown rate is too high to result in pulse height spectra of the typical shape. Instead, the peaks are broadened and flat-topped, and the determination of the over-voltage results in uncertainties which are too high to be of practical value. An example of such a pulse height spectrum is given in figure A.5 in appendix A.3.
Eventually the fact shall be remarked that the NSPM was able to measure also the light flux far into the nautical twilight without taking certifiable damage. Regarding the related measurements (shown in the two right plots of figure 7.25 and tagged with *facing dawn* and *dNSB during dawn*) the detected light fluxes are much higher and the dawn appears to commence much earlier on July 3 than on July 27. This is caused by the different directions of observations of the NSPM. During dawn of July 3 it was pointing directly towards the brightest region just above the horizon, while during the other dawn it was orientated towards an altitude of about 57° and an azimuth of about 266°.

In regions where the measured photon fluxes are reasonably constant with time the mean light flux $\bar{\phi}_\gamma$ is determined. The results are summarized in table 7.2. The given statistical uncertainties are the standard deviations of the distributions of individual measurements which contribute to a mean value, divided by $\sqrt{N}$ with N being the number of these individual measurements.
With the different nights there is a huge variation in the flux of the diffuse NSB. This is mainly caused by the phase of the Moon. In general, the diffuse NSB depends on the observational site, the time, the actual atmospheric conditions (since a different composition of the atmospheric constituents will lead to a different (back-) scattering of terrestrial and celestial light), and on the direction into which it is observed. Even without the consideration of scattered moonlight and sunlight, and without the consideration of artificial light, the dependence of the diffuse NSB on the observational direction persists [140]: with decreasing altitude the number of atoms along the line of sight and within the atmospheric layer which causes the airglow (cf. introduction of chapter 6) increases.
None of the mean photon fluxes $\bar{\phi}_\gamma$ given in table 7.2 is exclusively due to starlight. If the NSPM has been pointing at a star, photons originating from the star as well as from the diffuse NSB around it contribute to the stated flux. Since the diffuse NSB may vary between the different measurements, the given photon fluxes into the direction of a specific star do not necessarily have to be identical. In the next chapter we will isolate the starlight photon flux for further comparison of the measurement results.
The detected photon fluxes of the diffuse NSB measured on July 24 and July 27 are almost identical.[26] On the other hand, the photon flux originating from Vega measured on July 27 is less than 50% of the one measured three days before. The measurements on July 24 have been performed in Aachen, while the other ones took

[26] The differences in the uncertainties derive from the difference in the applied over-voltage.

Table 7.2: Mean detected photon fluxes $\bar{\phi}_\gamma$ for various measurements into the directions of the bright stars Arcturus and Vega, and into directions without bright stars (diffuse night-sky brightness (dNSB)). The data do not include dark counts of the SiPM. The identification numbers (ID) are also given in the plots of figure 7.25 at the related data points.

ID	Date [*1]	Location	Direction	$\bar{\phi}_\gamma$ / 10^9 photons $m^{-2}\,s^{-1}\,sr^{-1}$
I	June 23	Aachen	dNSB [*2]	$5531 \pm 77\,(\text{stat.}) \pm 732\,(\text{sys.})$
II	June 23	Aachen	dNSB	$232 \pm 23\,(\text{stat.}) \pm 29\,(\text{sys.})$
III	July 3	Aachen	Arcturus	$2514 \pm 36\,(\text{stat.}) \pm 329\,(\text{sys.})$
IV	July 3	Aachen	Arcturus	$2715 \pm 60\,(\text{stat.}) \pm 358\,(\text{sys.})$
V	July 3	Aachen	Arcturus	$2699 \pm 35\,(\text{stat.}) \pm 356\,(\text{sys.})$
VI	July 3	Aachen	dNSB	$1021 \pm 22\,(\text{stat.}) \pm 132\,(\text{sys.})$
VII	July 24	Aachen	Vega	$2990 \pm 26\,(\text{stat.}) \pm 413\,(\text{sys.})$
VIII	July 24	Aachen	Vega	$2836 \pm 63\,(\text{stat.}) \pm 373\,(\text{sys.})$
IX	July 24	Aachen	Vega	$2738 \pm 29\,(\text{stat.}) \pm 359\,(\text{sys.})$
X	July 24	Aachen	dNSB [*3]	$87 \pm 14\,(\text{stat.}) \pm 11\,(\text{sys.})$
XI	July 27	Eschauel	Vega	$1200 \pm 23\,(\text{stat.}) \pm 163\,(\text{sys.})$
XII	July 27	Eschauel	dNSB	$87 \pm 15\,(\text{stat.}) \pm 12\,(\text{sys.})$

[*1] all dates in 2012
[*2] no UV filter applied
[*3] the first 40 data points of the set are used

place at the southern end of the peninsula of Schmidt–Eschauel, Germany,[27] a quite rural place at the border of the Eifel National Park which is less light polluted than Aachen. The reason for the relatively low starlight photon flux and the relatively high diffuse NSB detected in Eschauel is given by a difference of the atmospheric conditions of the two considered nights. Although the sky was starlit, it was visible by the naked eye that the sight was less clear on July 27 than on July 24. Independent, quantitative measurements performed by the Jülich ObservatorY for Cloud Evolution (JOYCE) [169] and provided by the AErosol RObotic NETwork (AERONET) program [170] confirm a significant difference of the atmospheric conditions of the two considered nights. Especially the aerosol optical depth of the atmosphere was different, which has led to a reduced UV starlight flux at ground level for the night of July 27 compared to three nights earlier. The atmospheric effects on the measurements of the starlight fluxes will be discussed quantitatively in the following chapter.

[27] coordinates: N 50° 38′ 26″, E 6° 25′ 00″

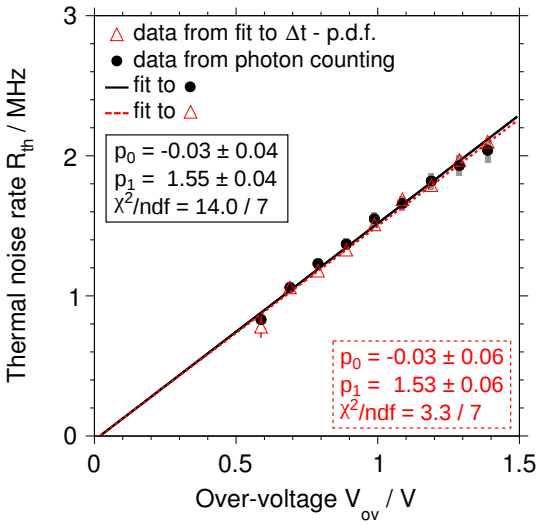

Figure 7.26: Thermal noise rate R_{th} as a function of the over-voltage V_{ov}. The red triangles are data derived from the exponential fits to the Δt distributions (cf. figure 7.9). The black points are data resulting from the photon counting technique. The correspondingly colored lines are linear fits to the data.

As mentioned previously in chapter 6 the goal of the measurements of the NSB is to understand the working principle of SiPMs, probe our understandings and models, and provide a reliable reconstruction of detected light fluxes rather than give an extensive set of NSB data. Nevertheless, the actual values of the detected NSB photon flux can be applied to detector simulations of FAMOUS to determine the detection threshold of air showers in terms of energy of the air shower and its distance to the fluorescence telescope (cf. section 5.2). A comparison of the measured signal-photon rates attributed to the light originating from stars with expectations derived from models provides a sanity and quality check of the used analysis method. The procedure will be discussed in detail in the next chapter. But prior to this, a further sanity and quality check will be presented. This one does not require NSB data but is performed on the data taken in the laboratory and previously used to determine the afterpulse probability.

Due to the circumstance that $R_{\mathrm{AP}}^{\mathrm{dark}}$, which is the detected cell breakdown rate corrected for afterpulses in the case of the dark measurements, is believed to include only thermal breakdowns, it can be compared to the thermal breakdown rate R_{th} measured already in section 7.4. R_{th} has been determined by the corresponding fit to the distribution of time differences Δt between a 1 p.e. pulse and its consecutive pulse. Hence, we have two methods which are independent of each other to determine the same quantity.
The data of the auxiliary measurement are analyzed in the same way as the data acquired with the NSPM in case of dark measurements. The only differences is that the last step is not performed, i.e. equation (7.44) which takes the telescope parameters into account is not applied.
The results are shown in figure 7.26 as a function of the over-voltage V_{ov}. The red

triangles are the same data of R_{th} as presented in section 7.4, i.e. the data of the Δt-method. The black data points are the results of the photon counting method. Error bars denote statistical uncertainties, while the vertical sizes of the gray boxes denote the systematic uncertainties. Linear fits to the data are also shown in the figure. The corresponding fit parameters of the two different approaches to determine the thermal noise rate agree well with each other. A linear fit to the data obtained from the Δt-method yields $R_{\mathrm{th}}^{\Delta t} = (1.52 \pm 0.01)\,\mathrm{MHz\,V^{-1}} \cdot V_{\mathrm{ov}}$ if the constant parameter is fixed to zero. The uncertainty of the photon counting method, which is defined as the spread of the corresponding data in relation to $R_{\mathrm{th}}^{\Delta t}$, is 3.1%.
This quality check certifies that the photon counting method is a reliable procedure to reconstruct a continuous photon flux measured with SiPMs.

8. Comparison of the Measured Starlight Flux with References

Bright stars, which are well-studied by observational astronomy, can be regarded as calibrated light sources for the night-sky photometer (NSPM).
Before the starlight flux detected with the NSPM can be compared to reference data, it has to be isolated from the contribution of the diffuse night-sky brightness (NSB). This will be performed in the first section of this chapter. In the subsequent section the reference data will be discussed. It is given in terms of spectral radiance and spectral irradiance. Both are radiometric quantities. The former describes the amount of radiation per unit wavelength which passed through or is emitted from a particular area and which is contained in a given solid angle in a specified direction. The unit of the spectral radiance is watts per square meter per steradian per nanometer. Radiance is used to describe the angle dependent emission of radiation from diffuse sources as well as the diffuse reflection of radiation at surfaces. The spectral irradiance is the power per unit wavelength per unit area incident on a surface. Its unit is watts per square meter per nanometer. It is used to decribe a received power.
To determine the amount of light received by the NSPM, the reference data have to be modified regarding the atmosphere of the Earth and the spectral photosensitivity of the experimental setup. In the last section, the reference data will be compared to the measured photon flux of the stars.

8.1 Background subtraction

The photons, which the NSPM detects while it is pointing into the direction of a star, do not exclusively originate from this star but also from the diffuse NSB. If the photon flux of the diffuse NSB is known, in principle it can be subtracted from the data to yield the isolated photon flux of the star. Nevertheless, the limited dynamic range of the SiPM can complicate the procedure and make a straightforward subtraction inappropriate. To study the dynamic range in the context of the detected night-sky photon flux the G4SiPM simulation toolkit (cf. section 4.3) is applied.

Within the simulation initial cell breakdowns of three types are generated: (a) thermal breakdowns with a constant rate of $R_{\mathrm{th}} = 7.6\,\mathrm{MHz}$ corresponding to the dark measurements of the NSPM, i.e. the measurements with a closed aperture of the

telescope,[1] (b) breakdowns due to signal-photons with a constant rate of $R_{\mathrm{dNSB}} = 2.5\,\mathrm{MHz}$ representing the signal of the diffuse NSB, and (c) breakdowns due to signal-photons with a rate ranging from 100 kHz to 100 GHz representing the signal of the star. A signal-photon detection rate of 2.5 MHz corresponds to a signal-photon flux of about $1.8 \cdot 10^{12}$ photons per square meter per second per steradian. This exceeds the maximum detected photon flux in the measured data when the NSPM was pointing into a direction without bright stars. R_{th} and R_{dNSB} are chosen to result in an upper limit of the cell breakdown rates which are not caused by photons originating from the star.
Thermal breakdowns are distributed uniformly over the entire sensitive area of the SiPM. Considering the exit aperture of the light concentrator, which is mounted in the NSPM in front of the SiPM, the breakdowns due to signal-photons may only occur on a circular area with a diameter of 3 mm centered on the sensitive area of the SiPM. For each run of the simulation, i.e. for each rate of signal-photons corresponding to (c), 10000 of these signal-photons are generated and the simulated time is calculated appropriately to result in the desired rate. An over-voltage of 1.4 V has been chosen, which exceeds the over-voltages which have been applied during the measurements of the starlight and the related diffuse NSB. The choice of the over-voltage of the simulation is also intended to lead to an upper limit of the cell breakdown rates which are not caused by photons originating from the star, since the probabilities of correlated noise increase with the over-voltage. The characteristics of the SiPM are set to follow the behavior as described in the previous chapter. Further technical details regarding the settings of the simulation are summarized in table A.2 in appendix A.3.

The simulation results are shown in figure 8.1. On first sight, the data in the left plot look familiar to the data shown in figure 4.14 where the dynamic range of SiPMs was introduced. But the plotted measures are different. Here the number of detected signal-photons per second R_{SiPM} is given as a function of the number of cell breakdowns per second attributed to the star R_{star}, i.e. cell breakdowns due to (c). This way the displayed data do not imply information on the correlated and thermal noise which is also contained in the simulation.
Regarding the left plot of figure 8.1, for small values of R_{star} the rate of detected photons converges to a constant value equal to the number of detected photons of the diffuse NSB per second R_{dNSB}, i.e. cell breakdowns due to (b). With an increase of R_{star} the rate of detected photons runs into a linear region before it commences to saturate at roughly 1 GHz. The dashed curve is the sum of R_{star} and R_{dNSB}. A deviation of the data points from this sum is caused by the limited dynamic range of the SiPM. To make the deviation clearer, $R_{\mathrm{SiPM}}/(R_{\mathrm{star}} + R_{\mathrm{dNSB}})$ as a function of R_{star} is shown in the right plot of figure 8.1. At $R_{\mathrm{star}} = 1\,\mathrm{GHz}$ about 10% of the signal-photons do not cause a detectable cell breakdown since the cells are not yet

[1] The thermal breakdown rate has been determined by means of a fit to the Δt distribution of consecutive SiPM pulses as discussed in chapter 7. The related data have been acquired from laboratory-based dark measurements at room temperature and an over-voltage of 1.4 V. The maximum thermal noise rate determined from the NSB data by means of the photon counting method is 4.3 MHz.

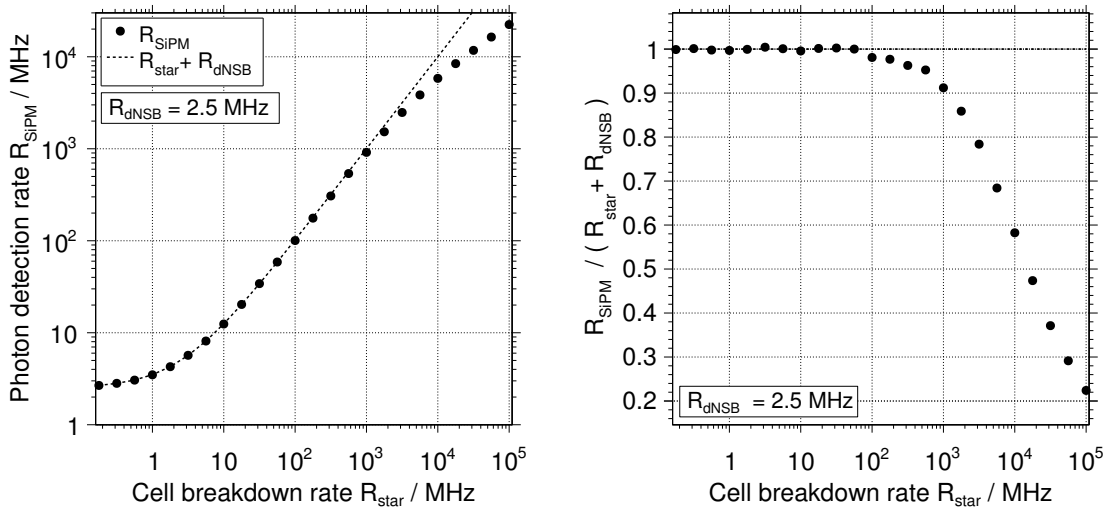

Figure 8.1: Simulated dynamic range of the SiPM applied to the night-sky photometer (900 cells, 100 µm cell pitch) in the context of the night-sky brightness measurements. The simulations use an over-voltage of $V_{\mathrm{ov}} = 1.4\,\mathrm{V}$. **Left:** Rate of detectable cell breakdowns R_{SiPM} as a function of R_{star}, which is the rate of cell breakdowns caused by photons originating from the star. Photons contributing to R_{SiPM}, i.e. signal-photons, are either due to the star or due to the diffuse night-sky brightness (dNSB) (i.e. plotted quantities do not contain cell breakdowns due to thermal or correlated noise). The sum of their rates $R_{\mathrm{star}} + R_{\mathrm{dNSB}}$ is given by the dashed curve. **Right:** Rate of detectable cell breakdowns normalized to the rate of cellbreakdowns caused by signal-photons $R_{\mathrm{SiPM}}/(R_{\mathrm{star}} + R_{\mathrm{dNSB}})$ as a function of R_{star}.

sufficiently recovered from the preceding breakdown.
Fortunately, the measured values of R_{star} are far below 1 GHz. The highest value of $R_{\mathrm{star}} + R_{\mathrm{dNSB}}$ in the measured data is about 4.3 MHz. At this rate the response of the simulation of the SiPM indicates that only a marginal amount of signal-photons is undetected due to dynamic range limitations. Hence, the photon flux measured with the NSPM pointing into a direction without bright stars can be subtracted directly from the photon flux measured while pointing into the direction of a bright star, assuming that the diffuse NSB is constant. If both kinds of measurements are performed rapidly after each other, and if the angular distance of the two directions is small, this assumption is provided. The subtraction results in the detected light flux of photons originating from the star.
These results are given in figure 8.2 for the measurements discussed in the previous chapter, where Arcturus and Vega were tracked and the slew control of the telescope was disabled after a while (cf. figure 7.24).[2] The mean detected starlight rates for

[2]In contrast to the plots in figures 7.24 and 7.25 where the normalized light flux is shown, here the photon detection rate is plotted. Unlike the normalized light flux it does not include systematic uncertainties raised by the telesope parameters (i.e. field of view of, optical efficiency, aperture area), but only those of the photon counting method.

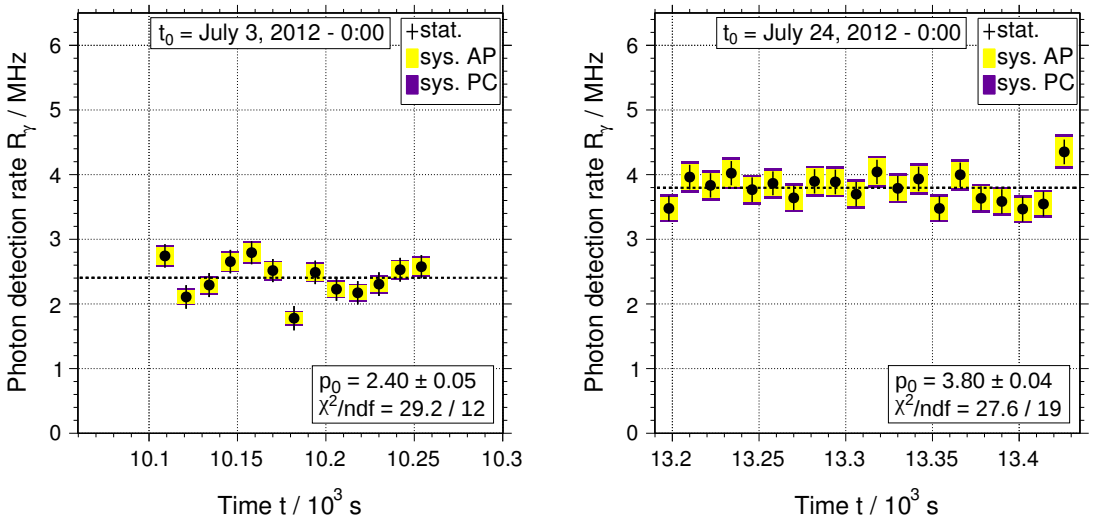

Figure 8.2: Rates of detected photons originating from the stars Arcturus (left) and Vega (right) as a function of the time elapsed since t_0. Statistical uncertainties are given by the error bars. The vertical size of the boxes denotes the systematical uncertainties (afterpulsing (AP), systematics of waveform analysis and photon counting (PC)). They are stacked onto each other. The horizontal size of the boxes denotes the duration of the individual measurements. The dashed lines are fits of contants to the data.

Arcturus and Vega are $R_\gamma^{\mathrm{Arct}} = (2.40 \pm 0.05)\,\mathrm{MHz}$ and $R_\gamma^{\mathrm{Vega}} = (3.80 \pm 0.04)\,\mathrm{MHz}$, respectively.[3]

8.2 Reference measurements and models of stars

The spectral sensitivity of the NSPM is predominantly specified by the spectral photon detection efficiency of the SiPM (cf. figure 4.10) and the spectral transmittance of the applied UV band-pass filter (cf. figure 5.7).
Folding these two characteristics with the spectral irradiance of a reference star observed at Earth, and taking further efficiencies of the optical components (Winston cone, PN-203 telescope, angular dependence of the photon detection efficiency of the SiPM) into account, yields the spectral irradiance corresponding to the detected photons. An integration of the irradiance and the consideration of the aperture of the NSPM result in the total power of the detected light flux. From this power the photon detection rate can be determined and compared to the measured data.

Modeling the spectral irradiance of a reference star as the one of a black body may not be the best choice depending on the specific star which is considered. For the Sun for instance the agreement is reasonably good as can be seen from figure 8.3 (left).

[3] In table 7.2 the detected photon fluxes $\phi_\gamma = R_\gamma/(\Omega\, A\, \epsilon)$ of the stars and the diffuse NSB are listed. Ω is the field of view of the NSPM, A is the aperture area, and ϵ is the efficiency of the PN-203 telescope; thus, R_γ^{Arct} and R_γ^{Vega} can be calculated from these fluxes.

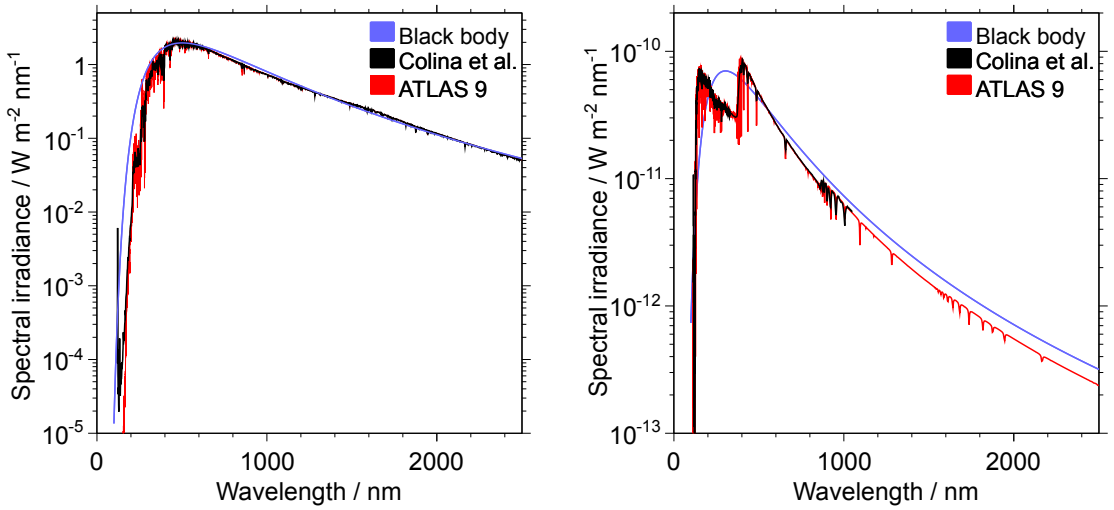

Figure 8.3: Spectral irradiances of the Sun (left) and Vega (right) at the top of Earth's atmosphere. The black curves are measurements according to references [171] and [172], respectively. The blue curves are for black body radiation with temperatures of 5777 K (Sun) and 9550 K (Vega). The red curves represent results from the ATLAS stellar atmosphere model. See text for further details.

Here, the spectral irradiance of the Sun observed at Earth without consideration of the atmosphere is shown. The blue curve is for a black body with the temperature of $T = 5777\,\mathrm{K}$ which is the effective temperature of the Sun [171]. The black curve denotes measurements according to reference [171], and the red curve derives from a set of tools referred to as the ATLAS suite [173, 174]. The ATLAS suite is one of the most popular tools to model stellar atmospheres and synthesize stellar spectra. It includes the codes ATLAS9 and ATLAS12 for the calculation of one-dimensional plane-parallel atmosphere models, SYNTHE for the calculation of synthetic spectra, WIDTH for the determination of chemical abundances from measured equivalent widths of spectral lines, and DFSYNTHE to produce precomputed opacity density functions. While ATLAS9 requieres these precomputed functions, ATLAS12 calculates the opacity during the model calculations. This allows arbitrary compositions of stellar atmospheres, which are of interest for chemically peculiar stars. ATLAS9 is not that flexible, and the entire stellar atmosphere is fixed to the one relating to the precomputed opacity density function. However, this is adequate for most applications, and ATLAS9 runs much faster than ATLAS12 [175].
The codes of the ATLAS suite are not executed within this work, but its inventor and key developer R. L. Kurucz provides spectra of various stars on his web page [176].[4] The data are spectral radiances given in absolute units at the surfaces of the stars. To obtain the spectral irradiance at top of the atmosphere of the Earth, the ATLAS data are normalized to measured reference values. It is a common procedure in ob-

[4]The data are available for different wavelength resolutions. Used for this work are the data sets arcallpr1.500 and vegallpr25.500. The relative differences of the integrated radiances for different data sets of the same star are below 0.1%.

servational astronomy to scale the models to absolute flux calibrated measurements in the V band of the Johnson photometric system (cf. for instance reference [171]).[5] Similar to this procedure, the irradiances of the Sun according to the ATLAS model and the black body model are scaled to a reference value of $1.82\,\mathrm{W\,m^{-2}\,nm^{-1}}$ at a wavelength of 548.3 nm. This value is taken from the measurements of reference [171] which is shown in figure 8.3 (left). The deviations of the data from smooth continuum spectra lead to relative systematic uncertainties of the scales of the modeled spectra of 1% and 2% for the black body and ATLAS model, respectively. The absolute scale of the reference measurement has itself a systematic uncertainty of $\sim 2\%$ [171].
Although the black body cannot feature the absorption lines of the spectrum of the Sun, its overall agreement is fair. Also with regard to the solar constant which can be determined by an integration of the Sun's spectral irradiance. The black body model yields a solar constant of $(1430 \pm 32)\,\mathrm{W\,m^{-2}}$, while the ATLAS model yields a value of $(1348 \pm 38)\,\mathrm{W\,m^{-2}}$. With a nominal solar constant of $1366\,\mathrm{W\,m^{-2}}$ [177] the deviations are about 5% and 1%, respectively. The determination of the solar constant from the reference data given by the black curve is not possible since the corresponding measurements have only been performed for wavelengths up to 2500 nm. The ATLAS data contain wavelengths up to 300 µm.

The black body model is less appropriate for the star Vega. The spectral irradiance of Vega at the top of the atmosphere of the Earth is shown in the right plot of figure 8.3. The different colors of the curves correspond again to the black body model (blue, $T = 9550\,\mathrm{K}$ [178]), reference measurements (black) [172], and the ATLAS model (red). The black body and the ATLAS model have been scaled to a measured reference flux of $3.55 \cdot 10^{-11}\,\mathrm{W\,m^{-2}\,nm^{-1}}$ at a wavelength of 548.3 nm as measured and reported in reference [172]. The systematic uncertainty in scaling the models to the reference measurements is 1% and 2% for the black body and the ATLAS model, respectively. The systematic uncertainty on the absolute scale of the measured reference point is about 2% [172]. A normalization of the black body model to a reference point measured within another band at a higher wavelength seems more appropriate to result in a better agreement of the falling edge of the black body spectrum with the reference data. Either way, the black body model does not describe the measured data with high accuracy, and will thus not be considered within the further course of this analysis.
In contrast to the spectrum of the black body the ones of the measurements and the ATLAS model show a hard cutoff at roughly 350 nm and a recovery to a black body-like shape for shorter wavelengths, which lead to the visible double peak feature.[6] This cutoff is referred to as the Balmer discontinuity or Balmer jump which is caused by ionization of hydrogen from its first excited state. To ionize a hydrogen atom whose electron is in the $n = 2$ level a minimum energy of 3.4 eV is required. The jump is therefore expected at a wavelength of 364.7 nm. The occurrence of the

[5] A photometric system is a set of well-defined optical filters. A widely used photometric system is the Johnson system, also referred to as UBV system. U stands for ultra-violet, B for blue and V for visual.

[6] see figure A.6 appendix A.3 for an enlarged display

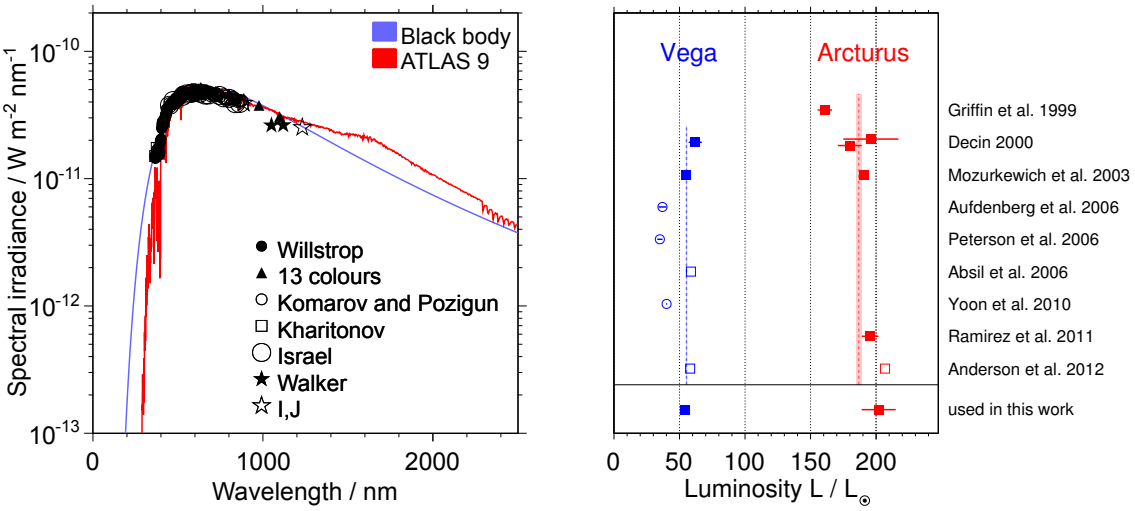

Figure 8.4: **Left:** Spectral irradiance of Arcturus at the top of Earth's atmosphere. The black data points represent measurements according to reference [179]. The blue curve is for black body radiation with a temperature of 4290 K. The red curve represents results from the ATLAS stellar atmosphere model. See text for further details. **Right:** Luminosity L of Vega (blue data points) and Arcturus (red data points) in units of the nominal solar luminosity $L_\odot$ taken from various references. The values of the bottom row are derived from the ATLAS models discussed in this work. Data points shown by open circles do not have an uncertainty. They do not contribute to the mean luminosities of the reference values shown by the colored, dashed horizontal lines. The band around these lines denote the uncertainties of the means. Also not contributing to the mean value of Vega are the data points shown by open squares. The corresponding reason, further details, and the references are given in the text.

Balmer jump and its characteristics depend (aside from the abundance of hydrogen) on the temperature of the considered star. If its temperature is too low, only very few hydrogen atoms will be in the first excited state. On the contrary, if the temperature is too high, the hydrogen will be entirely ionized and the photons with wavelengths $\lambda \lesssim 364.7\,\text{nm}$ can traverse the star without being absorbed.

The reference measurements of the spectral irradiance of Vega contain wavelengths up to 1050 nm. The integral of the measured data as shown in figure 8.3 (right) up to this wavelength yields $2.76 \cdot 10^{-8}\,\text{W m}^{-2}$. For the black body and the ATLAS models we find $(2.96 \pm 0.03) \cdot 10^{-8}\,\text{W m}^{-2}$ and $(2.71 \pm 0.05) \cdot 10^{-8}\,\text{W m}^{-2}$, respectively, which is a deviation from the nominal value of about 7% for the black body and 2% for the ATLAS model.
The deviation of the ATLAS model from the measured data is $\sim$ 5%, 2%, and 2% in the ultra-violet, visible, and infra-red region, respectively.

In figure 8.4 (left) the corresponding spectra of Arcturus are shown. As for the other stars they depict the spectral irradiance at the top of Earth's atmosphere.

The displayed measurements are a continuum flux according to reference [179] and contain only data for the interval of roughly 350 to 1250 nm. An enlarged display of this region in shown in figure A.6 in appendix A.3. The black body model uses a temperature of $T = 4290\,\mathrm{K}$ [180]. Both models are scaled at 550.9 nm to a flux of $4.63 \cdot 10^{-11}\,\mathrm{W\,m^{-2}\,nm^{-1}}$. This value is the mean of the relevant measured data at this particular wavelength, i.e. data labeled Willstrop, Komarov and Pozigun, and Israel. The wavelength has been chosen for a reference point since the individual measurements of the irradiance agree relatively well at this particular position. The systematic uncertainty in scaling the models to the reference measurements is 1% and 2% for the black body and the ATLAS model, respectively. A comparison of the flux measurements presented in references [179] and [180] lead to an estimate of the absolute scale of the measured reference flux of $\sim 6\%$.
An integration of the measured irradiances in the range from 363 nm to 887 nm yields mean value of $(2.03 \pm 0.18) \cdot 10^{-8}\,\mathrm{W\,m^{-2}}$. The uncertainty is the standard deviation of the integrated radiances divided by $\sqrt{N}$, with $N = 4$ being the number of considered measurements (Willstrop, 13 colours, Komarov and Pozigun, and Israel). Within the same wavelength range the black body model predicts an integrated irradiance of $(2.27 \pm 0.02) \cdot 10^{-8}\,\mathrm{W\,m^{-2}}$, while the ATLAS model predicts $(1.94 \pm 0.04) \cdot 10^{-8}\,\mathrm{W\,m^{-2}}$. The deviation of the ATLAS model from the measured data is $\sim 15\%$ for wavelength below 500 nm, $\sim 5\%$ for wavelength between 500 and 600 nm, and $\sim 2\%$ for wavelengths between 600 and 900 nm.

For sanity checks of the scaled ATLAS spectra the resulting stellar luminosities are compared to additional published data. The luminosity L of a star which emits its radiation isotropically is given by

$$L = 4\,\pi R^2 f = 4\,\pi R^2 \int_0^\infty s(\lambda)\,\mathrm{d}\lambda \tag{8.1}$$

with $s(\lambda)$ being the spectral irradiance of the star received at the Earth (without consideration of the atmosphere), f being the total irradiance, λ being the wavelength, and R being the distance between the star and the Earth. Thus, not only the entire electromagnetic spectrum emitted by a star has to be known to calcultae its luminosity, but also its distance. By means of the Hipparcos mission of the European Space Agency the parallaxes ρ of more than 100000 nearby stars and more than a million further stars have been determined with accuracies of about one and twenty milliarcseconds (mas), respectively [161, 181]. For Arcturus and Vega they are

$$\rho_{\mathrm{Arct}} = (88.83 \pm 0.54)\,\mathrm{mas} \qquad \text{and} \qquad \rho_{\mathrm{Vega}} = (130.23 \pm 0.36)\,\mathrm{mas}\,,$$

respectively. The distance of a star is $R = 1\,\mathrm{au}/\tan\rho$ with one astronomical unit (au) being approximately[7] $1.4960 \cdot 10^{11}\,\mathrm{m}$ [182]. The integration of the ATLAS data yields the irradiances and luminosities

$$\begin{aligned} f_{\mathrm{Arct}} &= (5.13 \pm 0.32) \cdot 10^{-8}\,\mathrm{W\,m^{-2}} \quad \text{and} \quad f_{\mathrm{Vega}} = (2.93 \pm 0.08) \cdot 10^{-8}\,\mathrm{W\,m^{-2}}\,, \\ L_{\mathrm{Arct}} &= (202 \pm 13)\,\mathrm{L_\odot} \quad \text{and} \quad L_{\mathrm{Vega}} = (54 \pm 2)\,\mathrm{L_\odot} \end{aligned}$$

[7] the astronomical unit is stated in reference [182] with a precision in the order of meters

for Arcturus and Vega, respectively. The luminosities are given in units of the nominal solar luminosity $L_\odot$. With the nominal irradiance of the Sun at the top of Earth's atmosphere $f_\odot = 1366\,\mathrm{W\,m^{-2}}$ we find the nominal solar luminosity to be

$$L_\odot = 4\,\pi\,(1\,\mathrm{au})^2\,f_\odot = 3.842 \cdot 10^{26}\,\mathrm{W}\,.$$

According to the Stefan–Boltzman law

$$F = \sigma\,T^4 \tag{8.2}$$

the total emitted power F per unit area of a black body is proportional to the fourth power of its temperature T. The constant of proportionality is the Stefan–Boltzman constant σ. According to equation (8.1) the total irradiance at the surface of a star with radius r is given by $f = L/(4\,\pi\,r^2)$. Since stars can be approximated by black bodies, and since a black body with the corresponding temperature provides an identical irradiance, the effective temperature T_eff of a star is defined by the relation of the temperature of a black body with the stellar luminosity

$$L = 4\,\pi\,r^2\,\sigma\,T_\mathrm{eff}^4\,. \tag{8.3}$$

To determine the effective temperature the luminosity does not necessarily have to be know. It can also be determined from Wien's displacement law which gives a direct relation between the maximum of the spectral emission of a black body λ_max and its temperature: $\lambda_\mathrm{max}\,T \approx 2.90 \cdot 10^{-9}\,\mathrm{nm\,K}$. Furthermore, the intensity of the absorption lines in stellar spectra correlates with the effective temperature. This fact can also be used to determine T_eff [183]. The radius of a star r can be determined for instance by stellar interferometry. Hence, the stellar luminosity can also be determined without knowledge of the entire electromagnetic spectrum emitted by a star.

Various luminosities of Arcturus and Vega as published directly or as calculated from published effective temperatures and stellar radii are shown in figure 8.4 (right). The data are according to references [180,184–191]. Additional data of Arcturus summarized in the scope of an extensive literature study published in reference [184] agree with the data shown in figure 8.4 (right). Also plotted are the luminosities derived from the scaled ATLAS models used in this work. The red markers are for Arcturus, and the blue ones are for Vega. Not all references state uncertainties. Those data points without an uncertainty are depicted as open squares. There are mainly two different values for the luminosity of Vega found in the literature which do not agree within their uncertainties. One is about $37\,\mathrm{L_\odot}$ while the other one is about $55\,\mathrm{L_\odot}$. This is caused by the fact that Vega is a rapidly rotating star. The ellipsoidal form of the star due to its rotation leads to a drop of the temperature of about 2400 K from its polar regions to its equator. From Earth we are looking almost directly onto one the poles [187]. Since Vega is far from being an isotropic source of radiation, equation (8.1) will result in a luminosity which is too high if the irradiance measured at Earth is taken directly into account, without further corrections. Though, for the purpose to determine the number of starlight photons detected with the NSPM the

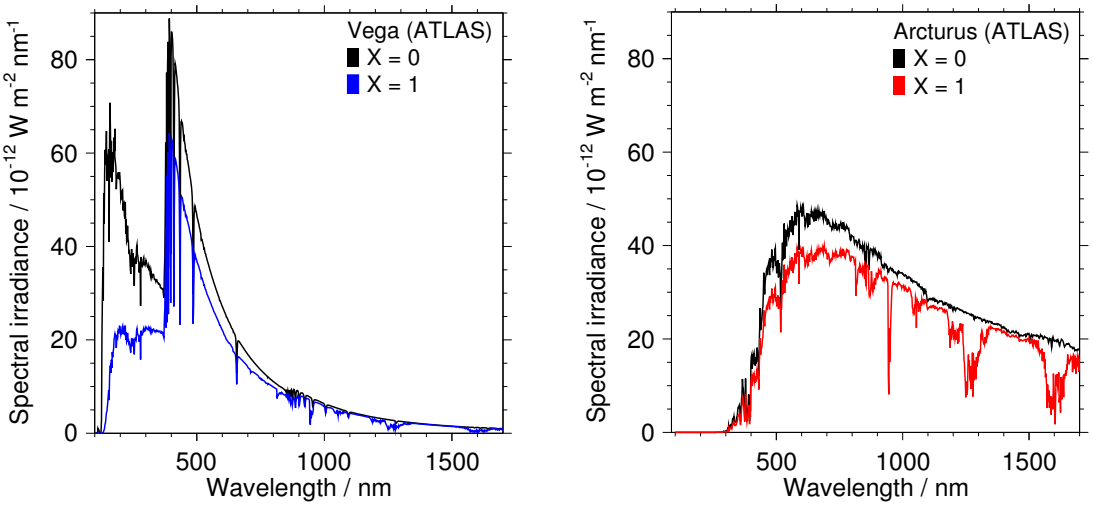

Figure 8.5: Spectral irradiances of Vega (left) and Arcturus (right) according to the ATLAS models. Shown are the irradiance at the top of Earth's atmosphere (air mass $X = 0$) and below one standard atmosphere ($X = 1$).

irradiance measured at Earth is the one which has to be considered. The luminosity derived from the ATLAS model is thus compared to the luminosities of Vega which favor the higher of the two typical literature values. Taking only these values into account which feature an uncertainty (i.e. Decin and Mozurkewich *et al.*) the mean luminosity is $L_{\mathrm{Vega}}^{\mathrm{Ref}} = (55.3 \pm 0.3)\,\mathrm{L}_\odot$. For Arcturus, all measurements which feature an uncertainty contribute to its mean luminosity $L_{\mathrm{Arct}}^{\mathrm{Ref}} = (186.7 \pm 2.1)\,\mathrm{L}_\odot$. Both values agree well with the luminosities $L_{\mathrm{Vega}} = (54 \pm 2)\,\mathrm{L}_\odot$ and $L_{\mathrm{Arct}} = (202 \pm 13)\,\mathrm{L}_\odot$ derived from the scaled ATLAS models used in this work. These models thus provide a reliable basis for the determination of the expected starlight photon flux detected with the NSPM.
Comparing L_{Arct} and $L_{\mathrm{Arct}}^{\mathrm{Ref}}$ it might seem to be appropriate to scale the ATLAS model of Arcturus down by about 8% and reduce the systematic uncertainty of its absolute scale to the corresponding uncertainty of the combined reference measurements. However, in this case the modeled and the measured spectral irradiances as shown in figure 8.4 (left) do not agree any longer within their uncertainties. Thus, the initial scaling of the model and its initial uncertainty are favored.

8.3 Atmospheric transmission of light

The data discussed in the previous section correspond to observations at Earth but without the consideration of the atmosphere. The atmosphere acts as a filter with the most significant contributions below wavelengths of 700 nm due to absorption of light by ozone and the scattering of light by molecules and aerosols (cf. figure 2.12). For higher wavelengths further gases and water become significant. The influence of the atmosphere on the data of the ATLAS models of Vega and Arcturus is shown in figure 8.5. Comparing the affected and the unaffected data, aside from some

absorption lines and the infrared stop-bands, the reduction of the irradiance is most significant for smaller wavelengths. Especially below 330 nm the absorption of light by ozone has a strong influence on the shape of the spectrum of Vega.
For the discussed plots the stars are considered to be at the zenith. Thus, their light has to traverse an air mass of $X = 1$ to reach ground level. The air mass X is the path length celestial light has to pass through the atmosphere normalized to the path length for vertical light reaching sea level. For most zenith angles z the air mass can be well-approximated by $X = 1/\cos(z)$. For high z the curvature of the atmosphere has to be taken into account. While the air mass differs for the various causes of extinction (i.e. the attenuation of light within the atmosphere due to absorption and scattering processes caused by a variety of interaction matter) a good overall representation according to reference [192] is given by

$$X = \frac{1}{\cos z + 0.025 \cdot \exp\left(-11 \cdot \cos z\right)} \,. \tag{8.4}$$

The transmittance of the atmosphere is calculated from spectral irradiances of the Sun corresponding to an observer on top of the atmosphere ($X = 0$), and corresponding to the observation of sunlight below one and a half standard atmospheres ($X = 1.5$). This standard atmosphere corresponds to the 1976 U.S. Standard Atmosphere with typical values of ozone and water vapor content, as well as a typical aerosol optical depth. The spectra of the Sun are provided by the National Renewable Energy Laboratory of the U.S. Departement of Energy [193]. The transmittance $T_{\mathrm{atm}}(\lambda)$ of the atmosphere at the wavelength λ for various air masses X is calculated from $T_{1.5\,\mathrm{atm}}(\lambda)$, which is the transmittance of the atmosphere at $X = 1.5$, by $T_{\mathrm{atm}}(\lambda) = T_{1.5\,\mathrm{atm}}(\lambda)^{X/1.5}$.

The characteristics of the real atmosphere change with time. Especially changes regarding the ozone content, the molecular composition, and the aerosol content of the atmosphere have to be considered for the wavelength bands in which the NSPM is sensitive (cf. 2.12). All effects have in common that the related transmission of light through the atmosphere is smaller for shorter wavelengths than for longer wavelengths.
The annual fluctuations of the ozone content is $\sim 8\%$ [194]. Though, it affects the number of photons originating from Arcturus and Vega and detected by the NSPM only very little. Ozone features its crucial absorption characteristics for wavelengths below 330 nm. In this region the acceptance of the NSPM is already very low due to different causes of light attenuating (i.e. photon detection efficiency of the SiPM, effects of atmospheric molecules and aerosols). Changes in the detected stellar light flux due to fluctuations of the ozone content are smaller than 1%.[8].
The annual changes in the molecular optical depth of the atmosphere are $\sim 3\%$ [195]. An optical depth τ of the atmosphere is defined according to the Beer–Lamber law $I = I_0 \cdot e^{-\tau}$, with I_0 being the intensity of radiation at the top of the atmosphere and I being the intensity at an air mass of $X = 1$. Typically it depends on the

[8]The consequences of the fluctuations of the ozone content and the molecular composition of the atmosphere are calculated on basis of the individual optical transmissions discussed in reference [59].

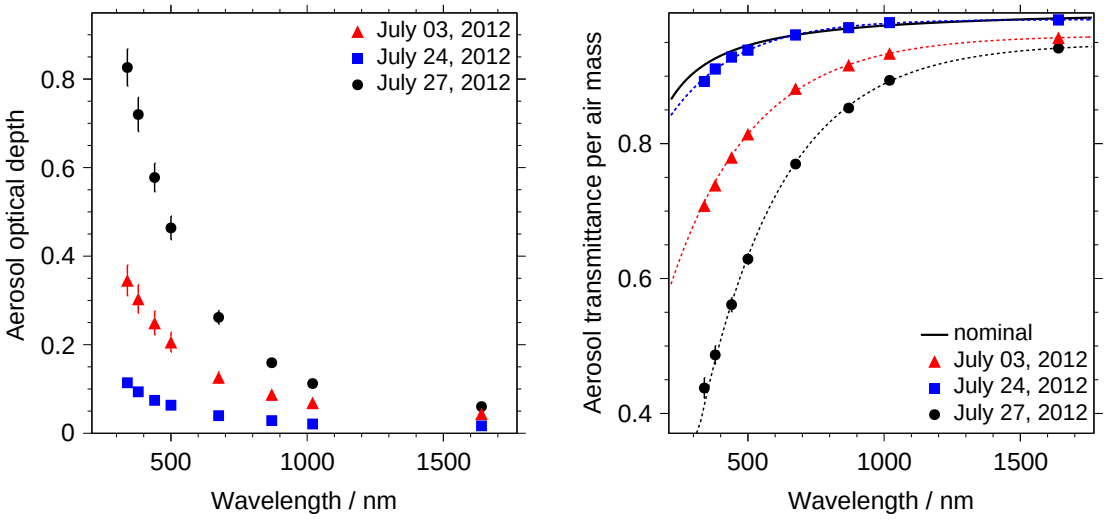

Figure 8.6: **Left:** Measured aerosol optical depth as a function of the wavelength. The red triangles, blue squares, and black points are for July 3, July 24, and July 27, respectively. On these dates the night-sky photometer has been measuring starlight fluxes. **Right:** Measured aerosol transmittance as a function of the wavelength. The color coding is identical to the left plot. The dashed curves are fits to the data according to equation (8.6). The black solid curve is the transmittance used for the nominal standard atmosphere.

wavelength. The change of the molecular optical depth leads to a relative variation of the detected photon flux originating from Vega of about 1%. For Arcturus the variation is smaller than 1%.
Changes in the aerosol optical depth are much larger than those in the molecular optical depth. They can happen on very short time scales. For example, a change in the wind conditions can have a significant effect on the aerosol content of the atmosphere. Aerosols are concentrated in an air layer with a height of typically 1 – 2.5 km above the ground [59]. For instance, the relative fluctuation of the aerosol optical depth at 340 nm for the local region where the NSPM has been operated was about 80% in July 2012. It is thus not appropriate to use averaged values for the aerosol optical depth (AOD).

The AOD is frequently measured by the **J**ülich **O**bsevartor**y** for **C**loud **E**volution (JOYCE) [169] and the data are provided by the **Ae**rosol **Ro**botic **Net**work (AERONET) [170]. The observatory is located at the Jülich Research Center[9] which is in a distance of about 30 km from either of the two observational sites in Aachen and Eschauel where the NSPM has been operated. The aerosol content of the atmosphere is a regional value, and the data acquired in Jülich can be used for the measurements of the night-sky brightness. This knowledge has been gained by studies which operated JOYCE detectors simultaneously in Jülich and Aachen [196].
JOYCE detectors measure the AOD during daylight. The inspection of additional

[9]coordinates: N 50° 54′ 23″, E 6° 24′ 14″

JOYCE data regarding different observables reveals that an interpolation of the surrounding days is appropriate to determine the AOD of the nights (or early mornings to be precise) of July 3 and July 24 [196]. These are two of the nights during which the NSPM has measured starlight fluxes. For additional measurements during the night of July 27 the JOYCE data show in some parts signs of high water vapor (i.e. clouds). An interpolation of the data of the surrounding days should thus be treated with caution [196].
The AOD as a function of the wavelength for the nights of interest is shown in the left plot of figure 8.6. The corresponding aerosol transmittance $T = e^{-\tau}$ according to the Beer–Lambert law is shown in the right plot of the same figure for an air mass of $X = 1$. For the nights of July 24 and July 27 these data are the linear interpolations of the JOYCE data of the two surrounding days. Unluckily, there are no data for July 3, but only for July 2 and July 4. Thus, the data of July 2 are taken into account for the subsequent night. July 4 is not considered for an interpolation since on this day the weather situation was different from the days before (heavy clouds and some rain).

The aerosol optical depth of the nominal standard atmosphere is given by

$$\tau_{\text{nom}} \approx 0.0254 \cdot \left(\lambda \cdot \mu\text{m}^{-1}\right)^{-1.14} . \tag{8.5}$$

It is expressed in a parametrization according to Ångström [197]. The numerical values have been determined from the ones provided with the spectra from which the standard atmosphere is calculated [193, 198]. The corresponding transmittance for one air mass $T_{\text{nom}} = e^{-\tau_{\text{nom}}}$ is shown in the right plot of figure 8.6 by the black solid line. To determine deviations from this nominal transmittance the corresponding data of the three nights of interest are parametrized by functions of the form

$$T = T_0 \cdot \left(1 - \exp\left(-\frac{\lambda - \lambda_0}{\Lambda_0}\right)\right) . \tag{8.6}$$

Parametrizations of the measured data according to the functional relation proposed by Ångström lead to less favorable results in these specific cases. Fits to the measured aerosol transmittance following the functional relation given by equation (8.6) are shown in figure 8.6 by the dashed lines. The fit parameters are summarized in table A.1 in appendix A.3. The systematic uncertainty of the number of detected stellar photons caused by accounting for the measured AOD is about 4% (8%) for Vega and about 2% (3%) for Arcturus with a consideration of an air mass of $X = 1$ ($X = 3$).[10]

8.4 Expected photon detection rate and comparison with measurements

Aside from the atmosphere, the photon detection efficiency (PDE) of the SiPM and the transmittance of the UV filter of the night-sky photometer affect the spectral

[10] an air mass of $X = 3$ corresponds to an altitude of about 20°

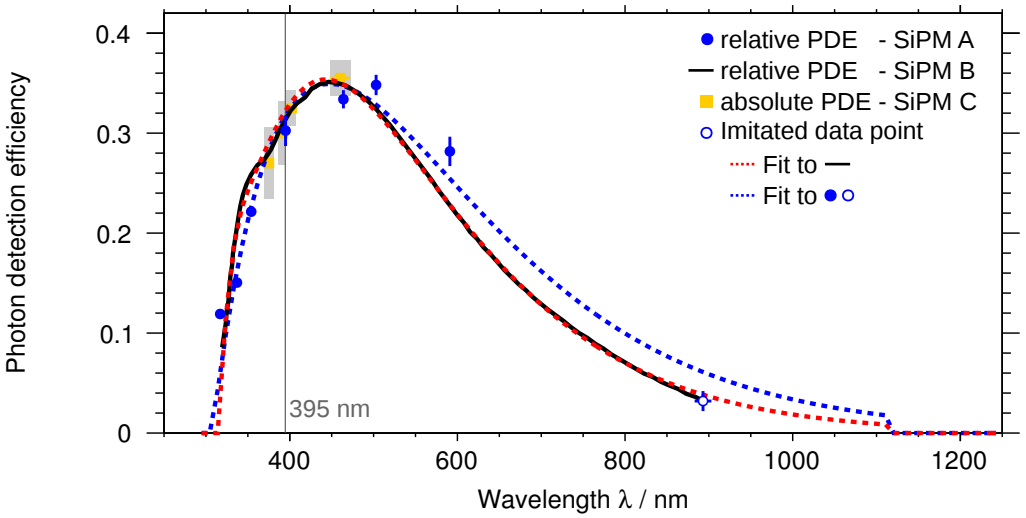

Figure 8.7: Photon detection efficiency (PDE) as a function of the wavelength. The blue filled data points are the relative PDE of the SiPM used for the night-sky photometer (SiPM A – type S10362-33-100C, $3\times3\,\mathrm{mm}^2$ sensitive area, 100 µm cell pitch). The solid black line is the relative PDE of a type S10362-33-050C SiPM measured by the manufacturer (SiPM B – $3\times3\,\mathrm{mm}^2$, 50 µm) [108]. The orange colored squares are the absolute PDE of a type S10362-11-100C SiPM (SiPM C – $1\times1\,\mathrm{mm}^2$, 100 µm) [105]. The widths of the gray boxes denote the systematic uncertainties. The red dashed curve is a fit to the PDE of SiPM B. The blue dashed curve is a fit to the PDE of SiPM A taking also the imitated data point at about 900 nm into account. The imitated data point serves as a lever for the fit. See text for details.

characteristics of the detected stellar irradiance.
The relative PDE of the SiPM used for the measurements of the night-sky brightness (S10362-33-100C, $3\times3\,\mathrm{mm}^2$ sensitive area, 100 µm cell pitch) has been measured with the SiPM characterization test setup presented in references [125] and [199] at wavelengths of 317, 337, 354, 395, 464, 503, and 591 nm. The measurement procedure is discussed in detail in reference [200]. The results are shown in figure 8.7 by the blue filled data points. The characterization test setup is in a development process and will provide measurements of the absolute PDE in the future as well. In addition, a monochromator will lead to an extended range of accessible wavelengths and an increased wavelength resolution. To scale the relative PDE, absolute measurements of an S10362-11-100C type SiPM ($1\times1\,\mathrm{mm}^2$ sensitive area, 100 µm cell pitch) according to reference [105] are considered. They are shown in figure 8.7 by the orange colored squares. The systematic uncertainty of the absolute scale is denoted by the vertical size of the gray boxes.
As a reference point for the scaling of the relative PDE a wavelength of 395 nm is chosen, since here the data of the absolute PDE feature two surrounding points close by. Regarding the two different types of SiPMs, the geometric fill factor and the structure of the semiconductor are identical. However, a difference in the absolute

PDE of the two types is caused by different optical coatings. The S10362-33-100C type is coated with epoxy resin while the S10362-11-100C type uses silicone. Both the epoxy resin and the silicone resin are highly transparent and absorption within the coatings at 395 nm is negligible (absorption coefficients are $\mathcal{O}(10^{-2}\,\mathrm{cm}^{-1})$ for UV-transparent types [141, 201, 202], and the thickness of the coatings is about 0.5 mm). Though, they feature slightly different reflection factors which lead to a relative reduction of the PDE of about 2% at the reference wavelength in case of the one with the epoxy resin compared to the one with the silicone resin (cf. discussion of refractive indices of resin in section 5.1 and references [141, 201, 202]).
The data of the absolute PDE are linearly interpolated to a value of 0.309 at 395 nm, and the data of the relative PDE are scaled to this reference point. The systematic uncertainty on the absolute scale of the PDE is 6%.

A measurement of the relative PDE of a S10362-33-050C type SiPM ($3\times3\,\mathrm{mm}^2$ sensitive area, 50 µm cell pitch), which has been provided by the manufacturer [108], is shown in figure 8.7 by the solid black curve.[11] It covers a broader range of wavelengths than the other measurements. Aside from the cell pitch, and thus a different geometric fill factor, this type of SiPM is identical to the one used for the night-sky photometer. The shapes of the two corresponding PDEs should therefore be very similar. The absolute scale of the PDE provided by the manufacturer is determined by fitting the corresponding data to the scaled data of the SiPM used for the night-sky photometer.[12] The data of the manufacturer are used to find an appropriate functional relation between the PDE and the wavelength. This relation is *a priori* not known. A satisfying parametrization is

$$\mathrm{PDE}(\lambda) = f_1(\lambda) + f_2(\lambda) \qquad \text{with} \tag{8.7}$$

$$f_{1,2}(\lambda) = \begin{cases} A_{1,2}\cdot\left(1 - e^{-(\lambda-\lambda_{1,2})/\Lambda_{1,2}}\right)\cdot e^{-(\lambda-\lambda_{1,2})/\Gamma_{1,2}} & , \text{ for } \lambda \geq \lambda_{1,2} \\ 0 & , \text{ for } \lambda < \lambda_{1,2} \\ 0 & , \text{ for } \lambda > 1117\,\mathrm{nm} \end{cases}$$

with the free parameters λ_i, Λ_i, and Γ_i, $i = 1, 2$. The superposition of the two similar functions f_1 and f_2 accounts for the shoulder in the rising edge of the PDE, while the constraint PDE = 0 for $\lambda > 1117$ nm accounts for the fact that the silicon becomes transparent at 1117 nm. A fit according to equation (8.7) to the data of the manufacturer is shown by the red dashed curve in figure 8.7. The relevant parameters are summarized in table A.3 in appendix A.3.
Corresponding fits to the data of the SiPM of the night-sky photometer lead to unsatisfying results since the resulting falling edge of the parametrization is far from matching the shape given by the data of the manufacturer (see figure A.7 in appendix A.3). A satisfying result can be obtained if a further data point, which acts a lever for the fit, is added. Following the data of the manufacturer, a PDE

[11] The PDE data provided in reference [108] are given in an absolute scale. But since the data contain effects of correlated noise the scale has to be treated as a relative one. The data have been shown previously in figure 4.9 and discussed in section 4.2.

[12] This scale differs relatively by 1% from the absolute scale which is achieved if the PDE of the manufacturer is scaled to the above mentioned reference point at 395 nm.

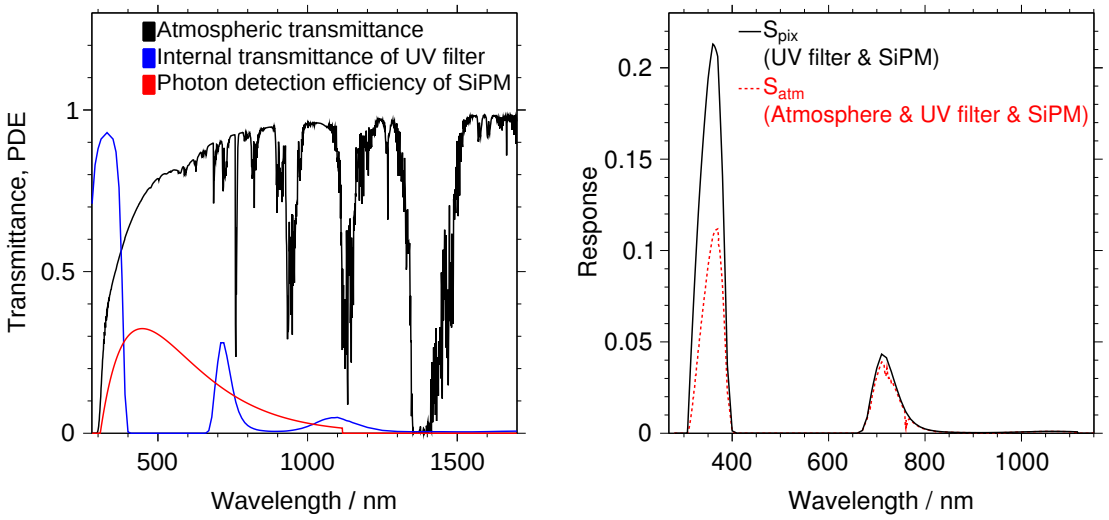

Figure 8.8: **Left:** Transmittance of a standard atmosphere for an air mass of $X = 1$, internal transmittance of the UV band-pass filter, and photon detection efficiency (PDE) of the SiPM as functions of the wavelength. **Right:** Optical response functions of the photometer. S_{atm} (red dashed curve) is defined as the product of the three quantities of the left plot. S_{pix} (black, solid line) is defined as the product of the internal transmittance of the UV filter and the PDE.

of 0.032 ± 0.010 at a wavelength of (893 ± 10) nm is chosen for this additional data point. It is shown by the open blue circle in figure 8.7. The best fit results are obtained if f_2 is fixed to zero. This fit is shown in figure 8.7 as the blue dashed curve. The relevant parameters are also summarized in table A.3 in appendix A.3.

Considering the detection of photons from the stars, the PDE introduces the systematic uncertainty of the absolute scale as mentioned above, as well an uncertainty raised by the lack of knowledge of the exact shape of the PDE. This uncertainty is estimated by a comparison of the two discussed parametrizations. It is larger at higher wavelengths and thus more relevant for Arcturus than for Vega since Arcturus is the cooler one of the two stars and its spectral radiance is shifted to longer wavelengths compared to the one of Vega. The uncertainty is also higher if the star is observed at a lower altitude. In this case the corresponding air mass is increased and the shorter wavelengths are more attenuated than the longer ones. The relative uncertainty is about 7% (8%) and 3% (5%) for Arcturus and Vega, respectively, at an air mass of $X = 1$ ($X = 3$).
Aside from its wavelength-dependence the PDE also depends on the over-voltage as presented in reference [105] (cf. figure 4.10). This dependence is accounted for in the determination of the expected starlight photon fluxes by considering the actual over-voltages at which the SiPM has been operated. For the plots in this section an over-voltage of 1.3 V is chosen.

In figure 8.8 (left) the transmittance of the standard atmosphere with an air mass of $X = 1$, the internal transmittance of the UV filter, and the PDE are shown as a

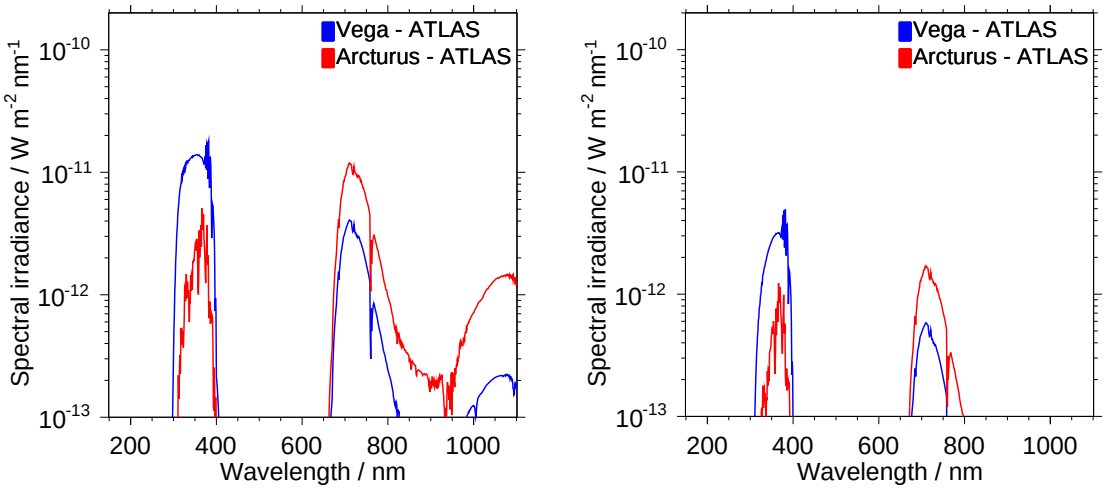

Figure 8.9: The spectral irradiances of Vega (blue) and Arcturus (red) according to the ATLAS models folded successively with the atmospheric filter ($X = 1$) and the UV band-pass filter of the night-sky photometer (left) and the photon detection efficiency of the SiPM at an over-voltage of 1.3 V (right).

function of the wavelength. The relative uncertainty of the scale of the transmittance of the UV filter is estimated to 4%. This estimation is based on measurements of the transmittance limited to the wavelength ranges 360–385 nm, 500–650 nm, and 705–710 nm. The product of the PDE and the internal transmittance of the UV filter defines the spectral photosensitivity of the pixel of the camera. It is referred to as response function S_{pix} and shown in the right plot of figure 8.8 by the black, solid curve. For comparison, an additional response function S_{atm}, which takes also the mentioned transmittance of the atmosphere into account, is shown by the red dashed curve. It is given by the product of S_{pix} and the transmittance of the standard atmosphere at $X = 1$.

The spectral bands in which the camera pixel is photosensitive are defined at a 10% level of the maximum response of S_{pix}. This maximum response is 0.212 ± 0.015 at a wavelength of (360 ± 3) nm. The dominant pass-band ranges from (311 ± 4) nm – (395 ± 3) nm. A second pass-band ranges from (688 ± 3) nm – (746 ± 4) nm. The response S_{pix} within this band reaches values up to 0.038 ± 0.004. This particular response value is located at (710 ± 3) nm. As the SiPMs of FAMOUS feature the same PDE as the one used in this work, and as the UV filters are also of the same type, the FAMOUS pixels are photosensitive in the same bands. We will refer to them as the UF-0 band for the domiant pass-band and the RF-0 band for the second bass-band.[13] In some cases it might be more convenient to quote the wavelengths where S_{pix} reaches 50% of its maximum value. These -3 dB cutoff wavelengths only

[13] As the spectral PDE might improve for revised versions of FAMOUS the names of the bands constructed from U and R for ultra-violet and red, respectively, and F for FAMOUS owns a suffix to allow for similar names of bands for future revisions.

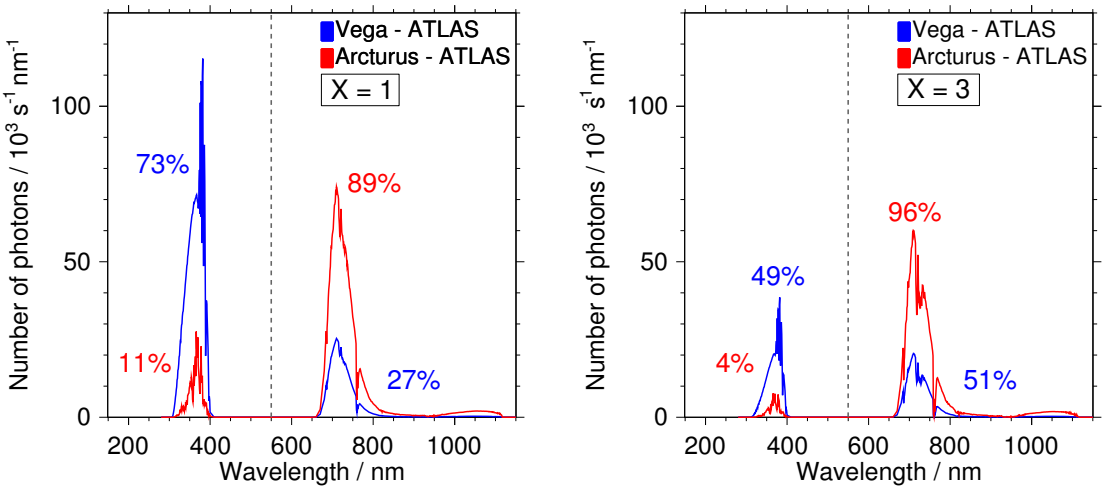

Figure 8.10: Spectral irradiances in terms of number of photons per unit wavelength per unit time (cf. figure 8.9). The blue curve is for the ATLAS model of Vega, the red one for the ATLAS model of Arcturus. The irradiances are modulated by the atmospheric filter and the complete experimental setup (i.e. PDE of the SiPM, aperture area and optical efficiency of the telescope, efficiency of the camera pixel). Air masses of $X = 1$ and 3 have been considered for the left and right plot, respectively. The percentage values refer the amount of photons with wavelengths smaller and greater than 550 nm.

exist in the UF-0 band. They are (327 ± 4) nm and (383 ± 3) nm.

In figure 8.9 the spectral irradiances of Arcturus and Vega according to the ATLAS models and multiplied by S_{atm} are shown. Additional reductions of the stellar irradiances whose wavelength dependencies are insignificant are caused by the optical efficiency of the PN-203 telescope, which is $\epsilon = 0.40 \pm 0.02$ for light which enters the telescope parallel to its optical axis, by the efficiency of the Winston cone, and by the dependence of the PDE on the incident angle of the light. The latter and the efficiency of the Winston cone are determined by means of a Geant4 simulation of the telescope and its camera. The simulation is performed in the same manner as the one of the relative optical efficiency of the telescope discussed in section 6.2. Anyhow, here it is sufficient to simulate only light which enters the telescope parallel to its optical axis. In the previous Geant4 simulation the UV filter and the camera of the night-sky photometer (NSPM), i.e. Winston cone and SiPM, have not been simulated. Instead the sensitive detector of the simulation has been placed at the position of the entrance aperture of the Winston cone. Now, the UV filter and the Winston cone are enabled in the simulation, and the sensitive detector is placed at the exit aperture of the cone. The absorbing effect of the filter is removed from the final result since it is already considered within S_{atm}. However, the reflecting and refracting effects might be of interest. Also the optical efficiency of the PN-203

Table 8.1: Integrated spectral irradiances f_{X0}, f_{X1}, and f_{NSPM} of Arcturus and Vega derived from the ATLAS models at the top of the atmosphere of the Earth, below one standard atmosphere, and detected by the night-sky photometer, respectively. f_{NSPM} is expressed in terms of watts and in terms of photons per second. An over-voltage of the SiPM of 1.3 V is considered.

Value	Unit	Arcturus	Vega
f_{X0}	$\mathrm{W\,m^{-2}}$	$(4.84 \pm 0.29) \cdot 10^{-8}$	$(2.52 \pm 0.09) \cdot 10^{-8}$
f_{X1}	$\mathrm{W\,m^{-2}}$	$(3.34 \pm 0.20) \cdot 10^{-8}$	$(1.49 \pm 0.06) \cdot 10^{-8}$
f_{NSPM}	W	$(1.32 \pm 0.20) \cdot 10^{-10}$	$(2.24 \pm 0.30) \cdot 10^{-10}$
f_{NSPM}	Hz	$(5.33 \pm 0.81) \cdot 10^{6}$	$(5.70 \pm 0.74) \cdot 10^{6}$

telescope is removed. The resulting optical efficiency is thus due to the reflecting and refracting effects of the filter, and the absorption of light within the Winston cone. From the angles under which the photons hit the sensitive area, the reduction of the optical efficiency due to the reduced PDE for higher incident angles is calculated. This calculation takes the Fresnel equations and multiple reflections of the light within the resin of the SiPM into account. The Fresnel equations and multilayer reflections have been discussed in section 5.1. The resulting optical efficiency is 0.87 ± 0.03.
An integration of the final stellar spectral irradiances, which account for the atmosphere and the experimental setup, yields for instance irradiances of $(1.32 \pm 0.20) \cdot 10^{-10}\,\mathrm{W}$ for Arcturus and $(2.24 \pm 0.3) \cdot 10^{-10}\,\mathrm{W}$ for Vega at an over-voltage of 1.3 V and an air mass of $X = 1$.

Considering the aperture area of the telescope $A = (3.24 \pm 0.01) \cdot 10^{-2}\,\mathrm{m^2}$ and the relation between the wavelength of a photon and its energy, the reference models of the stars result in detected photon rates of $(5.33 \pm 0.81)\,\mathrm{MHz}$ for Arcturus and $(5.70 \pm 0.74)\,\mathrm{MHz}$ for Vega at an over-voltage of 1.30 V and $X = 1$. Corresponding spectra depicting the number of photons per unit wavelength per unit time are shown in figure 8.10.
The integrated irradiances at the top of Earth's atmosphere, below one standard atmosphere, and detected by the NSPM are summarized in table 8.1, while the systematic uncertainties discussed in this chapter are summarized in table 8.2 for an air mass of $X = 1$. If they depend on the wavelength, they are stated at 360 nm and 710 nm. At these wavelengths the optical response function S_{pix} features its two local maxima.

The measured data of the stellar light fluxes are selected according to two quality criteria. The first relates to the subtraction of the background brightness (i.e. the diffuse night-sky brightness (NSB)) from the measured data to isolate the starlight flux as discussed in section 8.1. As the diffuse NSB varies with time and the considered region of the sky, the time difference between the two measurements used for the background subtraction has to be smaller than 30 minutes. Furthermore, the angular distance between the centers of the two corresponding regions of the sky

Table 8.2: Systematic uncertainties of the stellar photon fluxes detected with the night-sky photometer (NSPM) derived from the ATLAS models. If an uncertainty depends on the wavelength its value is given for 360 nm and 710 nm. At these wavelengths the optical response function S_{pix} of the NSPM features its two local maxima. Considered is an air mass of $X = 1$.

	Arcturus	Vega
Absolute scale of irradiance measurement	6%	2%
Variation of ATLAS model from measurement	20% ÷ 2%	5% ÷ 2%
Sub total (Stellar irradiance)	**21% ÷ 6%**	**5% ÷ 3%**
Ozone content	< 1%	
Molecular composition	1% ÷ < 1%	
Aerosol optical depth	5% ÷ 1%	
Sub total (Atmosphere)	**6% ÷ 1%**	
Absolute scale of PDE	6%	
Shape of spectral PDE	1% ÷ 8%	
Optical efficiency of PN-203 telescope	5%	
Transmittance of UV filter	4%	
Optical efficiency of camera pixel	4%	
Sub total (Photometer)	**10% ÷ 13%**	
	Arcturus	Vega
Total	**24% ÷ 14%**	**13% ÷ 13%**

has to be smaller than 10° in the horizontal coordinate system.[14] With its multi-pixel camera FAMOUS is able to perform both measurements simultaneously and the angular distance of the centers of the two observed regions is given by its field of view per pixel which is 1.5°. This is a great benefit since harder quality cuts can be considered for FAMOUS data without reducing the statistics. However, this analysis has to refrain from harder cuts since with only one camera pixel the NSPM is limited to consecutively conducted observations of stars and the diffuse NSB.
The second quality cut relates to the observational conditions. Data which have not been acquired during *confirmed clear conditions* are removed. Although the night-sky may appear starlit, a slight cloud coverage which is not visible by the naked eye might be present. Except from July 27, the nights during which the NSPM has been operated are confirmed by the JOYCE measurements (see previous section) as nights with clear conditions. However, on July 27 the presence of clouds cannot be excluded. The corresponding data are thus removed from the quality data. The measurements performed on July 27 themselves give a hint for the presence of clouds as well: The diffuse NSB was almost identical on July 24 and July 27, while the two corresponding measurements have been performed in an urbanized region and in a less light polluted rural environment, respectively (cf. table 7.2 at the end of section 7.5). The Moon is not responsible for the comparatively high diffuse NSB

[14] the horizontal, or altitude-azimuth system is fixed to the Earth

Table 8.3: Mean rates of detected starlight photons $\bar{R}_\gamma$ for measurements with quality cuts. Also stated are the expected rates of detected starlight photons derived from the ATLAS models R_γ^{exp} and the corresponding air mass X. Statistical uncertainties are labeled (stat.). Other uncertainties are systematic. The identification numbers (ID) are identical to the ones introduced in the previous chapter.

ID	Date	Star	$\bar{R}_\gamma$ / MHz	R_γ^{exp} / MHz	X
IV	July 3	Arct.	$2.44 \pm 0.09\,(\mathrm{stat.}) \pm 0.13$	2.95 ± 0.44	2.81 ± 0.03
V	July 3	Arct.	$2.40 \pm 0.05\,(\mathrm{stat.}) \pm 0.13$	2.67 ± 0.40	3.25 ± 0.03
VIII	July 24	Vega	$3.94 \pm 0.09\,(\mathrm{stat.}) \pm 0.21$	4.73 ± 0.59	1.23 ± 0.01
IX	July 24	Vega	$3.80 \pm 0.04\,(\mathrm{stat.}) \pm 0.19$	4.80 ± 0.60	1.26 ± 0.01

measured in the rural environment, since it was far below the horizon at the considered times. Furthermore, the considered regions of the sky have been high above the horizon and at similar equatorial coordinates. The comparatively high diffuse NSB measured on July 27 can be explained by clouds which have reflected terrestrial light.
For upcoming measurements with FAMOUS, the benefit of cloud identification with a simultaneously operated, independent camera which observes the sky at the same location and into the same direction as FAMOUS will be studied.

Regarding the quality data acquired with the night-sky photometer, the mean rates of detected stellar photons $\bar{R}_\gamma$ and the corresponding expectations from the ATLAS models R_γ^{exp} with consideration of Earth's atmosphere and the characteristics of the NSPM are given in table 8.3. Also given are the air masses X which relate to the individual measurements. The fact that the observational sites are at a height of about 250 m a.s.l. is accounted for. Compared to an observer at sea level the air mass is reduced by about 3%. To calculate the air mass, parametrizations of the density profiles of the different layers of the standard atmosphere as presented in reference [203] have been considered. The exact times of the observations, and the corresponding apparent altitudes of the stars, as well as the actual over-voltages at which the SiPM has been operated, are listed in table A.4 in appendix A.3.
The systematic uncertainties of the measured data include those raised by the photon counting method, but not those of the telescope parameters (i.e. optical efficiency of the PN-203 telescope, aperture area, cf. table 7.1). The latter are included in the systematic uncertainties of the expected rates R_γ^{exp}. The systematic uncertainty raised by the variation of the atmosphere from the nominal one does not necessarily have to tend into the same direction for different nights.
On average, the expected photon detection rates are systematically shifted to values which are 19% higher than the measured ones. The relative systematic uncertainties of the expected photon detection rates which tend always into the same direction (i.e. uncertainty of stellar irradiance and night-sky photometer) are 14% and 12% for Arcturus and Vega, respectively. The relative systematic uncertainty of the

measured rates are 5%. Thus, the measured data agree well with the reference data within their uncertainties.

At the end of the previous chapter the reliability of the photon counting method to determine signal-photon fluxes has been demonstrated. The comparison of the measured brightness of the stars with the expectations from models and reference measurements confirms this reliability. With only one pixel the NSPM has performed the proof-of-principle to measure the brightness of stars and the diffuse night-sky on an absolute scale. As a predecessor of FAMOUS it has pioneered for future measurements of the night-sky brightness with a multi-pixel camera.

9. Summary and Outlook

The observation of extensive air showers by means of fluorescence telescopes is a well-established and powerful detection technique providing direct measurement of the longitudinal shower development. With the prototype FAMOUS the first fluorescence telescope featuring a camera instrumented with novel semiconductor single photon detectors, referred to as silicon photomultipliers (SiPMs), has been developed and produced. SiPMs are arrays of avalanche photo diodes, referred to as cells, operated at an over-voltage V_{ov} beyond their breakdown voltage. The advantages of SiPMs compared to photomultiplier tubes, commonly used for the fluorescence detection of air showers, include a high photon detection efficiency (presently up to 60%), a small size, a low operational voltage, and the potential for low cost mass production.

FAMOUS is a refractive telescope employing a Fresnel lens with a diameter of 550 mm and a focal length of 502 mm. Its camera consists of 64 pixels. Each pixel is constituted of four SiPMs (type S10985-100C manufactured by Hamamatsu), which are housed in the same package, and which together provide a sensitive area of $6{\times}6\,\mathrm{mm}^2$. The cell pitch of the SiPMs is 100 µm. To increase the sensitive area of the pixels, each one features a non-imaging light-collector known as Winston cone. To result in an increased signal-to-noise ratio, UV band-bass filters are applied. A seven pixel version of FAMOUS has been constructed and commissioned recently.

To gain a deeper understanding of SiPMs and probe conceptions of their working principle, this work has presented a photometer to measure the night-sky brightness with a telescope which features a single pixel. This pixel is similar to the ones of FAMOUS. The photometer employs a commercial Newton reflector with an aperture of 203 mm and a focal length of 800 mm. The photometer is a predecessor to FAMOUS and has adduced the proof-of-principle to determine photon fluxes measured under field conditions. It uses an S10362-33-100C SiPM manufactured by Hamamatsu with a sensitive area of $3{\times}3\,\mathrm{mm}^2$ and a cell pitch of 100 µm.
Instead of calibrating the response of the SiPM to the level of incident light, a photon counting method has been applied. The signals referring to the detection of photons have been identified in the data. Since effects of thermal noise and correlated noise result in signal-like outputs of the SiPM, the acquired data have been corrected for these effects. This procedure demanded the determination of key characteristics of SiPMs, and thus led to extensive characterization studies and models of SiPM properties. These studies included the determination of the breakdown voltage, the gain, the thermal noise rate, the probabilities of afterpulsing and optical crosstalk, the

timing constants of slow and fast afterpulses, as well as the recovery time constant. A significant effect of the intrinsic dead time of the cells of the SiPM on the results of the photon counting method could be excluded. Furthermore, the non-linearity of the signal response of the photosensor to incident light and its dynamic range have been investigated in detail by means of the sophisticated SiPM simulation toolkit G4SiPM.

The results of the photon counting method are in good agreement with reference measurements. The former has been used to determine the rate of thermal breakdowns of cells of an SiPM, which can also be determined by an alternative method in which the time between two thermal cell breakdowns is studied. The photon counting method leads to the expected linear dependency of the thermal noise rate on the over-voltage of the SiPM. The thermal noise rate obtained from the photon counting method agrees within 3% with the reference measurements. This indicates that the presented models describe SiPMs reasonably well to reconstruct measured photon fluxes reliably. The systematic uncertainty of the signal-photon detection rates obtained from the photon counting method decreases with the over-voltage and ranges from 6.9% at $V_{\mathrm{ov}} = 1.15\,\mathrm{V}$ to 4.1% at $V_{\mathrm{ov}} = 1.45\,\mathrm{V}$.

The light fluxes of the bright stars Arcturus and Vega, which have been measured with the photometer, have been compared to reference models obtained from the ATLAS program suite, which is widely used in astrophysics. These models have been scaled to absolute flux calibrated measurements. To determine the expected stellar photon flux from the models, influences of a nominal standard atmosphere on the flux, and variations of the real atmosphere from this nominal one have been taken into account. The stellar irradiances for the nominal standard atmosphere are $(3.34 \pm 0.20) \cdot 10^{-8}\,\mathrm{W\,m^{-2}}$ and $(1.49 \pm 0.06) \cdot 10^{-8}\,\mathrm{W\,m^{-2}}$ at an air mass of $X = 1$ for Arcturus and Vega, respectively. Taking the characteristics of the night-sky photometer into account has resulted in the expected detection rate of stellar photons. The systematic uncertainty of this reference rate has been estimated to about 14%. The measured data agree with the reference data within their uncertainties. On average, the expectations yield 19% more detected photons than the measurements.

The brightness of the diffuse night-sky has been measured during several nights including operations during nights with a visible full Moon as well as with the Moon being far below the horizon. The corresponding detected light fluxes have been determined to $\big(1021 \pm 22\,(\mathrm{stat.}) \pm 132\,(\mathrm{sys.})\big) \cdot 10^9$ and $\big(87 \pm 14\,(\mathrm{stat.}) \pm 11\,(\mathrm{sys.})\big) \cdot 10^9$ photons per square meter per second per steradian, respectively. The measurements have been performed during summer 2012 close to the town of Aachen and in a rural environment in the Eifel, both located in Germany. The stated light fluxes are for the combination of the UF-0 and RF-0 bands, which are the wavelength bands in which the FAMOUS pixels are photosensitive. This sensitivity is described by the optical response function of a pixel which is given by the product of the spectral transmittance of the UV filter and the photon detection efficiency of the SiPM. The dominant pass-band UF-0 has been determined to $(311 \pm 4)\,\mathrm{nm}$ – $(395 \pm 3)\,\mathrm{nm}$ with a maximum response of 0.212 ± 0.015 at $(360 \pm 3)\,\mathrm{nm}$. Within the pass-band RF-0,

which ranges from (688 ± 3) nm to (746 ± 4) nm, the response reaches values up to 0.038 ± 0.004 at (710 ± 3) nm. The given borders of the pass-band are defined at a 10% level of the maximum response of a pixel.

The presented photon counting method provides reliable results and can be applied to photometric measurements of both continuous light sources and pulsed ones. The measured diffuse night-sky brightness can furthermore be applied to detector simulations of FAMOUS to evaluate the detection efficiency of cosmic rays.
Since the photometer has been established during the early design phase of FAMOUS, it employs only basic front-end electronics. The experience gained with the operation of SiPMs in general and with the photometer in particular has led to great achievements regarding the design of FAMOUS. The prototype fluorescence telescope features revised front-end electronics and an active bias voltage control to keep the key characteristics of the SiPMs independent of both changes of temperature and of the total luminous flux incident on the SiPM. Furthermore, a monitoring system is capable to acquire environmental data, as for instance the temperature, the air pressure, the relative air humidity, and the diffuse night-sky brightness with dedicated sensors. The quality of the determination of cloud covers and the aerosol optical depth with these sensors will be studied.
FAMOUS will pursue the measurements discussed in this work. With the mentioned features and its multi-pixel camera, FAMOUS offers numerous advantages compared to the photometer discussed in this work. FAMOUS is able to measure the light flux of stars and regions without bright stars simultaneously. Future measurements of the night-sky brightness will also benefit from masked pixels to provide simultaneous dark measurements. These advantages will allow to simplify the presented photon counting method at several points.

Furthermore, the gained understanding of SiPMs provides a basis to study laboratory-based calibration routines for FAMOUS. These routines aim at the direct relation between the signal response of the SiPMs and the radiance of pulsed and continuous reference light sources. Due to the limitation of the dynamic range of SiPMs and the non-linearity of their response caused by correlated noise, such routines are highly non-trivial. This is in particular the case, if the telescope is intended to measure the light flux of pulsed light sources, whose pulse widths are *a priori* unknown and vary from pulse to pulse. For individual camera pixels of FAMOUS such light sources are realized by air showers.

With the SiPM-based measurements of the night-sky brightness and the reconstruction of the absolute light fluxes, pioneering work for FAMOUS has been performed. Not only has the understanding of SiPMs been examined and approved, but also first steps towards absolute calorimetric measurements with SiPMs have been conducted. Altogether, an important step towards the detection of extensive air showers with SiPMs has been achieved.

A. Appendix

A.1 Fluorescence and Cherenkov light from air showers

In this section estimates of the numbers of fluorescence and Cherenkov photons generated by an air shower around its shower maximum are calculated. These numbers were given at the end of section 2.4.
The considered air shower is a vertical proton-induced one with the primary energy $E_0 = 10^{19}\,\mathrm{eV}$. The following calculations make some modest assumptions to keep it simple. The intention is to calculate rough numbers of produced photons to see in which orders of magnitude they are for the Cherenkov and fluorescence processes. For more sophisticated calculations with running parameters, shower simulation programs are the right choice to proceed.
From equation (2.15) we see that the number of Cherenkov photons N_{Ch} an electron ($Z = 1$) produces in the wavelength interval $[\lambda_1, \lambda_2]$ per unit path length $\mathrm{d}x$ is given by

$$\frac{\mathrm{d}N_{\mathrm{Ch}}}{\mathrm{d}x} = 2\,\pi\,\alpha\,\left(1 - \frac{1}{(\beta\,n(\lambda))^2}\right)\left(\frac{1}{\lambda_1} - \frac{1}{\lambda_2}\right)\,.$$

With $\lambda_1 = 290\,\mathrm{nm}$, $\lambda_2 = 430\,\mathrm{nm}$ (motivated by the spectrum and the typical acceptance of astroparticle telescopes), $1 - \beta = 1.5 \cdot 10^{-4}$ (according to a mean electron energy of 30 MeV, cf. figure 3 in reference [56]), $n - 1 = 2.87 \cdot 10^{-4}$ [139], $\alpha = 1/137$, we find

$$\frac{\mathrm{d}N_{\mathrm{Ch}}}{\mathrm{d}x} = 14\,\mathrm{m}^{-1}$$

According to reference [40] the atmospheric depth X for the U.S. 1976 Standard Atmosphere approximately relates to the height h as

$$\ln\left(X/(\mathrm{g\,cm}^{-2})\right) =$$

$$\begin{cases} 5.26 \cdot \ln\left[(44.34 - h/\mathrm{km})/11.86\right] & \text{for } h < 11\,\mathrm{km} \\ (45.5 - h/\mathrm{km})/6.34 & \text{for } 11\,\mathrm{km} < h < 25\,\mathrm{km} \\ 13.78 - 1.67\left[68.47 - 1.2 \cdot (48.63 - h/\mathrm{km})\right]^{1/2} & \text{for } h > 25\,\mathrm{km}\,. \end{cases}$$

Hence, $X_{\mathrm{max}} = 800\,\mathrm{g\,cm}^{-2}$ relates to $h_{\mathrm{max}} = 2.073\,\mathrm{km}$. At $X_1 = X_{\mathrm{max}} + \lambda_{\mathrm{e}} = 837\,\mathrm{g\,cm}^{-2}$ the altitude is reduced to $h_1 = 1.708\,\mathrm{km}$, thus, $\Delta x = h_{\mathrm{max}} - h_1 = 365\,\mathrm{m}$. From figure 2.8 we see that the number of electrons (and positrons) of the air shower

is about $N_e = 6.5 \cdot 10^9$. Hence, the number of Cherenkov photons in the UV range emitted within one radiation length λ_e starting at X_max is

$$N_\mathrm{Ch}^\mathrm{tot} = N_e \cdot N_\mathrm{Ch} \cdot \Delta x = 3.3 \cdot 10^{13} \,.$$

The total energy loss of an electron with an energy of 30 MeV in air is about $E_\mathrm{dep} = 2.87\,\mathrm{MeV\,g^{-1}\,cm}$ [204]. For the total number of fluorescence photons $N_\mathrm{Fl}^\mathrm{tot}$ emitted along the distance Δx, we take the fluorescence yield in the 337 nm-band $Y_{337} = 5.61\,\mathrm{MeV^{-1}}$, its relative intensity to the total amount of UV fluorescence light in the considered wavelength region $I_\mathrm{rel} = 0.26$ (cf. table 1 in reference [55]), and multiply it by the energy loss per electron and the number of electrons:

$$N_\mathrm{Fl}^\mathrm{tot} = N_e \cdot E_\mathrm{dep} \cdot X_0 \cdot 1/I_\mathrm{rel} \cdot Y_{337} = 1.5 \cdot 10^{13} \,.$$

A.2 Determination of SiPM pulse heights from simulated data

Within the G4SiPM simulations (cf. section 4.3) the functional form of an SiPM pulse i in time t is given by

$$f_i(t) = \begin{cases} w_i\, A_0 \left(1 - e^{-(t-t_i)/\tau_\mathrm{rise}}\right) e^{-(t-t_i)/\tau_\mathrm{fall}} & , \text{ for } t \geq t_i \\ 0 & , \text{ for } t < t_i \end{cases} \tag{A.1}$$

with the timestamp of the pulse t_i , its weight w_i, and the global pulse parameters A_0, τ_rise, and τ_fall. The latter are pre-set by the user, while the timestamp and the weights are diced. All parameters are known.

The output signal of the simulation $V_\mathrm{sim}(t)$ is then given by the sum over all signals of the individual pulses $i = 1, 2, \ldots, N$:

$$V_\mathrm{sim}(t) = \sum_{i=1}^{N} f_i(t) \tag{A.2}$$

After the occurance of a pulse i the subsequent pulse $i+1$ can take place (a) before pulse i reaches its minimum or (b) after pulse i reaches its minimum. Both cases are depicted in figure A.1.[1] For (a) the pulse height of pulse i is given by

$$V_i = V_\mathrm{sim}(t_{i+1}) - V_\mathrm{sim}(t_i) \tag{A.3}$$

while the pulse height of pulse $i+1$ is given by

$$V_{i+1} = V_\mathrm{sim}(t_{i+1}^\mathrm{min}) - V_\mathrm{sim}(t_{i+1}) \tag{A.4}$$

[1] It is worth mentioning that per construction the waveform analysis algorithm discussed in section 7.1 is not able to identify two pulses in the case of (a). Instead it will identify a single pulse with its amplitude being the sum of the pulse heights of the two pulses in the output signal.

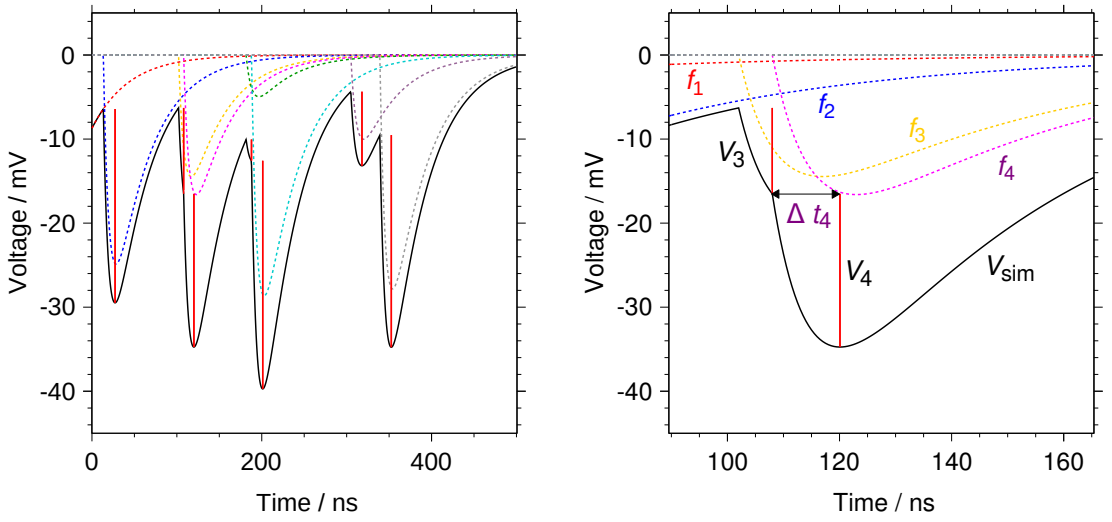

Figure A.1: **Left:** A simulated voltage trace containing seven cell breakdowns. An additional one happened before the time $t = 0$ and only the tail of the corresponding pulse reaches into the trace (red dashed line). The output signal of the SiPM is the black solid line, which is the sum of the contributions of the individual cell breakdowns (colored dashed lines). The red horizontal lines denote the pulse height of the seven pulses. **Right:** Zoomed display of the data shown in the left plot with notations as used in the text.

where $t_{i+1}^{\min}$ is the minimum of pulse $i+1$ in the output signal.
For (b) where both pulses have a distinct minimum, the pulse heights of both pulses are given in analogy by

$$V_i = V_{\mathrm{sim}}(t_i^{\min}) - V_{\mathrm{sim}}(t_i) \tag{A.5}$$

$$V_{i+1} = V_{\mathrm{sim}}(t_{i+1}^{\min}) - V_{\mathrm{sim}}(t_{i+1})\,. \tag{A.6}$$

To identify the minima $t_i^{\min}$ of the individual pulses within the output signal $V_{\mathrm{sim}}(t)$ for any number of pulses N we inspect the null of the first derivative of $V_{\mathrm{sim}}(t)$:

$$\frac{\mathrm{d}V_{\mathrm{sim}}(t_i^{\min})}{\mathrm{d}t} = \sum_{i=1}^{N} \frac{\mathrm{d}f_i(t_i^{\min})}{\mathrm{d}t} = \sum_{j=1}^{i} \frac{\mathrm{d}f_j(t_j^{\min})}{\mathrm{d}t} \stackrel{!}{=} 0 \tag{A.7}$$

The identity of the two sums in this equation is due to the fact that $f_i(t) = 0$ for $t \leq t_i$. For carrying out the calculations of the $t_i^{\min}$ it seems thus convenient to perform successive calculations starting with $t_1^{\min}$.

Generally, we find

$$\begin{aligned}\frac{\mathrm{d}f_i(t)}{\mathrm{d}t} &= w_i\,A_0\,\cdot\left[\left(\frac{1}{\tau_{\text{rise}}}e^{t_i/\tau_{\text{rise}}}\,e^{-t/\tau_{\text{rise}}}\right)\,e^{t_i/\tau_{\text{fall}}}\,e^{-t/\tau_{\text{fall}}}\right. \\ &\qquad \left. -\frac{1}{\tau_{\text{fall}}}\left(1-e^{t_i/\tau_{\text{rise}}}\,e^{-t/\tau_{\text{rise}}}\right)e^{t_i/\tau_{\text{fall}}}\,e^{-t/\tau_{\text{fall}}}\right] \qquad \text{(A.8)}\\ &= w_i\,A_0\,e^{t_i/\tau_{\text{fall}}}\,e^{-t/\tau_{\text{fall}}} \\ &\qquad \cdot\left[\frac{1}{\tau_{\text{rise}}}\,e^{t_i/\tau_{\text{rise}}}\,e^{-t/\tau_{\text{rise}}}+\frac{1}{\tau_{\text{fall}}}\,e^{t_i/\tau_{\text{rise}}}\,e^{-t/\tau_{\text{rise}}}-\frac{1}{\tau_{\text{fall}}}\right] \\ &= w_i\,A_0\,e^{t_i/\tau_{\text{fall}}}\,e^{-t/\tau_{\text{fall}}} \\ &\qquad \cdot\left[\left(\frac{1}{\tau_{\text{rise}}}+\frac{1}{\tau_{\text{fall}}}\right)e^{t_i/\tau_{\text{rise}}}\,e^{-t/\tau_{\text{rise}}}-\frac{1}{\tau_{\text{fall}}}\right]\end{aligned}$$

With the substitutions

$$\begin{aligned} a_i &= w_i\,A_0\,e^{t_i/\tau_{\text{fall}}} & X_{\text{rise}} &= e^{-t/\tau_{\text{rise}}} \qquad \text{(A.9)}\\ b_i &= \left(\frac{1}{\tau_{\text{rise}}}+\frac{1}{\tau_{\text{fall}}}\right)e^{t_i/\tau_{\text{rise}}} & X_{\text{fall}} &= e^{-t/\tau_{\text{fall}}} \\ c &= \frac{1}{\tau_{\text{fall}}} \end{aligned}$$

we find

$$\begin{aligned}\frac{\mathrm{d}f_i(t)}{\mathrm{d}t} &= a_i\,X_{\text{fall}}\cdot\left[b_i\,X_{\text{rise}}-c\right] \qquad \text{(A.10)}\\ &= a_i\,b_i\,X_{\text{fall}}\,X_{\text{rise}}-a_i\,c\,X_{\text{fall}}\,.\end{aligned}$$

Hence,

$$\begin{aligned}\frac{\mathrm{d}V_{\text{sim}}(t_i^{\min})}{\mathrm{d}t}\overset{!}{=}0 \quad &\Longleftrightarrow \quad \sum_{j=1}^{i}a_j\,b_j\,X_{\text{fall}}\,X_{\text{rise}}-a_j\,c\,X_{\text{fall}}=0 \qquad \text{(A.11)}\\ &\Longleftrightarrow \quad \sum_{j=1}^{i}a_j\,b_jX_{\text{rise}}-a_j\,c=\sum_{j=1}^{i}a_j\,b_jX_{\text{rise}}-\sum_{j=1}^{i}a_j\,c=0 \\ &\Longleftrightarrow \quad X_{\text{rise}}=e^{-t_i^{\min}/\tau_{\text{rise}}}=\frac{\sum_{j=1}^{i}a_j\,c}{\sum_{j=1}^{i}a_j\,b_j} \\ &\Longleftrightarrow \quad t_i^{\min}=-\tau_{\text{rise}}\,\ln\left(\frac{\sum_{j=1}^{i}a_j\,c}{\sum_{j=1}^{i}a_j\,b_j}\right) \qquad \text{(A.12)}\end{aligned}$$

The re-substitution yields

$$t_i^{\min} = -\tau_{\text{rise}} \cdot \left[\ln\left(\frac{\tau_{\text{rise}}}{\tau_{\text{rise}} + \tau_{\text{fall}}} \right) + \ln\left(\frac{\sum_{j=1}^{i} w_i \, e^{t_j/\tau_{\text{fall}}}}{\sum_{j=1}^{i} w_i \, e^{t_j/\tau_{\text{fall}}} \, e^{t_j/\tau_{\text{rise}}}} \right) \right] \tag{A.13}$$

and together with equations (A.1) - (A.6)) the pulse heights can be determined. Furthermore the knowledge of the positions $t_i^{\min}$ allows to distinguish between case (a) and case (b). The time difference between the initiation of a pulse and its minimum in the output signal is given by

$$\Delta t_i = t_i^{\min} - t_i \tag{A.14}$$

and can be calculated from equation (A.13). If for two consecutive pulses the successive pulse $i+1$ is initiated before pulse i has reached its minimum in the output signal, i.e.

$$\text{if} \qquad t_{i+1} - t_i < \Delta t_i \,, \tag{A.15}$$

then case (a) takes place. If not, case (b) takes place.
For $t_i \ll t_{i+1}$ the minimum positions of pulse $i+1$ is

$$\begin{aligned} t_{i+1}^{\min} &\approx -\tau_{\text{rise}} \cdot \left[\ln\left(\frac{\tau_{\text{rise}}}{\tau_{\text{rise}} + \tau_{\text{fall}}} \right) + \ln\left(e^{-t_{i+1}/\tau_{\text{rise}}} \right) \right] \\ &= t_{i+1} - \tau_{\text{rise}} \, \ln\left(\frac{\tau_{\text{rise}}}{\tau_{\text{rise}} + \tau_{\text{fall}}} \right) \end{aligned} \tag{A.16}$$

and

$$\Delta t_{i+1} \approx -\tau_{\text{rise}} \, \ln\left(\frac{\tau_{\text{rise}}}{\tau_{\text{rise}} + \tau_{\text{fall}}} \right) . \tag{A.17}$$

Especially

$$\Delta t_1 = -\tau_{\text{rise}} \, \ln\left(\frac{\tau_{\text{rise}}}{\tau_{\text{rise}} + \tau_{\text{fall}}} \right) \tag{A.18}$$

since there is no pulse prior to pulse 1.

A.3 Additional figures and tables

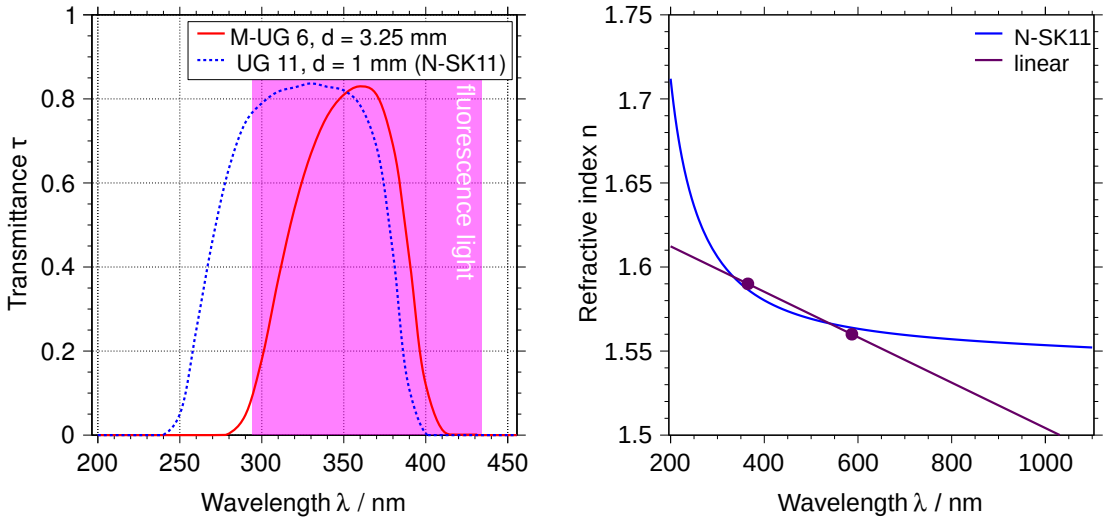

Figure A.2: **Left:** Spectral transmittance $\tau(\lambda)$ of Schott UV band-pass filters. Same data as displayed in the right plot of figure 5.7 but zoomed into the region of UV fluorescence light. **Right:** Refractive index n as a function of the wavelength λ. The two points are the values given by the datasheet of the UG 11 filter. Shown are also the straight line through these points (linear) and the refractive index of the glass Schott N-SK11 as given by [139]. The reference states these data only for wavelengths greater than 300 nm. For $\lambda < 300$ nm an extrapolation is shown.

Table A.1: Parameters of the fits to the aerosol optical transmittance shown in figure 8.6.

Parameter	Unit	Value		
		June 3	June 24	June 27
T_0	–	0.960428 ± 0.00021	0.98422 ± 0.00003	0.98835 ± 0.00037
λ_0	nm	-74.4 ± 10.0	-267.4 ± 1.6	167.6 ± 6.0
Λ_0	nm	305.2 ± 4.0	250.3 ± 0.6	302.2 ± 3.2
χ^2 / ndf	–	8.3 / 5	3756 / 5	15.4 / 5

Table A.2: Settings applied to the G4SiPM simulation of the Hamamatsu S10362-33-100C SiPM. These are the default setting used within this work. If a particular simulation uses different settings, it is stated in the text where the simulation is discussed. The simulations are performed with revision 7691966c.

Property	Symbol	Value	Unit
Geometrical properties			
Number of cells	N_{cells}	900	-
Cell pitch	d_{cell}	100	µm
Fill factor	ϵ	78.5	%
Performance properties[*1]			
Breakdown voltage	V_{bd}	69.5	V
Bias voltage range	V_{bias}	70.8	V
Thermal noise rate	R_{th}	7.02	MHz
Probability of fast afterpulse	$P_{\text{AP,f}}$	0.242	-
Probability of slow afterpulse	$P_{\text{AP,s}}$	0.291	-
Time constant of fast afterpulses	τ_{f}	54.7	ns
Time constant of slow afterpulses	τ_{s}	175.4	ns
Probability of optical crosstalk[*2]	$P_{\text{OXT},\geq 1}$	0.264	-
Spectral photon detection efficiency	PDE(λ)	see footnote[*3]	
Normalized angular photon detection efficiency	PDE(Θ)	see footnote[*4]	
Recovery time constant	τ_{rec}	43.0	ns
Intrinsic dead time	τ_{dead}	1.0	ps
Settings of pulse shaper module			
Amplitude	A_0	-51.0	mV
Time constant of rising edge	τ_{rise}	5.1	ns
Time constant of falling edge	τ_{fall}	43.0	ns
Baseline	V_0	4.7	mV
RMS of noise generator	RMS(noise)	1.2	mV

[*1] Performance properties may depend on the over-voltage and the temperature. They are parametrized according to the parametrizations given in chapter 7. Values given here correspond to an over-voltage of $V_{\text{ov}} = 1.3\,\text{V}$ at a temperature of 23° C.

[*2] nominal number of crosstalk neighbors $n = 4$

[*3] according figure 8.7 (SiPM A)

[*4] calculated from Fresnel equations (cf. equation (5.3) et seqq.)

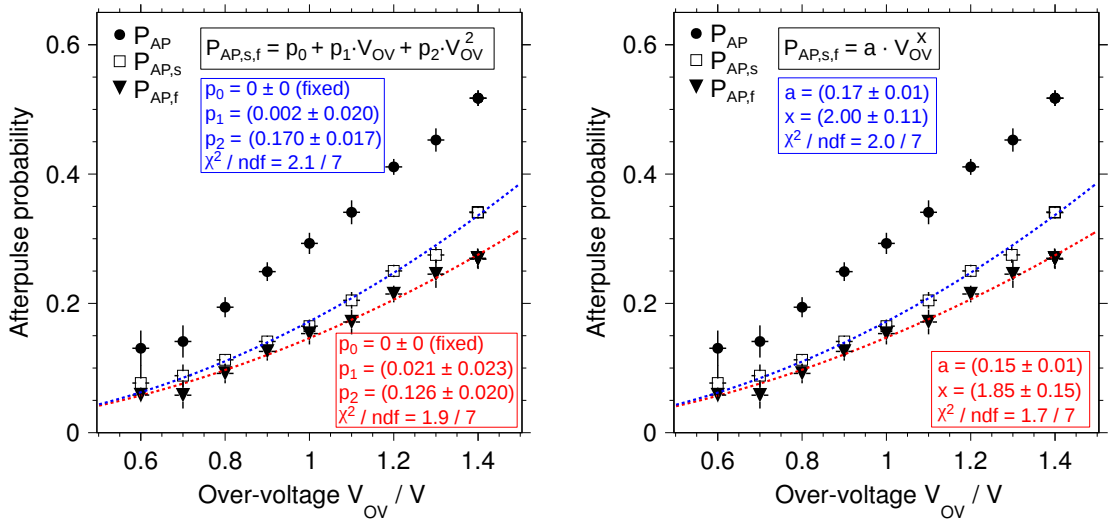

Figure A.3: **Left:** Afterpulse probabilities depending on the over-voltage V_{ov} as determined in section 7.4. The squares are the probability $P_{\mathrm{AP,s}}$ of slow afterpulses. The triangles are the probability $P_{\mathrm{AP,f}}$ of fast afterpulses. The circles are the combined probability P_{AP}. The dashed curves are fits of second order polynomials. **Right:** The markers show the same data as in the left plot. The dashed curves are fits of power functions $P(V_{\mathrm{ov}}) = a \cdot V_{\mathrm{ov}}^{x}$.

Table A.3: Parametrizations of photon detection efficiencies according to equation (8.7) as shown in figure 8.7 of section 8.4

Parameter	Value	Parameter	Value
SiPM A (used for the night-sky photometer)			
A_1	730.3	A_2	0
λ_1	307 nm	λ_2	0
Λ_1	107925 nm	Λ_2	0
Γ_1	140 nm	Γ_2	0
SiPM B (reference of manufacturer)			
A_1	11.1	A_2	5.5
λ_1	315 nm	λ_2	326 nm
Λ_1	462 nm	Λ_2	670 nm
Γ_1	15 nm	Γ_2	129 nm

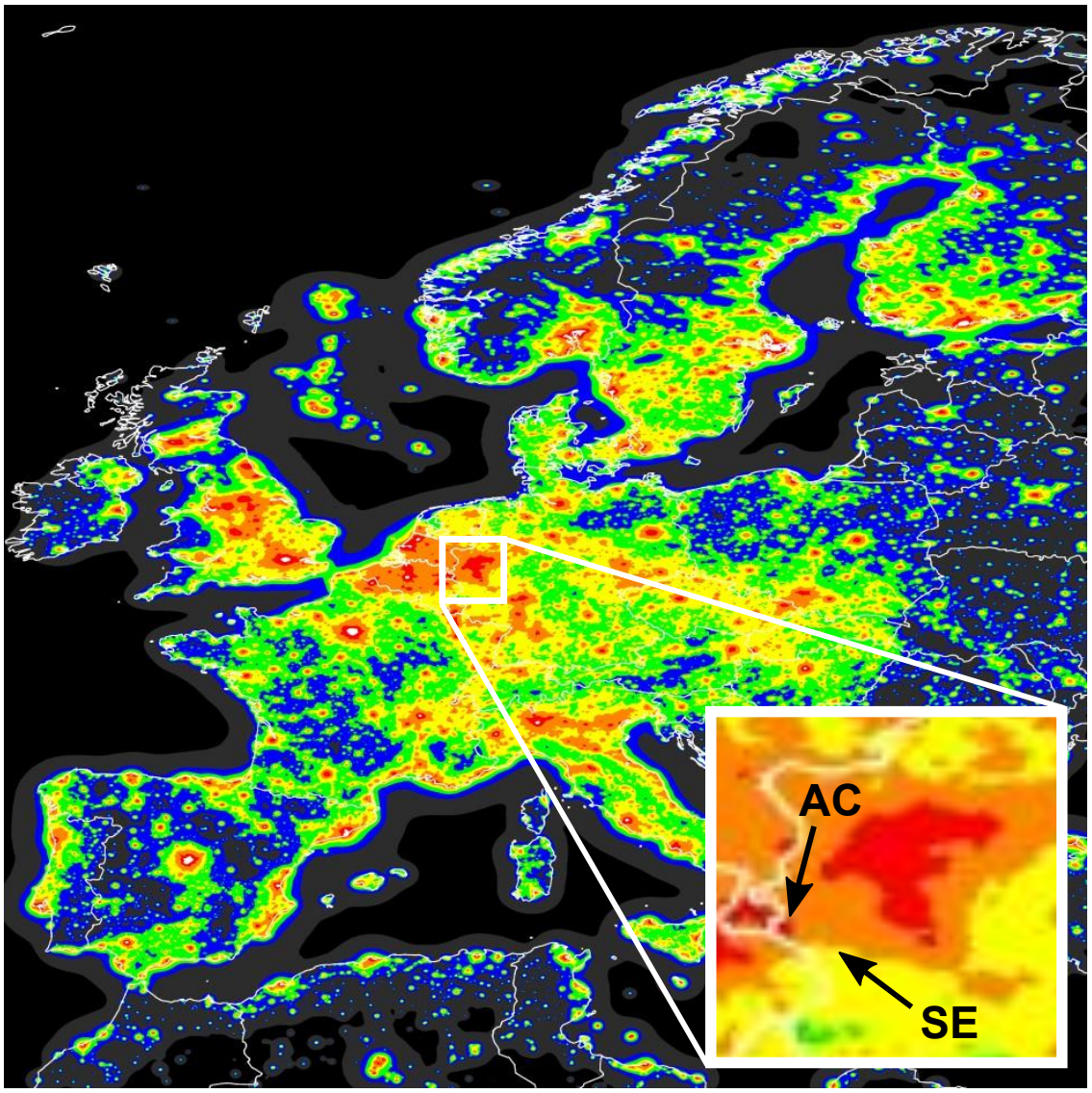

Figure A.4: Artificial night-sky brightness at sea level for Europe. The map has been computed for the photometric astronomical V band (V stands for visible, the maximum transmittance of V filters is at about 540 nm), at the zenith, for a clean atmosphere. The color denote the measured light flux in photons $\mathrm{cm}^{-2}\,\mathrm{s}^{-1}\,\mathrm{sr}^{-2}$: $9.47{\cdot}10^6 - 2.84{\cdot}10^7$ (blue), $2.84{\cdot}10^7 - 8.61{\cdot}10^7$ (green), $8.61{\cdot}10^7 - 2.58{\cdot}10^8$ (yellow), $2.58 \cdot 10^8 - 7.75 \cdot 10^8$ (orange), $7.75 \cdot 10^8 - 2.32 \cdot 10^9$ (red), and $> 2.32 \cdot 10^9$ (white). Country boundaries are approximate. The inset is an enlarged display showing parts of Belgium, Germany, and the Netherlands. Marked are the approximate positions of Aachen (AC) and Schmidt–Eschauel (SE). While the town of Aachen might be identified as the red region in the border triangle, Schmidt–Eschauel appears to be either in an orange or a yellow region. Modified, original taken from reference [162].

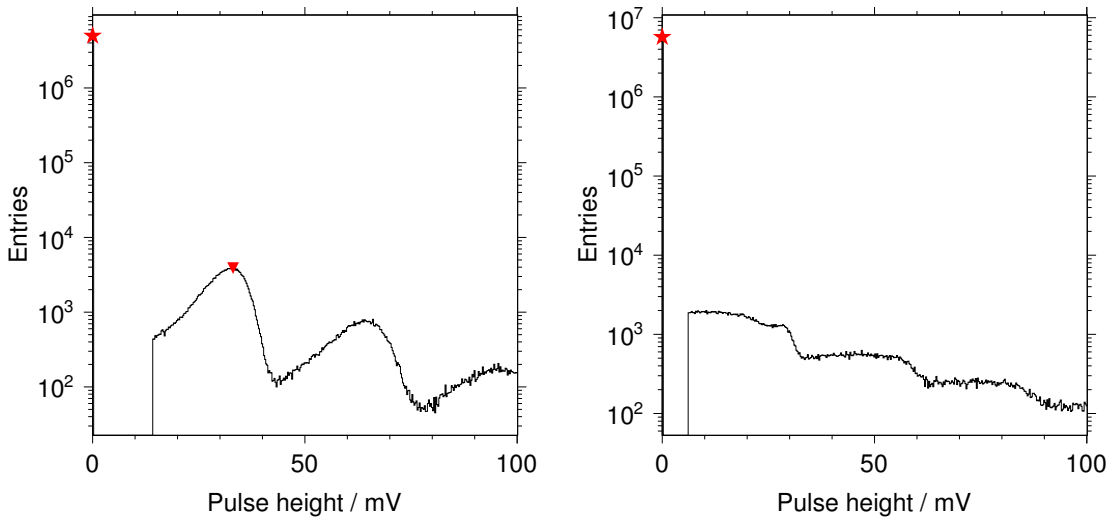

Figure A.5: Pulse height spectra determined from measurements with the night-sky photometer facing into the direction of the bright star Arcturus. Left for a measurement with the UV filter, right for a measurement without the UV filter. If the filter is not applied the peaks of the spectrum are broadened and flat-topped and the determination of the position of the 1 p.e. peaks leads to high systematic uncertainties.

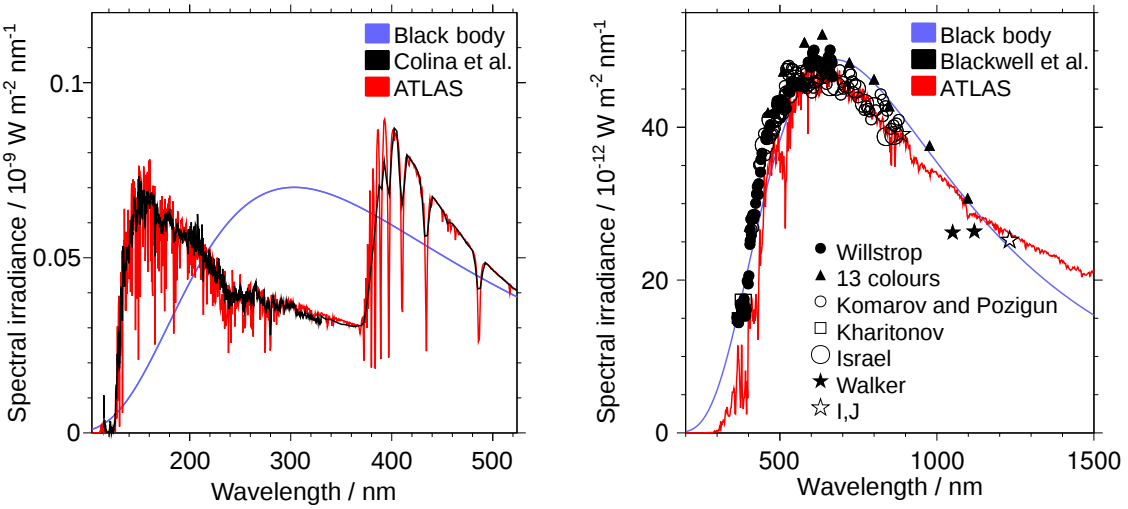

Figure A.6: Spectral irradiances of the Vega (left) and Arcturus (right). The same data as shown in figures 8.3 (right) and 8.4 (left), but with different scales. The measured data are given by the black curve and the black data points, while the models are given by the blue (black body radiation) and red (ATLAS) curves. The apparent disagreement of the measured and modeled (ATLAS) data with respect to the depth of the absorption lines shown in the left plot is due to the different resolutions. However, the irradiances obtained from ATLAS data with different resolutions differ only insignificantly from each other.

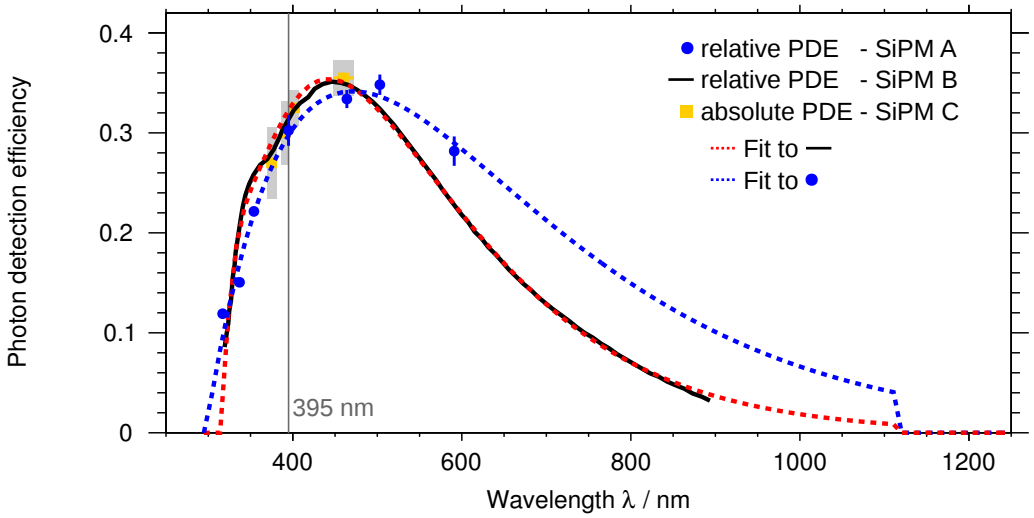

Figure A.7: Photon detection efficiency (PDE) as a function of the wavelength as shown in figure 8.7. The blue filled data points are the relative PDE of the SiPM used for the night-sky photometer (SiPM A – type S10362-33-100C, $3\times3\,\mathrm{mm}^2$ sensitive area, 100 µm cell pitch). The solid black line is the relative PDE of a type S10362-33-050C SiPM measured by the manufacturer (SiPM B - $3\times3\,\mathrm{mm}^2$, 50 µm) [108]. The orange colored squares are the absolute PDE of a type S10362-11-100C SiPM (SiPM C – $1\times1\,\mathrm{mm}^2$, 100 µm) [105]. The widths of the gray boxes denote the systematic uncertainties. The red dashed curve is a fit to the PDE of SiPM B. The blue dashed curve is a fit to the PDE of SiPM A.

Table A.4: Observational locations and times, apparent altitudes of stars, and over-voltages of various measurements into the directions of the bright stars Arcturus and Vega, and into directions without bright stars (diffuse night-sky brightness (dNSB)). The identification numbers (ID) are also given in table 7.2 and in the plots of figure 7.25 at the related data points. The observational times are given in Central European Summer Time (UTC+2).

ID	Date [*1]	Location	Direction	Time	Apparent altitude	Over-voltage V_{ov} / V
I	June 23	Aachen	dNSB [*2]	1:14 – 1:21	—	1.23 ± 0.01 (stat.) ± 0.02 (sys.)
II	June 23	Aachen	dNSB	1:58 – 2:48	—	1.44 ± 0.01 (stat.) ± 0.02 (sys.)
III	July 3	Aachen	Arcturus	1:02 – 1:32	$34° 14' 59''$ – $29° 33' 31''$	1.28 ± 0.01 (stat.) ± 0.02 (sys.)
IV	July 3	Aachen	Arcturus	2:28 – 2:35	$20° 42' 43''$ – $19° 36' 40''$	1.24 ± 0.01 (stat.) ± 0.02 (sys.)
V	July 3	Aachen	Arcturus	2:48 – 2:51	$17° 34' 33''$ – $17° 06' 29''$	1.24 ± 0.01 (stat.) ± 0.02 (sys.)
VI	July 3	Aachen	dNSB	2:52 – 2:57	—	1.31 ± 0.01 (stat.) ± 0.02 (sys.)
VII	July 24	Aachen	Vega	0:48 – 1:28	$75° 48' 49''$ – $71° 05' 44''$	1.13 ± 0.01 (stat.) ± 0.02 (sys.)
VIII	July 24	Aachen	Vega	3:26 – 3:34	$53° 05' 48''$ – $51° 49' 48''$	1.25 ± 0.01 (stat.) ± 0.02 (sys.)
IX	July 24	Aachen	Vega	3:39 – 3:44	$51° 02' 20''$ – $50° 14' 55''$	1.27 ± 0.01 (stat.) ± 0.02 (sys.)
X	July 24	Aachen	dNSB	3:45 – 3:53	—	1.34 ± 0.01 (stat.) ± 0.02 (sys.)
XI	July 27	Eschauel	Vega	2:07 – 2:49	$63° 27' 52''$ – $56° 51' 53''$	1.17 ± 0.01 (stat.) ± 0.02 (sys.)
XII	July 27	Eschauel	dNSB	3:02 – 4:02	—	1.23 ± 0.01 (stat.) ± 0.02 (sys.)

[*1] all dates in 2012
[*2] no UV filter applied

References

[1] V. F. Hess. Beobachtungen der durchdringenden Strahlung bei sieben Freiballonfahrten. *Phys. Z.*, 13:1084, 1912.

[2] P. Auger, et al. Extensive Cosmic-Ray Showers. *Rev. Mod. Phys.*, 11(3-4):288–291, 1939.

[3] A. Haungs. AugerNext: innovative research studies for the next generation ground-based ultra-high energy cosmic ray experiment. In *Europ. Phys. J. Web of Conf.*, volume 53, page 8019, 2013.

[4] J. R. Hörandel. Models of the knee in the energy spectrum of cosmic rays. *Astroparticle Phys.*, 21(3):241 – 265, 2004.

[5] J. Milke, et al. Investigation of Hadronic Interaction Models with the KASCADE-Grande Hadron Calorimeter. In *Proc. of 29th Intern. Cosmic Ray Conf., Pune, India*, volume 6, page 125, 2005.

[6] T. Pierog. Connecting accelerator experiments and cosmic ray showers. In *Europ. Phys. J. Web of Conf.*, volume 53, page 1004, 2013.

[7] E. S. Seo, et al. Measurement of cosmic-ray proton and helium spectra during the 1987 solar minimum. *Astrophys. J.*, 378:763–772, 1991.

[8] I. P. Ivanenko, et al. Energy Spectra of Cosmic Rays above 2 TeV as Measured by the SOKOL Apparatus. In *Proc. of 23rd Intern. Cosmic Ray Conf., Calgary, Canada*, volume 2, page 17, 1993.

[9] N. L. Grigorov, et al. Energy Spectrum of Primary Cosmic Rays in the $10^{11} - 10^{15}$ eV According to the Data of Proton-4 Measurements. In *Proc. of 12th Intern. Cosmic Ray Conf., Hobart, Australia*, volume 1, page 170, 1971.

[10] M. A. K. Glasmacher, et al. The cosmic ray energy spectrum between 10^{14} and 10^{16} eV. *Astroparticle Phys.*, 10(4):291 – 302, 1999.

[11] The IceCube Collaboration (R. Abbasi, et al.). All-particle cosmic ray energy spectrum measured with 26 IceTop stations. *Astroparticle Phys.*, 44(0):40 – 58, 2013.

[12] T. Antoni, et al. KASCADE measurements of energy spectra for elemental groups of cosmic rays: Results and open problems. *Astroparticle Phys.*, 24(1):1 – 25, 2005.

[13] W. Apel, et al. The spectrum of high-energy cosmic rays measured with KASCADE-Grande. *Astroparticle Phys.*, 36(1):183 – 194, 2012.

[14] The HiRes Collaboration (R. U. Abbasi, et al.). First Observation of the Greisen-Zatsepin-Kuzmin Suppression. *Phys. Rev. Lett.*, 100(10):101101, 2008.

[15] D. Ivanov. *Energy Spectrum Measured by the Telescope Array Surface Detector*. Ph.D. thesis, Rutgers, The State University of New Jersey, 2012.

[16] A. Schulz for the Pierre Auger Collaboration. The measurement of the energy spectrum of cosmic rays above $3 \cdot 10^{17}$ eV with the Pierre Auger Observatory. In *Proc. 33rd Intern. Cosmic Ray Conf., Rio de Janeiro, Brazil*, 2013.

[17] J. Blümer, et al. Cosmic rays from the knee to the highest energies. *Progr. in Part. and Nucl. Phys.*, 63(2):293 – 338, 2009.

[18] K. Greisen. End to the Cosmic-Ray Spectrum? *Phys. Rev. Lett.*, 16(17):748–750, 1966.

[19] G. T. Zatsepin, et al. Upper Limit of the Spectrum of Cosmic Rays. *J. of Exp. and Theor. Phys. Lett.*, 4:78–80, 1966.

[20] J. W. Cronin. The highest-energy cosmic rays. *Nucl. Phys. B Proc. Suppl.*, 138:465–491, 2005.

[21] F. W. Stecker, et al. Photodisintegration of Ultra-High-Energy Cosmic Rays: A New Determination. *Astrophys. J.*, 512:521–526, 1999.

[22] E. Khan, et al. Photodisintegration of ultra-high-energy cosmic rays revisited. *Astroparticle Phys.*, 23(2):191 – 201, 2005.

[23] K. V. Ptitsyna, et al. Physical conditions in potential accelerators of ultra-high-energy cosmic rays: updated Hillas plot and radiation-loss constraints. *Phys.–Uspekhi*, 53:691–701, 2010.

[24] E. Fermi. On the Origin of the Cosmic Radiation. *Phys. Rev.*, 75:1169–1174, 1949.

[25] V. Berezinsky. UHECR: Signatures and models. In *Europ. Phys. J. Web of Conf.*, volume 53, page 1003, 2013.

[26] The HESS Collaboration (F. Aharonian, et al.). A detailed spectral and morphological study of the gamma-ray supernova remnant RX J1713.7-3946 with HESS. *Astron. & Astrophys.*, 449:223–242, 2006.

[27] The HESS Collaboration (F. Aharonian, et al.). Primary particle acceleration above 100 TeV in the shell-type supernova remnant RX J1713.7-3946 with deep HESS observations. *Astron. & Astrophys.*, 464:235–243, 2007.

[28] The Pierre Auger Collaboration (P. Abreu, et al.). Update on the correlation of the highest energy cosmic rays with nearby extragalactic matter. *Astroparticle Phys.*, 34:314–326, 2010.

[29] A. M. Hillas. The Origin of Ultra-High-Energy Cosmic Rays. *Ann. Rev. Astron. Astrophys.*, 22:425–444, 1984.

[30] H. Blümer, et al. Die Suche nach den Quellen der kosmischen Strahlung. *Phys. Bl.*, 56N3:39–45, 2000.

[31] The Pierre Auger Collaboration (J. Abraham, et al.). Correlation of the Highest-Energy Cosmic Rays with Nearby Extragalactic Objects. *Science*, 318(5852):938–943, 2007.

[32] K.-H. Kampert. Highlights from the Pierre Auger Observatory. In *Proc. of the 32nd Intern. Cosmic Ray Conf., Beijing*, volume 12, pages 55–66, 2011.

[33] O. Deligny, et al. Review of the anisotropy working group at UHECR-2012. In *Europ. Phys. J. Web of Conf.*, volume 53, page 1008, 2013.

[34] The Particle Data Group (J. Behringer, et al.). The Review of Particle Physics. *Phys. Rev. D*, 86:010001, 2012.

[35] E. Barcikowski, et al. Mass composition working group report. In *Europ. Phys. J. Web of Conf.*, volume 53, page 1006, 2013.

[36] A. Letessier-Selvon for the Pierre Auger Collaboration. Highlights from the Pierre Auger Observatory. In *Proc. 33rd Intern. Cosmic Ray Conf., Rio de Janeiro, Brazil*, 2013.

[37] M. Stephan. *Design and Test of a Low Noise Amplifier for the Auger Radio Detector*. Diploma thesis, RWTH Aachen University, 2009.

[38] M. Risse. Properties of Extensive Air Showers. *Acta Phys. Pol. B*, 35:1787, 2004.

[39] M. Boratav et al. Summary of the school: A critical view on the origin of the ultra-high-energy cosmic rays. In M. Lemoine et al., editors, *Physics and Astrophysics of Ultra-High-Energy Cosmic Rays*, volume 576 of *Lecture Notes in Physics*, pages 300–317. Springer Berlin Heidelberg, 2001. ISBN 978-3-540-42899-2.

[40] T. Stanev. *High Energy Cosmic Ray*. Springer-Verlag, Berlin, 2004. ISBN 3-540-40653-0.

[41] P. Billoir. Phenomenology of ultra-high-energy atmospheric showers. In M. Lemoine et al., editors, *Physics and Astrophysics of Ultra-High-Energy Cosmic Rays*, volume 576 of *Lecture Notes in Physics*, pages 27–44. Springer Berlin Heidelberg, 2001. ISBN 978-3-540-42899-2.

[42] T. K. Gaisser, et al. Reliability of the method of constant intensity cuts for reconstructing the average development of vertical showers. In *Proc. of 15th Intern. Cosmic Ray Conf., Plovdiv, Bulgaria*, volume 8, pages 353–357, 1977.

[43] D. Góra, et al. Universal lateral distribution of energy deposit in air showers and its application to shower reconstruction. *Astroparticle Phys.*, 24:484–494, 2006.

[44] W. Heitler. *The Quantum Theory of Radiation*. Oxford University Press, Oxford, third edition, 1954. ISBN 0-486-64558-4.

[45] J. Matthews. A Heitler model of extensive air showers. *Astroparticle Phys.*, 22(5-6):387 – 397, 2005.

[46] C. Meurer, et al. Muon production in extensive air showers and its relation to hadronic interactions. *Czechoslovak J. of Phys.*, 56(26):A260000–A219, 2006.

[47] J. Alvarez-Muñiz, et al. Hybrid simulations of extensive air showers. *Phys. Rev. D*, 66(3):033011, 2002.

[48] F. Schmidt. CORSIKA Shower Images, 2013. URL http://www.ast.leeds.ac.uk/~fs/showerimages.html.

[49] D. Heck, et al. CORSIKA: A Monte Carlo Code to Simulate Extensive Air Showers. Report FZKA 6019, Karlsruhe Research Center, 1998.

[50] J. Allen, et al. Air shower simulation and hadronic interactions. In *Europ. Phys. J. Web of Conf.*, volume 53, page 1007, 2013.

[51] T. Bergmann, et al. One-dimensional hybrid approach to extensive air shower simulation. *Astroparticle Phys.*, 26(6):420 – 432, 2007.

[52] T. Pierog, et al. EPOS Model and Ultra High Energy Cosmic Rays. *Nucl. Phys. B Proc. Suppl.*, 196:102–105, 2009.

[53] S. Ostapchenko. Monte Carlo treatment of hadronic interactions in enhanced Pomeron scheme: QGSJET-II model. *Phys. Rev. D*, 83(1):014018, 2011.

[54] E.-J. Ahn, et al. Cosmic ray interaction event generator SIBYLL 2.1. *Phys. Rev. D*, 80(9):094003, 2009.

[55] M. Ave, et al. Spectrally resolved pressure dependence measurements of air fluorescence emission with AIRFLY. *Nucl. Inst. & Meth. A*, 597(1):41 – 45, 2008.

[56] M. Risse, et al. Energy release in air showers. *Astroparticle Phys.*, 20:661–667, 2004.

[57] F. Arqueros, et al. Air fluorescence relevant for cosmic-ray detection: Summary of the 5th fluorescence workshop, El Escorial 2007. *Nucl. Inst. & Meth. A*, 597(1):1 – 22, 2008.

[58] M. Ave, et al. Precise measurement of the absolute fluorescence yield of the 337 nm band in atmospheric gases. *Astroparticle Phys.*, 42:90–102, 2013.

[59] K. Bernlöhr. Impact of atmospheric parameters on the atmospheric Cherenkov technique. *Astroparticle Phys.*, 12:255–268, 2000.

[60] The Pierre Auger Collaboration. Image Gallery, 2013. URL http://www.auger.org/observatory/image_gallery_index.html.

[61] I. Allekotte, et al. for the Pierre Auger Collaboration. The surface detector system of the Pierre Auger Observatory. *Nucl. Inst. & Meth. A*, 586:409–420, 2008.

[62] H. P. Dembinski. *Measurement of the flux of ultra high energy cosmic rays using data from very inclined air showers at the Pierre Auger Observatory.* Ph.D. thesis, RWTH Aachen University, 2009.

[63] X. Bertou, et al. for the Pierre Auger Collaboration. Calibration of the surface array of the Pierre Auger Observatory. *Nucl. Inst. & Meth. A*, 568(2):839 – 846, 2006.

[64] The Pierre Auger Collaboration (J. Abraham, et al.). Properties and performance of the prototype instrument for the Pierre Auger Observatory. *Nucl. Inst. & Meth. A*, 523(1–2):50 – 95, 2004.

[65] The Pierre Auger Collaboration (J. Abraham, et al.). Trigger and aperture of the surface detector array of the Pierre Auger Observatory. *Nucl. Inst. & Meth. A*, 613(1):29 – 39, 2010.

[66] The Pierre Auger Collaboration (J. Abraham, et al.). The Fluorescence Detector of the Pierre Auger Observatory. *Nucl. Inst. & Meth. A*, 620:227–251, 2010.

[67] Bergische Universität Wuppertal. Neues Fenster zum Kosmos, 2013. URL http://www.presse-archiv.uni-wuppertal.de/html/module/medieninfos/archiv/2007/0911_kosmos.htm.

[68] R. Smida (Karlsruhe Institute of Technology). Private communication.

[69] B. Fick, et al. The Central Laser Facility at the Pierre Auger Observatory. *J. of Instrum.*, 1:P11003, 2006.

[70] D. Allard, et al. A guide-line to the Auger-Surface-Detector Analysis. *GAP Note (Pierre Auger Collab. Internal Report)*, 24:1–109, 2006.

[71] K. Greisen. Cosmic Ray Showers. *Ann. Rev. of Nucl. Sci.*, 10(1):63–108, 1960.

[72] K. Kamata, et al. The Lateral and the Angular Structure Functions of Electron Showers. *Progr. of Theor. Phys. Suppl.*, 6:93–155, 1958.

[73] D. Newton, et al. The optimum distance at which to determine the size of a giant air shower. *Astroparticle Phys.*, 26(6):414 – 419, 2007.

[74] D. Kuempel, et al. Geometry reconstruction of fluorescence detectors revisited. *Astroparticle Phys.*, 30:167–174, 2008.

[75] The Pierre Auger Collaboration (P. Abreu, et al.). The rapid atmospheric monitoring system of the Pierre Auger Observatory. *J. of Instrum.*, 7:9001, 2012.

[76] V. Verzi for the Pierre Auger Collaboration. The Energy Scale of the Pierre Auger Observatory. In *Proc. of 33rd Intern. Cosmic Ray Conf., Rio de Janeiro, Brazil*, 2013.

[77] D. Ravignani for the Pierre Auger Collaboration. Measurement of the energy spectrum of cosmic rays above $3 \cdot 10^{17}$ eV using the AMIGA 750 m surface detector array of the Pierre Auger Observatory. In *Proc. of 33rd Intern. Cosmic Ray Conf., Rio de Janeiro, Brazil*, 2013.

[78] F. Suarez for the Pierre Auger Collaboration. The AMIGA muon detectors of the Pierre Auger Observatory: overview and status. In *Proc. of 33rd Intern. Cosmic Ray Conf., Rio de Janeiro, Brazil*, 2013.

[79] D. García-Gámez for the Pierre Auger Collaboration. Observations of the longitudinal development of extensive air showers with the surface detectors of the Pierre Auger Observatory. In *Proc. of 33rd Intern. Cosmic Ray Conf., Rio de Janeiro, Brazil*, 2013.

[80] K. F. Weidenhaupt. *Antenna Calibration and Energy Measurement of Ultra-High Energy Cosmic Rays with the Auger Engineering Radio Array.* Ph.D. thesis, RWTH Aachen University, 2014.

[81] T. H.-J. Mathes for the Pierre Auger Collaboration. The HEAT Telescopes of the Pierre Auger Observatory — Status and First Data. In *Proc. of 32nd Intern. Cosmic Ray Conf., Beijing, China*, 2011.

[82] T. Huege for the Pierre Auger Collaboration. Probing the radio emission from cosmic-ray-induced air showers by polarization measurements. In *Proc. of 33rd Intern. Cosmic Ray Conf., Rio de Janeiro, Brazil*, 2013.

[83] T. Huege. Theory and simulations of air shower radio emission. In R. Lahmann, et al., editors, *Amer. Inst. of Phys. Conf. Ser.*, volume 1535, pages 121–127, 2013.

[84] F. Schröder for the Pierre Auger Collaboration. Radio detection of air showers with the Auger Engineering Radio Array. In *Proc. of 33rd Intern. Cosmic Ray Conf., Rio de Janeiro, Brazil*, 2013.

[85] The Pierre Auger Collaboration (P. Abreu, et al.). Antennas for the detection of radio emission pulses from cosmic-ray induced air showers at the Pierre Auger Observatory. *J. of Instrum.*, 7:11P, 2012.

[86] M. Stephan for the Pierre Auger Collaboration. Antennas, filters and preamplifiers designed for the radio detection of ultra-high-energy cosmic rays. In *Asia-Pacific Microwave Conf. Proc.*, pages 1455–1458, 2010.

[87] R. Gaïor for the Pierre Auger Collaboration. Detection of cosmic rays using microwave radiation at the Pierre Auger Observatory. In *Proc. of 33rd Intern. Cosmic Ray Conf., Rio de Janeiro, Brazil*, 2013.

[88] P. W. Gorham, et al. Observations of microwave continuum emission from air shower plasmas. *Phys. Rev. D*, 78:032007, 2008.

[89] M. Stephan for the Pierre Auger Collaboration. Radio and microwave detection of cosmic rays at the Pierre Auger Observatory and the low-energy enhancement HEAT. In *Proc. of 14th ICATPP Conf. on Astroparticle, Particle, Space Phys. and Detectors for Phys. Appl., Como, Italy*, 2013.

[90] D. Renker, et al. Advances in solid state photon detectors. *J. of Instrum.*, 4(04):P04004, 2009.

[91] E. Hering, et al. *Elektronik für Ingenieure und Naturwissenschaftler*. Springer-Lehrbuch. Springer Berlin Heidelberg, 2005. ISBN 978-3-540-24309-0.

[92] S. Kasap, et al. Illustrated Dictionary of Electronic Materials and Devices - Concise 3rd Student Ed. In *Principles of Eletronic Materials and Devices*, McGraw-Hill, New York, 2006. ISBN 007-124458-1. Provided on enclosed CD-ROM.

[93] International Commission on Illumination. CIE Standard Illuminants for Colorimetry, 2013. URL http://www.cie.co.at/publ/abst/s005.html.

[94] K. K. Ng. *Complete Guide to Semiconductor Devices*. McGraw–Hill Series in Electrical and Computer Engineering. McGraw–Hill Inc., 1995. ISBN 978-0-07-035860-7.

[95] J. Rennefeld. *Studien zur Eignung von Silizium Photomultipliern für den Einsatz im erweiterten CMS Detektor am SLHC*. Diploma thesis, RWTH Aachen University, 2010.

[96] P. Hallen. *Determination of the Recovery Time of Silicon Photomultipliers*. Bachelor thesis, RWTH Aachen University, 2012.

[97] sensL. M-Series Detectors, 2013. URL http://sensl.com/products/silicon-photomultipliers/mseries/.

[98] P. Buzhan, et al. Silicon photomultiplier and its possible applications. *Nucl. Inst. & Meth. A*, 504(1-3):48–52, 2003.

[99] F. Corsi, et al. Electrical Characterization of Silicon Photo-Multiplier Detectors for Optimal Front-End Design. In *IEEE Nucl. Sci. Symp. Conf. Rec.*, volume 2, pages 1276–1280, 2006.

[100] F. Scheuch. *Measurement and simulation of electrical properties of SiPM photon detectors*. Master thesis, RWTH Aachen University, 2012.

[101] J. Schumacher. *Front-End Electronics for Silicon Photomultipliers*. Master thesis, RWTH Aachen University, 2014.

[102] sensL. SL Press Page, 2013. URL http://sensl.com/slpress/.

[103] K. Yamamoto, et al. Assembly technology of 4-side buttable MPPC. *Nucl. Inst. & Meth. A*, 732(0):547 –550, 2013.

[104] M. Stephan, et al. Future use of silicon photomultipliers for the fluorescence detection of ultra-high-energy cosmic rays. *Proc. SPIE*, 8155:81551B–14, 2011.

[105] M. Lauscher. *Characterisation Studies of Silicon Photomultipliers for the Detection of Fluorescence Light from Extensive Air Showers*. Master thesis, RWTH Aachen University, 2012.

[106] M. Ramilli. Characterization of SiPM: Temperature dependencies. In *IEEE Nucl. Sci. Symp. Conf. Rec.*, pages 2467–2470, 2008.

[107] J. Schumacher. *Characterization Studies of Silicon Photomultipliers: Noise and Relative Photon Detection Effciency*. Bachelor thesis, RWTH Aachen University, 2011.

[108] Hamamatsu Photonics K.K. Multi-Pixel Photon Counter Product Catalog, 2012.

[109] K. Sato, et al. The UV sensitivity improvement of MPPC. *Nucl. Inst. & Meth. A*, 732(0):427 – 430, 2013.

[110] T. Toyama, et al. for the CTA Consortium. Novel Photo Multiplier Tubes for the Cherenkov Telescope Array Project. In *Proc. of 33rd Intern. Cosmic Ray Conf., Rio de Janeiro, Brazil*, 2013.

[111] P. Eckert, et al. Characterisation studies of silicon photomultipliers. *Nucl. Inst. & Meth. A*, 620:217–226, 2010.

[112] D. Wilson. *Angular Dependence of the Relative Photon Detection Efficiency of Silicon Photomultipliers*. Bachelor thesis, RWTH Aachen University, 2012.

[113] S. Villa, et al. Photon emission from hot electrons in silicon. *Phys. Rev. B*, 52:10993–10999, 1995.

[114] A. N. Otte. *Observation of VHE γ-Rays from the Vicinity of magnetized Neutron Stars and Development of new Photon-Detectors for Future Ground based γ-Ray Detectors*. Ph.D. thesis, Technische Universität München, 2007.

[115] H. Otono, et al. Study of MPPC at Liquid Nitrogen Temperature. *Proc. of Sci.*, PD07:007, 2007.

[116] T. Kowalew. *Dynamic Range Characterisation of Silicon Photomultipliers*. Bachelor thesis, RWTH Aachen University, 2013.

[117] T. Niggemann, et al. G4SiPM, 2013. URL https://forge.physik.rwth-aachen.de/projects/g4sipm.

[118] T. Niggemann. *New Telescope Design with Silicon Photomultipliers for Fluorescence Light Detection of Extensive Air Showers*. Master thesis, RWTH Aachen University, 2012.

[119] S. Agostinelli, et al. Geant4 — a simulation toolkit. *Nucl. Inst. & Meth. A*, 506(3):250 – 303, 2003.

[120] Hamamatsu Photonics K.K. Multi-pixel photon counter, 2014. URL http://www.hamamatsu.com/us/en/product/category/3100/4004/4113/index.html.

[121] B. Dolgoshein, et al. Large area UV SiPMs with extremely low cross-talk. *Nucl. Inst. & Meth. A*, 695(0):40 – 43, 2012.

[122] Philips. Philips Digital Photon Counting, 2013. URL http://www.research.philips.com/initiatives/digitalphotoncounting/index.html.

[123] Philips. Digital Silicon Photomultiplier — Short Data Sheet, 2013. URL http://www.research.philips.com/initiatives/digitalphotoncounting/index.html.

[124] T. Frach, et al. The digital silicon photomultiplier — System architecture and performance evaluation. In *IEEE Nucl. Sci. Symp. Conf. Rec.*, pages 1722–1727, 2010.

[125] B. Glauss. *Optical Test Stand and SiPM characterisation studies*. Master thesis, RWTH Aachen University, 2012.

[126] T. Niggemann, et al. Status of the Silicon Photomultiplier Telescope FAMOUS for the Fluorescence Detection of UHECRs. In *Proc. of 33rd Intern. Cosmic Ray Conf., Rio de Janeiro, Brazil*, 2013.

[127] M. Lauscher, et al. FAMOUS: a prototype silicon-photomultiplier telescope for the fluorescence detection of ultra-high-energy cosmic rays. *Proc. SPIE*, 8460:84601N–15, 2012.

[128] T. Niggemann, et al. The optics and detector-simulation of the air fluorescence telescope FAMOUS for the detection of cosmic rays. *Proc. SPIE*, 8444:844430–13, 2012.

[129] M. Stephan, et al. FAMOUS - A prototype silicon photomultiplier telescope for the fluorescence detection of ultra-high-energy cosmic rays. In *Europ. Phys. J. Web of Conf.*, volume 53, page 8015, 2013.

[130] H. M. Eichler. *Characterisation of the Optics for the Prototype Fluorescence Telescope FAMOUS*. Master thesis, RWTH Aachen University, 2014.

[131] T. Niggemann (RWTH Aachen University). Private communication.

[132] R. Winston, et al. *The Optics of Nonimaging Concentrators: Light and Solar Energy*. Academic Press, New York, 1978. ISBN 0-127-45350-4.

[133] R. Winston, et al. *Nonimaging Optics*. Academic Press, New York, 2005. ISBN 978-0-127-59751-5.

[134] S. Mann. *Measurement of the UV Reflectivity of Aluminium in Different Stages of Oxidation*. Bachelor thesis, RWTH Aachen University, 2012.

[135] P. Assis, et al. Simulation of the fluorescence telescopes of the Pierre Auger Observatory using GEANT4. *GAP Note (Pierre Auger Collab. Internal Report)*, 104:1–31, 2009.

[136] Schott AG. Optical Filters, 2013. URL http://www.schott.com/advanced_optics/english/products/optical-filters/index.html.

[137] Schott AG. Definitions — Glass Filters. Technical Note 10229 ENG-INT 02100.9, 2009.

[138] Schott AG. Optisches Glass — Beschreibung der Eigenschaften. Pocket Catalog Version 1.8d, 2009.

[139] M. Polyanskiy. Refractive Index Database, 2013. URL http://refractiveindex.info/.

[140] C. R. Benn, et al. Brightness of the night sky over La Palma. *New Astron. Rev.*, 42:503–507, 1998.

[141] H. Ma, et al. Polymer-Based Optical Waveguides: Materials, Processing, and Devices. *Adv. Mater.*, 14(19):1339 – 1365, 2002.

[142] S. Argirò, et al. The offline software framework of the Pierre Auger Observatory. *Nucl. Inst. & Meth. A*, 580:1485–1496, 2007.

[143] C. Peters. *Design Studies for an Air Fluorescence Telescope with Silicon Photomultipliers for the Detection of Ultra-high-energy Cosmic Ray*. Master thesis, RWTH Aachen University, 2013.

[144] Omega micro. MAROC Front-end Chip, 2013. URL http://omega.in2p3.fr/index.php/products/maroc-front-end-chip.html.

[145] Altera Corporation. Cyclone III FPGA Family, 2013. URL http://www.altera.com/devices/fpga/cyclone3/cy3-index.jsp.

[146] P. Assis, et al. R&D for future SiPM cameras for Fluorescence and Cherenkov Telescopes. In *Proc. of 32nd Intern. Cosmic Ray Conf., Beijing, China*, 2011.

[147] J. Grothoff. *Development of a Data Acquisition System for the Air Shower Fluorescence Telescope FAMOUS*. Bachelor thesis, RWTH Aachen University, 2013.

[148] F. H. Knuth. *Commissioning Of The Air Shower Fluorescence Telescope Prototype FAMOUS*. Bachelor thesis, RWTH Aachen University, 2014.

[149] H. Anderhub, et al. Design and operation of FACT — the first G-APD Cherenkov telescope. *J. of Instrum.*, 8:P06008, 2013.

[150] The FACT Collaboration (M. L. Knoetig, et al.). FACT — Long-term stability and observations during strong Moon light. In *Proc. of 33rd Intern. Cosmic Ray Conf., Rio de Janeiro, Brazil*, 2013.

[151] The HEGRA Collaboration. The HEGRA Experiment, 2013. URL http://www.mpi-hd.mpg.de/hfm/HEGRA/HEGRA.html.

[152] The MAGIC Collaboration. The MAGIC Telescopes, 2013. URL https://magic.mpp.mpg.de/.

[153] R. Meißner. *Brightness Measurements of Stars and the Night-Sky with a Silicon-Photomultiplier-Telescope*. Bachelor thesis, RWTH Aachen University, 2012.

[154] NASA National Aeronautics and Space Administration. Human Space Flight Gallery, 2013. URL http://spaceflight.nasa.gov/gallery/.

[155] Alex Cherney. Terrastro, 2013. URL http://www.terrastro.com/.

[156] C. R. Benn, et al. La Palma Night-Sky Brightness. La Palma Technical Note 115, Isaac Newton Group of Telescopes, 2007.

[157] Bresser GmbH. Bresser Messier PN-203 203/800 Newton f/4 auf LXD-75, 2012. URL http://www.bressershop.de/item.php5?id=4703801.

[158] CAEN S.p.A. V1729 Digitizers, 2014. URL http://www.caen.it/csite/CaenProd.jsp?idmod=465&parent=11.

[159] Teledyne LeCroy. Digital Oscilloscope Wavejet 350A Series, 2014. URL http://teledynelecroy.com/japan/products/scopes/wj/.

[160] J. Mutlaq, et al. INDI Library, 2013. URL http://www.indilib.org/api/index.html.

[161] European Space Agency. The Hipparcos Catalogue, ESA SP-1200, 2013. URL http://vizier.u-strasbg.fr/viz-bin/VizieR-5?-out.add=.&-source=I/239/hip_main&HIP=69673.

[162] P. Cinzano, et al. The first World Atlas of the artificial night sky brightness. *Mon. Not. of the Roy. Astron. Soc.*, 328:689–707, 2001.

[163] Strasbourg astronomical Data Center. SIMBAD Astronomical Database, 2013. URL http://simbad.u-strasbg.fr/simbad/.

[164] Fabien Chéreau. Stellarium, 2013. URL http://www.stellarium.org/en/.

[165] S. Cova, et al. Avalanche photodiodes and quenching circuits for single-photon detection. *Appl. Opt.*, 35(12):1956–1976, 1996.

[166] R. Mirzoyan, et al. Light emission in Si avalanches. *Nucl. Inst. & Meth. A*, 610:98–100, 2009.

[167] T. Frach, et al. The digital silicon photomultiplier — Principle of operation and intrinsic detector performance. In *IEEE Nucl. Sci. Symp. Conf. Rec.*, pages 1959–1965, 2009.

[168] L. Gallego, et al. Modeling crosstalk in silicon photomultipliers. *J. of Instrum.*, 8:P05010, 2013.

[169] Institute for Geophysics and Meteorology, University of Cologne. JOYCE - Jülich ObservatorY for Cloud Evolution, 2014. URL http://www.geomet.uni-koeln.de/en/general/research/joyce/.

[170] NASA Goddard Space Flight Center. Aerosol Robotic Network (AERONET), 2014. URL http://aeronet.gsfc.nasa.gov/.

[171] L. Colina, et al. The 0.12-2.5 micron Absolute Flux Distribution of the Sun for Comparison With Solar Analog Stars. *Astron. J.*, 112:307, 1996.

[172] L. Colina, et al. Absolute Flux Calibrated Spectrum of Vega, Instrument Science Report CAL/SCS-008. Technical report, Space Telescopes Science Institute, 1996.

[173] R. L. Kurucz. ATLAS9 Stellar Atmosphere Programs and 2 km/s grid. Kurucz CD-ROM No.13. Cambridge, Mass.: Smithsonian Astrophysical Observatory, 1993.

[174] R. L. Kurucz. ATLAS12, SYNTHE, ATLAS9, WIDTH9, et cetera. *Mem. Soc. Astron. Ital. Suppl.*, 8:14, 2005.

[175] L. Sbordone, et al. ATLAS 9 and ATLAS 12 under GNU-Linux. In *Convection in Astrophysics*, volume 2 of *Proc. of the Intern. Astron. Union*, pages 71–73, 2006.

[176] R. L. Kurucz. Stars, 2013. URL http://kurucz.harvard.edu/stars.html.

[177] C. Fröhlich, et al. The Sun's total irradiance: Cycles, trends and related climate change uncertainties since 1976. *Geophys. Res. Lett.*, 25(23):4377–4380, 1998.

[178] R. C. Bohlin, et al. Hubble Space Telescope Absolute Spectrophotometry of Vega from the Far-Ultraviolet to the Infrared. *Astron. J.*, 127:3508–3515, 2004.

[179] D. E. Blackwell, et al. The continuum flux distribution for Arcturus. *Mon. Not. Roy. Astron. Soc.*, 171:425–439, 1975.

[180] R. E. M. Griffin, et al. The Effective Temperature of Arcturus. *Astron. J.*, 117(6):2998, 1999.

[181] F. van Leeuwen. Validation of the new Hipparcos reduction. *Astron. & Astrophys.*, 474:653–664, 2007.

[182] J. Petit and B. Luzum (eds.). IERS Conventions (2010). IERS Technical Note 36, International Earth Rotation and Reference System Service, 2010. URL http://www.iers.org/IERS/EN/Publications/TechnicalNotes/tn36.html.

[183] K. Biazzo, et al. Precise determination of stellar temperatures from spectroscopic data. *Mem. Soc. Astron. Ital. Suppl.*, 5:109, 2004.

[184] L. Dekin. *Synthetic spectra of cool stars observed with the Short-Wavelength Spectrometer: improving the models and the calibration of the instrument.* Ph.D. thesis, University of Leuven, 2000.

[185] D. Mozurkewich, et al. Angular Diameters of Stars from the Mark III Optical Interferometer. *Astron. J.*, 126:2502–2520, 2003.

[186] J. P. Aufdenberg, et al. First Results from the CHARA Array. VII. Long-Baseline Interferometric Measurements of Vega Consistent with a Pole-On, Rapidly Rotating Star. *Astrophys. J.*, 645(1):664, 2006.

[187] D. M. Peterson, et al. Vega is a rapidly rotating star. *Nature*, 440:869–899, 2006.

[188] O. Absil, et al. Circumstellar material in the Vega inner system revealed by CHARA/FLUOR. *Astron. & Astrophys.*, 452:237–244, 2006.

[189] J. Yoon, et al. A New View of Vega's Composition, Mass, and Age. *Astrophys. J.*, 708:71–79, 2010.

[190] I. Ramírez, et al. Fundamental Parameters and Chemical Composition of Arcturus. *Astrophys. J.*, 743(2):135, 2011.

[191] E. Anderson, et al. XHIP: An extended hipparcos compilation. *Astron. Lett.*, 38:331–346, 2012.

[192] D. W. E. Green. Magnitude Corrections for Atmospheric Extinction. *Intern. Comet Quaterly*, 14:55–59, 1992.

[193] National Renewable Energy Laboratory. Reference Solar Spectral Irradiance: ASTM G-173, 2013. URL http://rredc.nrel.gov/solar/spectra/am1.5/ASTMG173/ASTMG173.html.

[194] World Meteorological Organization. Ozone Mapping Centre, 2014. URL http://lap.physics.auth.gr/ozonemaps2/index.php.

[195] C. M. Will. *Atmospheric Monitoring for Ground-Based Cosmic Ray Detection*. Ph.D. thesis, Karlsruhe Institute of Technology, 2012.

[196] B. Bohn (Jülich Research Center). Private communication.

[197] A. Ångström. Techniques of Determinig the Turbidity of the Atmosphere. *Tellus*, 13(2):214–223, 1961.

[198] D. Myers, et al. Outdoor meteorological broadband and spectral conditions for evaluating photovoltaic modules. In *Conf. Rec. of the 28th IEEE Photovoltaic Specialists Conf.*, pages 1202–1205, 2000.

[199] T. Enzweiler. *Development of a multipurpose light source for SiPM characterization*. Master thesis, RWTH Aachen University, 2013.

[200] C. Heidemann, et al. Optical test setup for Silicon Photo Multipliers. In *Proc. of 7th Intern. Conf. on New Developments in Photon Detection, Tours, France, 2014*. To be published (submitted).

[201] K. McIntosh, et al. An optical comparison of silicone and EVA encapsulants for conventional silicon PV modules: A ray-tracing study. In *Conf. Rec. of the 34th IEEE Photovoltaic Specialists Conf.*, pages 000544–000549, 2009.

[202] W. Li, et al. Optical characterization of RTV615 silicone rubber compound. *J. of Instrum.*, 9(07):P07012, 2014. URL http://stacks.iop.org/1748-0221/9/i=07/a=P07012.

[203] B. G. Keilhauer. *Investigation of Atmospheric Effects on the Development of Air Showers and their Detection with the Pierre Auger Observatory*. Ph.D. thesis, Karlsruhe University, 2004.

[204] National Institute of Standards and Technology. ESTAR database, 2013. URL http://physics.nist.gov/PhysRefData/Star/Text/ESTAR.html.

Declaration of Pre-released Extracts

The following conference proceeding contains pre-released extracts of this work.

- M. Stephan, et al. Future use of silicon photomultipliers for the fluorescence detection of ultra-high-energy cosmic rays. *Proc. SPIE*, 8155:81551B-14, 2011.

The proceeding contains parts of chapter 6. The data of the night-sky brightness discussed in the proceeding are from different data sets than the ones used in this work.

Acknowledgements

With great pleasure I would like to thank the people who supported me and helped to make this work possible.

I am deeply grateful to my doctoral advisor Thomas Hebbeker who has given me the opportunity to follow my research interest and conduct these very exciting and diverse studies. His knowledge and experience have been of priceless value for my work and he has provided unique guidance. Furthermore, I am very thankful for the various occasions to present current research results at conferences and to travel to the collaboration meetings.
I would also like to express my sincere thanks to Martin Erdmann for refereeing my thesis and for valuable discussions during the meetings of the Auger group in Aachen.

For the cooperative and pleasant working atmosphere and inspiring meetings I thank everybody from the Auger group in Aachen. Special thanks go out to the colleagues who contributed with commitment to the implementation of FAMOUS and all of its aspects. These colleagues are Julian Grothoff, Christine Meurer, Sebastian Mann, Tobias Kowalew, Daniel Wilson, and the FAMOUS core team consisting of Michael Eichler, Markus Lauscher, Rebecca Meißner, Lukas Middendorf, Tim Niggemann, Christine Peters, and Johannes Schumacher. The latter supported my work over many years with countless fruitful discussions, helping hands, and a spirit of cooperation which cannot be imagined in a better way. Thanks guys! You are great team! In this sense I am also truly thankful to my former officemate Nils Scharf.
I would like to express my exceptional gratitude to Rebecca Meißner. Rebecca and I operated the night-sky photometer together. We literally worked day and night, and our shifts belong to some of the most memorable moments during my studies.

Furthermore, I am thankful to Tim Enzweiler, Carsten Heidemann, Markus Merschmeyer, Sergio Navas, Florian Scheuch, and Tobias Winchen for discussions concerning SiPMs and related measurement procedures, Christopher Wiebusch for discussions regarding astronomical photometry, and Birger Bohn and Martin Will for discussions regarding the atmosphere. I thank Carsten Heidemann for the PDE measurements with the characterization test stand.
For assistance related to electronics I am grateful to Franz Beißel and Eric Bock. Regarding the production of mechanical components I thank Josef Grooten and Barthel Philipps.

For critical proofreading of my manuscript I would like to express my thanks to Thomas Hebbeker, Markus Lauscher, Lukas Middendorf, Christine Peters, Matthias Plum, Tim Niggemann, and Klaus Weidenhaupt.

The last years would have lacked a lot of insights, motivation, and fun without my friend and colleague Klaus Weidenhaupt and our countless (physics) discussions. I am deeply grateful for his true friendship and glad that we experienced the fabulous joy of being Ph.D. students together. Thanks, Klaus, for keeping the spirit of *That's it! That's science!* alive for so many years!

For her outstanding support, assistance, and encouragement I am profoundly thankful to Frauke Wildangel. I deeply appreciate her sympathy and patience when I had to work unexpectedly *a little bit* longer or when I could not stop talking about physics or making up crazy analogies to explain correlated noise.

I sincerely thank my family and friends for their exceptional support and for contributing to this work by keeping my mind and heart at the right place, by providing the perfect music, taking care of me eating enough fruit and vegetables, and for reminding me what it is all worth for.

I thank Birger Bohn and his staff for their efforts in establishing and maintaining the FZJ-JOYCE site of the Aerosol Robotic Network (AERONET) program. I thank Alex Cherney for providing the photo of the zodiacal light shown in the introduction of chapter 6. I gratefully acknowledge the effort of the many programmers of the free software which has been used for my studies.

This work was supported by the Bundesministerium für Bildung und Forschung (BMBF), the Astroparticle Eranet (ASPERA), and the Helmholtz-Gemeinschaft Deutscher Forschungszentren e.V.